ΕΘΝΙΚΟ ΜΕΤΣΟΒΙΟ ΠΟΛΥΤΕΧΝΕΙΟ
ΣΧΟΛΗ ΕΦΑΡΜΟΣΜΕΝΩΝ ΜΑΘΗΜΑΤΙΚΩΝ ΚΑΙ ΦΥΣΙΚΩΝ ΕΠΙΣΤΗΜΩΝ

ΤΟΜΕΑΣ ΦΥΣΙΚΗΣ

ΜΕΛΕΤΗ ΑΛΛΗΛΕΠΙΔΡΑΣΗΣ ΑΙΩΡΟΥΜΕΝΩΝ ΣΩΜΑΤΙΔΙΩΝ ΚΑΙ ΝΕΦΩΝ ΜΕ ΧΡΗΣΗ ΤΕΧΝΙΚΩΝ ΤΗΛΕΠΙΣΚΟΠΗΣΗΣ

ΔΙΔΑΚΤΟΡΙΚΗ ΔΙΑΤΡΙΒΗ

ΡΩΜΑΝΟΣ Γ. ΦΩΣΚΙΝΗΣ

ΣΥΜΒΟΥΛΕΥΤΙΚΗ ΕΠΙΤΡΟΠΗ:

ΑΛΕΞΑΝΔΡΟΣ ΠΑΠΑΓΙΑΝΝΗΣ, ΚΑΘ. Ε.Μ.Π. (ΕΠΙΒΛΕΠΩΝ)
ΑΘΑΝΑΣΙΟΣ ΝΕΝΕΣ, ΚΑΘ. EPFL
ΚΩΝΣΤΑΝΤΙΝΟΣ ΕΛΕΥΘΕΡΙΑΔΗΣ, ΕΡΕΥΝΗΤΗΣ Α'-ΕΚΕΦΕ-ΔΗΜΟΚΡΙΤΟΣ

ΕΠΤΑΜΕΛΗΣ ΕΞΕΤΑΣΤΙΚΗ ΕΠΙΤΡΟΠΗ:

Α. ΠΑΠΑΓΙΑΝΝΗΣ, ΚΑΘΗΓΗΤΗΣ Ε.Μ.Π. (ΕΠΙΒΛΕΠΩΝ)
Α. ΝΕΝΕΣ, ΚΑΘΗΓΗΤΗΣ EPFL (ΜΕΛΟΣ)
Κ. ΕΛΕΥΘΕΡΙΑΔΗΣ, ΔΙΕΥΘΥΝΤΗΣ ΕΡΕΥΝΩΝ Α' ΕΚΕΦΕ-ΔΗΜΟΚΡΙΤΟΣ (ΜΕΛΟΣ)
Ε. ΡΕΜΟΥΝΤΑΚΗ, ΚΑΘΗΓΗΤΡΙΑ Ε.Μ.Π. (ΜΕΛΟΣ)
Π. ΦΡΑΓΚΟΣ, ΚΑΘΗΓΗΤΗΣ ΕΜΠ (ΜΕΛΟΣ)
Ι. ΠΑΠΑΔΟΠΟΥΛΟΣ, ΑΝΑΠΛ. ΚΑΘΗΓΗΤΗΣ Ε.Μ.Π. (ΜΕΛΟΣ)
Μ. KOMPPULA, ΕΡΕΥΝΗΤΗΣ Α' FMI (ΜΕΛΟΣ)

ΑΘΗΝΑ, ΔΕΚΕΜΒΡΙΟΣ 2023

Ρωμανός, Γ. Φωσκίνης

Υπ. Διδάκτωρ Φυσικός Ε.Μ.Π.

ΕΚΤΕΝΗΣ ΠΕΡΙΛΗΨΗ ΣΤΗΝ ΕΛΛΗΝΙΚΗ ΓΛΩΣΣΑ

Οι αλληλεπιδράσεις μεταξύ των αιωρούμενων σωματιδίων-νεφών (ή αλλιώς αερολύματα), καθώς και το αποτύπωμά τους στη λευκαύγεια του νέφους και στο κλίμα παραμένουν εξαιρετικά αβέβαιες (Seinfeld et al., 2016; Quaas et al., 2020; IPCC, 2021), λόγω των μη γραμμικών και πολλαπλών ανατροφοδοτήσεων που προκαλούν τα αερολύματα, μεταβάλλοντας έτσι τη δυναμική καθώς και την διάδοση της ακτινοβολίας εντός των νεφών (Stevens και Feingold, 2009). Ένας από τους παράγοντες από τους οποίους πηγάζουν αυτές οι αβεβαιότητες, είναι οι ανθρωπογενείς δραστηριότητες που προκαλούν διακυμάνσεις στις συγκεντρώσεις των πυρήνων συμπύκνωσης νεφών (CCN), οδηγώντας με τη σειρά τους σε διακυμάνσεις στον αριθμό των νεφοσταγονιδίων (N_d) καθώς και στο οπτικό βάθος των νεφών, επηρεάζοντας έτσι το ισοζύγιο της ακτινοβολίας στην ατμόσφαιρα και κατ' επέκταση στο γήινο κλίμα.

Ωστόσο, δεν υπάρχει μια μονοσήμαντη σχέση η οποία να περιγράφει την αύξηση των N_d σε σχέση με τις συγκεντρώσεις των CCN, καθώς η δημιουργία των νεφών εξαρτάται από τον υπερκορεσμό των σταγονιδίων εντός αυτών (Feingold et al., 2001; Ghan et al., 1998; Reutter et al., 2009). Έχει αποδειχθεί ότι τα νέφη μπορούν να είναι, είτε σε μια κατάσταση "*περιορισμένα από τα αερολύματα*", όταν ο υπερκορεσμός τους είναι υψηλός και το N_d ευαίσθητο στις μεταβολές των αερολυμάτων, είτε στην κατάσταση "*περιορισμένα από δυναμική*", όταν ο υπερκορεσμός τους είναι χαμηλός, οπότε το N_d είναι αμετάβλητο σε σχέση με τη συγκέντρωση των αερολυμάτων σε αυτές (Reutter et al., 2009), καθώς ο υπερκορεσμός εξαρτάται από την ατμοσφαιρική τύρβη και τα ανοδικά ρεύματα του αέρα (Bougiatioti et al., 2020; Georgakaki et al., 2021; Kacarab et al., 2020), τα οποία αποτελούν έναν δεύτερο παράγοντα αβεβαιοτήτων, καθώς υπάρχει σημαντική έλλειψη αντίστοιχων μετρήσεων σε παγκόσμια κλίμακα (Rosenfeld et al., 2016). Επομένως, οι τεχνικές τηλεπισκόπησης έρχονται να καλύψουν ένα τέτοιο κενό και αποτελούν τη μόνη προσέγγιση που μπορεί να προσφέρει δεδομένα σε παγκόσμια κάλυψη προκειμένου να βελτιωθούν οι τρέχουσες μέθοδοι ανάκτησης των N_d και να μειώσουν έτσι τις τρέχουσες αβεβαιότητες που συνοδεύουν την ανάκτηση της συγκέντρωσης των N_d (Quaas et al., 2020).

Η παρούσα Διδακτορική Διατριβή, εκτός από μια εκτενή περίληψη των κύριων αποτελεσμάτων που εξήχθησαν στο πλαίσιο της υλοποίησής της, συμπληρώνεται από τέσσερα επιστημονικά άρθρα που έχουν κοινό χαρακτηριστικό τη συνέργεια ενεργητικών και παθητικών τεχνικών τηλεπισκόπησης σε συνδυασμό με επιτόπιες μετρήσεις για την ανάκτηση του ύψους του Ατμοσφαιρικού Οριακού Στρώματος (ΑΟΣ), τη μελέτη της δυναμικής των αερίων μαζών εντός αυτού, αλλά και στην ελεύθερη τροπόσφαιρα, και κυρίως, στη βελτίωση των υφιστάμενων προσεγγίσεων που χρησιμοποιούνται για την ανάκτηση των μικροφυσικών ιδιοτήτων των νεφών (π.χ. N_d) που αναπτύσσονται, τόσο στην κορυφή του ΑΟΣ, όσο και στην ελεύθερη τροπόσφαιρα, χρησιμοποιώντας έναν συνδυασμό επιτόπιων παρατηρήσεων (*in situ*) και δεδομένων παθητικής και ενεργητικής τηλεπισκόπησης, καθώς και δεδομένων από διάφορα μοντέλα παραμετροποίησης ατμοσφαιρικών παραμέτρων.

Ειδικότερα, οι κύριοι στόχοι αυτής της Διατριβής αυτής είναι οι εξής:

α) η βελτίωση του υπάρχοντος αλγορίθμου ανάκτησης αριθμού των νεφοσταγονιδίων με τη χρήση δορυφορικής τηλεπισκόπησης (Bennartz, 2007) με την προσθήκη της εξάρτησης της φασματικής διασποράς των νεφοσταγονιδίων, χρησιμοποιώντας τις μεταβλητές που παρέχονται από το προϊόν των μικροφυσικών ιδιοτήτων των νεφών από δεδομένα METEOSAT και η μελέτη της απόδοσης του

αλγορίθμου ανάκτησης σε σχέση με επιτόπιες εκτιμήσεις της συγκέντρωσης των N_d που προκύπτουν από την παραμετροποίηση ενεργοποίησης νεφοσταγονιδίων του μοντέλου των Nenes και Seinfeld (2003) σε νέφη που αναπτύσσονται υπεράνω του ΑΟΣ (**Άρθρο Ι**),

β) ο χαρακτηρισμός του ρόλου του ΑΟΣ στην αέρια κυκλοφορία, στα μοτίβα τοπικής κυκλοφορίας και της συγκέντρωσης των αιωρούμενων σωματιδίων στο Λεκανοπέδιο της Αττικής με τη χρήση της ενεργητικής τηλεπισκόπησης lidar μέτρησης του ανέμου (Wind Doppler Lidar) για τον προσδιορισμό του ύψους του ΑΟΣ (**Άρθρο ΙΙ**),

γ) ο προσδιορισμός ενός αξιόπιστου κατωφλίου της τυρβώδους ροής για τον χαρακτηρισμό το ύψους του ΑΟΣ με την χρήση lidar Doppler και επιτόπιων μετρήσεων αερολυμάτων στον σταθμό υποβάθρου, με την ονομασία: "Σταθμός τροποσφαιρικού αερολύματος και κλιματικής αλλαγής Χελμού" (HAC)[2] (**Άρθρο ΙΙΙ**)

δ) τη μέτρηση της υγροσκοπικότητας των αιωρούμενων σωματιδίων που συμμετέχουν στον ορογραφικό σχηματισμό νεφών, καθώς και τον χαρακτηρισμό της κατάστασης του σχηματισμού των νεφών (καθεστώτα περιορισμένα σε αερολύματα ή δυναμικής) σε σχέση με την προέλευσή της αέριας μάζας (ΑΟΣ ή ελεύθερη τροπόσφαιρα) (**Άρθρο ΙV**).

Η Διδακτορική Διατριβή (στην Αγγλική γλώσσα) διαρθρώνεται ως εξής:

Στο **Κεφάλαιο 1** παρουσιάζεται, συνοπτικά, το θεωρητικό υπόβαθρο αναφορικά με τη σύσταση της ατμόσφαιρας και τα θέματα που πραγματεύεται η Διδακτορική Διατριβή. Στο **Κεφάλαιο 2** παρουσιάζεται το ενεργειακό ισοζύγιο της ατμόσφαιρας, τα ατμοσφαιρικά αιωρούμενα σωματίδια και ο ρόλος τους στο ενεργειακό ισοζύγιο της γήινης ατμόσφαιρας, στους μηχανισμούς δημιουργίας των νεφών, καθώς και στις αλληλεπιδράσεις μεταξύ αερολυμάτων-νεφών. Στ**ο Κεφάλαιο 3** παρουσιάζονται τα πειραματικά όργανα των επιτόπιων μετρήσεων που χρησιμοποιήθηκαν στην πλαίσιο της παρούσας Διδακτορικής Διατριβής. Στο **Κεφάλαιο 4** παρουσιάζεται το θεωρητικό υπόβαθρο των μεθόδων ενεργητικής και παθητικής τηλεπισκόπησης, και των εφαρμογών τους στον χαρακτηρισμό της ατμοσφαιρικής τύρβης και την ανάκτηση των μικροφυσικών ιδιοτήτων των νεφών. Στο **Κεφάλαιο 5** παρουσιάζονται τα ατμοσφαιρικά μοντέλα και παραμετροποιήσεις που χρησιμοποιήθηκαν. Τέλος, στο **Κεφάλαιο 6** παρουσιάζονται τα κυριότερα αποτελέσματα που δημοσιεύθηκαν σε διεθνή επιστημονικά περιοδικά με κριτές, ως αυτοτελείς ερευνητικές εργασίες και τέλος, αναφέρονται τα κύρια αποτελέσματα της Διδακτορικής Διατριβής.

Ακολούθως, αναφέρουμε, με αναλυτικότερο τρόπο, τα τέσσερα (δημοσιευμένα, είτε υπό κρίση, είτε σε στάδιο υποβολής) άρθρα που εκπονήθηκαν στο πλαίσιο της παρούσας Διδακτορικής Διατριβής, τα οποία έχουν σαν κοινό χαρακτηριστικό τη συνέργεια των τεχνικών τηλεπισκόπησης με τις επιτόπιες μετρήσεις.

Συνοπτικά, στο **Άρθρο Ι** αρχικά αναβαθμίσαμε τον υπάρχοντα αλγόριθμο ανάκτησης του αριθμού των νεφοσταγονιδίων (N_d) με τη χρήση δορυφορικής τηλεπισκόπησης (Grosvenor, 2018 με βάση δορυφορικές μετρήσεις, προσθέτοντας την ρητή εξάρτηση του N_d ως προς τη φασματική διασπορά των σταγονιδίων (β). Στην συνέχεια ο αλγόριθμος εφαρμόσθηκε με μεταβλητές εισόδου τις μικροφυσικές παραμέτρους (οπτικό πάχος (τ), ενεργή ακτίνα νεφοσταγονιδίων (r_{eff}) και θερμοκρασία κορυφής του νέφους (T_{ct})) από το δορυφορικό προϊόν "Optimal Cloud Analysis" της METEOSAT, τις κατακόρυφες κατανομές της πίεσης και θερμοκρασίας από το μοντέλο ERA5 (Hersbach κ.α., 2018), και τέλος, υπολογίσθηκε ο συνολικός ρυθμός συμπύκνωσης των νεφών (Zhu κ.α., 2018) με βάση το ύψος της κορυφής των μελετούμενων νεφών. Ακολούθως, συνοψίσαμε τις υπάρχουσες σχέσεις (β-N_d) μεταξύ της φασματικής διασποράς των σταγονιδίων β και του αριθμού

των νεφοσταγονιδίων N_d με βάση τη διαθέσιμη βιβλιογραφία και ανακτήσαμε τις τιμές του αριθμού των νεφοσταγονιδίων (N_d^{sat}) για κάθε σχέση (β-N_d) ξεχωριστά, και τις αξιολογήσαμε ως προς τις επιτόπιες (*in situ*) εκτιμήσεις του N_d, μέσω της παραμετροποίησης ενεργοποίησης των σταγονιδίων, κατά Nenes και Seinfeld (2003). Τα αποτελέσματα των αξιολογήσεων έδειξαν ότι στην περίπτωση που χρησιμοποιούμε μία σταθερή κατανομή των σταγονιδίων (σταθερή τιμή του β, όπως προτείνουν οι Z06, GCMs και F11), οι ανακτώμενες τιμές του N_d^{sat} τείνουν να υποεκτιμούν τον αριθμό των νεφοσταγονιδίων κατά 34% ±16%, ενώ στην περίπτωση που χρησιμοποιούμε μια εξαρτώμενη κατανομή των σταγονιδίων από τον αριθμό των νεφοσταγονιδίων (όπως προτείνουν οι RL03, και PL03), τότε οι ανακτώμενες τιμές του N_d^{sat} τείνουν να υπερεκτιμώνται σημαντικά στην περίπτωση των RL03, ενώ για την περίπτωση των RL03 οι τιμές του N_d^{sat} υποεκτιμώνται κατά 13.2% ± 34.8%.

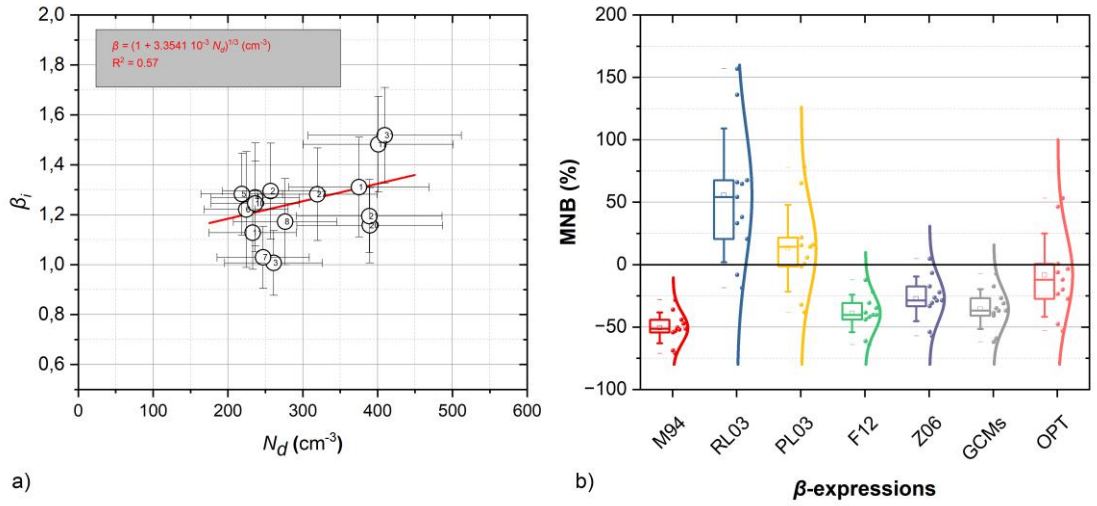

Εικόνα 1. (Αριστερά): Η γραμμική προσαρμογή ευθείας για τον προσδιορισμό της σχέσης μεταξύ της φασματικής διασποράς των σταγονιδίων και του αριθμού των νεφοσταγονιδίων (β-N_d) με βάση τις επιτόπιες μετρήσεις, (Δεξιά): Η κατανομή του μέσου κανονικοποιημένου σφάλματος (MNB) (N_d - N_d^{sat}) χρησιμοποιώντας τις βιβλιογραφικές σχέσεις i) M94, ii) RL03, iii) PL03, iv) F11, v) Z06, vi) GCMs, καθώς και την βελτιστοποιημένη στις επιτόπιες παρατηρήσεις, και vii) OPT, αντίστοιχα.

Επίσης, υπολογίσθηκε μία νέα σχέση (β-N_d) η οποία βασίζεται στις εκτιμήσεις των επιτόπιων N_d η οποία ελαχιστοποιεί την απόκλιση μεταξύ N_d-N_d^{sat} κατά 8.4% ± 33.4%. Η τάξη της ακρίβειας πλέον είναι συγκρίσιμη με αυτή, όταν συγκρίνεται η απόδοση της παραμετροποίησης με τις επιτόπιες μετρήσεις νεφοσταγονιδίων. Αν και τα αποτελέσματα αυτής της σχέσης (β-N_d) που προτάθηκε είναι αρκετά ενθαρρυντικά, απαιτείται περισσότερη έρευνα για να αξιολογηθεί ο βαθμός αξιοπιστίας της, ώστε η μέθοδός μας να μπορεί να εφαρμοσθεί και σε άλλες γεωγραφικές θέσεις, καθώς και σε κλιματικά μοντέλα.

Στο **Άρθρο ΙΙ**, εξετάσαμε τα μοτίβα της τοπικής μεταφοράς νεοσύνθετων (fresh) και γηρασμένων (aged) αιωρούμενων σωματιδίων στον σταθμό παρακολούθησης και χαρακτηρισμού των αιωρούμενων σωματιδίων του Εθνικού Κέντρου Έρευνας Φυσικών Επιστημών (Ε.Κ.Ε.Φ.Ε.) «Δημόκριτος» (DEM) στην Αγία Παρασκευή (Αττικής), καθώς και του τρόπου με τον οποίο επηρεάζονται οι συγκεντρώσεις των αιωρούμενων σωματιδίων σε σχέση με τη θέση του σταθμού ως προς το ύψους του ΑΟΣ (εντός, ενδιάμεσα και εκτός ΑΟΣ).

Το ύψος του ΑΟΣ υπολογίσθηκε με βάση την τύρβη του ατμοσφαιρικού στρώματος μέσω μετρήσεων της κατακόρυφης κατανομής της διεύθυνσης και έντασης του οριζόντιου ανέμου, με χρήση

συστήματος Lidar Doppler. Παράλληλα, χρησιμοποιήθηκαν επιτόπιοι δειγματολήπτες για τον χαρακτηρισμό της χημικής σύνθεσης και της κατανομής μεγέθους των αιωρούμενων σωματιδίων κατά τη διάρκεια της περιόδου από 15 Μαρτίου έως 2 Ιουλίου 2020. Δεδομένου ότι τα νεοσύνθετα αιωρούμενα σωματίδια έχουν μέγεθος μικρότερο των 200 nm, ενώ τα γηρασμένα είναι αρκετά μεγαλύτερα, διαχωρίσαμε τον συνολικό αριθμό αιωρούμενων σωματιδίων με βάση την κατανομή μεγέθους τους σε λεπτά ($N_{10\text{-}200nm}$) (διάμετρος < 200 nm και σε αδρά ($N_{200\text{-}500nm}$) (διάμετρος > 200 nm), αντίστοιχα.

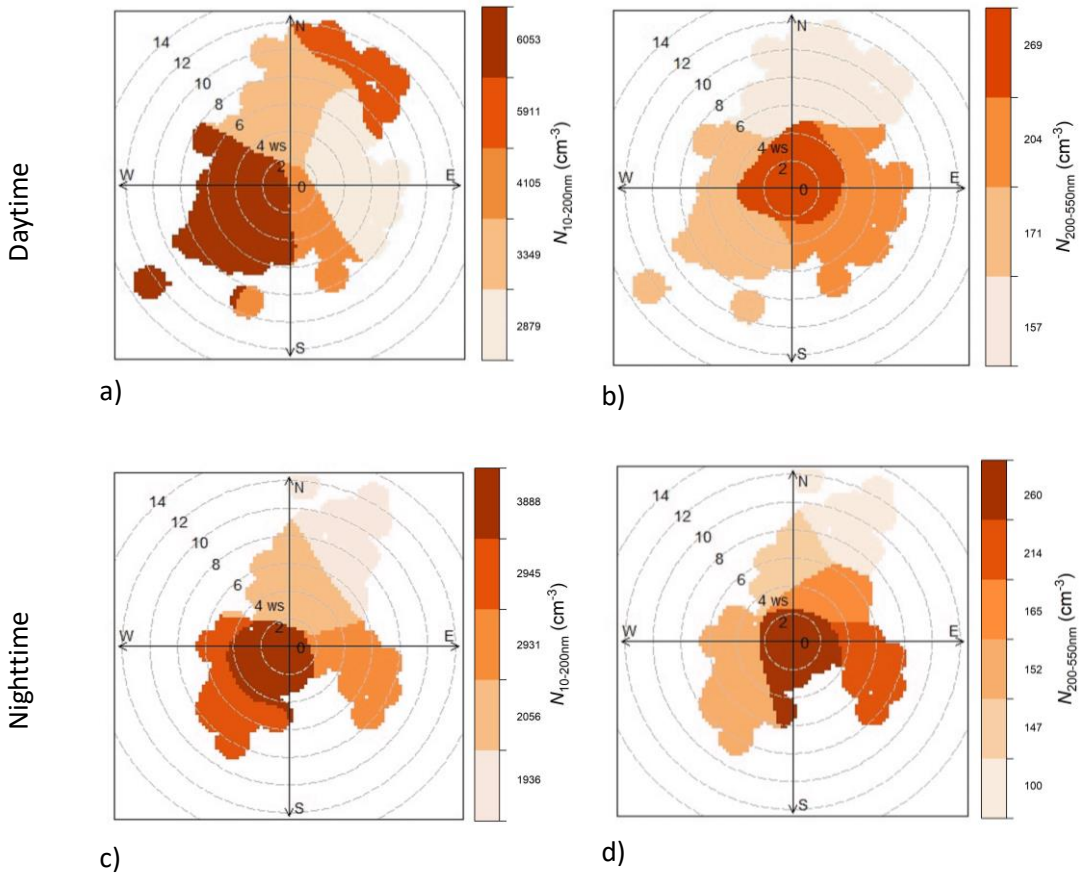

Εικόνα 2. Ομαδοποίηση (Clustering) των $N_{10\text{-}200nm}$ και $N_{200\text{-}550nm}$ με βάση την ένταση και την προέλευση του οριζόντιου ανέμου στο σταθμό DEM κατά την διάρκεια της ημέρας και νύχτας, αντίστοιχα. Η χρωματική κλίμακα της κάθε ομάδας (cluster) αντιπροσωπεύει τη συγκέντρωση αερολυμάτων.

Διαπιστώσαμε λοιπόν, ότι η συγκέντρωση των αιωρούμενων σωματιδίων αυξάνεται σημαντικά όταν οι αέριες μάζες προέρχονται από τον Ν-ΝΔ τομέα της Αττικής, ο οποίος σχετίζεται με εκπομπές κυρίως, από την κυκλοφορία των οχημάτων (6053 ± 3784 cm^{-3} και 171 ± 123 cm^{-3}, αναφορικά με τα νεοσύνθετα και γηρασμένα σωματίδια, αντίστοιχα), καθώς και στις περιπτώσεις στις οποίες ο άνεμος προέρχεται από τον Β-ΒΑ τομέα για τα νεοσύνθετα σωματίδια (5911 ± 3252 cm^{-3}).

Αντίθετα, στην περίπτωση όπου ασθενείς άνεμοι πνέουν από τον ΒΑ-ΝΑ τομέα, οι αέριες μάζες προέρχονται από την περιοχή των Μεσογείων, Αττικής, η οποία χαρακτηρίζεται ως μια περιφερειακή περιοχή χαμηλών εκπομπών, μεταφέρονται, αντίστοιχα, χαμηλές συγκεντρώσεις σε αερολύματα (2879 ± 1832 cm^{-3} και 204 ± 127 cm^{-3} αναφορικά με τα νεοσύνθετα και γηρασμένα σωματίδια, αντίστοιχα). Επιπλέον, εντοπίσαμε καταβατικές ροές ανέμου κατά τη διάρκεια της νύχτας από τον Υμηττό, οι οποίες περιστασιακά, είτε μεταφέρουν ρύπους από ανώτερες στρωματώσεις ενισχύοντας τα επεισόδια αέριας ρύπανσης (2931 ± 1770 cm^{-3} και 214 ± 152 cm^{-3}

αναφορικά με τα νεοσύνθετα και γηρασμένα σωματίδια, αντίστοιχα, όταν η ταχύτητα του ανέμου είναι μεγαλύτερη από 4 m s^{-1}), είτε μεταφέρουν λιγότερο ρυπασμένες αέριες μάζες από το Λεκανοπέδιο της Αθήνας, μειώνοντας σημαντικά τις συγκεντρώσεις των αιωρούμενων σωματιδίων στην περιοχή στον σταθμό του ΕΚΕΦΕ-Δημόκριτος στην Αγία Παρασκευή.

Επίσης, χρησιμοποιήσαμε την προσέγγιση (προσομοίωση) ενός *δυναμικού κουτιού* Hanna et al. (1982) για να υπολογίσουμε το αποτύπωμα της μεταβολής του ύψους του ΑΟΣ στις συγκεντρώσεις των αέριων ρύπων (δηλ. $N_{10\text{-}200nm}$, $N_{200\text{-}500nm}$ και του ισοδύναμου μαύρου άνθρακα-*eBC*). Γενικά, το ύψος του ΑΟΣ επηρεάζει την ικανότητα των αέριων ρύπων να διαχυθούν και να μεταφερθούν οριζόντια μέσα σε αυτό, καθώς σε ένα ρηχό στρώμα ΑΟΣ, δηλαδή με χαμηλό ύψος, η επίδραση της επιφανειακής τριβής του εδάφους γίνεται σημαντική μειώνοντας την ταχύτητα του ανέμου σε αυτό και καταλήγει σε μειωμένη οριζόντια μεταφορά αέριων ρύπων, ενώ στην αντίθετη περίπτωση, ένα βαθύ ΑΟΣ επιτρέπει την καλύτερη διάχυση των αέριων ρύπων και τους μεταφέρει σε μεγαλύτερες αποστάσεις. Τα αποτελέσματα της ανάλυσης μας έδειξαν ότι η μεταβολή του ύψους του ΑΟΣ επιδρά στις συγκεντρώσεις σωματιδίων που παρατηρούνται στο έδαφος, καθώς οποιαδήποτε διακύμανση του ύψους του ΑΟΣ σχετίζεται, εν μέρει, με αλλαγές στην οριζόντια μεταφορά, ενώ το ακριβές ισοζύγιο εξαρτάται από τις αλλαγές στις εκπομπές ή εναποθέσεις σωματιδίων στο Λεκανοπέδιο Αττικής.

Στο **Άρθρο ΙΙΙ**, εξετάσθηκε η δυνατότητα προσδιορισμού του ύψους του ΑΟΣ με χρήση συστήματος lidar ανέμου (Wind Doppler Lidar) στην κορυφή του όρους Χελμός. Η μέθοδος αυτή βασίζεται στη μέτρηση της κατακόρυφης κατανομής της τύρβης (σ_w) που αφορά την κατακόρυφη συνιστώσα του ανέμου w, η οποία μπορεί να μετρηθεί με το σύστημα αυτό, ενώ το ύψος του ΑΟΣ προσδιορίζεται σε εκείνη την τιμή, όπου η τιμή του σ_w γίνεται μικρότερη από μια χαρακτηριστική τιμή κατωφλίου, την οποία προσδιορίσαμε με ακρίβεια. Έτσι, για τον προσδιορισμό της τιμής κατωφλίου, εκμεταλλευτήκαμε την υψομετρική διαφορά που υπάρχει μεταξύ του σταθμού παρακολούθησης της ατμοσφαιρικής ρύπανσης και της κλιματικής αλλαγής στη κορυφή του Χελμού $(HAC)^2$, και ενός χαμηλότερου σημείου (Βαθιά Λάκα) όπου είχε εγκατασταθεί ένα σύστημα lidar ανέμου, ικανό να παρέχει συνεχείς μετρήσεις της τύρβης στο ύψος του $(HAC)^2$.

Δεδομένου ότι η φυσικο-χημική σύσταση της ελεύθερης τροπόσφαιρας διαφέρει από εκείνη εντός του ΑΟΣ (πχ. η ελεύθερη τροπόσφαιρα, συνήθως χαρακτηρίζεται από ξηρές αέριες μάζες, με χαμηλές συγκεντρώσεις σωματιδίων και βιοσωματιδίων σε σχέση με το ΑΟΣ), και δεδομένου ότι ο σταθμός $(HAC)^2$ ευρισκόμενος στην κορυφή του Χελμού, μπορεί να ευρίσκεται στην ελεύθερη τροπόσφαιρα, ή εντός του ΑΟΣ, ή ακόμα σε μια ζώνη μετάβασης μεταξύ του ΑΟΣ και της ελεύθερης τροπόσφαιρας, συσχετίσαμε τις επιτόπιες μετρήσεις των αέριων ρύπων (βιοσωματίδια, αιωρούμενα σωματίδια, *eBC*) στον $(HAC)^2$, της σχετικής υγρασίας, με τις μετρήσεις τύρβης στο ύψος του $(HAC)^2$ και εντοπίσαμε τρεις χωρο-χρονικές περιόδους, όταν:

α) ο $(HAC)^2$ευρίσκεται εντός του ΑΟΣ, και περιβάλλεται από υγρές αέριες μάζες, με υψηλές συγκεντρώσεις αιωρούμενων σωματιδίων, βιοσωματιδίων και ανθρωπογενούς ρύπανσης (στο ύψος του $(HAC)^2$ η τύρβη σ_w > 0.1 m s^{-1}).

β) ο $(HAC)^2$ ευρίσκεται εντός της ελεύθερης τροπόσφαιρας, και περιβάλλεται από σχετικά ξηρές αέριες μάζες, με χαμηλές συγκεντρώσεις αιωρούμενων σωματιδίων, βιοσωματιδίων και ανθρωπογενούς ρύπανσης (στο ύψος του $(HAC)^2$ η τύρβη σ_w < 0.1 m s^{-1}).

γ) ο $(HAC)^2$ ευρίσκεται στη ζώνη μετάβασης μεταξύ του ΑΟΣ και της ελεύθερης τροπόσφαιρας, όπου η επίδραση του ΑΟΣ αναφορικά με τους αέριους ρύπους παραμένει ακόμα σημαντική, αλλά τείνει να εξασθενεί.

Επομένως, χρησιμοποιώντας μια τιμή σ_w = 0.1 m s^{-1} σαν τιμή κατωφλίου, μπορέσαμε να διαχωρίσουμε, με επιτυχία, πότε ο $(HAC)^2$ ευρίσκεται εντός της ελεύθερης τροπόσφαιρας και κατ' επέκταση να προσδιορίσουμε το ύψος του ΑΟΣ συμπεριλαμβάνοντας και τη ζώνη μετάβασης.

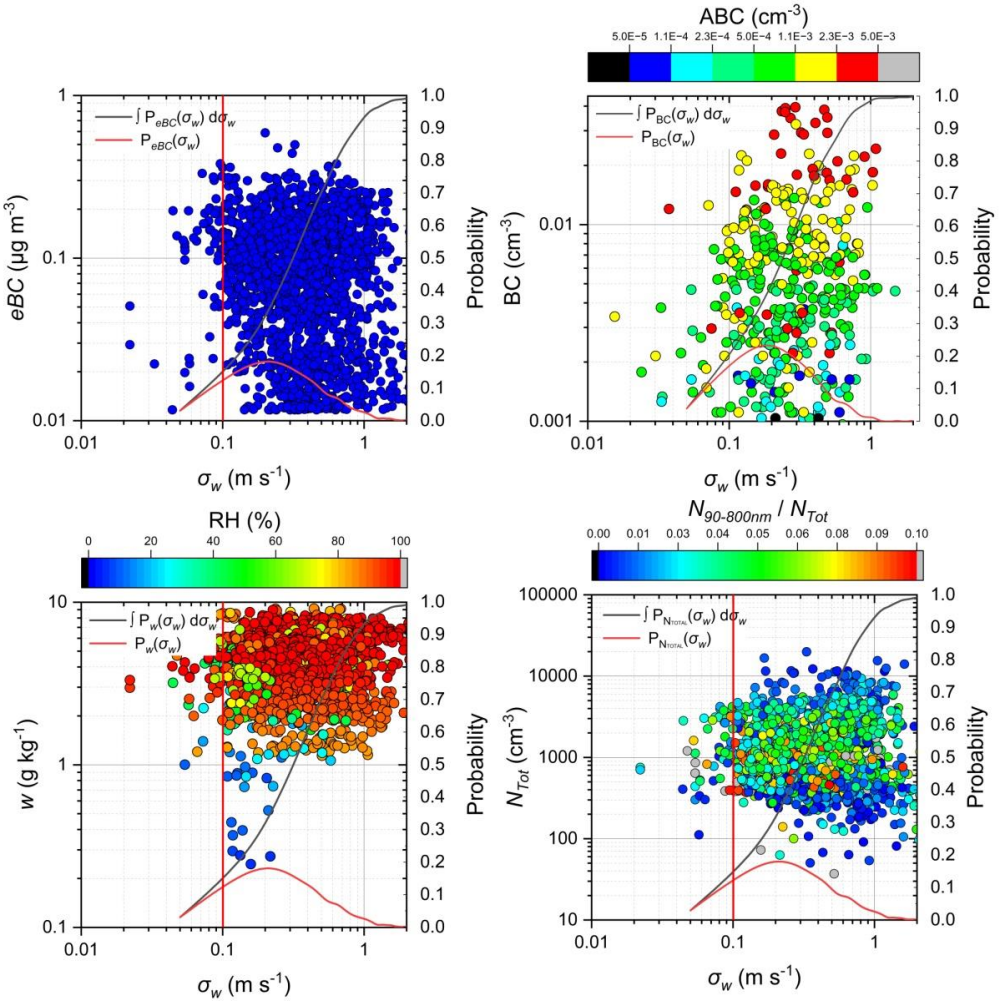

Εικόνα 3. Διάγραμμα διασποράς των a) eBC (μg m^{-3}), b) BC και ABC (cm^{-3}), c) N_{tot} (cm^{-3}) and $N_{90\text{-}800nm}$ /N_{tot} και d) w (g kg^{-1}) και RH (%) σε σχέση με το σ_w (m s^{-1}) στο ύψος του $(HAC)^2$. Οι κόκκινες καμπύλες αντιπροσωπεύουν την κανονικοποιημένη συχνότητα της κάθε μέτρησης, ενώ οι μαύρες καμπύλες αντιπροσωπεύουν την αθροιστική πιθανότητα εμφάνισης της μέτρησης. Οι κατακόρυφες ευθείες παρουσιάζουν την τιμή κατωφλίου 0.1 m s^{-1} επισημαίνοντας την μετάβαση μεταξύ της ελεύθερης τροπόσφαιρας (αριστερά της κόκκινης) και του ΑΟΣ (δεξιά της κόκκινης γραμμής).

Στο **Άρθρο IV**, εξετάσαμε την υγροσκοπικότητα των αιωρούμενων σωματιδίων πριν την δημιουργία των νεφών, καθώς και των μη ενεργοποιημένων σωματιδίων σε νεφοσταγονίδια κατά τον σχηματισμό ορογραφικών νεφών σε σχέση με την προέλευση της αέριας μάζας που σχημάτισε τα μελετούμενα νέφη (στο ΑΟΣ και στην ελεύθερη τροπόσφαιρα), για να κατανοήσουμε τον τρόπο σχηματισμού των νεφών (καθεστώτα περιορισμένα από σωματίδια/δυναμικής). Για το σκοπό αυτό ήταν αναγκαίο να αναπτύξουμε μια τεχνική εικονικού φίλτρου, η οποία μπορεί να χρησιμοποιηθεί σε συστήματα ενός συλλέκτη με δεδομένη τη συνεχή μέτρηση του μεγέθους των σταγονιδίων, ώστε να διαχωρίσουμε τα αποξηραμένα νεφοσταγονίδια από τα μη ενεργοποιημένων σωματιδίων. Η μέθοδος αυτή βασίζεται στον προσδιορισμό του ελάχιστου μεγέθους σταγονιδίων που μπορούν να διεισδύσουν στη γραμμή ροής (χαρακτηριστικό μέγεθος).

Χρησιμοποιώντας την τεχνική εικονικού φίλτρου, διαχωρίσαμε τις στιγμές κατά τις οποίες η δειγματοληψία που πραγματοποιούνταν εντός των νεφών, αποτελούταν από ένα μίγμα μεταξύ μη ενεργοποιημένων σωματιδίων και αποξηραμένων σταγονιδίων, είτε μόνο από τα μη ενεργοποιημένα σωματίδια. Έτσι, υπολογίσαμε τη μέση υγροσκοπικότητα των σωματιδίων (*κ**) πριν την δημιουργία των νεφών, καθώς επίσης και την υγροσκοπικότητα των ενεργοποιημένων και μη σωματιδίων.

Στην περίπτωση όπου το αερόλυμα (ή τα σωματίδια) προέρχονται από την ελεύθερη τροπόσφαιρα, η υγροσκοπικότητα τους πριν την δημιουργία του νέφους βρέθηκε 0.34 ± 0.09, ενώ κατά την δημιουργία των νεφών η υγροσκοπικότητα των ενεργοποιημένων σωματιδίων βρέθηκε 0.45 ± 0.20, ενώ των μη 0.31 ± 0.15. Ομοίως, στην περίπτωση όπου το αερόλυμα προέρχονται από το ΑΟΣ, η υγροσκοπικότητα τους πριν την δημιουργία του νέφους βρέθηκε 0.43 ± 0.12, ενώ κατά την δημιουργία των νεφών 0.44 ± 0.18 και 0.29 ± 0.19 και για τα ενεργοποιημένα και μη, αντίστοιχα. Επιπλέον, χρησιμοποιώντας ένα θάλαμο ενεργοποίησης σωματιδίων, (θέτει τα σωματίδια σε διαφορετικούς υπερκορεσμούς και μετράει τον αριθμό των ενεργοποιημένων), υπολογίσαμε τον χαρακτηριστικό υπερκορεσμό (*s**) του κάθε νέφους και βρήκαμε ότι όταν τα νέφη σχηματίζονται πάνω από προϋπάρχοντα σωματίδια που προέρχονται από την ελεύθερη τροπόσφαιρα, τότε τα νέφη είναι ευαίσθητα σε μεταβολές της συγκέντρωσης των αερολυμάτων (Reutter et. al., 2009), ενώ όταν τα νέφη σχηματίζονται από αερόλυμα προερχόμενο από το ΑΟΣ, είναι κυρίως ευαίσθητα σε μεταβολές στις μεταβολές ταχύτητας.

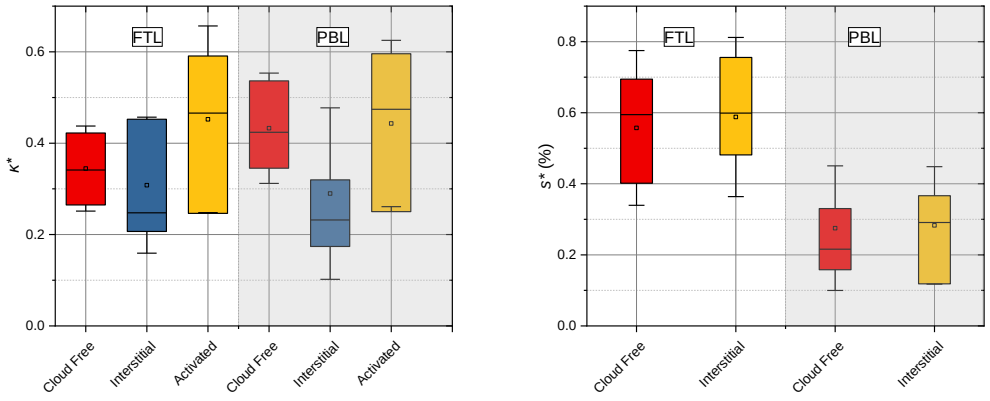

α) β)

Εικόνα 4. Τα στατιστικά του s (α) και κ* (β) σε δείγματα πριν τη δημιουργία νεφών, σε μίγματα μη ενεργοποιημένων σωματιδίων και αποξηραμένων σταγονιδίων, και των ενεργοποιημένων, για κάθε δείγμα όταν αυτά προήλθαν είτε από την ελεύθερη τροπόσφαιρα, είτε από το ΑΟΣ, αντίστοιχα.*

Επίσης, χρησιμοποιήσαμε μια παραμετροποίηση ενεργοποίησης σταγονιδίων η οποία βασίζεται στις μετρήσεις αερολυμάτων που προέρχονται είτε κάτω από τη βάση του νέφους είτε εντός του νέφους (in-cloud), αντίστοιχα, και υπολογίζει τον αριθμού των νεφοσταγονιδίων καθώς και τον μέγιστο υπερκορεσμό.

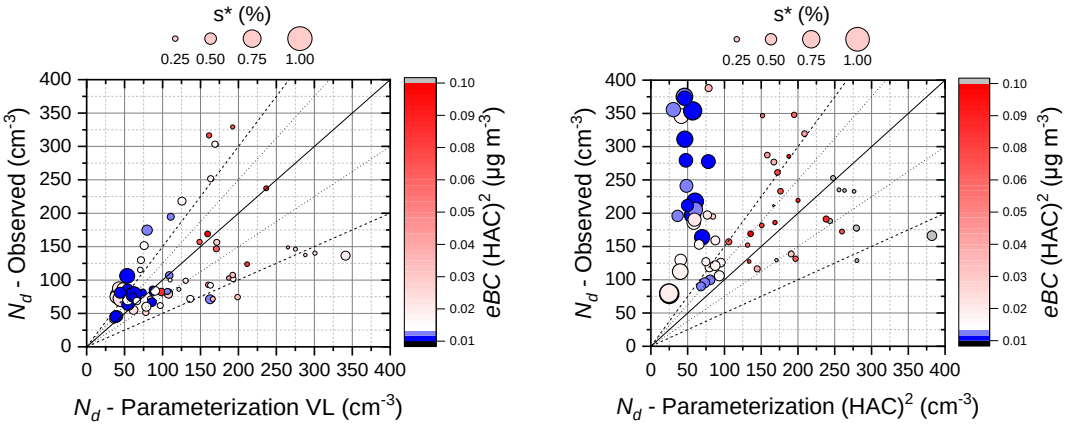

Εικόνα 5. Η σύγκριση του N_d της παραμετροποίησης σε σχέση με τις επιτόπιες μετρήσεις, χρησιμοποιώντας τα αερολύματα που προέρχονται είτε εντός του νέφους ((HAC)^2) (α), είτε κάτω από την βάση του (VL) (β), αντίστοιχα. Η χρωματική κλίμακα αντιστοιχεί στην συγκέντρωση του eBC που είναι αντιπροσωπευτική για τον χαρακτηρισμό της προέλευσης του αερολύματος (χαμηλές τιμές – ελεύθερη τροπόσφαιρα, υψηλές τιμές – ΑΟΣ) , ενώ το μέγεθος του συμβόλου αντιστοιχεί στο s (s*<0.1% καθεστώτα όπου τα νέφη είναι ευαίσθητα σε μεταβολές της ταχύτητα, ενώ όταν το s* ~ 1 τα νέφη είναι ευαίσθητα σε μεταβολές του αερολύματος).*

Χρησιμοποιώντας το αερόλυμα κάτω από τη βάση του νέφους, επιτεύχθηκε συμφωνία στον αριθμού των νεφοσταγονιδίων (N_d) εντός ±25%, όταν αυτός προκύπτει από την παραμετροποίηση σε σχέση με τις επιτόπιες μετρήσεις. Στην περίπτωση που μετρήσεις αερολυμάτων που προέρχονται μέσα από το νέφος (in-cloud), διαπιστώσαμε ότι το N_d που προκύπτει είναι υποτιμημένο σε σύγκριση με τις επιτόπιες μετρήσεις, ειδικά σε νέφη που είναι ευαίσθητα σε μεταβολές του αερολύματος. Καταλήγοντας, ότι το αερόλυμα εντός νέφους μπορεί να χρησιμοποιηθεί μόνο όταν τα νέφη είναι ευαίσθητα σε μεταβολές της ταχύτητας. Ενώ όταν τα αερολύματα προέρχονται κάτω από τη βάση του νέφους είναι αντιπροσωπευτικά για τις περιόδους πριν και μετά τη δημιουργία του νέφους.

Επίσης, διαπιστώσαμε ότι η κατάσταση περιορισμένης ταχύτητας (κατάσταση όπου τα νέφη είναι ευαίσθητα στις μεταβολές στη ταχύτητας) επιβεβαιώνεται όταν ο χαρακτηριστικός υπερκορεσμός του νέφους είναι χαμηλός και συμφωνεί με τις προβλέψεις παραμετροποίησης.

Λέξεις Κλειδιά

Ενεργητική και Παθητική Τηλεπισκόπηση, LiDAR, Δορυφόροι, Ατμοσφαιρικά Αιωρούμενα Σωματίδια, Νέφη, Επιτόπιες Μετρήσεις

NATIONAL TECHNICAL UNIVERSITY OF ATHENS
SCHOOL OF APPLIED MATHEMATICAL AND PHYSICAL SCIENCES

DEPARTMENT OF PHYSICS

STUDY OF AEROSOL AND CLOUDS USING REMOTE SENSING TECHNIQUES

DOCTORAL DISSERTATION THESIS

ROMANOS, G. FOSKINIS

SUPEVISORS:

ALEX PAPAYANNIS, PROF. NTUA (SUPEVISOR)
ATHANASIOS NENES, PROF. EPFL (CO-ADVISOR)
KONSTANTINOS ELEFTHERIADIS, RESEARCH DIRECTOR NCSRD (CO-ADVISOR)

EXAMINATION COMMITTEE:

ALEX PAPAYANNIS, PROF. NTUA (SUPEVISOR)
ATHANASIOS NENES, PROF. EPFL (MEMBER)
KONSTANTINOS ELEFTHERIADIS, RESEARCH DIRECTOR NCSRD (MEMBER)
E. REMOUNTAKIS, PROF. NTUA (MEMBER)
P FRAGOS, PROF. NTUA (MEMBER)
I. PAPADOPOULOS, PROF. NTUA (MEMBER)
M. KOMPPULA, RESEARCHER FMI (MEMBER)

ATHENS, DECEMBER 2023

ABSTRACT

Aerosol-cloud interactions and their imprint on cloud albedo and climate still remain highly uncertain (Seinfeld et al., 2016; Quaas et al., 2020; IPCC, 2021), given the highly buffered, nonlinear and multiscale nature of clouds and their interactions with atmospheric dynamics, radiation, and aerosols (Stevens and Feingold, 2009). A major reason for these uncertainties corresponds to anthropogenic activities that cause variations in cloud condensation nuclei concentrations (CCN) leading to modulations in cloud droplet number concentration (N_d) and the cloud's optical thickness, thus, affecting the Earth's radiation budget and climate. However, there is no single relation to describe the increase of N_d in respect to CCN since the cloud formation depends on the supersaturation level inside the clouds (Feingold et al., 2001; Ghan et al., 1998; Reutter et al., 2009). It has been shown that there are two regimes: the "aerosol-limited", when supersaturation is high and N_d is very sensitive to aerosol changes and the "velocity-limited", when the supersaturation is so low that N_d is insensitive to aerosol changes (Reutter et al., 2009). The supersaturation depends only on the intensity of atmospheric turbulence within the PBL (Bougiatioti et al., 2020; Georgakaki et al., 2021; Kacarab et al., 2020) which is a second major reason for the uncertainties on the N_d, since there is lack of such global datasets especially regarding the cloud-base updrafts (Rosenfeld et al., 2016). The remote sensing techniques are the only ones with the potential to obtain global datasets to improve the current retrieval algorithms (Quaas et al. (2020) and to contribute to minimizing the current uncertainties on the estimation of the N_d

This Doctoral Thesis aims to implement and further improve existing remote sensing approaches for the retrieval of N_d in non-precipitating Planetary Boundary Layer clouds (PBLC), and for the study of the Planetary Boundary Layer (PBL) dynamics, using a combination of *in situ* observations, ground-based remote sensing and model data. This Thesis is based on four original papers, focusing mainly on the use of the synergies of remote sensing and *in situ* techniques in atmospheric applications for retrieving the aerosol and cloud properties, as well as the Planetary Boundary Layer (PBL) dynamics.

The main objectives of this Thesis are: a) to further improve an established satellite droplet number retrieval algorithm (Bennartz, 2007), which illustrates the cloud microphysical variables derived by the METEOSAT, at non-precipitating PBLC where the dependence on spectral dispersion of droplets droplet number is explicitly accounted, and to examine its performance against the *in situ* N_d estimations obtained by the droplet activation parameterization of the Nenes and Seinfeld (2003) (**Paper I**); b) to use a wind Doppler lidar to measure the height of PBL (PBLH), and investigate the effect of local air mass circulation and transport patterns on the aerosol load in respect of the PBLH diurnal cycle (**Paper II**); to determine a reliable threshold to be used at the PBLH retrieving technique using wind Doppler lidar in an orographic environment (**Paper III**); to utilize the *in situ* measurements obtained at the high-altitude station Hellenic Atmospheric Aerosol and Climate Change station (HAC)^2 at the Helmos mountain (Greece), alongside the established threshold for retrieving the PBLH (**Paper III**), to measure the pre-cloud aerosol hygroscopicity, as well as the hygroscopicity of the cloud residuals during orographic clouds formation in respect of its relation to airmass origin, and understand the cloud formation state (aerosol-/velocity-limited regimes) and its link to airmass origin (PBL, free tropospheric, etc.) (**Paper IV**).

This Doctoral Thesis is organized as follows: the theoretical background of the atmospheric radiation, aerosol particles, cloud microphysics, and aerosol-cloud interactions are described in Section 2; the *in situ* measuring experimental techniques are described in Section 3; the remote sensing experimental techniques are described in Section 4; the models and parameterizations used are presented in Section 5; the main results of each original papers are presented in Section 6; while the conclusions/findings are described in Section 7.

Keywords

Active and Passive remote sensing, LiDAR, Satellite, Aerosols, Clouds, *in situ* observations

ACKNOWLEDGMENTS

This Thesis has been conducted at the Laser Remote Sensing Unit (LRSU) of the Laboratory of Optoelectronics and Lasers, at the Physics Department of the School of Applied Mathematics and Physical Sciences of the National Technical University of Athens (NTUA), in collaboration with the Environmental Radioactivity & Aerosol technology for atmospheric and Climate impacT Laboratory (ENRACT) of the Institute of Nuclear & Radiological Sciences & Technology, Energy & Safety (INRASTES) of the National Centre for Scientific Research (NCSRD) 'Demokritos', the Center of Studies on Air quality and Climate Change (C·STACC) of the Institute of Chemical Engineering of the Foundation for Research and Technology Hellas at Patras (FORTH/ICE-HT) and the Laboratory of Atmospheric Processes and their Impacts (LAPI) of the at Swiss Federal Institute of Technology in Lausanne (EPFL). We acknowledge the Finnish Meteorological Institute (FMI) for providing the wind Doppler Lidar "HALO" and the NCSRD for hosting the HALO lidar at the Demokritos and Helmos sites.

This Thesis is not just an individual work of mine, but results from a continuous work with my supervisors and my collaborators at LRSU, ENRACT, C·STACC, and LAPI. Thus, I would like to deeply thank all of them.

I am grateful to my supervisor Prof. Alexandros Papayannis (NTUA/EPFL) for trusting me and being so consultative and encouraging throughout this Thesis. I would also like to express my gratitude to my co-supervisors: Prof. Athanasios Nenes (EPFL) for advising me, spending time discussing and commenting on my results on each single step, and giving me the opportunity to collaborate with the LAPI members; Research Director Konstantinos Eleftheriadis (NCSR) for giving me the opportunity to collaborate with ENRACT members and for his valuable scientific ideas, comments, and useful advices.

The aforementioned persons form my Thesis Advisory committee; they initiated me into their research groups and gave me the opportunity to work on challenging, yet interesting research projects and field campaigns; they spent a lot of time at various experimental campaigns despite the difficulties and the technical problems, usually under extreme weather conditions, they spent a lot of time on discussing my concerns, scientific ones or not. They were always pleasant, and I am grateful for all the support they provided me. They pushed me every time to try harder, to find my own solutions and overcome the difficulties, and become a better scientist.

Thanks to all of you for trusting me, for being motivative, willing to help, and available anytime I needed your help to construct a scientific view and critical thinking and thus introducing me to the scientific world; it has been my pleasure to work with you.

I would also like to thank the Associate Prof. Panos Kokkalis (Univ. of Kuwait) for his advices, the scientific discussions and his proofreading comments. My thanks also go to the members of LRSU, ENRACT, C·CSTAC and EPFL.

Finally, my warmest thanks to my family for supporting me all these years, and they keep on.

Athens, December 2023.

FUNDING AND FELLOWSHIPS

This research was funded jointly by the:

- PANhellenic infrastructure for Atmospheric Composition and climatE change (PANACEA) research project (MIS 5021516), implemented under the Action Reinforcement of the Research and Innovation Infrastructure, and the Operational Program Competitiveness, Entrepreneurship, and Innovation (NSRF 2014–2020), co-financed by Greece and the European Union (European Regional Development Fund).

- European Research Council, CoG-2016 project PyroTRACH (726165) funded by H2020-EU.1.1. – Excellent Science, and from the European Union Horizon 2020 project FORCeS under grant agreement No 821205.

- General Secretariat of Research and Innovation 105658/17-10-2019 in the framework of the research program "National Research Network for climate change and its effects" E.E-12365" at NCSR.

- Basic Research Program, NTUA (PEVE) under contract PEVE0011/2021.

CONTENTS

LIST OF PEER-REVIEWED JOURNAL PUBLICATIONS

This Doctoral Thesis is based on research presented in the following research papers cited by the numbers I-IV:

I. **Foskinis, R.**, Nenes, A., Papayannis, A., Georgakaki, P., Eleftheriadis, K., Vratolis, S., Gini, M. I., Komppula, M., Vakkari, V., and Kokkalis, P. (2022). Towards reliable retrievals of cloud droplet number for non-precipitating planetary boundary layer clouds and their susceptibility to aerosol. *Frontiers in Remote Sensing*, 3. https://doi.org/10.3389/frsen.2022.958207

II. **Foskinis, R.**, Gini, M., Kokkalis, P., Diapouli, E., Vratolis, S., Granakis, K., Zografou, O., Komppula, M., Vakkari, V., Nenes, A., Papayannis, A., and Eleftheriadis, K. (2024). On the relation between the planetary boundary layer height and in situ surface observations of atmospheric aerosol pollutants in an urban area. *Atmospheric Research.* https://doi.org/10.2139/SSRN.4536471

III. **Foskinis R.**, Gao K., Gini, M. I., Diapouli E., Vratolis S., Granakis K., Zografou O., Kokkalis P., Kommpula M., Vakkari V., Eleftheriadis K., Nenes A., and Papayannis A. (2024). The Influence of the Planetary Boundary Layer on the Atmospheric State at an Orographic Site at the Eastern Mediterranean. (2024). *Tellus B*: Chemical and Physical Meteorology, X(X): 1–13. https://doi.org/10.16993/tellusb.1876 .

IV. **Foskinis R.**, Motos M., Gini M. I., Zografou O., Gao K., Vratolis S., Granakis K., Vakkari V., Violaki K., Aktypis A., Kaltsonoudis C., Shi X., Komppula M., Pandis S., Eleftheriadis K., Papayannis A., and Nenes A. (2024). Drivers of Droplet Formation in East Mediterranean Orographic Clouds, *EGUsphere*. https://doi.org/10.5194/egusphere-2024-490

1 INTRODUCTION

The atmosphere contains several distinct stratified layers based on the temperature vertical profile; most of the atmospheric mass (consisting of a mixture of water vapour, gases, aerosols, and molecules) is contained in the first two layers, the troposphere, and the stratosphere. The troposphere is the lower atmospheric layer which extends from the Earth's surface up to about 7-17 km depending on the geographic latitude (Wallace and Hobbs, 2006). In this atmospheric layer the main weather phenomena occur, including chemical reactions, clouds, and precipitation.; the stratosphere, is located above the tropopause and extends up to about 50-55 km height and is characterized by very low water content and very high ozone concentrations (ozone layer) acting as a filter of the incoming ultraviolet solar radiation. The Earth's energy budget is controlled by the exchange of energy between the incoming shortwave solar radiation and the outgoing Earth's longwave radiation, the top of the atmosphere, as well as the atmospheric gases, aerosols, and clouds (Hansen et al., 2005, Wallace and Hobbs, 2006)

The primary composition of the atmosphere is of 78% N_2, 21% of O_2, 0.93% of Ar, as well as of other gases, like CO_2, CH_4, O_3, which play a crucial in the global warming effect, due to their increasing concentration in the troposphere. Besides gases, the atmosphere contains aerosol particles (primary or secondary ones) which are solid or liquid particles of different chemical composition and origin; their size varies from a few nm to several μm. Although the aerosol particles are found in rather small quantities in the atmosphere, they play a key role in the climate sensitivity since they can influence the Earth's radiation budget by scattering (cooling effect) or absorbing (warming effect) the incoming solar radiation and the outgoing Earth's radiation (*c.f.* Figure 1.1). Last, but not least, the aerosols can act as CCN, affecting the cloud formation and their physical properties (e.g., lifetime). The aerosols also participate in complex chemical reactions in the atmosphere, leading in the formation of secondary aerosols (*c.f.* Figure 1.1). Thus, the aerosol particles and their interactions with clouds are of great scientific interest, given the large uncertainty of modeling them, as they participate in the radiation budget in the atmosphere and impact on the air quality and climate (McCormick and Ludwig, 1967; Twomey, 1974; Lohmann and Feichter, 2005; IPCC, 2014).

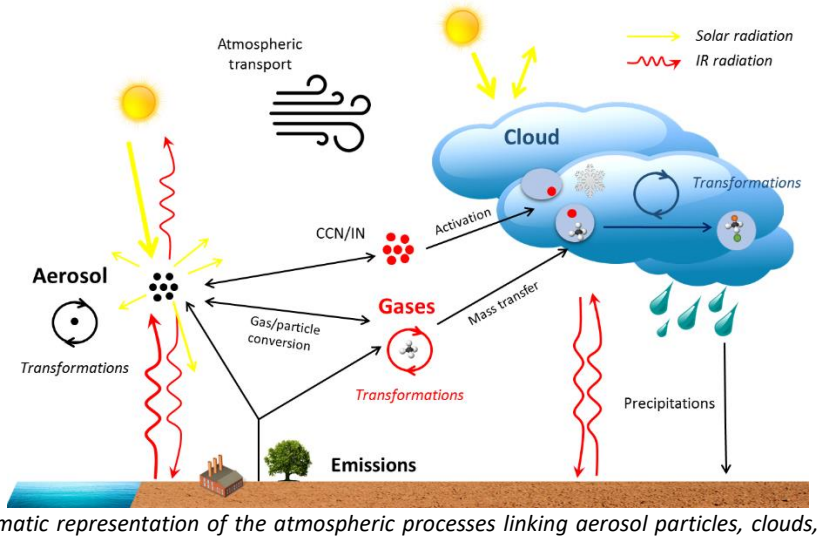

Figure 1.1. A Schematic representation of the atmospheric processes linking aerosol particles, clouds, precipitation, and radiation (Baray et al., 2020).

The aerosol particles are characterized as natural and anthropogenic ones, based on their source origin. The natural aerosols belong to the bioaerosols, when they are released from plants, animals or oceans, including seeds, pollen, and spores (usually 1–250 μm in diameter), bacteria, algae, protozoa, fungi, and viruses (generally less than 1 μm in diameter), or from oceanic organic material injected by jet drops when an air bubble bursts; when these drops are evaporated they release sea-salt particles and other materials in the atmosphere; the natural aerosols are mainly emitted from large natural sources such as desert areas, volcanic eruptions, biomass burning (e.g. wildfire events).

The anthropogenic particles are mostly emitted from processes like fuel combustion, biomass burning, road dust from roads, and industrial processes. The global input of anthropogenic particles into the atmosphere contributes to about 20% of the average mass of the global natural sources and their concentration increases in relation to the extent of the human activities. The aerosol particles can be also formed *in situ* by the condensation of gases, leading to the formation of secondary particles (Seinfeld and Pandis, 2016)

The residence times of the aerosols in the atmosphere vary from a few days in the lower troposphere to some months in the upper troposphere and the stratosphere (Seinfeld and Pandis, 2016). The residence time is generally related to their size and mass (aerosols with diameters <0.01 μm can be removed by diffusion to cloud particles and coagulation in the atmosphere, while those with diameters >20 μm can be removed, by sedimentation, impaction onto surfaces, and from precipitation scavenging. The aerosols with diameters 0.2-2 μm may stay much longer, usually reaching several hundred days in the upper troposphere, or a few weeks in the middle and lower troposphere and are removed by precipitation scavenging (Seinfeld and Pandis, 2016).

When a moist air parcel becomes supersaturated, the water vapour condenses onto the aerosol particle's surface and forms droplets, the so-called “Cloud Condescension Nuclei” (CCN), while in extremely low temperatures the water vapour spontaneously freezes on its self (called homogeneous freezing), or onto the aerosol particle's surface so-called “Ice Nuclei” (IN) (called heterogeneous freezing).

The clouds are characterized based on their content, as *warm clouds*, when they consist of cloud droplets and interstitial aerosols, as *mixed-phased clouds*, when they consist of cloud droplets and ice crystals and as *ice clouds*, when they only consist of ice crystals and interstitial aerosols. Each type of cloud is found at different atmospheric heights in relation to their temperature. Thus, the warm clouds are found at heights where the temperature is above 0^{o} C. The mixed-phased where the temperature is above -35^{o}C and below 0^{o} C, while the ice phase clouds are found in heights where the temperature is below -35^{o}C.

Given the different cloud top temperatures, each cloud type exhibits contrasting net radiative effects (Ramanathan et al., 1989). As a result, the low-level clouds, reflect the incoming solar radiation (shortwave radiation) into space, thus reducing the amount of the incoming radiation reaching the Earth’s surface. These clouds have typically a cooling effect on the Earth's surface (Lynch, 1996), but they can also absorb and re-emit the outgoing longwave radiation (infrared radiation), thus producing a warming effect in the atmosphere. The high-level clouds are highly transparent to shortwave radiation, but they can readily absorb the outgoing longwave radiation, mostly contributing to warming effect. In contrast, several recent studies showed that low-level Arctic clouds have a warming effect (Intrieri et al., 2002; Cronin and Tziperman, 2015) and that is why the ice-covered ground surface is more efficient in reflecting incoming radiation, thus the presence of low-

level clouds contribute to warming. As a result, not only the type and the cloud microphysical properties affects the radiation budget, but also the location (*e.g.* above ice) where the clouds are formed.

However, the efficient modeling of aerosols in cloud-scale remains still unclear, since some aerosols were found to be more efficient in acting as CCN or IN than others (Demott et al., 2003; Atkinson et al., 2013; Kanji et al., 2017), thus, their importance in cloud-scale remains debatable (Ansmann et al., 2009; Zhang et al., 2015; Li et al., 2017; Zamora et al., 2018). As a result, even though the understanding of the clouds and the aerosols separately is quite well, the aerosol-cloud interactions overall are still one of the low scientific understating aspects, while they are the stronger factor that contributes to climate cooling effect, which mitigates some of the greenhouse gas warming and affects climate sensitivity (Boucher et al., 2013; Stevens and Feingold, 2009; Calvin et al., 2023). Therefore, there is a pressing need for continuous monitoring of the aerosol particles and clouds, having extensive global datasets to understand their relative importance (Rosenfeld et al., 2016), while the only remote sensing techniques offer the potential of obtaining global datasets with frequent coverage, carrying many uncertainties that require constraints that can only be addressed with *in situ* and/or ground-based remote sensing observations (Quaas et al., 2020) - and that is why this doctoral dissertation emphasizes on studying the aerosols and clouds using multiple remote sensing techniques and synergies of *in situ* instrumentation.

Remote sensing techniques refer to obtaining information about a target remotely by analyzing how the target interacts with electromagnetic radiation. There are two types of remote sensors, those that are focused on how a target interacts with the solar radiation, so-called “passive”, and those that emit their electromagnetic radiation in various wavelengths, so sensors are focused on these separately. For instance, the geostationary meteorological satellites (METEOSAT) operated by the European Organization for the Exploitation of Meteorological Satellites (EUMETSAT) are equipped with a multi-spectral which range from 0.4 to 14.40 μm to collect the backscattered solar radiation from the clouds or the Earth’s surface, while the elastic or Raman Light Detection and Ranging (lidar) instrument, transmits a pulsed single-wavelength laser beam (*e.g.,* at 355nm) into the atmosphere and collects as a time-resolved the backscattered signal from the aerosols or clouds, and that is the way we obtain the cloud microphysical quantities and the aerosol properties remotely to initialize the weather forecasting models. The key point of remote sensing is to use suitable wavelength ranges where the given target is sensitive to them, given that the scatterers follow the Mie scattering, the cloud droplets are sensitive to the visual band, while the aerosols are on near-/infrared band. As a result, each of the targets (clouds or aerosols) can reflect, scatter, or absorb a fraction of the incident electromagnetic radiation.

Nowadays, the lidar applications in atmospheric research have been increasingly employed in aerosol monitoring (Weitkamp, 2005), while they have been extended to wind retrievals using the Doppler shifting effect by measuring the relevant motion of the moving aerosols with high vertical/temporal resolution of a few meters/seconds, respectively. Additionally, the new METEOSAT series (MSG-3/4) satellites offer highly detailed imagery with a high spatial resolution (a few kilometers) every 15 minutes in 12 channels (within visible and thermal range) for cloud applications. Thus, these applications give a great potential to study and improve our current knowledge of aerosols and clouds by offering the potential of obtaining global datasets in high frequency and spatial coverage, while using the synergy of lidar-satellite and *in situ* observations, making them a powerful tool to study aerosol-cloud interactions.

2 FUNDAMENTALS

2.1 RADIATION AND EARTH'S ATMOSPHERE

Talking about radiation in atmospheric science, what matters is the radiation budget within the atmosphere. The incoming radiation is emitted by the sun (solar) while the outgoing is by the Earth (terrestrial), while each radiation differs in its spectral width and shape; the spectral width of the emitted spectrum of the Sun ranges from 0.15 to 4 μm, while that of the Earth emits in the infrared from 0.1 μm to 100 μm. As the Earth's atmosphere contains gases, molecules, and aerosols, all of them contribute to the extinction of the incoming solar and terrestrial radiation, while the different types of land cover and clouds contribute to the reflection and scattering of both radiations. The incoming solar radiation at the Top of the Atmosphere (TOA) equals 340 ± 1 W m^{-2}, of which 75 W m^{-2} are reflected from the clouds and 25 W m^{-2} from the Earth's surface back to space, while 239 ± 3 W m^{-2} are emitted in the thermal spectrum to space both from clouds and the Earth's surface. Additionally, 80 ± 9 W m^{-2} are absorbed by the atmosphere, 103 ± 3 W m^{-2} are converted to evaporation and sensible heat, while 342 ± 5 W m^{-2} are remitted from the atmosphere back to the Earth, giving an imbalance of 0.7 ± 0.2 W m^{-2} which is responsible for the global warming effect (Calvin et al., 2023). However, this is not always the case since the cloud coverage and their reflectance, the aerosol spatial concentrations and the land-cover show large spatiotemporal variations leading to a modification of the Earth's radiation budget (*c.f.* Figure 2.1).

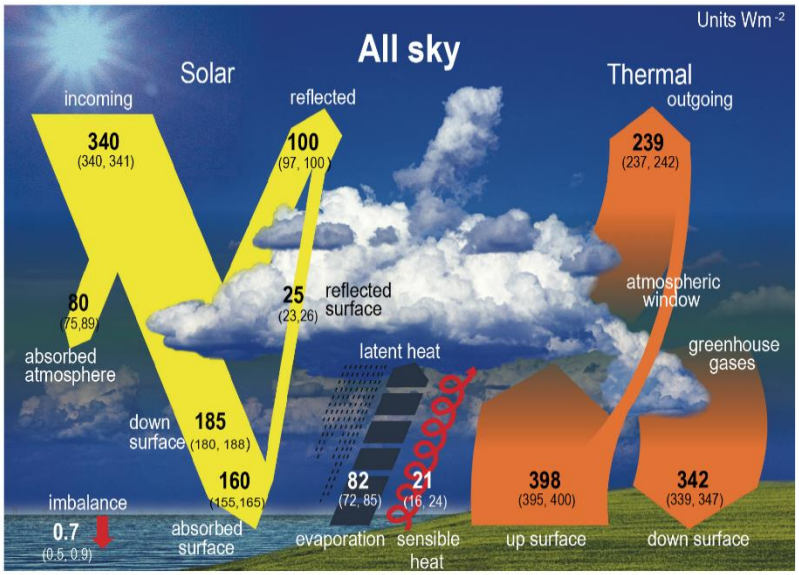

Figure 2.1. Schematic representation of the global mean energy budget of the Earth the numbers indicate the estimates for the magnitudes of the globally averaged energy balance components in W m^{-2} together with their uncertainty ranges (IPCC, 2021).

Other strong modulators of the radiation budget (not shown in Figure 2.1) are the atmospheric aerosol particles. The Atmospheric particles hold a key role in the Earth's radiative budget, through the so-called aerosol "direct" and "indirect" radiative effects. The direct effect represents the ability of particles to absorb and scatter short-wave radiation and thus, they can directly affect the amount of the incoming radiation reaching the Earth's surface. These effects primarily depend on the aerosol optical properties and their size distribution (Bond et al., 2013) especially when their diameters range

from 50 nm to 50 µm (Charlson et al., 2016). Moreover, as particles play the important role of CCN and ice nuclei (IN), they can modulate the cloud properties (*e.g.* cloud albedo, precipitation and lifetime), an effect called the "indirect" effect, which finally has a strong role in the Earth's radiation energy balance. Thus, the aerosol-cloud interactions constitute the largest source of uncertainty in the anthropogenic climate change (IPCC, 2023; WMO, 2022).

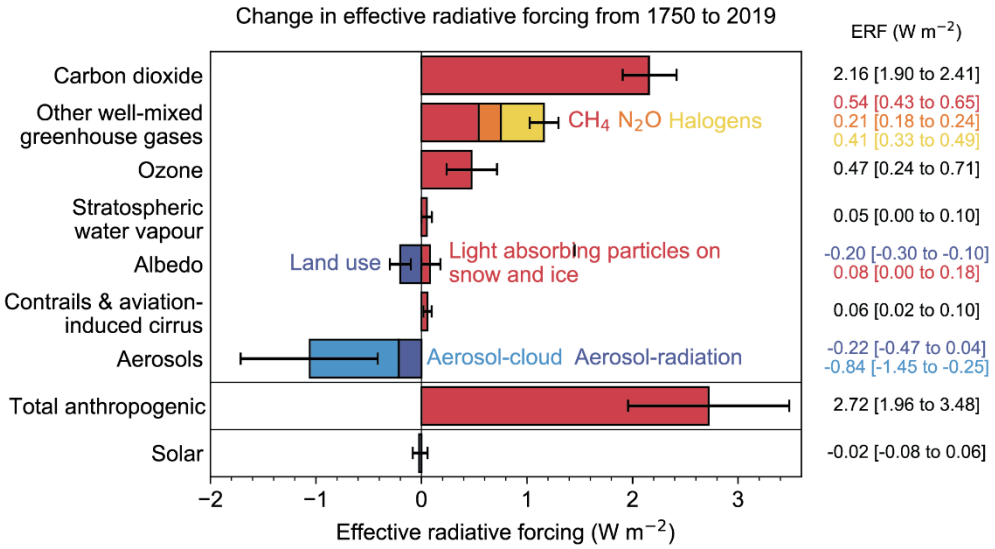

Figure 2.2. The change in effective radiative forcing from 1750 to 2019 in W m^{-2}, Figure 7.6 in IPCC (2021).

Overall, the aerosol particles have direct and indirect effects on the radiation budget having a significant contribution in climate change, but still now, the exact relationship between aerosols and clouds is not fully understood. Thus, understanding their effects and interactions with other climate factors is crucial for accurate climate modeling and effective climate change mitigation strategies (IPPC 2021; Quaas et al. 2022). For this purpose, the Effective Radiative Forcing (ERF) (units: W m^{-2}) has been proposed to quantify the change in the net TOA energy flux of the Earth system due to adjustments in aerosol concentrations, greenhouse gases, etc., including any consequent adjustment to the climate system (Calvin et al., 2023). Thus, what we know based on the ERF is that the high concentrations of greenhouse gases (CO_2, CH_4, N_2O, Halogens, O_3, stratospheric H_2O), of contrails and aviation-induced cirrus, of the light absorbing particles on snow and ice, have a positive feedback on the effective radiation forcing of about 2.72 ± 0.76 W m^{-2}, while the change on the Earth's surface albedo due to the change of its land-use, and last but not least, that the aerosol-cloud interactions and the aerosol-radiation effects produce a climate cooling of the order of 1.26 ± 0.63 W m^{-2} (*c.f.* Figure 2.2). It is also important to mention that the high sensitivity of climate on the aerosol-cloud interactions and the aerosol-radiation interactions considering the large uncertainty are the only parameters comparable to the ERF caused by CO_2 which contributes the most to global warming and climate change, respectively.

2.2 PLANETARY BOUNDARY LAYER

The majority of the aerosol particles and air pollutants emitted from the Earth's surface are trapped within the Planetary Boundary Layer (PBL), which is the lowest part of the troposphere, is responsible for the energy and mass fluxes from the surface to the atmosphere (Stull, 1988). The structure and diurnal evolution of the PBLH regulate the dispersion of air pollutants and aerosol particles contained within the PBL (Seinfeld, 2003; Singh & Kumar, 2022; Haywood, 2021) with profound impacts on climate, ecosystems and health (Seinfeld et al. 2016, IPCC 2021). The PBLH is a result of the thermal expansion of air adjacent to the surface and thus tends to follow the diurnal cycle of sunlight: increasing during morning hours, becoming maximum around noon, gradually decaying in the afternoon and becoming minimum after sunset and into the night (*c.f.* Figure 2.3).

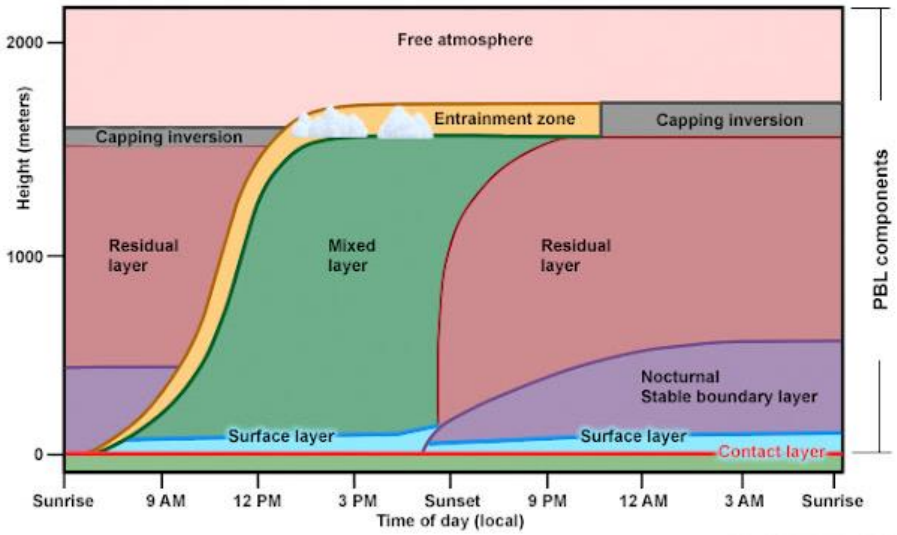

Figure 2.3. The diurnal evolution of PBL (Source: COMET/METED adapted from Stull, 1988).

Studying the PBL is challenging because it is not strictly defined, but rather a conceptual construct that can be characterized in different ways, since there are numerous approaches exist for its determination, each of which can yield different values of the PBLH, meaning that the quantity is inherently subject to uncertainty (Kotthaus et al., 2023), while it is crucial to determine since it has fundamental mechanisms that affect the aerosol transport and the cloud formation, respectively.

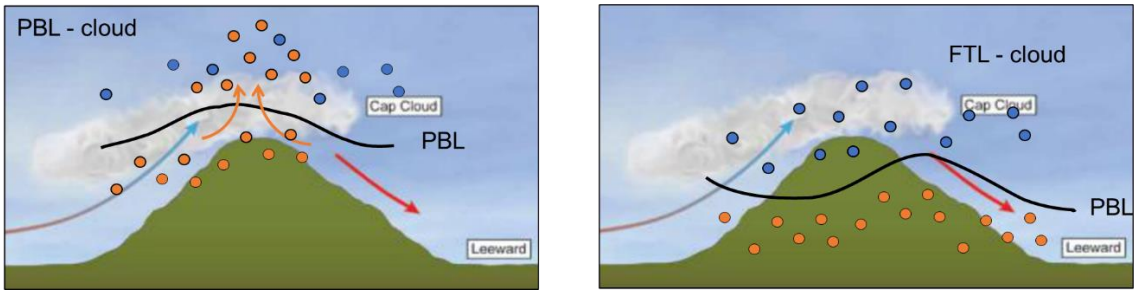

Figure 2.4. A typical example of the PBL-aerosol intrusion during a cloud formation on the left, while the right represents a cloud formation over preexisted aerosol particles within the Free Tropospheric Layer (FTL).

Given that, a deep layer contacts easier air pollutants to be transferred longer distances driven by the horizontal winds compared to shallow layers, thus the horizontal advection depends on the

extend of the PBL. Thus, the changes during the diurnal cycle of the PBLH affect the volume of the PBL, hence primary pollutants, emitted within the PBL, tend to be diluted more during daytime conditions than during nighttime ones (Duc et al., 2022), although this may vary considerably in urban regions and near intense aerosol sources (*e.g.*, Foskinis et al., in review).

Additionally, given that the majority of the aerosol particles and air pollutants are confined within the PBL, and given the lower formatted PBLC are formed at the interface of the PBL, the updrafts in the scale of the cloud base advects aerosols from PBL into the clouds (so-called "aerosol feeding mechanism") which impact on the cloud properties such as the cloud supersaturation, the cloud droplet number and the droplet sizes, as well to determine if the cloud is sensitive to aerosol or velocity changes (*c.f.* Figure 2.4).

2.3 Atmospheric Aerosol Particles

The atmospheric aerosols are solid or liquid particles produced by natural or anthropogenic sources. Their lifetime varies from several hours (for the resuspended coarse dust particles) to several days (for the fine primary and secondary aerosols (soot, sulfate, etc.) (Seinfeld and Pandis, 2016). The natural aerosol sources comprise the wind-borne dust, sea spray, volcanic debris, biogenic aerosols, etc., while the anthropogenic ones comprise industrial emissions (such as sulfates and nitrates), agricultural emission activities (such as the wind-forced mineral dust mobilized in exploited areas), the fossil fuel combustion in general, waste and biomass burning (Tomasi and Lupi, 2016). Their composition can be directly influenced by anthropogenic emissions of primary particles and gases, the condensation of gaseous precursors of anthropogenic or natural origin, and natural sources such as the sea and erodible soils (Seinfeld and Pandis, 2016).

The aerosol size varies in the range of a few nanometers to several tens of microns and can be categorized as *coarse* when their size ranges within 2.5-10 μm, *fine* with diameters of 5 nm-2.5 μm, and ultrafine with diameters less than 5nm (Hinds, 1999) (*c.f.* Figure 2.5). In general, the aerosols generated by primary combustion processes have diameters less than 50 nm; when produced by clean combustion their diameter is within a few tens of nanometers; the secondary aerosols are formed from gas-to-particle conversion processes and their diameter is within a few hundred of nanometers; finally, the particles with diameters from 50 nm to 2 μm correspond to aerosols originating from photochemical reactions (Seinfeld and Pandis, 2016).

Recent studies by Eleftheriadis et al. (2014); Laden et al. (2006); Stafoggia and Bellander (2020); WMO (2022) showed that the aerosol particles have a serious impact on human health, air quality, and atmospheric visibility, and climate which remain uncertain, creating a great need for monitoring their size distribution and physico-chemical composition to further understand their role in these scientific open issues. Brook et al. (2010) and Olstrup et al. (2019) showed that a wide range of effects on human health, including respiratory and cardiovascular diseases, increased mortality, and decreased life expectancy (Liu et al., 2019; Lelieveld et al., 2020) are associated mostly with high concentrations of fine and ultrafine particles. For instance, it has been shown that the fine particles have detrimental effects on humans (Dockery and Pope, 1994; Ostro et al., 2006) as they act as carriers for toxicants and mutagenic components Beddows et al., 2004), and can penetrate the cell membranes (Salma et al., 2002; N. Li et al., 2003; Bell et al., 2009).

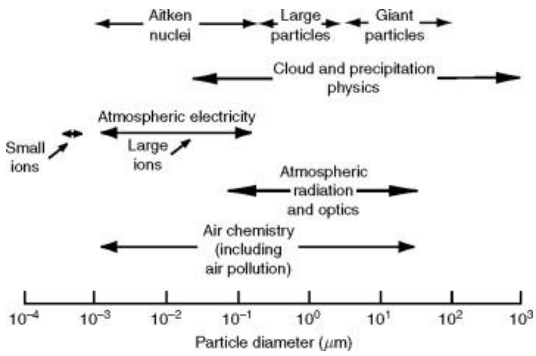

Figure 2.5. The size range of the atmosphere particles and their interactions (Wallace & Hobbs, 2006).

The interaction of light with a scatterer (molecule or particle) comprises the absorption, reflection, diffraction, emission or scattering of radiation. In the frame of this interaction, we will be limited to two main scattering processes (*c.f.* Figure 2.6): a) the *elastic* scattering when the particles scatter the incident radiation at the same wavelength, or the molecules absorb and re-emit radiation at the same wavelength as the incident one, thus, the excited molecule returns to its initial energy state, and b) the Raman scattering where the re-emitted radiation is shifted (Stokes and anti-Stokes shifting) compared to the incident one, due vibrational and/or rotational transitions (Wandinger, 2005).

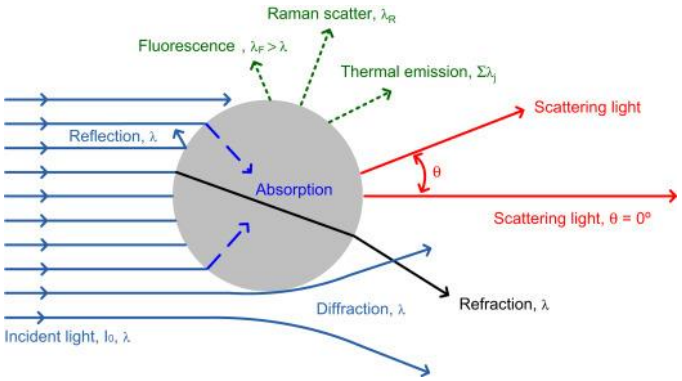

Figure 2.6. Potential interactions between an incident radiation (light) and a spherical particle (Nakayama et al., 2021).

The scattering effect is highly dependent on the dimensionless size parameter $x = \frac{2\pi r}{\lambda}$ of the scatterer and the refraction index ($m = m_r + m_i i$) of the particles, where m_r is the ratio of the speed of light in a vacuum to the speed light travels when it passes through the particle, which is defined by the chemical composition of the particle; λ is the light's wavelength and r is the particle's radius (*c.f.* Figure 2.7). Thus, there are three regions in Figure 2.5, based on the size (diameter) parameter of the scatterer which defines the scattering properties: a) when the scatterer's size is much larger than the wavelength ($x \ll 1$) the scattering is considered as "Geometric", b) when the scatterer's size is comparable to the wavelength ($x \sim 1$) the scattering is called "Mie" from particles and c) when the scatterer's size is much smaller than the wavelength ($x \gg 1$) the scattering is called "Rayleigh" from molecules.

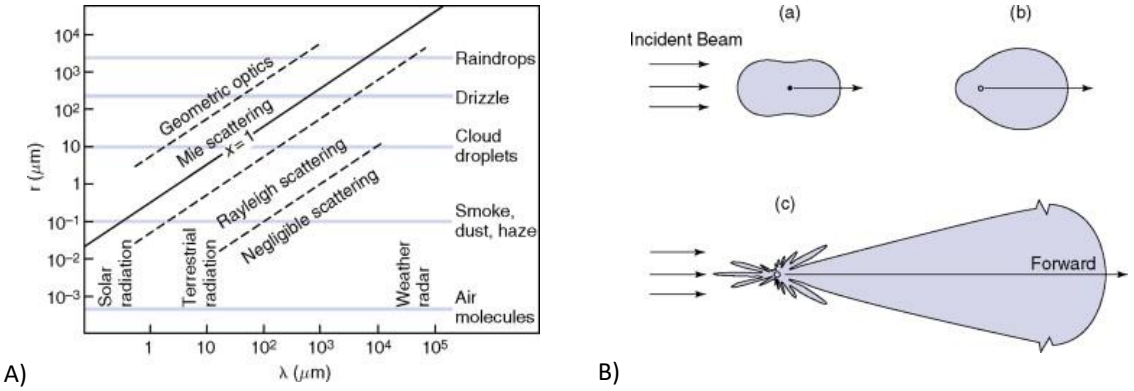

Figure 2.7. A) Atmospheric scattering in respect to particle radius and incident radiation wavelength; and B) a schematic representation of the angular distribution of the radiation, when the incident radiation at visible (0.5 μm) is scattered by spherical particles with a radius of (a) 10–4 μm, (b) 0.1 μm, and (c) 1 μm (Fu, 2006).

For instance, given that the incoming shortwave solar radiation ranges in the visible region (0.4-0.7 μm), the scattering of the aerosol particles with sizes up to a few microns is described by the Mie theory (Mie, 1908), the scattering due to the air molecules in the atmosphere by the Rayleigh theory (Twersky, 1964; Andrews, 2017), while the droplets have geometric scattering (*c.f.* Figure 2.7). According to the Rayleigh theory, the scattered intensity by the molecules is proportional to λ^{-4} (which means, the shorter wavelengths are more efficient in scattering), while in the case of aerosols the scattering intensity varies is proportional to the wavelength (Fu et al. 2006) while the scattering by the water droplets is non-selective and is better described by geometric optics.

2.4 CLOUDS

The clouds are characterized relevant to their content as warm-/or mixed-/ or ice-phase clouds. The warm clouds consist of cloud droplets that were formed when the air parcel became supersaturated with respect to liquid water, which similarly happens in the case of ice. The most common way for an air parcel to become supersaturated is through the fast ascent of air parcels which results in the expansion of the parcel and its resulting adiabatic cooling. Thus, when the air parcel becomes supersaturated the water vapour condenses onto some of the aerosol particles to form small cloud droplets or ice particles; this mechanism is called “heterogeneous” nucleation. Furthermore, a second mechanism to form cloud droplets is by condensation from a supersaturated vapour without the aid of particles, the so-called “homogeneous” nucleation, but this is not very efficient in the atmosphere, since it is feasible when the ambient temperature is below -40 ^{o}C (Anderson et al., 1980). Here we only focus on the heterogeneous nucleation processes.

The cloud formation mechanism is described by the Gibbs free energy:

$$\Delta E = 4\pi R^2\sigma - \frac{4}{3}\pi R^3 n\, k_B T ln\frac{e}{e_s} \quad (2.1)$$

where e and T is the water vapour pressure and temperature, respectively, e_s is the saturation vapor pressure over a plane surface of the water, R is the droplet radius, k_B is the Boltzmann constant, and n is the number of water molecules per unit volume. The first term ($4\pi R^2\sigma$) describes

the surface energy of the liquid, while the second term ($\frac{4}{3}\pi R^3 n\, k_B T ln\frac{e}{e_s}$) the decrease in the Gibbs free energy of the system due to the droplet condensation.

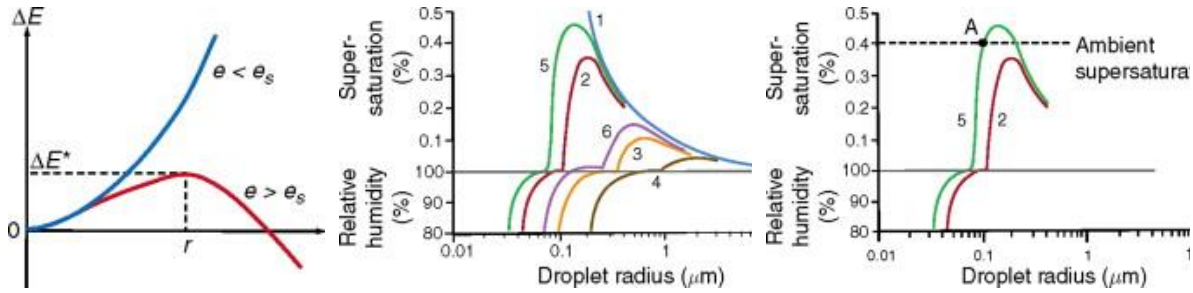

Figure 2.8. The Increase of Gibbs Energy ΔE due to the droplet formation of radius r from water vapour pressure e and saturation vapor pressure e_s (left); Variations of the relative humidity and supersaturation adjacent to droplets of (1) pure water (blue) and adjacent to solution droplets containing the following fixed masses of salt: (2) 10^{-19}, (3) $10^{-18}$and (4) 10^{-17}kg of NaCl, while corresponding to (5) 10^{-19}, and (6) 10^{-18} kg of $(NH_4)_2SO_4$ (middle); and the dashed line is an assumed ambient supersaturation along with Köhler curves (2) and (5) (Wallace and Hobbs, 2006b).*

Under subsaturated conditions ($e < e_s$), the surface energy of a liquid is greater than the decrease due to the condescension, as a result, the ΔE (in Eq. 2.1) is always positive, so the formation of droplets is not favoured, while under supersaturated conditions ($e > e_s$) ΔE is either positive or negative, when the droplet size exceeds a plateau (*c.f.* Figure 2.8a). The droplets can grow by collisions to a radius that just exceeds the plateau and will continue to grow spontaneously by condensation from the vapour phase; otherwise, the droplets will evaporate back to the gas phase. In the case of heterogeneous nucleation, the hygroscopic aerosol particles can offer their surface upon which water vapour condenses. Thus, the droplets can form and grow on these aerosol particles at much lower supersaturation rates than those required for homogeneous nucleation, depending on the hygroscopicity of the aerosol particles as described by the κ -Kölher theory (Köhler, 1936) (*c.f.* Figure 2.8b).

Later, Petters and Kreidenweis (2007) based on the κ-Kölher theory (Köhler, 1936) showed that the particles with size larger than a critical size

$$D_{cr} = \left(\frac{4\,A^3}{27\,\kappa\,s^2}\right)^{\frac{1}{3}} \quad (2.2)$$

can activate to droplets depending on the supersaturation ratio s ($s = \frac{e}{e_s} - 1$), the aerosol hygroscopicity parameter κ, where $A = \frac{4\,M_w\sigma}{R\,T\,\rho_w}$ is the Kelvin parameter, M_w (kg mol^{-1}) is the molar mass of water, σ (J m^{-2}) is the surface tension of the solution droplet, R (J mol^{-1} K^{-1}) is the universal gas constant, and ρ_w is the density of the liquid water. Thus, at the given s value, the aerosol particles larger than the D_{cr} are considered as Cloud Condescension Nuclei (CCN), while, as the s value increases, smaller particles can activate to droplets, while the same form can be used and *vice versa* to calculate the critical supersaturation where an aerosol particle with a given size will be able to activate into a droplet (*c.f.* Figure 2.8).

2.5 AEROSOL-CLOUD INTERACTIONS

The atmospheric aerosols affect the climate both directly (aerosol–radiation interactions) and indirectly (aerosol–cloud interactions). The *direct* effect represents the ability of the atmospheric particles to absorb (leading to local heating) and scatter (leading to local cooling) short-wave or long-wave radiation and thus, directly influence the Earth's radiation budget, especially when they have diameters ranging from 50 nm to 50 μm (Charlson et al., 2016). These effects primarily depend on the aerosol physico-chemical properties and their size distribution (Bond et al., 2013, add more papers).

For instance, the black carbon absorbs the short-wave radiation in the whole wavelength range, the brown carbon significantly absorbs in the ultraviolet and visible spectral range (Moosmüller et al., 2009), while the organic aerosols (except the brown carbon), nitrate and sulfate particles contribute mainly to scattering (Cabada et al., 2004). Additionally, given that the aerosol particles travel over long distances (Bougiatioti et al., 2014; Titos et al., 2016) and thus show a large spatial variability their radiative effects are difficult to predict using models (Collaud Coen et al., 2020; Ramachandran and Rupakheti, 2020).

The term "*aerosol–cloud interactions*" (Twomey, 1991; Twomey and Warner, 1967) are the indirect effects of the aerosols on clouds. Twomey and Warner (1967) have shown that, under the assumption that the aerosols act as condensation nuclei under constant moisture, any increase in the aerosol concentration levels inside a cloud generally reduces the droplet size, and increases the cloud droplet number (N_d), and thus, enhances the cloud albedo, which in turn manipulates the amount of solar radiation reflected back to space (called "*albedo effect*"). This effect is represented in Figure 2.9 (upper figure) where a clean cloud contains a small number of big cloud droplets and precipitates, while a polluted cloud containing a larger number of smaller droplets, is more reflecting (higher albedo) and less precipitating than the clean cloud. Additionally, the aerosols have "*semi-direct effects*" on droplets, where the absorbing particles such as soot, in the polluted clouds, can heat the clouds, and evaporate the water droplets, resulting in the shrinking of the cloud (*c.f.* Figure 2.9, middle figure). Last but not least, the increase of the aerosols concentration (polluted cloud) in the case of vertically developing clouds, such as cumulus, results in delaying freezing, leading to higher and colder clouds, which ends up in an increase in the concentration of ice crystals (effect known as "*Glaciation effect*") resulting in more precipitation compared to the polluted cloud (IPCC, 2021) (*c.f.* Figure 2.9, lower figure).

Thus, all these effects tend to cool or warm the atmosphere, for example, the cloud albedo effect tends to have a negative radiative effect on warm clouds at TOA, while the Semi-direct effect and the Glaciation effect tend to have a positive radiative effect at TOA (IPCC, 2021).

Although the exact footprint of the aerosol–cloud interactions depend on many factors, which include the cloud dynamics (cloud scale vertical velocity distributions), the aerosol size distribution and their hygroscopicity, it is generally accepted that not all clouds are equally sensitive to changes in the CCN, or the subset of aerosols which activate into cloud droplets. Thus, clouds can be either "*aerosol-limited*", when supersaturation is high and N_d is very sensitive to aerosol changes, or "*velocity-limited*" when the supersaturation is so low that N_d is insensitive to aerosol changes (Reutter et al., 2009) depending on the intensity of the turbulence (Bougiatioti et al., 2020; Kacarab et al., 2020; Georgakaki et al., 2021).

Thus, when the water vapour availability (supersaturation) is large, the aerosol variations readily translate to droplet variations, while when there is a large competition for water vapour during the initial stages of cloud formation (supersaturation is very low), this translates to negligible changes in droplets for relatively large changes in aerosol amounts (Reutter et al., 2009; Georgakaki et al., 2021). Therefore, the aerosol particles may affect the clouds' microstructure, their reflectance and lifetime (Zhu et al., 2018).

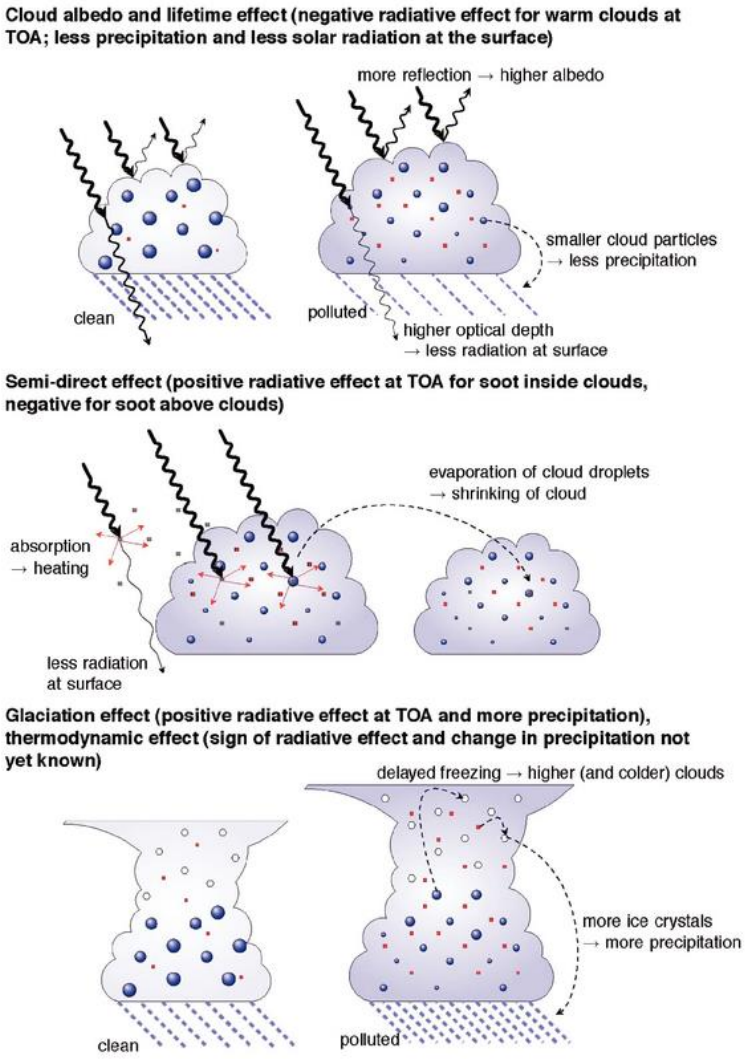

Figure 2.9. A schematic representation of the albedo effect due to aerosol increase (IPCC, 2007b).

This effect remains highly uncertain due to the high spatial and temporal variability of aerosols and clouds, their characteristics (hygroscopicity, size distribution and mixing state), as well as the vertical velocities distributions and the resulting supersaturations. Another large fraction of this uncertainty arises from the impact of aerosols on the droplet formation in liquid and mixed-phase clouds (Boucher et al., 2013; Lohmann, 2017), due to the large source of uncertainty in the prediction of anthropogenic climate change (IPCC, 2021, 2013, 2007b). The difficulty of describing realistically all these dependencies in models poses a challenge that only advances using high-resolution models with large observation datasets as input.

As a result, the aerosol-radiation interactions and the aerosol-clouds interactions still represent one of the highest uncertainties in the assessment of climate change due to their key role in

atmospheric dynamics, chemistry, and climate (IPCC, 2013), due mainly to the wide variety of aerosol sources and mixing processes, as well as their high spatial and temporal variability in their properties and types (Hamill et al., 2016).

3 SAMPLING AEROSOLS AND CLOUDS

This section briefly describes the ground-based instrumentation used in this Thesis for sizing and counting aerosol particles, measuring the aerosol chemical composition, the black carbon and the bioaerosol concentrations, as well as the cloud particle number size distributions.

3.1 SCANNING MOBILITY PARTICLE SIZER

The Scanning Mobility Particle Sizer (SMPS) measures the dried particle size range from 10 to 800 nm and provides the size distributions every 5 minutes. It consists of an electrostatic classifier, a cylindrical differential mobility analyzer column, and a condensation particle counter, while the sample and sheath flow were dried (RH < 40%) before their introduction in the instrument by using Nafion driers (*c.f.* Figure 3.1). Here, we used the electrostatic classifier (TSI Inc., model 3080), a cylindrical differential mobility analyzer column (TSI Inc., model 3081) and a condensation particle counter (TSI Inc., model 3772).

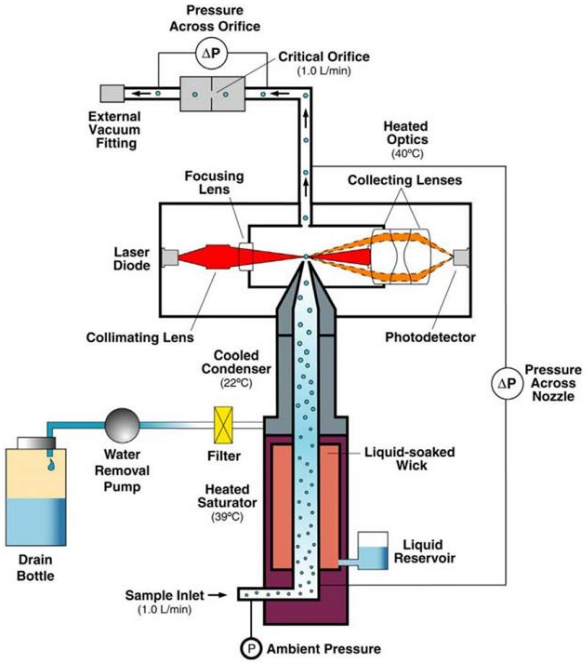

Figure 3.1. Flow schematic of the Model 3772 CPC, adapted from the manufacturer's manual.

3.2 Time-of-Flight Aerosol Chemical Speciation Monitor

The Time-of-Flight Aerosol Chemical Speciation Monitor (ToF-ACSM) (Aerodyne Research Inc., Billerica, MA, USA) measures the non-refractory submicron aerosol mass and chemical composition (ammonium, sulfate, nitrate, chloride, and organics) in real-time (Fröhlich et al., 2013) of submicron aerosols (40-1000 nm). It consists of a $PM_{2.5}$ virtual impactor, a Nafion drier (RH<40%), an orifice, and an aerodynamic particle focusing lens on high vacuum conditions (*c.f.* Figure 3.2). Thus, the non-refractory material is vaporized on a tungsten plate for flash vaporization (600 °C) and subsequently ionized by electron impact ionization at 70 eV, while a time-of-flight mass analyzer by Tofwerk is used to detect the resulting ions. At ambient atmospheric conditions, the lens system focuses on the detection of submicron aerosols of ~40-1000 nm vacuum aerodynamic diameters.

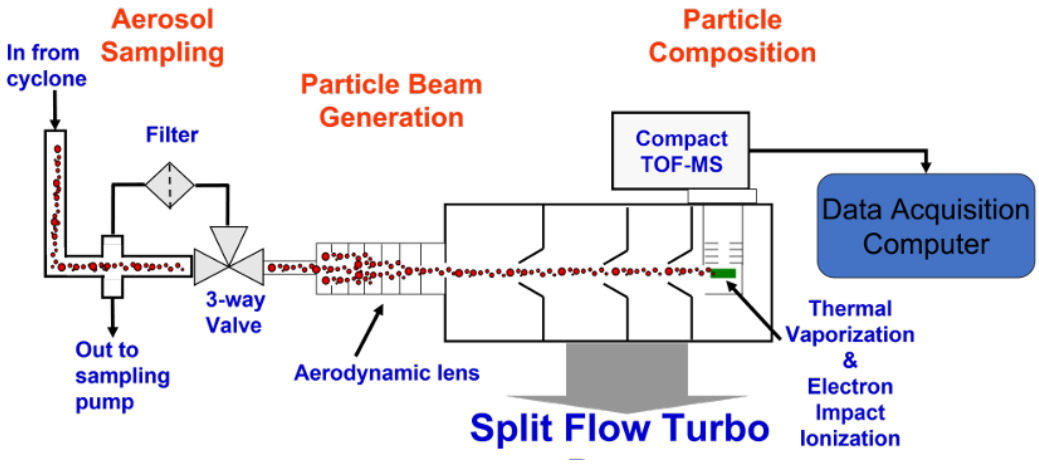

Figure 3.2. The Schematic diagram of the ToF-ACSM (Aerodyne Inc.)

A collection efficiency factor (CE) CE=0.5 (Zografou et al., 2022) was used to account for the fraction of the non-refractory particles that bounce off the vaporizer and are not detected. During the measurement period, the ambient air was drawn into the ToF-ACSM through a $PM_{2.5}$ aerosol inlet. The inlet aerosol flow was, as previously, dried to a RH lower than 40% by using a Nafion dryer.

3.3 Aethalometer Monitor

The Aethalometer AE31 measures the equivalent black carbon (*eBC*) concentration based on (Hansen et al. (1982) and Petzold et al. (2013). The AE31 operates at seven wavelengths (370, 470, 520, 590, 660, 880, and 950nm), where an on-line light-transmission measurements were performed through a filter tape.

In principle, the AE31 (Drinovec et al., 2015) uses a dual spot system to compensate for the loading effect artefact and to calculate the absorption and the compensation of *eBC* concentrations from measurements of light transmission at seven wavelengths, while here we use only the calculation based on 880nm (*c.f.* Figure 3.3**Error! Reference source not found.**). The operation of the aethalometer consists of the continuous collection of aerosols on a filter, forming a sample-laden spot, where a light source illuminates the spot on the filter and, on the opposite side, a sensor measures the intensity of light transmitted through it. Then the light transmission is also measured

through a sample-free area on the filter and is used as reference, thus the change in the attenuation is assumed that is caused by the black carbon amount that has been deposited on the filter.

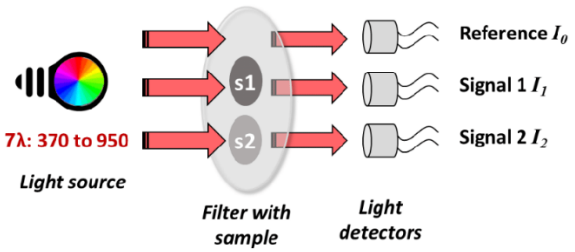

Figure 3.3. Schematic representation of the optical chamber in the Aethalometer AE31 (Cuesta-Mosquera et al. 2021).

In **Paper III**, given that the black carbon primarily stems from anthropogenic fossil fuel emissions (the wildfire cases are excluded from our study) within the PBL, we can use the *eBC* as an index to ascertain the conditions under which the (HAC)^2 resides either within the PBL or the FTL. This determination depends on whether the *eBC* concentration obtains large or small values (Lund et al., 2018; Motos et al., 2020), respectively.

3.4 NEPHELOMETER

The TSI 3563 nephelometer measures the scattering coefficient of the dried aerosol particles (RH below 40%), after a PM10 inlet, at three different wavelengths (450, 550 and 700nm). The nephelometer provides the aerosol backscatter coefficient and by using the Beer-Lambert law calculates the aerosol total extinction coefficient at 450, 550 and 700nm.

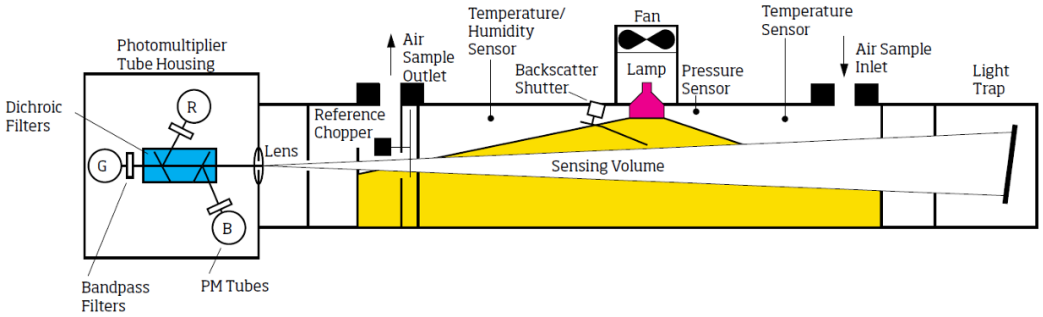

Figure 3.4. The diagram of the Nephelometer functional, adapted from the manufacturer's manual

The main body of the TSI 3563 nephelometer is made of an aluminium tube, where along the axis is a smaller (in diameter) tube set with aperture plates (*c.f.* Figure 3.4). The plates orientation ranges from 7 - 170° on the horizontal range of the lamp, while the backscatter shutter blocks the angles from 7 - 90° to obtain only the backscatter measurement. The receiving optics are located on the other side of the tube from the trap, where the light that passes through the lens is separated by dichroic filters into three wavelengths. The first is a color splitter that allows only the wavelengths in the range of 500-800 nm and reflects the wavelengths within 400-500 nm. The reflected wavelengths passed through a filter centred at 450 nm into a photomultiplier tube (PMT) (B). The wavelengths that pass through the first splitter go to a second splitter which allows it to pass only the wavelengths within the 500-600 nm and reflects the 600-800 nm wavelengths. The reflected wavelengths, then, pass through a filter centered at 700 nm into a second PMT (R). The wavelengths that pass through both splitters, following pass through a filter centred at 550 nm into a third PMT (G). Thus, the TSI 3563 splits the scattered light into R (700 nm), G (550 nm), and B (450 nm) wavelengths and measures

the scattering (*sc*) and the backscattering (*bc*) coefficients of the dried aerosol particles on each wavelength (Anderson et al., 1998, TSI Inc.).

In **Paper III**, the scattering intensity was used as a proxy to identify regimes where the $(HAC)^2$ is within PBL of FTL, respectively. Given that within the PBL increased aerosol concentrations are typically found, the relevant total scattering coefficient tends to obtain large values (Farah et al., 2018). Moreover, in this study, we used the aerosol total scattering and backscattering coefficients at 550nm (*sc550* and *bc500*, respectively).

3.5 Wideband Integrated Bioaerosol Sensor

The Wideband Integrated Bioaerosol Sensor (WIBS-5/NEO, Droplet Measurement Technologies), was used in **Paper III** to measure the biological material, like pollen, bacteria, and fungi with size between 0.5 to 30 μm (optical) diameter. It consists of two UV-filtered flashlamp sources (one at 280nm and one at 370nm) that are used to excite fluorescence in individual particles to cause the fluorescence of the bioaerosols, and two detection band ranges (one within 310-400nm and the other one at 420-650nm) (*c.f.* Figure 3.5a).

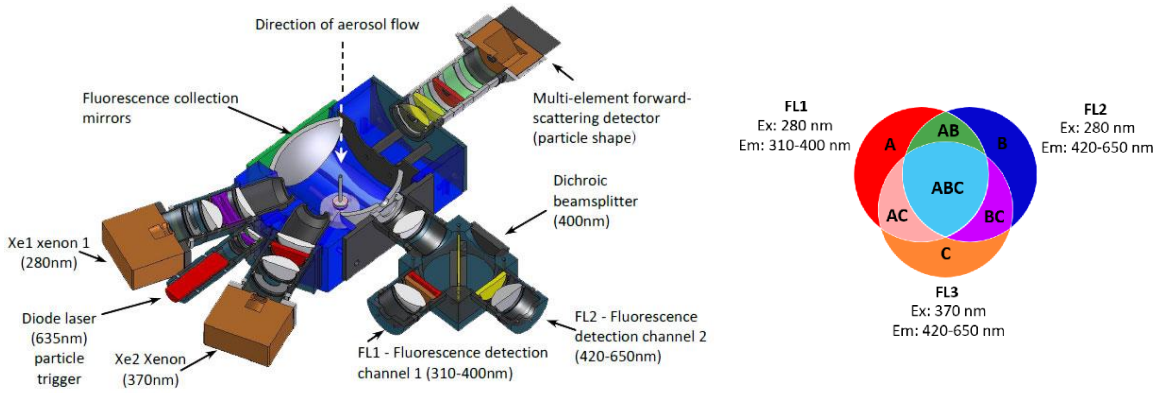

Figure 3.5. The WIBS-4 instrument structure. (Li et al., 2019); b) The particle type classification, as introduced by introduced by Perring et al. (2015), where each circle represents one fluorescence channel (FL1, FL2, FL3), while the colored zones represent the particle types that exhibit fluorescence in each one, two, or three channels. (Savage et al., 2017)

Thus, the fluorescent particles are classified into three channels depending on their fluorescent properties, including the FL1 channel with the pair of excitation wavelength at 280 nm and emission detection at the waveband 310-400 nm, FL2 channel and FL3 channels with an emission detection waveband of 420-650 nm probing particles excited at 280 and 370 nm respectively (Perring et al., 2015; Savage et al., 2017) (*c.f.* Figure 3.5a and b). These channels are tuned to detect the fluorescence from three classes (A, B and C) for ubiquitous biological fluorophores, including tryptophan-containing proteins, NAD(P)H co-enzymes and riboflavin (Kaye et al., 2005; Savage et al., 2017; Pöhlker et al., 2012). When the aerosol particles fluoresce in more than one class, the extra classes are defined as AB, BC, AC, and ABC, respectively. Given that non-biological particles, such as some black carbon and dust particles, may show fluorescence signals in one of the channels (Toprak and Schnaiter, 2013), aerosol particles showing fluorescence in all three channels are those most likely to be of biological origin (Savage et al., 2017), *e.g.*, pollen, bacteria, and fungi.

3.6 CLOUD CONDENSATION NUCLEI COUNTER

The Cloud Condensation Nuclei Counter (CCN-100) (Droplet Measurement Technologies, DMT) operates with a continuous flow thermal-gradient diffusion chamber for measuring aerosols that can act as cloud condensation nuclei (*c.f.* Figure 3.6a). The aerosol sample flows into a 50-cm tall column, where the columns, create a thermodynamic instability, where the water vapor becomes supersaturated due to the difference in diffusion rates between water vapor and heat. The water vapor diffuses from the warm, wet column walls toward the centerline at a faster rate than the heat, thus the wall temperature along the column gradually increases to create a controlled and quasi-uniform centerline supersaturation (*c.f.* Figure 3.6b). Then, the aerosols during the flow, activate to cloud condensation nuclei and form droplets, where at last, an optical particle counter (OPC) which measures the droplet size distribution (in the range of 0.75 – 10 μm) and of the activated droplets (*c.f.* Figure 3.6a).

Given that the temperature gradient and flow rate can be selectively changed, this results in different supersaturations, which allows for obtaining the number of the condensed particles (or the droplets) at a given supersaturation (CCN spectra) (Roberts and Nenes, 2005). In our case, the CCN-100 was used in **Paper IV** to measure the concentration of the condensed aerosol particles to cloud droplets in different supersaturations, from 0.1% to 1% with a 6-minute time resolution.

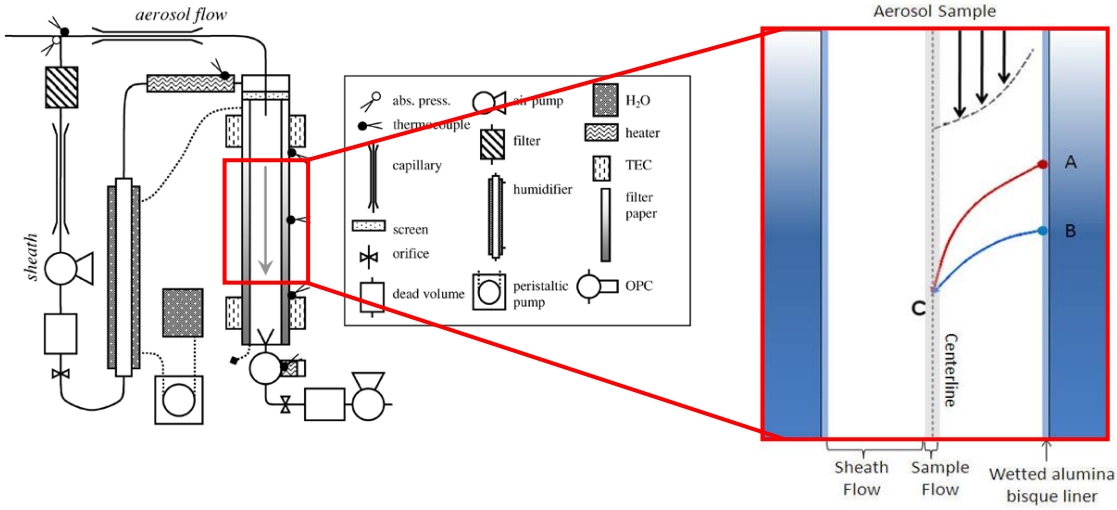

a) b)

Figure 3.6. a) A flowchart of the streamwise thermal gradient cloud condensation nuclei (CCN) instrument; b) The sample flow along the humified columns where the Water vapor becomes saturated. The diffusing heat originates at point A, the diffusing mass originates at point B, while the actual partial water pressure of water vapor at point C equals the partial pressure of water vapor at point B. The temperature at C is lower than at B, meaning there is more water vapor than thermodynamically allowed (Source: DMT Inc.).

4 REMOTE SENSING TECHNIQUES

This section describes the remote sensing techniques and principles that were used in this Thesis for measuring the wind velocity, the atmospheric turbulence, and the cloud microphysical properties.

4.1 ACTIVE REMOTE SENSING - LIDAR

The lidar (LIght Detection And Ranging) technique was introduced in the early sixties based on Synge's idea (Synge, 1930) who proposed the measurement of the air density profiles by analyzing the backscattering intensity using multiple light beams (Middleton and Spilhaus, 1954). When the radar was invented, Schawlow and Townes (1958) applied this idea using a maser beam, while after the invention of the Q-switched lasers (Maiman, 1960; McClung and Hellwarth, 1962) the first lidar system was developed to measure the distance between the Earth and the Moon (Smullin and Fiocco, 1962). Later, Chanin and Hauchecorne (1981) developed a lidar system in which they replaced the former ruby lasers by a Nd:YAG (neodymium-doped yttrium aluminium garnet; $Nd:Y_3Al_5O_{12}$) laser. Afterwards, the lidar technique was rapidly applied in the atmospheric sciences focusing on measurements of atmospheric gases (SO_2, H_2O, NO_x, CO_2, etc.), aerosols, clouds, wind, etc. The lidar systems starting from ground-based ones, they became airborne (McCormick and Ludwig, 1967) and finally, spaceborne (Fouladinejad et al. 2019, and references therein).
The lidar system consists of a transmitting and a receiving unit. The transmitter sends a laser beam to the atmospheric volume under study. It consists of a pulsed solid-state laser source, usually of a Nd:YAG, emitting at 1064, 532, 355, or even down to 213 nm. The receiving telescope collects the backscattered laser beam which is spectrally separated in different optical channels by a spectrometer, which is equipped with photomultiplier tubes (PMTs) and avalanche photodiodes (APDs) to convert the detected photons into photo-electrons to finally produce electrical pulses (voltage or current). This pulsed signal after digitization is fed to a computer for further analysis.

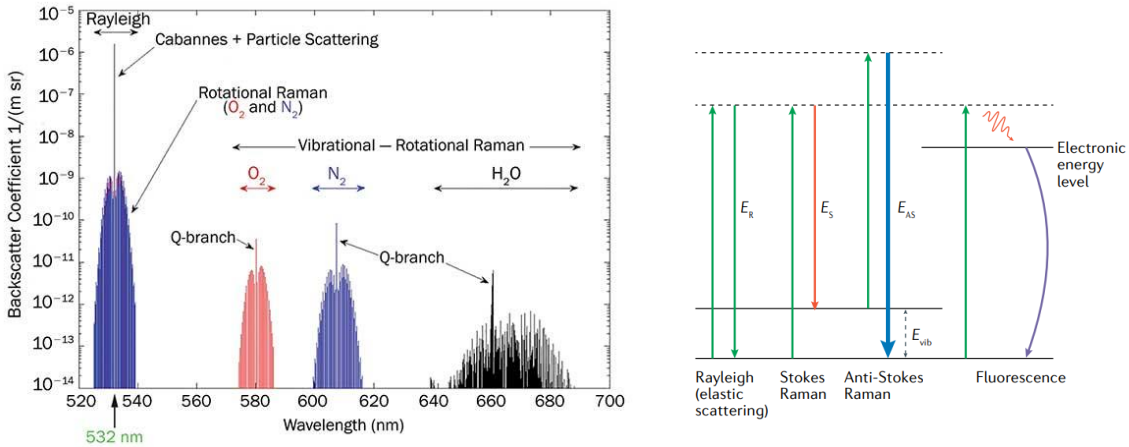

Figure 4.1. (Left): The atmospheric Raman backscatter spectrum for an exciting laser beam at 355 nm (Fraczek et al., 2012).; (Right): An example of the electronic energy levels after stimulation in respect of the de-excitation by the Rayleigh, Stokes or fluorescence scattering (Mosca et al., 2021).

Some of the widely used lidars are the elastic and inelastic (or Raman), differential absorption (DIAL), and Doppler (Wandinger, 2005; Weitkamp, 2005) ones. The elastic lidars provide information on the vertical structure of the atmosphere, detecting the presence of aerosols and/or clouds, as well as the aerosol backscatter coefficient; the Raman lidars are used to measure the vertical profiles of

the aerosol backscatter and extinction coefficients using the vibrational-rotational Raman scattering of nitrogen and of the water vapor to provide the vertical profiles of the water vapor mixing ratio (*c.f.* Figure 4.1); finally, the Doppler lidars provide the wind turbulence mostly in the PBL and the lower free atmosphere (Werner, 2005). In the next paragraphs, we will detail the working principle and applications of the wind lidar technique.

4.1.1 WIND DOPPLER LIDAR

The wind Doppler lidar measures the velocity of the scattering particles along the line of sight (LOS) of the propagating laser beam. The moving aerosol particles driven by the atmospheric turbulent eddies are considered ideal tracers to infer the wind velocity. A wind lidar system emits a spectrally ultra-stable and very narrow pulsed laser beam (at wavelength λ_0) and detects the Doppler shifting of the backscattered laser radiation (at wavelength λ_{LOS}) by the moving atmospheric molecules and aerosols (*c.f.* Figure 4.2). The wind lidars are based mostly on solid-state, diode pumped-Optical Parametric Oscillators (OPO) or CO_2 pulsed lasers (at wavelengths 355 nm, 532 nm, 850-950 nm or 1.5-10.59 μm). Lidar systems working in the UV spectral region are sensitive to both molecular (Rayleigh) and particulate (Mie) scattering, while those working in the NIR or IR spectral regions are sensitive mostly to particulate (Mie) scattering.

The detected backscattered lidar signal at a frequency $f = f_0 + \Delta f = f_0(1 + \frac{2u}{c})$ permits the retrieval of the LOS velocity or radial velocity u, once f_0 and Δf are measured with high accuracy. The value of Δf can be detected in the *direct* mode (direct or incoherent detection) or *indirect* mode (coherent detection) using the heterodyne detection technique (Weitcamp, 2005).

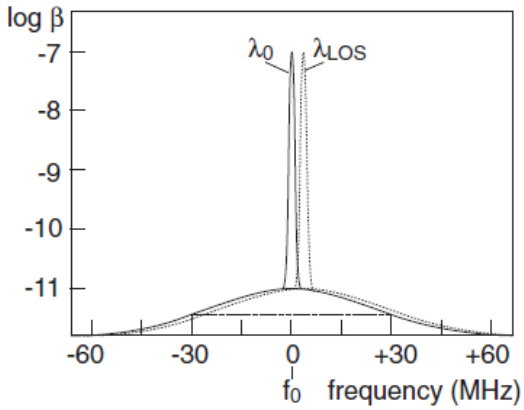

Figure 4.2. A schematic representation of the Doppler spectrum shift due to molecular and aerosol motion (Weitkamp, 2005).

In the case of the direct detection mode (mostly used in the near UV at 355 nm), the backscattered lidar signal is spectrally separated by using a Fizeau interferometer (aerosol component around f_0) and a Fabry-Perot interferometer (molecular component) (cf. Figure 4.2), and after optical filtering is recorded by PMTs or CCDs detectors.

In the case of the heterodyne detection, a well-characterized continuous waves (cw) laser beam from a local oscillator (LO) at frequency f_0 is fed to an Acousto-Optic Modulator (AOM) to produce a pulsed laser beam which pumps a laser crystal to produce a pulsed laser beam at frequency $f_0 + f^*$, which is then emitted to the atmosphere. The backscattered lidar "weak" signal at frequency

$f_0 + f^* + \Delta f$ is mixed with the "stronger" signal of the LO and fed to a detector. Therefore, the mixed signal contains the sum and the difference of the frequencies of both components (f_0 and $f_0 + f^* + \Delta f$). The difference of these frequencies $f^* + \Delta f$ can then be determined with very high accuracy using a Fourier autocovariance transformation to obtain the Doppler power spectrum, which is used to determine the wind velocity along the LOS (Newsom and Krishnamurthy, 2020) separately for each of the time-packages, that correspond to the aerosol's velocity at different heights (or otherwise, the profile of the vertical velocity).

In the frame of this Thesis, we used a pulsed wind scanning lidar called "HALO" (StreamLine XR Doppler lidar, HALO Photonics) emitting at 1.565 μm. The lidar was operated in Athens and Helmos mountain, both in stare vertical azimuth display and vertical azimuth display (VAD) modes, as deployed by the Finnish Meteorological Institute (FMI). The range resolution of the measurements was 30 m, the temporal resolution 20 s, while the maximum measurement range was 2-3 km depending on the atmospheric aerosol load and the corresponding uncertainty of ±0.038 m s^{-1} for the retrieved wind velocity in the stare mode. A signal-to-noise-ratio (SNR) greater than 1.003 is usually required to define the useful lidar signals (Weitkamp, 2005).

4.1.1.1 Estimation of the Planetary Boundary Layer Height

Measuring the PBLH is challenging because it is not strictly defined, but rather a conceptual construct that can be characterized in different ways. Numerous approaches exist for its estimation, each yielding different values of the PBLH, meaning that this parameter is inherently subject to uncertainty (Kotthaus et al., 2023). *In situ* instruments to determine the PBLH are carried by radiosondes and airborne platforms (*e.g.*, aeroplanes, helicopters, UAVs, tethered balloons), while remote sensing techniques are based on aerosol/wind lidars, microwave radars, ceilometers, sodars, and microwave radiometers (Emeis, 2011).

One of the widely used robust techniques to determine the PBLH is based on remote sensing techniques by the use of wind Doppler lidars. Given the profile of the wind vertical velocity (*w*) can be measured by wind Doppler lidars, we can calculate the turbulence within the PBL and thus, estimate the PBLH. Milne and Taylor (1922), and Taylor (1935) shown that the vertical size of a growing turbulent plume is proportional to the σ_w; as a result, the σ_w values can be used as an indicator of the vertical mixing in the lower atmosphere, and changes thereof from transitioning inside and out of the PBL. Based on this parameter, Kaimal et al. (1976), Tucker et al. (2009), Pearson et al. (2010), Barlow et al. (2011), Träumner et al. (2011), and Schween et al. (2014) determined the PBLH, where the σ_w values fall below a characteristic threshold ranging between 0.17 m s^{-1} and 0.40 m s^{-1}. This large variation of the σ_w threshold may reflect uncertainties in the retrieval of the vertical velocity, or simply the natural variability in the PBL in different environments. According to Schween et al. (2014), a ±25 % change in the threshold is translated to a $\mp$7 % change in the PBLH.

In **Papers II, III** and **IV**, we used the wind vertical velocity data retrieved by HALO, to calculate the corresponding σ_w values using ±15 min interval averaging of the w data, with 5 min temporal resolution and 30 m height spatial resolution. This 30-minute time window, as pointed out by Schween et al. (2014), is representative of convective plumes and eddy fluxes since the latter need about 16 min to travel through a PBL mixing layer of 1 km height (a typical height during day hours considering an average ascent speed of 1 m s^{-1}. So, this 30-minute average window is almost twice the lifetime of such a plume. In **Paper II**, we proposed the determination of the PBLH as the first

height where the value of σ_w falls below a threshold value of 0.20 m s^{-1} (Tucker et al., 2009), while in **Paper III** we performed a synergistic study with *in situ* measurements to define a more realistic threshold which equals to 0.10 m s^{-1}.

4.1.1.2 Wind components retrieval using a wind lidar system

Using the velocity-azimuth-display (VAD) conical scan technique (Browning and Wexler, 1968; Caya and Zawadzki, 1992) we can obtain the components of the wind velocity: *u*, *v*, and *w*, along the east-west, south-north and the vertical axis components, using the measured radial velocity V_r as follows (*c.f.* Figure 4.3a and b):

$$V_r(r,\theta,\varphi) = u(r,\theta,\varphi)\, sin\theta\, cos\varphi + v(r,\theta,\varphi)\, cos\theta\, cos\varphi + w(r,\theta,\varphi)\, sin\varphi \quad (4.1)$$

where θ is the azimuth angle clockwise from North and φ is the elevation angle.

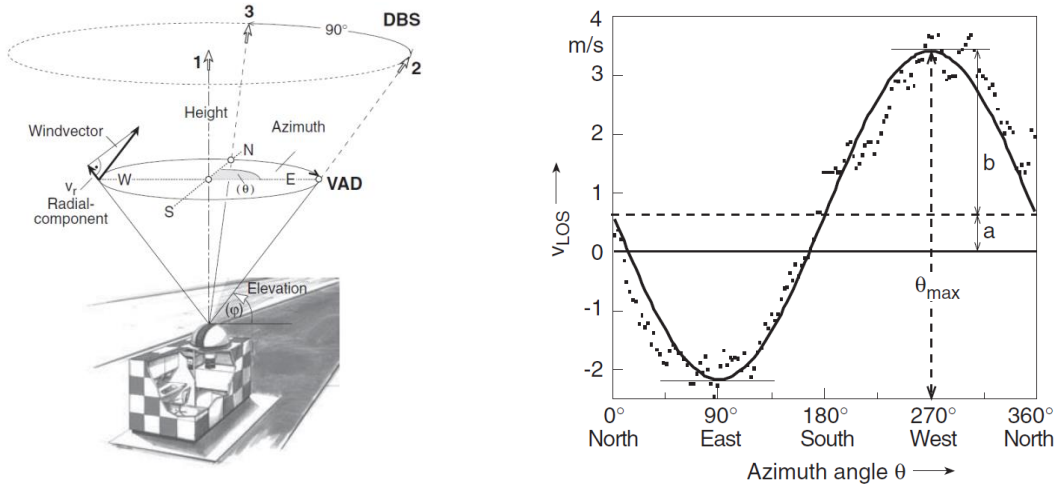

a) b)

Figure 4.3. a) Schematic example of the VAD scan technique of a Doppler lidar; b) a fitting example of sine over the radial wind velocity derived in VAD technique to obtain the horizontal wind velocity and direction (Weitkamp, 2005).

Considering that the VAD mode (*c.f.* Figure 4.3), with a vertical resolution of 30 m and angular resolution of 15° for each time step, we calculated the average radial velocity within 3 spatial bins, giving a final vertical resolution of 100 m for each azimuth angle. Then, we applied a linear fit between the averaged radial velocities and the azimuth angles using Eq. 4.1 to determine the u, v components for each time step to be used to calculate the horizontal velocity V_h profile and the azimuthal wind direction V_ϑ angle profile, with the resolution given above.

4.2 Passive Remote Sensing - Meteorological Satellites

The meteorological satellites offer cloud monitoring for several decades (Stephens et al., 2019) based on polar-orbiting and geostationary imaging systems. In general, the use of polar orbits offers high spatial resolution, but lack of temporal coverage, while the geostationary orbits offer higher sampling over certain regions. For instance, the Moderate Resolution Imaging Spectroradiometer (MODIS) (Platnick et al., 2017) offers measurements of the same region twice per day (crossing the equatorial at 10:30 (Terra) and 13:30 (Aqua)) with a nominal spatial resolution of 250 meters, while the Spinning Enhanced Visible and Infrared Imager (SEVIRI), which is on board to the geostationary

satellites MSG-8, 9, 10 and 11 (Meteosat Second Generation satellites) are located at the 0.0° latitude/longitude and the 9.5° east longitude, providing a rapid scan almost every 15 minutes with a 3 kilometers (at nadir) resolution (Schmetz et al., 2002).

In general, the meteorological satellites are equipped with passive radiometers with various spectral coverage from the visible up to the near-infrared (NIR) spectrum, to assess useful parameters in the retrieval of cloud microphysical properties. The visible channel data are used to constrain the cloud optical thickness (τ), which is representative of the liquid or water content of a cloud, since the clouds are non-absorbing and sensitive to the reflectance variations in this spectral region; while given that clouds are sensitive to the absorbing variations within the NIR spectral region, the NIR channel data are used to constrain the effective radius of the cloud droplets (r_{eff}) (Benas et al., 2019).

As an example, SEVIRI consists of 11 spectral channels from the visible to the thermal infrared, where the three shortwave channels (0.6, 0.8 and 1.6 μm) are calibrated based on the near nadir reflectances from Aqua MODIS, following the methodology described in Meirink et al. (2013) and are used to determine the τ; the near-infrared channel (3.7 μm) is used to determine the cloud phase and the particle size and shape; while the mid-infrared channels (8.5, 11 and 12 μm) are used to determine the cloud top temperatures, based on the cloud brightness temperature.

4.2.1 Cloud Microphysical Retrievals

Recently, the third edition of the CLoud property dAtAset using SEVIRI (CLAAS) released by EUMETSAT's Satellite Application Facility on Climate Monitoring (CM SAF) 021) (Meirink et al., 2022), provides data of the cloud parameters (τ, r_{eff},T_{ct}), along with the Earth's surface albedo, radiation fluxes at the top of the atmosphere and the surface, atmospheric temperature and water vapour profiles, vertically integrated water vapour (total, layered integrated), turbulent flux parameters and precipitation at the ocean surface, etc.

The cloud parameters, used in **Paper I**, were provided from the Inversion algorithm "Optimal Cloud Analysis algorithm" (OCA) which illustrates, among the radiance records, the collocated variables from a Numerical Weather Prediction (NWP) model, including surface pressure, column integrated water vapor and 155 temperatures at specific pressure levels. This algorithm uses as a reference the radiances from cloud observations obtained from the spaceborne lidar Cloud-Aerosol Lidar with Orthogonal Polarization (CALIOP) to train the SEVIRI radiances measured at channels within the visible range. Then, the retrieval of cloud optical and microphysical properties, for liquid and ice clouds, based on a Look-Up Table (LUT) which is used to define the τ and r_{eff} using the combination of one visible channel (0.6 μm) and one NIR channel (1.6 or 3.9 μm). The reflectance values of LUT are calculated using a radiative transfer model assuming a flat-plane stratiform PBL cloud (Bennartz and Rausch (2017)) and vertically homogenous in respect to water vapor content (Stephens, 1978), where the Rayleigh scattering is dominant, with negligible interferences from aerosol layers. In fact, this is a commonly used technique in satellite retrievals, introduced first by Nakajima and King (1990) and later applied to the SEVIRI reflectances (Roebeling et al., 2006).

The methodology to define τ and r_{eff} under different illumination conditions is described in detail in Benas et al. (2019), where a match between the radiation measurements and the LUT is obtained yielding the cloud optical properties. This methodology uses an array of different droplet size distributions simulating the radiance at TOA for SEVIRI channels, in respect to different r_{eff} values and of the droplet size distribution width.

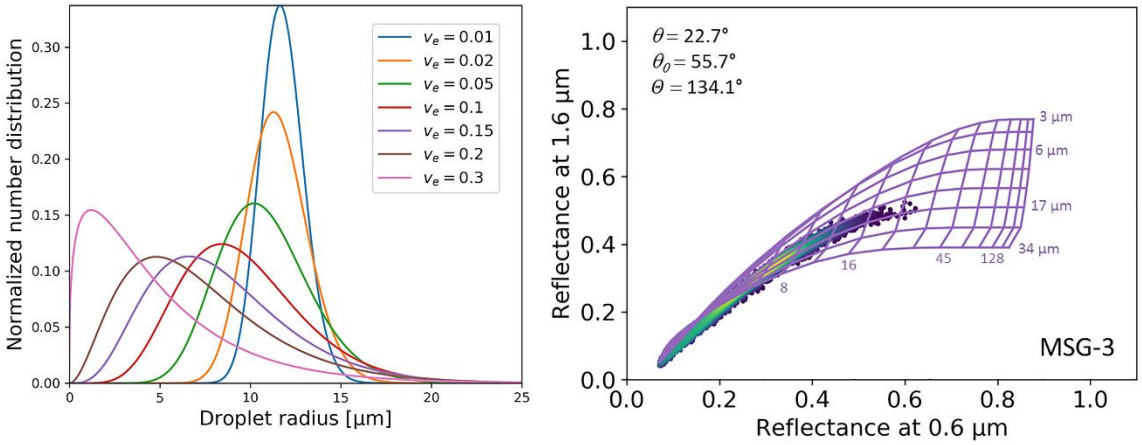

Figure 4.4. The normalized droplet size distributions with constant r_{eff} equal to 12 μm, for the seven values of effective variance b (left); An example of the reflectance observations from cloudy pixels (based on a case study of Benas et al. (2019), in respect of the Look-at-Table values (Benas et al., 2019) (right).

More precisely, a normalized gamma size distribution of liquid cloud droplets is assumed (*c.f.* Figure 4.4a):

$$n(r, r_{eff}, ab) = N_0 \, r^{\frac{1-3b}{b}} exp\left(-\frac{r}{r_{eff}}\frac{1}{ab}\right) \quad (4.2)$$

ere a is the average effective radius, b the effective variance, and N_0 the total droplet number is based on Hansen (1971) and Petty & Huang (2011). Then, Mie scattering calculations are performed to generate the scattering matrix, considering the multiple scattering effects, the solar zenith angle, and the surface albedo; a radiative transfer model is then used to simulate the cloud reflectances at TOA (at different spectral channels) and finally, the reflectances are stored into the LUTs. Thus, each LUT corresponds to a droplet different size distribution width, where a match between the radiation measurements and the LUT is obtained to retrieve, finally, the values of τ and r_{eff} for each cloud separately (*c.f.* Figure 4.4b).

5 TOOLS AND MODELS

5.1 ECMWF REANALYSIS 5TH GENERATION (ERA5)

In **Paper I**, we used the ECMWF Reanalysis 5th Generation (ERA5) hourly temperature and specific humidity data on 37 pressure levels (1000 hPa to 1 hPa) at a resolution of 0.25°×0.25° (Hersbach et al., 2018), to estimate the *T*- and *q*- profiles at the site using a weighted average of the surrounding grid-points. Moreover, a linear interpolation for every pressure level was applied on each variable to produce a 15-min timeseries that is compatible with the satellite timeseries. To link P_{ct} with the H_{ct} and T_{ct}, used subsequently for cloud detection and inversion, we applied the hypsometric equation to the grid-level quantities of *T* and *q* to develop their vertical profiles.

5.2 HYGROSCOPICITY AND CCN CONCENTRATION

The particle hygroscopicity parameter (κ) (Petters and Kreidenweis, 2007) characterizes the ability of particles to absorb water vapor during the formation of cloud droplets and is required for calculating CCN concentrations. The value of κ is estimated from ACSM measurements as follows: the ion concentrations of ammonium, sulfate, nitrate, chloride, and organics are converted to inorganic salt mixtures using the simplified ion-pairing scheme of Q-AMS model (Gysel et al., 2007), and the mole number of NH_4NO_3, NH_4HSO_4, $(NH_4)_2SO_4$, H_2SO_4 and organic aerosols, respectively. The value of κ is calculated using the volume fraction-averaged hygroscopicity of each organic and inorganic salt in the aerosol (Petters and Kreidenweis, 2007), with κ being 0.68 for NH_4NO_3, 0.56 for NH_4HSO_4, 0.53 for $(NH_4)_2SO_4$, (Petters and Kreidenweis, 2007), 0.97 for H_2SO_4 (Biskos et al., 2009) and 0.1 for organic aerosol (Duplissy et al., 2011). Aerosol types often have characteristic values of κ; for example, low values between 0.1-0.2 are associated with organic-rich aerosol (such as biogenic or biomass burning aerosol), ~0.35 with continental aerosol – which is often a ~ 50/50 mixture of organic species and inorganic salts with a hygroscopicity close to that of $(NH_4)_2SO_4$ (~0.6) (Petters and Kreidenweis, 2007). The κ timeseries was calculated on an hourly basis. We also examined the importance of constraining the uncertainty of organic κ; which equals $\delta\kappa_{org}$= ± 0.064 (Duplissy et al., 2011), and we found that the propagated error into the overall κ gives a total uncertainty of ± 0.035.

The CCN at a water vapor supersaturation level s is determined by integrating the particle size distribution from D_{cr}, which is calculated from κ-Kölher theory (Köhler, 1936), up to the largest particle size measured by the SMPS, i.e.,

$$CCN(s) = \int_{D_{cr}}^{\infty} n(D_p) dD_p \tag{5.1}$$

where $n(D_p)$ is the aerosol size distribution measured by the SMPS.

5.3 DROPLET ACTIVATION PARAMETERIZATION

The physically based aerosol activation parameterization (Nenes and Seinfeld, 2003), with extensions introduced by Fountoukis and Nenes (2005, 2007), Barahona et al. (2010) and Morales Betancourt and Nenes (2014) is used to calculate the droplet number that would form in PBLCs, from knowledge of the wind vertical velocity and the aerosol characteristics. The parameterization solves the equations that describe droplet formation in an ascending air parcel containing aerosols and water vapor, specifically at the point where supersaturation becomes maximum, s_{max}; N_d is then equal to the number of CCN with critical supersaturation less than s_{max} (Nenes et al., 2001). The parameterization uses as inputs the pressure and the temperature, the aerosol size distribution data from the SMPS, the hygroscopicity parameter κ derived from the ACSM data and the updraft velocities from HALO. Given that aerosol measurements are carried out at ground level, we convert the concentrations to cloud-top conditions using the ideal gas law.

As the droplet number depends strongly on the vertical velocity, which in turn varies considerably in the PBL over time, we compute the N_d that characterizes PBLCs – being a weighted average over the PDF of vertical velocities, by using the characteristic velocity, w^* according to the approach of Morales and Nenes (2010). For this purpose, the vertical velocity data are sampled in

segments within a 4-hour time moving window, and the positive updrafts were fit to a half-Gaussian PDF with a zero mean and standard deviation σ_w as follows:

$$p(w) = \frac{1}{\sigma_w \sqrt{2\pi}} e^{-\left(\frac{w}{\sqrt{2}\sigma_w}\right)^2} \quad (5.2)$$

The value of σ_w was determined every 15 minutes, for which the characteristic vertical velocity w^* was obtained and used at the parameterization. Additionally, in **Paper I**, we examined how the sampling time with a 1-, 2- and 4-hour window affects the calculated value of σ_w; in all cases the value of σ_w was found not to change the N_d value more than the inherent uncertainty of 30 % of the *in situ* N_d estimation. Based on this, we chose the 4-hour segments to ensure sufficient sampling of the PDF (about 400 updraft velocities per PDF). This approach is valid for boundary layers that are not influenced by deep convection and, hence are on average are characterized by a mean velocity of a few cm s^{-1} at most (the typical speed of boundary layer ascent/descent over a diurnal cycle). The PDF-averaging approach with a Gaussian PDF and the usage of the w^* has been shown to successfully predict cloud-scale values of N_d in field studies for cumulus and stratocumulus clouds (e.g., Conant et al., 2004; Meskhidze et al., 2005; Fountoukis et al., 2007; Kacarab et al., 2020, Georgakaki et al. 2021).

Another significant parameter considered was the role of the lateral entrainment, meaning the mixing of dry air in the ascending cloudy air parcel. The entrainment effect can be significant for cumulus and convective clouds (much less for stratocumulus), affecting the vertical distribution of liquid water and the number of droplets (Morales et al., 2011). Given that the clouds studied here are cumuliform, we consider the modest impact of entrainment effects on droplet number using the approach of Barahona and Nenes (2007) and Morales et al. (2011); this entails using an adiabatic activation parameterization, and reducing the vertical velocity that causes activation by a factor, called "entrainment parameter", that depends on the entrainment rate (which in effect captures the reduction in maximum supersaturation from mixing of dry air, compared to adiabatic droplet formation).

Barahona and Nenes (2007) and Morales et al. (2011) concluded that the best approach for the entrainment parameter is based on the adiabaticity (i.e., deviation of the vertical water profile from the adiabatic value). Thus, Morales and Nenes (2011) calculated the entrainment parameter for several clouds sampled during the CRYSTAL-FACE (Key West, Florida, July 2002) and CSTRIPE (Monterey, California, July 2003) campaigns, which proposed an average value of the entrainment parameter of 0.68 (see data in Table 2 of Morales and Nenes, 2011). Assuming this parameter is applied uniformly to the vertical velocity distribution, we, therefore, consider the effects of lateral entrainment in the cumuliform cloud sampled by multiplying the characteristic velocity for adiabatic activation w^* by 0.68.

According to Morales and Nenes (2010), the calculation of w^* (for diabatic activation) is obtained by multiplying σ_w with a parameter λ which depends on the type of aerosol found in the cloudy updraft. For continental aerosols with a concentration range between 1000-10000 cm^{-3}, λ equals 0.67 (see Figure 2a of Morales and Nenes, 2010) with an uncertainty of 0.02. This is the value of λ, which we apply in our calculations. Given the above considerations, the characteristic vertical velocity w^* used for calculating the droplet formation (and used to estimate *in situ* N_d) is given by $w^* = 0.68\,\lambda\,\sigma_w = 0.68 \times 0.67\,\sigma_w = 0.456\,\sigma_w$. Moreover, the relevant uncertainty of the characteristic velocity w^* can be estimated as $\delta w^* = 0.456\,\delta\sigma_w$, where the error $\delta\sigma_w$ is estimated as the standard deviation of σ_w in the fitting process.

The approach used to estimate *in situ* N_d makes the important assumption that calculations of activated N_d using observations of vertical velocity, aerosol and chemical composition are representative of the non-precipitating PBLCs. Numerous studies to date have shown that this approach, when carefully applied, can provide estimates of in-cloud droplet number for non-precipitating boundary layer clouds within a constrained uncertainty. For example, Conant et al. (2004) performed a droplet closure study, using a dataset of 21 cumulus clouds by the Center for Interdisciplinary Remotely-Piloted Aircraft Studies (CIRPAS) Twin Otter aircraft during NASA's Cirrus Regional Study of Tropical Anvils and Cirrus Layers–Florida Area Cirrus Experiment (CRYSTAL-FACE), and evaluated the performance of the Nenes and Seinfeld (2003) parameterization against *in situ* observations. They found that the measured droplet concentration close to the cloud base was within 15% of the predicted N_d. Meskhidze et al. (2005), evaluated the revised parameterization of Fountoukis and Nenes (2005), against data from cumuliform clouds collected during NASA's Cirrus Regional Study of Tropical Anvils and Cirrus Layers–Florida Area Cirrus Experiment (CRYSTAL-FACE, Key West, Florida, July 2002). On average, the predicted N_d was within 20% of observations at the base of cumuliform clouds, and within 30% of observations at different altitudes throughout the stratiform clouds; at the same time the observational uncertainty of N_d was estimated to be 30%. Fountoukis et al. (2007) evaluated the parameterization of Nenes and Seinfeld (2003) and Fountoukis and Nenes (2005) with data from 27 cumuliform and stratiform clouds sampled during the 2004 International Consortium for Atmospheric Research on Transport and Transformation (ICARTT) experiment. Droplet closure was achieved within 20% of the measurements. Morales et al. (2011) also showed that considering lateral entrainment effects diagnosed from the diabaticity (diagnosed from the liquid water vertical profile) provides N_d to within 31% for non-precipitating convective clouds. Georgakaki et al. (2021), using a combination of wind lidar data and in situ aerosol measurements, predicted N_d for orographic clouds in the Swiss Alps during the RACLETS campaign that agreed with *in situ* observations to within 25%. We therefore apply this methodology to estimate droplet number in the clouds considered here, assuming an inherent method uncertainty of 30%.

5.4 ISORROPIA

ISORROPIA II is a thermodynamic equilibrium model (Fountoukis and Nenes, 2007) which uses as inputs the observed inorganic components measured by ToF-ACSM, to calculate the mixture of inorganic salts (which can include NH_4HSO_4, NH_4Cl, NH_4NO_3, $(NH_4)_2SO_4$, $CaCO_3$, $CaCl_2$, $Ca(NO_3)_2$, $CaSO_4$, $(NH_4)_3H(SO_4)_2$, $KHSO_4$, K_2SO_4, $NaHSO_4$, Na_2SO_4 and H_2SO_4) found in the aerosol. Then, by using the Zdanovskii, Stokes and Robinson (ZSR) mixing rule the bulk hygroscopicity parameter (Petters and Kreidenweis, 2007) can be derived based on the volume fraction of the inorganic salts, given the hygroscopicity of each salt (can be obtained from Table 2 of Padró et al., 2010) and further expanded by including the volume fraction of *eBC*, considering the hygroscopicity of *eBC* equal to 0.2 based on Ding et al., 2021). This method was used in **Paper IV**, while a simpler form of the ISORROPIA called "Ion-Pairing Scheme" was used in **Paper I** to calculate the bulk hygroscopicity parameter and so to be used to initialize the aerosol activation parameterization, respectively.

6 EXPERIMENTAL SITES

6.1 URBAN BACKGROUND ENVIRONMENT IN ATHENS METROPOLITAN AREA (AMA)

Our observations where the **Paper I** and **II** are based on where took place at the AMA in the Attica peninsula in Greece.

The AMA is surrounded by four mountains: Egaleo (468 m), and Parnitha (1413 m) to the northwest, Penteli (1109 m) to the north and Hymettus (1026 m) to the east, with a major opening to the sea on the south-western part (Saronikos Gulf) (*c.f.* Figure 6.1), while it hosts a densely populated urban area of about 3.8 million inhabitants within about 3000 km^2.

The AMA is characterized by a variety of anthropogenic emissions, and a complex topography with about 2.5 million vehicles leading to heavy traffic conditions, having as a result important local aerosol emissions. Despite that Athens has been heavily deindustrialized over the recent decades, there are still emissions linked to factories and oil distilleries. The major industrial units currently located in AMA are two refineries, one fertilizer plant, two iron steel plants and one cement plant. These industrial plants are concentrated along the South West to North East axis, which includes the western quarters of the city and the central parts of Athens and the nearby city of Piraeus (Kalabokas et al., 1999). Furthermore, there are also about 100 medium-sized industries, mainly in the domain of food processing, plastic and textile production (Katsoulis, 1996).

The studied region is located at the NCSRD station (37.995° N, 23.816° E, at 270 m above sea level-asl.), which is a member of the World Meteorological Organisation (WMO) Global Atmospheric Watch (GAW) network, the Aerosol, Clouds and Trace Gases Research Infrastructure (ACTRIS) and the PANACEA., and lays within the AMA on the foothills of Mount Hymettus (Vratolis et al., 2020), about 8 km to the north of Athens city center and is characterized as an urban background station, due to its proximity to the city centre. Therefore, it is influenced by fresh and aged traffic-related aerosol particles, especially when the prevailing wind has western (W) directions, and the regional background aerosol (Kostenidou et al., 2015; Vratolis et al., 2019; Eleftheriadis et al., 2021).

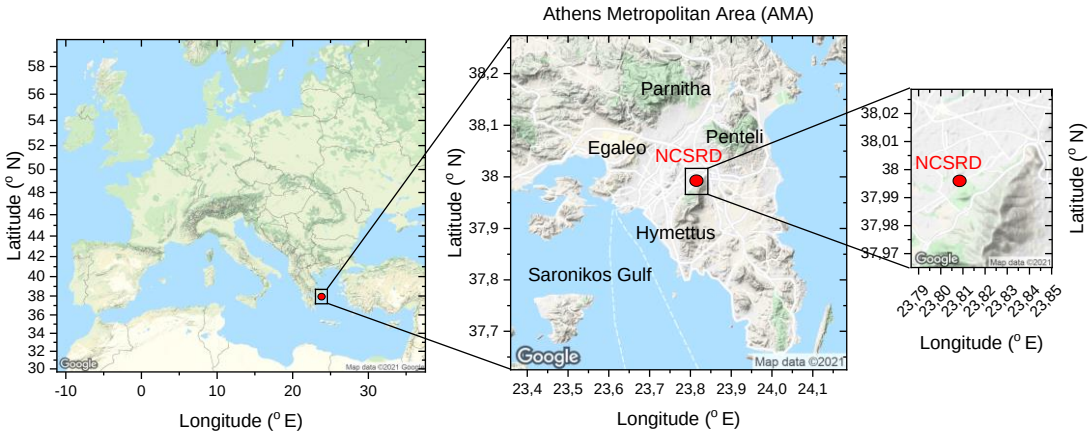

Figure 6.1 Study area (left) and the sub-domain over the AMA (middle) marked by a red dot (Foskinis et al., 2022).

The selected experimental site offers a great variety of aerosol types and meteorological conditions (Kostenidou et al., 2015; Vasilatou et al., 2017). The prevailing northern winds transport continental polluted air masses to the AMA, mixed with local emissions along the Balkans-Aegean

Sea axis (Diapouli et al., 2014; Vratolis et al., 2019). Southern winds are usually associated with the transport of marine aerosols, and, occasionally, with mineral dust from the Saharan desert (Diapouli et al., 2017b; Soupiona et al., 2020), while under stagnant atmospheric conditions, locally emitted anthropogenic aerosols dominate aerosol concentrations in the PBL (Kalogridis et al., 2018).

6.2 High Altitude Background Environment at Mt. Helmos

Our observations regarding **Paper III** and **IV** concern the $(HAC)^2$ station, which is located at the top of the Helmos mountain in the Peloponnese at an altitude of 2.314 m (37.984033 °N, 22.196060 °E; *c.f.* Figure 6.2). $(HAC)^2$ is the only high-altitude station for atmospheric research in the Eastern Mediterranean region focusing on the study of the physico-chemical characteristics of aerosols and climate-related gases (*e.g.*, CO_2, CH_4, H_2O, etc). $(HAC)^2$ has been established and operated by the Environmental Radioactivity Laboratory (ERL) of the NCSRD since 2015. According to Collaud et al. (2018), $(HAC)^2$ has very low PBL-TopoIndex values, which means that the influence of the PBL is statistically low compared to other high-elevation sites.

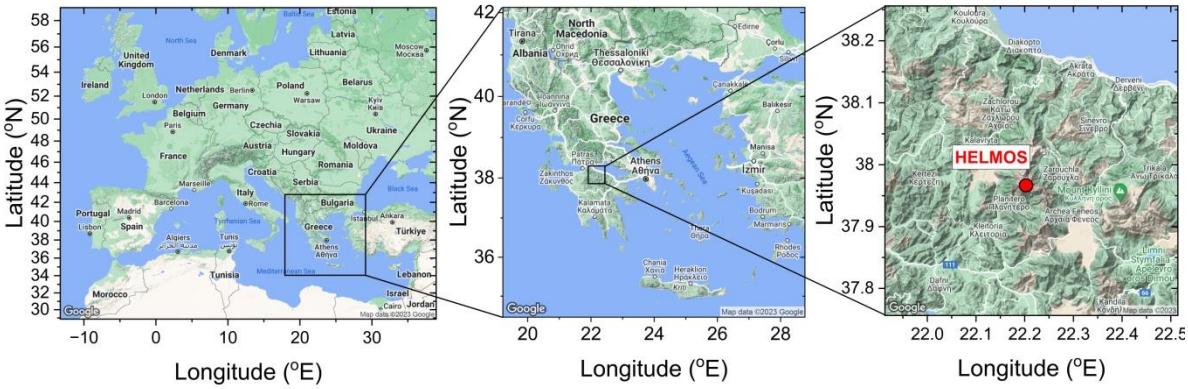

Figure 6.2. The study area (left) and the sub-domain over Greece (middle), and the regional area around $(HAC)^2$ is marked by a red dot.

The dataset used in this study has been obtained during the Cloud-AerosoL InteractionS in the Helmos background TropOsphere Campaign (CALISTHO) (https://calishto.panacea-ri.gr/), which took place at the Helmos mountain, from October to November of 2021, and was extended up to March of 2022, aiming to study the cloud microphysical properties using *in-situ* and remote sensing techniques.

A second station, called "Vathia Lakka" (VL), was located at the lee side of the mountain approximately ~1.7 km away (coordinates 37.999473°N, 22.193391°E) and 500m below $(HAC)^2$. *In situ* measurements are available at both $(HAC)^2$ and Vathia Lakka, the latter being used as a pre-cloud proxy, as well, a wind Doppler Lidar, was placed at this location to provide the vertical profiles of updrafts along the lee side.

7 MAIN RESULTS

This chapter presents a synopsis of the main results, while for the detailed ones, kindly refer to the original publications included below in the supplementary material.

7.1 PAPER I: TOWARDS RELIABLE RETRIEVALS OF CLOUD DROPLET NUMBER FOR NON-PRECIPITATING PLANETARY BOUNDARY LAYER CLOUDS AND THEIR SUSCEPTIBILITY TO AEROSOL

7.1.1 SUMMARY

Remote sensing has been a key resource for developing extensive and detailed datasets for studying and constraining aerosol-cloud-climate interactions. However, aerosol-cloud collocation challenges, algorithm limitations, as well as difficulties in unravelling dynamics from aerosol-related effects on cloud microphysics, have long challenged precise retrievals of cloud droplet number concentrations. By combining a series of remote sensing techniques and *in situ* measurements at ground level, we developed a semi-automated approach that enables us to address several retrieval issues for a robust estimation of cloud droplet number for PBLCs. The approach is based on satellite retrievals of the PBLC cloud droplet number (N_d^{sat}) using the geostationary meteorological satellite data of the OCA product, which is obtained by the SEVIRI of the EUMETSAT. The parameters of the retrieval are optimized through closure with droplet number obtained from a combination of ground-based remote sensing data and *in situ* observations at ground level. More specifically, the remote sensing data are used to retrieve cloud-scale vertical velocity, while the *in situ* aerosol measurements at ground level were used to determine the aerosol size distribution and the chemical composition. Finally, we used all these data as input to a state-of-the-art droplet activation parameterization to predict the respective CCN spectra, cloud maximum supersaturation and N_d, accounting for the effects of vertical velocity distribution and lateral entrainment.

Closure studies between collocated N_d and N_d^{sat} are then used to evaluate the droplet spectral width parameter used in the retrieval of droplet number and determine the optimal retrieval algorithm. This methodology, used to study aerosol-cloud interactions for non-precipitating clouds formed over the AMA, Greece, during the springtime period from March to May 2020, shows that droplet closure can be achieved within 30%, comparable to the level of closure obtained in many *in situ* studies. Given this, the ease of applying this approach with satellite data obtained from SEVIRI with high temporal (15 min) and spatial resolution (3.6 km × 4.6 km), opens the possibility of continuous and reliable N_d^{sat}, giving rise to high-value datasets for aerosol-cloud-climate interaction studies.

7.1.2 OBJECTIVES

Aerosol-cloud interactions constitute one of the most uncertain aspects of anthropogenic climate change (Seinfeld et al., 2016; IPCC, 2021). Central to these interactions are the variations in CCN concentrations from anthropogenic activities, as they modulate the N_d in clouds and the τ, and thus, affect the atmospheric radiation budget and climate. CCN activate into cloud droplets in supersaturated air generated within cloudy updrafts, and the supersaturation level required for each particle to act as a CCN, is well described by Köhler's theory (Köhler, 1936), modified later to include the effects of organic compounds and multiple hygroscopic species (*e.g.*, Petters and Kreidenweis, 2007). Supersaturation in clouds is mostly generated by expansion cooling in updrafts, driven by turbulence, convection, or gravity waves (Quaas et al., 2020).

Initial studies by Twomey and Warner (1967) showed that elevated concentrations of CCN in clouds increase N_d, reduce their size and thus enhances the amount of solar radiation reflected back to space. This effect, which tends to cool the climate, is known as the "aerosol indirect effect" (Twomey, 1991) or "cloud albedo effect" (IPCC, 2021) on climate. Later studies showed that this N_d increment exists but varies considerably depending on the supersaturation level that develops in clouds – which in turn depends on the vertical velocity (w), and aerosol/CCN presence (Feingold et al., 2001; Ghan et al., 1998; Reutter et al., 2009). It is now generally accepted that droplet formation tends to be either "aerosol-limited", when supersaturation is high and N_d is very sensitive to aerosol changes, or "velocity-limited", when the supersaturation is so low that N_d is insensitive to aerosol changes (Reutter et al., 2009). However, more recent studies showed that when approaching "velocity limited" conditions, N_d tends to come near an asymptotic upper limit, the so-called limiting droplet number (N_d^{lim}), which depends only on the intensity of the turbulence (Bougiatioti et al., 2020; Georgakaki et al., 2021; Kacarab et al., 2020).

Changes in N_d, apart from modifying the average size of cloud particles, also affects the shape of the droplet size spectrum and the resulting cloud radiative properties. Thus, the first generation of global climate models (GCM) with explicit consideration of N_d initially assumed that all droplets have the same diameter (i.e., monodisperse droplet population) which can directly be linked to the r_{eff} and to τ. Liu and Daum (2002) showed that this assumption leads to important biases in the calculations of τ and cloud radiative forcing, as monodisperse droplets scatter differently than a distribution with the same N_d and liquid water content (LWC). Known as the "dispersion effect", this bias can be mitigated using the effective radius factor (β) that quantifies the droplet spectral dispersion so that when it is combined with the average droplet radius and cloud LWC, gives the correct τ. Several formulations have been proposed in the literature to represent the relationship between β and cloud microphysical quantities resolved in models - N_d and LWC. Expressions proposed by Martin et al. (1994), Liu and Daum (2002), Peng and Lohmann (2003) and Rotstayn and Liu (2003) were based on observations, while more recent formulations are derived from the adiabatic parcel theory (Chen et al., 2016, 2018; Liu et al., 2014). Altogether, these expressions show a positive correlation between β and N_d for aerosol- and velocity-limited regimes.

Despite decades of research, the imprint of aerosol effects on cloud albedo and climate still remains highly uncertain (Seinfeld et al., 2016; Quaas et al., 2020; IPCC, 2021), owing to the highly buffered, nonlinear and multiscale nature of clouds and their interactions with dynamics, radiation and aerosol (Stevens and Feingold, 2009). Therefore, there is a pressing need to have extensive global datasets of N_d aerosol concentration, and cloud-scale dynamics (w especially) to understand their

relative importance (*e.g.*, Rosenfeld et al., 2016). Recently, Quaas et al. (2020) showed that satellite remote sensing is the only approach that offers the potential to obtain global datasets with frequent coverage; current retrieval algorithms, however, carry many uncertainties and require constraints that can only be addressed with *in situ* and/or ground-based remote sensing observations. Particularly important is constraining *w,* which is seldom-evaluated in models (Sullivan et al., 2016). Furthermore, *w* can change along with aerosol and affect the response of clouds, as demonstrated recently by Bougiatioti et al. (2020) and Kacarab et al. (2020) for very different cloud systems, showing that a co-variability of aerosol concentration with w magnifies the inherent response of droplets to aerosol variations by up to 5 times.

It has long been known that *w* exhibits significant spatio-temporal variability even at the scale of single clouds. This presents a challenge about which velocity to use to link aerosol with N_d. Morales and Nenes (2010) proposed using a "characteristic" velocity, computed from the probability distribution function (PDF) of *w* in the airmass or cloud of interest, to provide a PDF-averaged N_d, which in turn is used to represent cloud-scale N_d. The characteristic velocity approach can be automated and easily applied to data either from *in situ* probes or ground-based remote sensing systems (Doppler lidars/radars). The calculation of N_d by using this characteristic velocity and *in situ* ground level data has been shown to agree with *in situ* measurements at the cloud base level of cumulus and stratocumulus clouds in numerous studies to date (Fountoukis and Nenes, 2007; Kacarab et al., 2020; Meskhidze, 2005).

A more empirical approach to determine cloud base updrafts, based on cloud base height, has been proposed by Rosenfeld et al. (2016), using ground-based Doppler lidar measurements along with satellite data from the Visible Infrared Imaging Radiometer Suite (VIIRS). Their approach gave closure to within ± 25-30%, when applied to PBL convective clouds, non-obscured by upper layer clouds or including semitransparent cirrus. Although skilful, Rosenfeld et al. (2016) point out that this methodology cannot be applied globally, because the distribution of CCN and cloud base updrafts are lacking.

Thus, we improved an existing remote sensing approach for the retrieval of N_d in non-precipitating PBLC, by considering the spectral dispersion of cloud droplets through β. The retrieval is evaluated using published dispersal relationships by comparing the N_d obtained from a combination of *in situ* observations, ground-based remote sensing data and parcel theory. The same data are then used to determine an optimal dispersal- N_d relationship that minimizes the closure error between retrieved and *in situ* N_d. During the optimization process, the cloud-scale w distributions, CCN spectra, and cloud maximum supersaturation, along-with the N_d, are obtained. We apply this methodology to a highly variable semi-urban environment and discuss future directions and perspectives.

7.1.3 METHODOLOGY AND CASE STUDIES

Our methodology is based on the concurrent use of remote sensing, model data and expressions for β, applied to non-precipitating PBLCs in well-mixed PBLs and associated cloud-base vertical velocities. The remote sensing retrievals of N_d^{sat} are compared against estimations of *in situ* N_d obtained from the application of the Nenes and Seinfeld (2003) activation parameterization, with extensions introduced by Fountoukis and Nenes (2005), Barahona et al., (2010) and Morales Betancourt and Nenes (2014). As input data to the droplet parameterization, we use the vertical velocity variation inside the PBL provided by the HALO wind lidar, as well as the aerosol size distribution and chemical composition at ground level, based on a Scanning Mobility Particle Sizer (SMPS) and a Time-of-Flight Aerosol Chemical Speciation Monitor (ToF-ACSM), respectively.

The satellite retrievals of N_d^{sat} of the PBLCs were performed using the algorithm of Bennartz (2007), which uses the principal cloud parameters (***e.g.***, r_{eff} and the τ, along with a constant value of β. The explicit expression of β, which is related to N_d^{sat}, can be obtained by modifying the Bennartz (2007) algorithm and solving this form numerically. Then, we examine the closure of the satellite retrieval algorithm by using the $\beta - N_d$ relationships, called *"*β −expressions", found in the literature (M94 - Martin et al., 1994; RL 03 - Rotstayn and Liu, 2003; PL03 - Peng and Lohmann, 2003; Z06 - Zhao et al., 2006; GCMs - Rotstayn and Liu 2009; F11 - Freud et al. 2011). Additionally, we propose a new β −expression which minimizes the closure error between $N_d - N_d^{sat}$, based on the cloud parameters.

The cloud parameters r_{eff}, τ and the cloud top pressure (P_{ct}) were obtained from the OCA product (EUMETSAT, 2015) which is based on geostationary meteorological MSG satellite data, and the atmospheric pressure-temperature profiles from the ERA5 (Hersbach et al., 2018), to calculate the cloud top temperature (T_{ct}) and the cloud top height (H_{ct}) in respect of P_{ct}. Additionally, we used the "limiting droplet number", N_d^{lim} at cloud top, to examine the degree to which clouds are susceptible to changes in aerosol content, while it was estimated from the relationship given by Georgakaki et al. (2021):

$$N_d^{lim}(\sigma_w) = 1137.9\,\sigma_w - 17.1 \quad (7.1)$$

where N_d^{lim} is expressed in cm^{-3}, and σ_w in m s^{-1}.

Our observations took place at the AMA in the Attica peninsula in Greece at the facilities of NCSRD, while we focused on the period between March and May 2020, where 5-days of data with PBLC formation were analyzed: 18, 28 March, and 01, 02, and 07 of April (*c.f.* Figure 7.1).

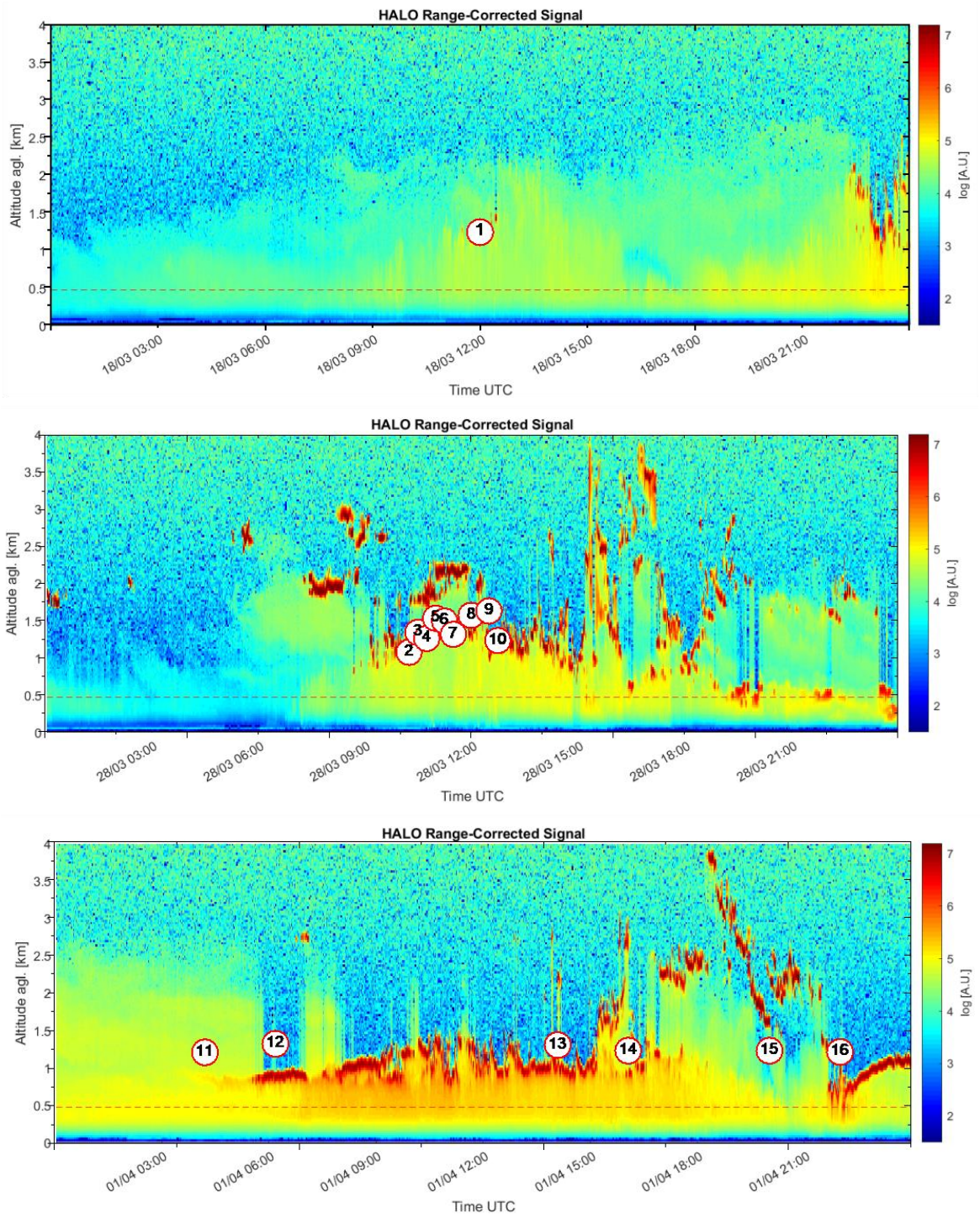
HALO Range-Corrected Signal
Altitude agl. [km]
Time UTC
log [A.U.]
18/03 03:00
18/03 06:00
18/03 09:00
18/03 12:00
18/03 15:00
18/03 18:00
18/03 21:00
1
HALO Range-Corrected Signal
Altitude agl. [km]
Time UTC
log [A.U.]
28/03 03:00
28/03 06:00
28/03 09:00
28/03 12:00
28/03 15:00
28/03 18:00
28/03 21:00
2
3
4
5
6
7
8
9
10
HALO Range-Corrected Signal
Altitude agl. [km]
Time UTC
log [A.U.]
01/04 03:00
01/04 06:00
01/04 09:00
01/04 12:00
01/04 15:00
01/04 18:00
01/04 21:00
11
12
13
14
15
16

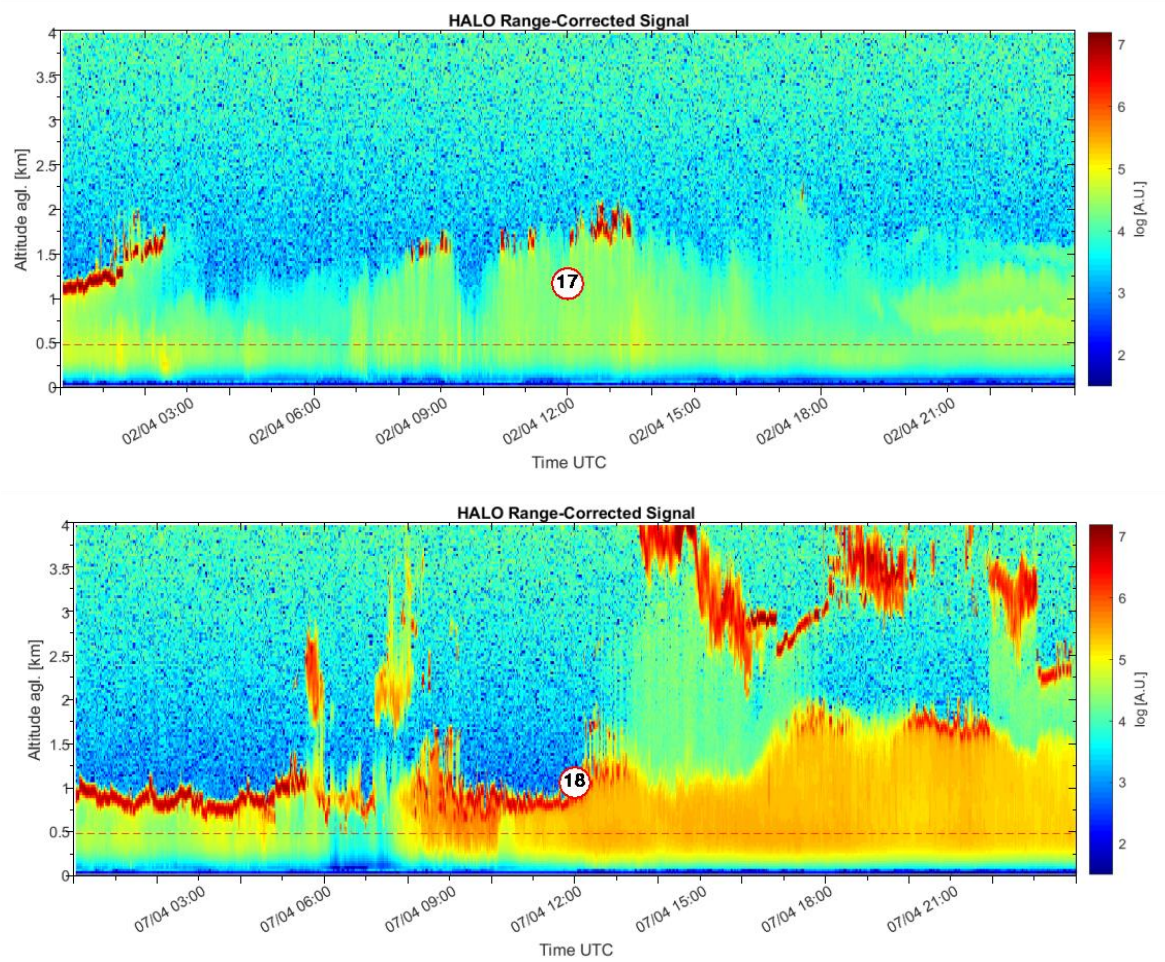

Figure 7.1 Spatio-temporal evolution of RCS of 18-March 2020, 28-March 2020, 1-April 2020, 2-April 2020, and 7-April 2020; the symbol indicates the satellite detected cloud regarding H_{ct}. The red dashed horizontal line indicates the altitude where the updrafts were sampled in 4-hour segments for the calculation of σ_w (Foskinis et al., 2022).

Figure 7.1 presents the spatio-temporal evolution of the range-corrected co-polar backscattered lidar signal (RCS) obtained by HALO and the detected clouds (presented as numbered circle symbols). The red dashed horizontal line indicates the altitude where the updrafts were sampled in 4-hour segments for the calculation of σ_w. The aerosol load within the PBL can be seen in the color scale up to 5 arbitrary units (A.U.), while the higher values of the backscattered signal (>7 A.U.) indicate the cloud bases. In the case of thick clouds, the transmitter signal attenuates within the clouds due to multiple scattering, reducing the backscatter signal intensively.

7.1.3.1 Modeling and Data Preprocessing

Figure 7.2a presents the timeseries of total aerosol concentration (N_{aer}) integrated over the SMPS size distributions, and σ_w, with the symbols colored by κ, for the period 18 March to 07 April 2020, while Figure 7.2b presents the corresponding N_d values with the symbols colored by N_d/N_d^{lim}. The periods of weaker turbulence (low σ_w, Figure 7.2a) force N_d to persistently approach N_d^{lim} (*e.g.*, Figure 7.2b, 01 April 2020). As a result, the droplet formation is strongly velocity-limited and tends

to be insensitive to aerosol variations. The opposite is seen when $N_d/N_d^{lim} < 0.5$, as droplet formation becomes aerosol-limited and less sensitive to σ_w variations.

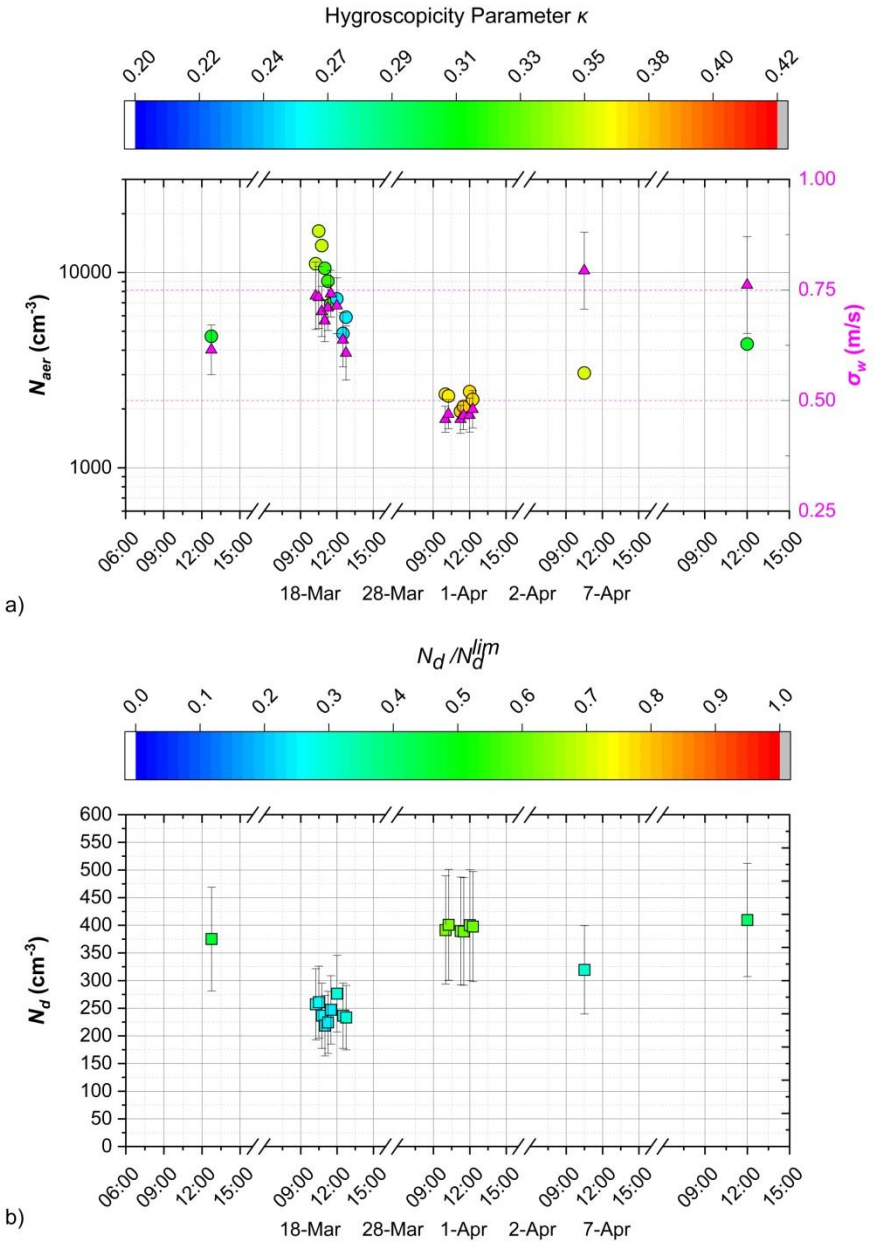

Figure 7.2. a) Timeseries of N_{aer} versus κ and σ_w values, for the period 18 March to 07 April 20230. b) The corresponding in situ derived N_d values are colored by the ratio N_d/N_d^{lim} as derived by the parameterization (Foskinis et al., 2022).

7.1.3.1.1 Effective radius factor β

The β was introduced to mitigate the bias known as the "dispersion effect", related to the width of the cloud droplet size spectrum, and combined with the average droplet radius, to give the

correct τ. According to Liu and Daum (2002), β is related to relative dispersion of the droplet spectrum (ε):

$$\beta = \frac{(1+2\varepsilon^2)^{\frac{2}{3}}}{(1+\varepsilon^2)^{\frac{1}{3}}} \quad (7.2)$$

In the literature several studies are attempting to quantify ε. Martin et al. (1994), using aircraft observations of the microphysical characteristics of warm marine stratocumulus clouds from the eastern Pacific, South Atlantic, subtropical regions of the North Atlantic, and the sea areas around the British Isles, proposed an expression of $\varepsilon = 0.000574\, N_d(cm^{-3}) + 0.2714$, while, Rotstayn and Liu (2003) based on the observations of Liu and Daum (2002), suggested an expression of $\varepsilon = 1 - 0.7e^{-0.003 \times 10^{-6} N_d(cm^{-3})}$. Using aircraft data collected from a region influenced by polluted marine aerosol conditions, Zhao et al. (2006) suggested a value of $\varepsilon = 0.4$. Using Eq.7.2, we inserted the above-mentioned expressions of ε to obtain the β −expressions (*c.f*. Table 7.1). Peng and Lohmann (2003) suggested an expression of $\beta = 1.18 + 4.5\ 10^{-4}\ N_d(cm^{-3})$ using aircraft measurements over the ocean, near coastal areas, and far from the interior of continents, through the coast of Nova Scotia in the Canadian and the United States Arctic. Freud and Rosenfeld (2012), using measurements of cloud droplet size distribution in various locations, found an average value of β equal to 1.08, as indicated by the line of best fit between r_{eff} and mean volume radius. Rotstayn and Liu (2009) pointed out that most GCM studies adopt a β of 1.1 (*c.f*. Table 7.1).

Reference	Acronym	Literature expressions, N_d in cm^{-3}	Expression of β, N_d in cm^{-3}
Martin et al., 1994	M94	$\varepsilon = 5.74\ \times 10^{-4}\ N_d + 27.14 \times\ 10^{-2}$	$\frac{(1+2(5.74 \times 10^{-4}\ N_d + 27.14\ \times 10^{-2})^2)^{\frac{2}{3}}}{(1+(5.74\ \times 10^{-4}\ N_d + 27.14\ \times 10^{-2})^2)^{\frac{1}{3}}}$
Rotstayn and Liu, 2003	RL03	$\varepsilon = 1 - 0.7e^{-3\times\ 10^{-9}\ N_d}$	$\frac{\left(1+2(1-0.7e^{-3\times 10^{-9}\ N_d})^2\right)^{\frac{2}{3}}}{\left(1+(1-0.7e^{-3\times 10^{-9}\ N_d})^2\right)^{\frac{1}{3}}}$
Peng and Lohmann, 2003	PL03	$\beta = 1.18 + 4.5 \times 10^{-4}\ N_d$	$1.18 + 4.5 \times\ 10^{-4}\ N_d$
Zhao et al., 2006	Z06	$\varepsilon = 0.4$	1.145
Freud et al., 2011	F11	$\beta = 1.08$	1.08
Rotstayn and Liu, 2009	GCMs	$\beta = 1.1$	1.1

Table 7.1. β-expressions based on literature according to: 1) Martin et al. (1994)—M94, b) Rotstayn and Liu (2003)—PL03, c) Peng and Lohmann (2003)—PL03, Zhao et al. (2006)—Z06, d) Freud and Rosenfeld (2012)—F12 and e) GCMs studies–Rotstayn and Liu (2009), respectively (Foskinis et al., 2022).

7.1.3.1.2 Satellite Remote Sensing - Optimal Cloud Analysis Product and Droplet Number

The OCA product determined from EUMETSAT (EUMETSAT, 2015) provides τ, r_{eff} and P_{ct} accompanied with their errors $\delta\tau$, δr_{eff} and δP_{ct} with a spatial resolution of 3.6 km x 4.6 km for the study region, as derived from SEVIRI with a temporal resolution of 15 min. The OCA algorithm uses a synergy of data to calculate the cloud parameters; however, there are always assumptions which

have consequent limitations affecting the accuracy of r_{eff} and τ. According to the description of the OCA algorithm (EUMETSAT, 2015), the algorithm utilizes the land surface reflection, along with other model parameters derived from the Numerical Weather Prediction sources.

In Figure 7.3 we summarize the τ, T_{ct}, and r_{eff} which were used as input to the satellite algorithm to retrieve the N_d^{sat} data. Additionally, we chose to prevent the dataset from high or multi-layer clouds, and isolate the PBL clouds by excluding clouds with P_{ct} lower than 800 hPa. Moreover, we applied a parallax correction, according to Koenig (2020), for each detected cloud based on H_{ct} in order to calculate the true geolocation of each cloud and then, we isolated the clouds that are collocated over our measuring site. This step helps to correct the displacement that is created due to the satellite angle of view, along with H_{ct}.

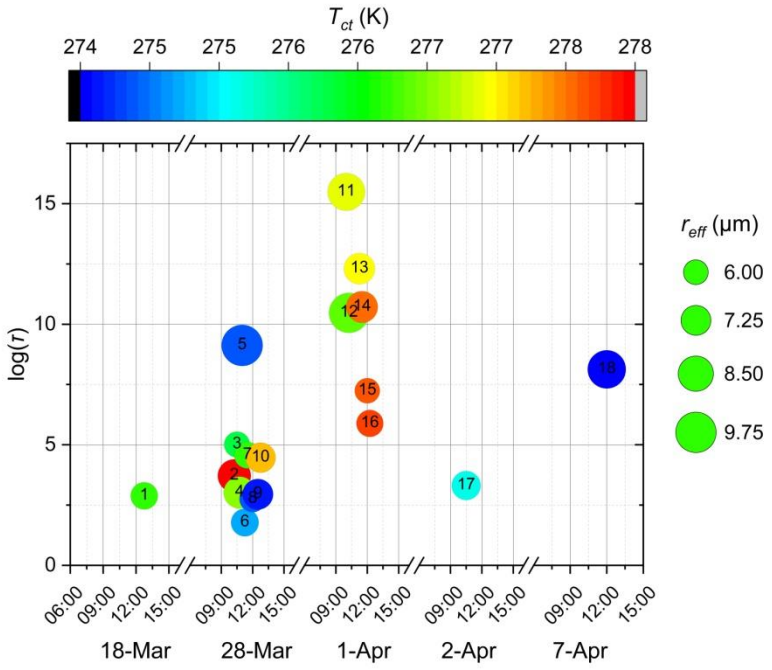

Figure 7.3: The τ, r_{eff} provided by OCA against with T_{ct}, which is calculated via the ERA5 T-Profile, for the clouds studied; the labelling refers to the serial number of each cloud (Foskinis et al., 2022).

According to Grosvenor et al. (2018), the N_d^{sat} algorithm can be determined as:

$$N_d^{sat} = \frac{\sqrt{5}}{2\pi}\sqrt{\frac{f_{ad}\, c_w}{\rho_w\, Q_{ext}}}\,\tau\,\beta^3\, r_{eff}{}^{-\frac{5}{2}} \quad (7.3)$$

in which Q_{ext} is the Mie extinction efficiency factor, which is equal to 2 for large droplets of diameters greater than 5 μm (Hulst, 1958). The condensation rate c_w (Brenguier et al., 2000) provides the liquid water released in an adiabatic updraft per meter of ascent, and is given by $c_w = 0.0016 + 4.86\,10^{-5}\,T_{ct} - 3.42\,10^{-7}{T_{ct}}^2$ (Zhu et al., 2018), where c_w is in g m^{-3} m^{-1} and T_{ct} expressed in °C, while f_{ad} is the adiabatic value here equal to 1. The water density ρ_w is considered constant, equal to 997 kg m^{-3}, while T_{ct} is used to characterize the in-cloud environment. Moreover, we calculated the propagation error δN_d^{sat} of N_d by using the Chain rule to Eq.7.3, which corresponds to the diffusional error due to each variable to the N_d^{sat} retrieval, as follows:

$$\delta N_d^{sat} = \sqrt{\left(\frac{\partial N_d^{sat}}{\partial c_w}\delta c_w\right)^2 + \left(\frac{\partial N_d^{sat}}{\partial \tau}\delta \tau\right)^2 + \left(\frac{\partial N_d^{sat}}{\partial r_{eff}}\delta r_{eff}\right)^2 + \left(\frac{\partial N_d^{sat}}{\partial \beta}\delta \beta\right)^2}$$

in which the terms $\frac{\partial N_d^{sat}}{\partial c_w}$, $\frac{\partial N_d^{sat}}{\partial \tau}$, $\frac{\partial N_d^{sat}}{\partial r_{eff}}$, and $\frac{\partial N_d^{sat}}{\partial \beta}$ are the sensitivity of N_d^{sat}concerning τ, r_{eff}, c_w and β, respectively. The condensation rate error δc_w was estimated from the lapse rate along with the δP_{ct}. δc_w $\delta \tau$, δr_{eff} were estimated for the whole dataset and on average were found to be equal to 6 10^{-6} g m^{-3} m^{-1}, 1.07, 0.76 μm, respectively. We note here that $\frac{\partial N_d^{sat}}{\partial c_w}\delta c_w$ was on average relatively small (±11 cm^{-3}), and contributes ±3% on the total bias of N_d^{sat}. Therefore, we decided to omit it from Eq.5. $\frac{\partial N_d^{sat}}{\partial \tau}\delta \tau$ and $\frac{\partial N_d^{sat}}{\partial r_{eff}}\delta r_{eff}$ were found on average equal to ±39 cm^{-3}, ±84 cm^{-3}, contributing ±13% and ±27% to the error, respectively. Furthermore, given that the uncertainty $\delta\beta$ it is not available from published literature, we used the $\delta\beta$ which derived from the optimization process (see Section 3.1) and found it equals to 0.22, thus the $\frac{\partial N_d^{sat}}{\partial \beta}\delta \beta$ found to contribute ±52% to the droplet error which translates to ±165 cm^{-3}. This implies that of all parameters considered in this study, optimally constraining β is of prime importance for the N_d^{sat} retrieval, compared to the other variables.

For expressions where β depends on N_d^{sat}, β (N_d^{sat}), the retrieval Eq.7.3 can be modified as follows:

$$f(N_d^{sat}) = N_d^{sat} - \frac{\sqrt{5}}{2\pi}\sqrt{\frac{f_{ad}\, c_w}{\rho_w\, Q_{ext}}\tau\, \beta^3(N_d^{sat})\, r_{eff}{}^{-\frac{5}{2}}} = 0 (7.5)$$

where N_d^{sat} is determined from the numerical solution of Eq.7.5 using the $\beta(N_d^{sat})$ expressions in Table 7.1. We discard the less reliable retrievals when the droplet uncertainty is significant, which corresponds to the solutions of Eq.7.5 having δN_d^{sat} > 600 cm^{-3}, $\delta N_d^{sat} / N_d^{sat}$ > 0.5, N_d^{sat} > 2000 cm^{-3}, or N_d^{sat}<100 cm^{-3}.

Finally, we performed closure studies between the accepted solutions of N_d^{sat} using each literature based β-expression, against to the estimations of *in situ* derived N_d from the parameterization (section 2.4.3). By using the M94, RL03, PL03, Z06, GCMs, and F11 expressions, the corresponding averaged mean normalized bias (MNB) between N_d^{sat} and estimations of *in situ* N_d is equal to -50.7±12.4%, 55.5±53.5%, 13.2±34.8%, -27.3±17.9%, -35.6±15.9%, and -39.1±15.0%, respectively (*c.f.* Figure 7.6b; Table 7.1).

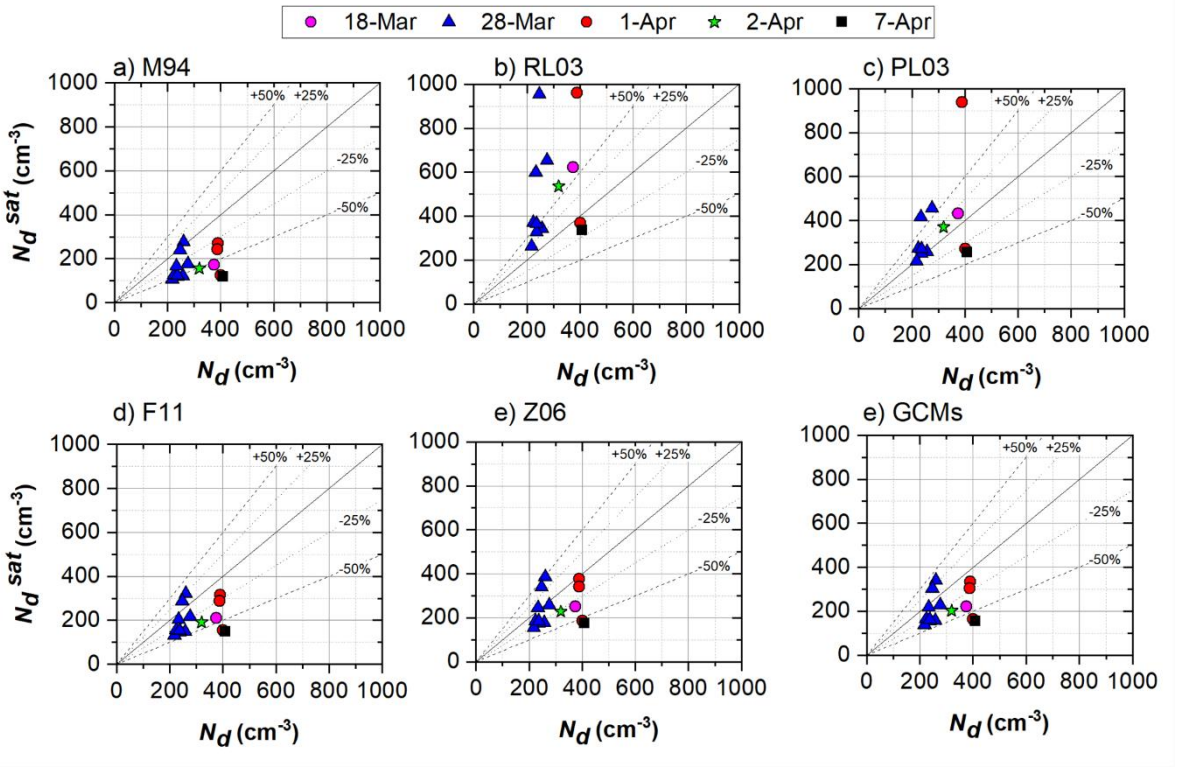

Figure 7.4. Droplet number closure between N_d and N_d^{sat} using the literature β-expressions according to a) M94, b) RL03, c) PL03, d) F11, e) Z06, and f) GCMs compared to N_d, respectively (Foskinis et al., 2022).

Overall, we found that in the case of using a constant value of β, such as Z06, GCMs, and F11, the N_d^{sat} values tend to be underestimated, since the estimated mean bias is of the order of 34%, while the standard deviation is reduced by 16% on average. On the other hand, by using the RL03 expression, the N_d^{sat} is overestimated, although comparable compared to those values that were derived when expressions of constant value of β are used (Z06, GCMs, and F11), while in case of PL03 the average bias was found 13.2% ± 34.8%. In case of using the M94 explicit relation, N_d^{sat} is significantly underestimated, but the standard deviation is reduced by almost a factor of two compared to PL03. Usage of the RL03 relation provides N_d^{sat} values that are considerable overestimated along with their standard deviation (*c.f.* Figure S12, while the MNBs presented in box plots can be found in Figure 7.6b.

7.1.4 Results and Discussion

7.1.4.1 Optimization of β-expression

As a next step, we determined the β values from Eq. 7.6, using each derived values of N_d and the corresponding values $c(c_w)$, τ, r_{eff} as follows:

$$\beta(N_d^{sat}) = \left(N_d^{sat} \left(\frac{\sqrt{5}}{2\pi} \sqrt{\frac{f_{ad}\, c_w}{\rho_w\, Q_{ext}}}\, \tau \right)^{-1} r_{eff}^{\frac{5}{2}} \right)^{\frac{1}{3}} \quad (7.6)$$

We then fit the β and N_d data to a linear relationship, $\beta_{opt} = (a + b\, N_d)^{1/3}$, to determine the "optimal β −expression" (OPT). According to Bevington et al. (1993), we used a weighted linear interpolation method, which considers both $\delta\beta$ (calculated by using the Chain rule on Eq.7.6) and δN_d (δN_d = $0.25 N_d$ from Morales and Nenes, (2010)) of each β and N_d datum, to determine the OPT.

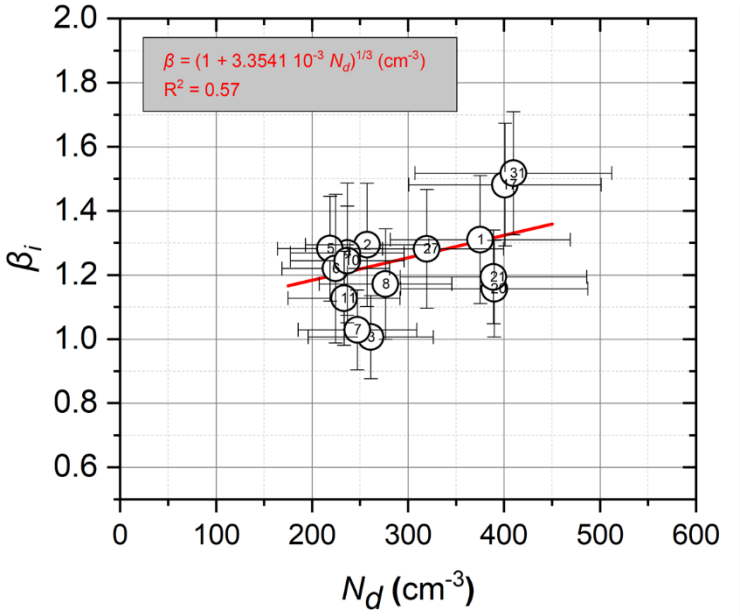

Figure 7.5: The linear interpolations over the β-N_d data for the diabatic derived N_d; the labelling refers to the serial number of each cloud (Foskinis et al., 2022).

The coefficients of OPT, *a* and *b* were estimated to be equal to 1, and 3.3541 10^{-3} ± 1.0623 10^{-3}, respectively (Figure 7.5), while the average $\delta\beta_{opt}$ was estimated to be equal to 0.22 for the whole dataset. Additionally, we calculated the *P*-value of the fit and found them equal to 0.05, respectively, while the fitting confidence R^2 was found equal to ~0.57. Then, we applied the OPT expression to Eq.7.5, to calculate the solutions of N_d^{sat}, while we disregarded the solutions where $\beta_{opt} > 2.5$, and $\beta_{opt} < 1$. Finally, we validated the accepted solutions in respect to the N_d. The results of this closure are presented in Figure 7.6a.

Additionally, we present the MNB boxplots, using the literature based β −expressions (M94, RL03, PL03, Z06, RL09, and F11), versus our proposed expression (OPT) in Figure 7.6b.

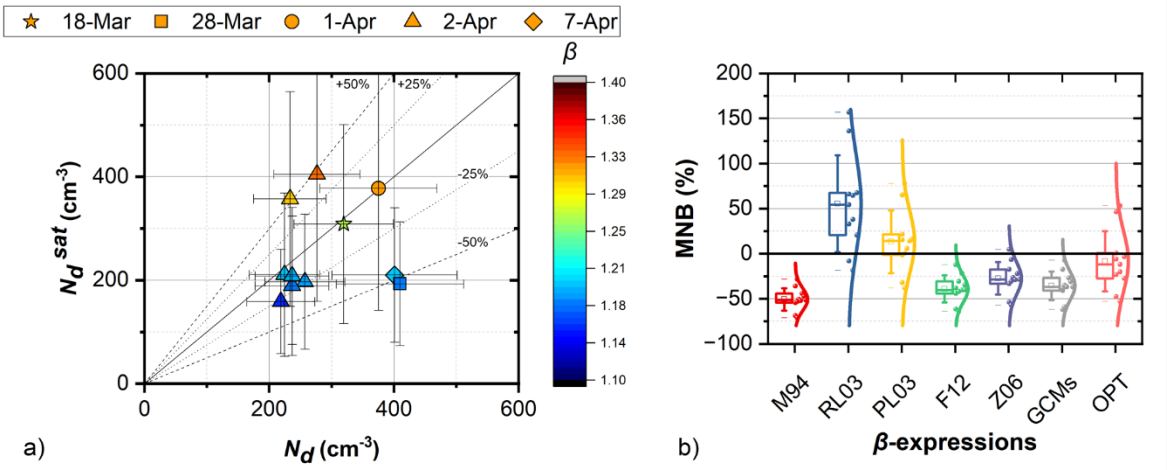

Figure 7.6: a) Droplet number closure between N_d and N_d^{sat} using the OPT compared to N_d in respect of β_{opt} on the colorscale; b) The MNB of the closure of N_d^{sat} – N_d by using each β-expression: i) M94, ii) RL03, iii) PL03, iv) F11, v) Z06, vi) GCMs, and vii) OPT, respectively (Foskinis et al., 2022).

Based on the results presented in Figure 7.6b and Table 7.1, we see that the proposed β −expression OPT exhibits the lowest mean MNB value (-8.4%) with a standard deviation 33.4%, while the performance of the rest *β*-expression can be ranked by their MNB values, as follows: PL03 (13.2), Z06 (-27.3%), GCMs 35.6%), F11 (-39.1%), M94 (-50.7%), and RL03 (55.5%) (see also Table 3) along with the resulting standard deviation values (expressed as the length of the box in the vertical axis) of MNB (*c.f.* Figure 7.6b).

7.1.5 Conclusions

The study presented here expands an established droplet number retrieval algorithm for non-precipitating PBLCs (Grosvenor et al., (2018) to explicitly account for the spectral dispersion of droplets and its dependence on droplet number in terms of β. The revised algorithm uses the cloud microphysical variables τ and r_{eff}, as derived from with a temporal resolution of 15 min and with a spatial resolution 3.6 km × 4.6 km, along with an improved calculation of the total condensation rate (Zhu et al., 2018) with respect to cloud top height which can be obtained by using the ERA5 atmospheric pressure-temperature profiles (Hersbach et al., 2018). We found that the optimal retrieval of N_d^{sat} is most sensitive to biases of the *β* values, rather than biases in τ and r_{eff}, pointing to the need for an optimal *β*-expression for the most accurate N_d^{sat} retrievals.

We retrieved N_d^{sat} values by using the literature-based *β*-expressions and we evaluated them against the *in situ* N_d estimations obtained by a state-of-the-art droplet activation parameterization. We found that when using a constant value of *β* such as, Z06, GCMs, and F11, the droplet number is captured to on average ±16% and a bias of -34%. When using a linear relation between *ε* or *β* to N_d^{sat}, such as PL03, N_d^{sat} overestimates N_d by 13.2% ±34.8%. In the case of using more complex relation of *β* to N_d, such as of M94 or RL03, the bias of N_d^{sat} increases significantly. Additionally, we proposed a new *β*-N_d expression, based on the *in situ* N_d estimations, that minimize the bias of closure between N_d^{sat} and N_d (8.4% ±33.4%).

Although more work needs to be done to evaluate the extent to which our approach can be applied elsewhere in the globe, the results presented here are both encouraging and may suggest

ways to develop high-value products for climate models that can take advantage of the rich ground-based aerosol datasets available to the community

7.2 Paper II: On the Relation Between the Planetary Boundary Layer Height and In Situ Surface Observations of Atmospheric Aerosol Pollutants in an Urban Area

7.2.1 Summary

In this study, we present the role of the PBLH on the air pollutant concentrations measured at an urban background station at the Metropolitan area of Athens, Greece, an area characterized by complex topography. For this purpose, we utilized *in situ* measurements of aerosol number concentrations at different size bins (10-200 nm) $N_{10\text{-}200nm}$, (200-550 nm) $N_{200\text{-}550nm}$, *eBC*, and wind speed data, for the period of May – July 2020.

According to our analysis, both horizontal transport and vertical mixing and dispersion of air pollutants play a critical role in air quality. More precisely, PBLH is negatively correlated with aerosol concentration. The increase in the height of the PBL favors a reduction in aerosol concentration, which, to some extent, compensates for the increase in aerosol load due to emission sources and horizontal transport from the city center. The horizontal advection process is related to the PBLH, since a deep PBL drives the advection, while a shallow PBL is characterized by weak horizontal wind velocities. On the other hand, under stagnant air mass conditions, when the PBL shrinks, the concentrations of air pollutants increase. On average, a 25% increase in the PBLH results in a 15% reduction in aerosol concentration, whereas a 15% reduction in the PBLH may result in a 10% increase in aerosol concentrations. Overall, $N_{10\text{-}200nm}$ particle concentrations increase, when air masses arrive from the S-NW sector (city center) due to traffic and vehicle emissions, while transport of continental pollution mixed with local and regional emissions along the Balkans-Aegean Sea axis, is originating from the NE axis under high wind speeds. The latter is more clearly recognized from aged aerosol components such as sulphate. Whereas, the $N_{200\text{-}550nm}$ and *eBC* showed increased concentration load under stagnant air mass conditions, independently of the wind direction.

7.2.2 Objectives

The objective of this study is to present the role of the PBLH and its variability on the air pollutant concentrations. This variability is driven by the energy fluxes within the layer and changes the aerial volume where aerosols and other pollutants are dispersed therein, affecting the aerosol number concentration measured within the layer (Su et al., 2018; Jiang et al., 2022). On the other hand, Su et al. (2018) showed a strong negative correlation between the PBLH and the air pollutant concentrations. Under stagnant meteorological conditions, when the PBL becomes shallow, an increase in the concentration of the pre-existed aerosol is usually observed, an effect which is further amplified in valleys and basin areas surrounded by mountains (Papanikolaou et al., 2022). This seems to be a bidirectional relation, since according to Kokkalis et al. (2020) and Gini et al. (2022), aerosol intrusions inside the PBL, as well as the presence of transboundary transport aerosol layers above the PBL, may affect the top-height of the PBL and its evolution time during the day.

Our study aimed to investigate the effect of local air mass circulation and transport patterns on the aerosol load and its major chemical components, along with the PBLH diurnal cycle. To achieve this, we combined *in situ* measurements of key aerosol parameters with laser remote sensing (lidar) techniques, to measure the horizontal component of the wind, retrieve the PBLH and decouple the effect of its variability on the air pollutant levels.

7.2.3 METHODOLOGY AND INSTRUMENTATION

To implement the objectives of our study we used a synergy of active remote sensing and *in situ* measuring techniques. Where the horizontal components of the wind; speed (V_h) and direction (V_{dir}) were measured by using a HALO wind lidar in the VAD mode (Henderson et al., 2005), while by using a SMPS, a ToF-ACSM and an AE31 we measured the aerosol size distribution, the non-refractory aerosol mass and chemical composition of the organic and inorganics components and the *eBC*, respectively.

Given, that particles within the size range of 10-200 nm are associated to fresh traffic and vehicle emissions (Vratolis et al., 2019), while the aerosol particles within the range of 200–550 nm, correspond mainly to aged particles partly circulated in the broad Attica region over several hours/days and partly transported from distant areas (e.g. Mediterranean, the Balkans, western Europe), we split the measured size distribution data into two fractions with diameters ranging between 10–200 nm ($N_{10\text{-}200nm}$) and 200–550 nm ($N_{200\text{-}550nm}$) to examine each one separately. Additionally, using the ToF-ACSM instrument we measured the mass concentrations of sulfate (SO_4^{2-}), and nitrate (NO_3^-) particles, and the AE31 to derive the *eBC* as well.

Then, we combined the V_h and V_{dir} values with the *in situ* aerosol data obtained from SMPS, ToF-ACSM, and AE31 into a common dataset, averaged on an hourly basis. Moreover, we divided the dataset into two groups: the first concerns the data obtained during the "day-hours" (between 07:00-23:00 LTC), while the second is related to the data sampled during the "night-hours" (23:00-07:00 LTC). Finally, we performed a cluster analysis using the PAM method (see Section Airmass Cluster Analysis) to determine the clusters of the *in situ* variables ($N_{10\text{-}200nm}$, $N_{200\text{-}550nm}$, SO_4^{2-}, NO_3^-, and *eBC*) with respect to the wind conditions for each data group (day-hours and night-hours). Then, we correlated these clusters with the prevailing wind flows in the AMA.

Additionally, we examine the role of PBLH's variation on the concentrations of $N_{10\text{-}200nm}$, $N_{200\text{-}550nm}$ and *eBC*. In general, most of the surface-emitted aerosols and air pollutants are trapped within the PBL, especially in the case of temperature inversions at the top of the PBL, which inhibit the aerosols from penetrating the lower free troposphere. As mentioned previously, the PBLH is driven by the energy balance of the surface. Here, we consider any entrainment of aerosols at the interface of the PBL top to be relatively small.

Relevant studies (Su et al., 2018) have also shown a strong negative correlation between the PBLH and the air pollutants concentration at the surface, indicating that in the case of a shallow PBL, the total atmospheric volume within it, decreases and consequently, the particle concentration increases and vice versa. In this study, the PBLH was estimated by using a threshold technique on the standard deviation of the vertical wind velocities (σ_w) within the PBL (Barlow et al., 2011; Schween et al., 2014) using the stare mode of HALO. Then, we decouple the effect of PBLH using a dynamic box algorithm approach based on Hanna et al. (1982) and Jiang et al. (2022) which manages the terms of sources within the box, and the horizontal transports through the box, considering a vertical dynamic non-transparent top boundary.

In this study, we used a dataset derived from air pollution measurements inside the AMA performed from 15 March to 2 July of 2020, including the COVID-19 lockdown period in Greece. In brief, during this period, starting on 11 March 2020, a series of mitigation measures against the spread of the COVID-19 pandemic were gradually implemented in Greece. For instance, the operation of all educational institutions was suspended nationwide, two days later all commercial and social recreation activities were also suspended, except those related to basic needs (*e.g.* food supply, etc.); finally, from 22 March to 4 May, the lockdown measures were applied, including the restriction of all non-essential transportation throughout the country. It is well documented that the measures taken during the COVID-19 pandemic had a remarkable imprint on anthropogenic emissions by dramatically reducing traffic emissions (Kokkalis et al., 2020), and by increasing residential emissions since there was a restriction on all non-essential travel throughout the country, and the citizens had to stay indoors and make use of the residential heating on a continuous basis.

7.2.3.1 Airmass Cluster Analysis

Carslaw et al. (2006) showed that by using air mass cluster analysis we can categorize the *in situ* aerosol loads records, according to the local transport patterns namely the wind velocity and direction. One of the commonly used clustering techniques in atmospheric applications is the Partition Around Medoids (PAM) clustering. The PAM technique is quite similar to the *k*-means algorithm (Beddows et al., 2009; Carslaw and Beevers, 2013), and depends on the chosen number of clusters *"k",* while the classifications of each datum into a cluster come up by minimizing the intra-partition Euclidian's distances, regarding each *k-mean.*

The partitioning method, initially, divides the aerosol data into *k* distinct clusters, and all data points are assigned to the nearest cluster centers. Then, the cluster centers are re-calculated as the centroids of the newly formed clusters and the data points are re-assigned to the nearest cluster centers that just re-calculated. This process is repeated until the clusters reach the minimum intra-partition distances. The goodness of the clustering can be determined by using the Silhouette coefficient (Rousseeuw, 1987), which shows which objects lie well within their cluster, and which ones are merely somewhere in between clusters. In our study, we used the PAM clustering partitioning to classify in clusters the $N_{10\text{-}200nm}$, and $N_{200\text{-}550nm}$ considering both day- and night-time samples, using the optimal *k* of each. The way to determine the optimal number of clusters is by gradually increasing the number of clusters *"k*" stepwise from 2 to 10, and recording the Silhouette coefficient (Rousseeuw, 1987). When the Silhouette coefficient reaches a desirable high plateau, then this *k* is considered as optimal. In our case, the results of the optimal *k* values of $N_{10\text{-}200nm}$, and $N_{200\text{-}550nm}$ were found 5 and 4, and 5 and 6 for the day-hours and night-hours samples, respectively. Therefore, we classified the aerosol data in clusters using the optimal *k* values of each sample.

7.2.3.2 Dynamic Box model approximation

Using a Dynamic Box model approximation, we examined the role of the PLBH variability on the observed aerosol concentrations., We initially chose as a metric the $N_{200\text{-}550nm}$ concentrations considering that this fraction is not generally affected by primary fresh emissions. In addition, we examined together the $N_{10\text{-}200nm}$ and the *eBC* concentrations since they both are highly influenced by the anthropogenic aerosol emissions.

According to Hanna et al. (1982), we can approach the physical system by considering the particle mass balance equation applied inside the PBL, described in terms of a square "box" control volume, the top/bottom surfaces of which correspond to the ground/PBLH, respectively. The horizontal transport of air inside the PBL is characterized through the vertical box boundaries, while the *in situ* measurements of pollutant concentration are used to characterize the aerosol concentrations and other process rates. The original mass balance equation can be given as:

$$\frac{\partial C_i}{\partial t} = \frac{Q_s}{H_{PBL}} - \frac{u\ (C_i - C_b)}{L} - \frac{1}{H_{PBL}} \frac{\partial H_{PBL}}{\partial t} (C_i - C_a) \quad (7.7)$$

where C_i is the pollutants concentration in particles cm^{-3}, Q_s is a term related to the sources, sinks, production, chemical dissolution and decomposition of the pollutant i, u is the mean air mass horizontal velocity in the box, H_{PBL} is the PBLH, the C_a and C_b are the concentrations above the box's top and the upwind background concentration of the pollutant i, respectively. L is the length of the box and C_i is the concentration of the pollutant i above the PBLH.

In our study, we considered an ideal box with a horizontal cross section of 1×1 km and a free moving non-transparent cap at the vertical axis. The non-transparent cap means, that the term C_a can be considered equal to zero simplifying the equation. Following that, the equation still contains C_b and Q_s, which cannot be distinguished by solving Eq.7.7 at the same time. To overcome this limitation, we considered the term which is related to the sources or sinks, production, etc. very small and close to zero within the box ($Q_s = 0$) given the background location of the site. This assumption can be balanced by increasing the contribution of the horizontal transported aerosol loads, i.e. the value of C_b. Since this study aims only to decouple the effect of the variability of PBLH and not to decouple the source and transport fraction, we can only investigate the third term, and consider as one term the combined effect of transport, local sources and sinks. Hence, Eq.7.7 can be written in a differential form, as follows:

$$\frac{\boldsymbol{\Delta C_i}}{\boldsymbol{\Delta t}}(\boldsymbol{t}) = \frac{\boldsymbol{C_i(t+\Delta t) - C_i(t-\Delta t)}}{\boldsymbol{2\Delta t}} \quad (\boldsymbol{7.8a})$$

$$\frac{\boldsymbol{\Delta H_{PBL}}}{\boldsymbol{\Delta t}}(\boldsymbol{t}) = \frac{\boldsymbol{H_{PBL}(t+\Delta t) - H_{PBL}(t-\Delta t)}}{\boldsymbol{2\Delta t}} \quad (\boldsymbol{7.8b})$$

$$\boldsymbol{DC_i}^{\boldsymbol{t+s}}(\boldsymbol{t}) = -\frac{\boldsymbol{u\,(t)\big(C_i(t) - C_b(t)\big)}}{\boldsymbol{L}} \quad (\boldsymbol{7.8c})$$

$$\boldsymbol{DC_i}^{\boldsymbol{h}}(\boldsymbol{t}) = -\frac{\boldsymbol{C_i(t)}}{\boldsymbol{H_{PBL}(t)}} \frac{\boldsymbol{\Delta H_{PBL}}}{\boldsymbol{\Delta t}}(\boldsymbol{t}) \quad (\boldsymbol{7.8d})$$

$$\boldsymbol{DC_i(t)} = \boldsymbol{DC_i}^{\boldsymbol{t+s}}(\boldsymbol{t}) + \boldsymbol{DC_i}^{\boldsymbol{h}}(\boldsymbol{t}) \quad (\boldsymbol{7.8e})$$

where Δt is the time resolution between each measurement of the timeseries, which is equal to 15 min, while the terms DC_i^{t+s}, DC_i^{h} are the decoupled variances of the aerosol concentrations within the control volume due to the horizontal transport, sources and sinks and the one related to the PBLH variation, respectively; the latter will be called from now on "PBLH enhancement", of the pollutant i, where i corresponds to the $N_{10\text{-}200nm}$, $N_{200\text{-}550nm}$ and *eBC* concentrations, respectively. Finally, the term DC_i is the variance in time of the *in situ* measured aerosol concentration on each moment t.

7.2.4 Results & Discussion

7.2.4.1 Local transport pattern analysis

The orientation of the four surrounding mountains in the AMA are: Egaleo, Parnitha to the northwest, Penteli to the north and Hymettus to the east (*c.f.* Figure 6.1). This topography favours the formation of synoptic winds or the sea breeze cells following towards two directions, from the N-NE or SW (Kallos et al., 1993), respectively. When a strong pressure gradient occurs over the Aegean Sea, then the N winds are linked with the AMA ventilation (Kallos et al., 1993). According to Diapouli et al. (2014) and Vratolis et al. (2019), the winds from the N sector are also related to the transport of continental pollution mixed with local and marine emissions along the Balkans-Aegean Sea axis. These air masses usually reach the AMA region from the eastern side of Hymettus, while passing over the South Euboean Gulf and Mesogea plain, transporting a significant load of particles in the range of 10-200 nm (*c.f.* Figure 7.7a) and increasing the SO_4^{2-} component (*c.f.* Figure 7.7e).

On the other hand, when a low-pressure gradient over the Central Mediterranean or Ionian Sea occurs, then S & SW winds are developed over AMA, usually related to Saharan dust transport events over the Athens basin (Soupiona et al., 2019), while air pollutants ($N_{10\text{-}200nm}$ & *eBC*) produced in the densely populated part of the Athens basin are also transported towards DEM station (Kalogridis et al., 2018; Gini et al., 2022). As AMA is surrounded by mountains except from its southwestern side, which is an extended opening towards the Saronikos Gulf, the sea breeze cells can be developed under relatively weak synoptic flow conditions over Greece, affecting the ventilation of AMA. In general, the sea-breeze tends to stratify the atmosphere above the city, trapping air pollutants at a relatively small height above ground (Kallos et al., 1993), while under stagnant atmospheric conditions, locally emitted anthropogenic aerosols dominate inside the PBL (Kalogridis et al., 2018).

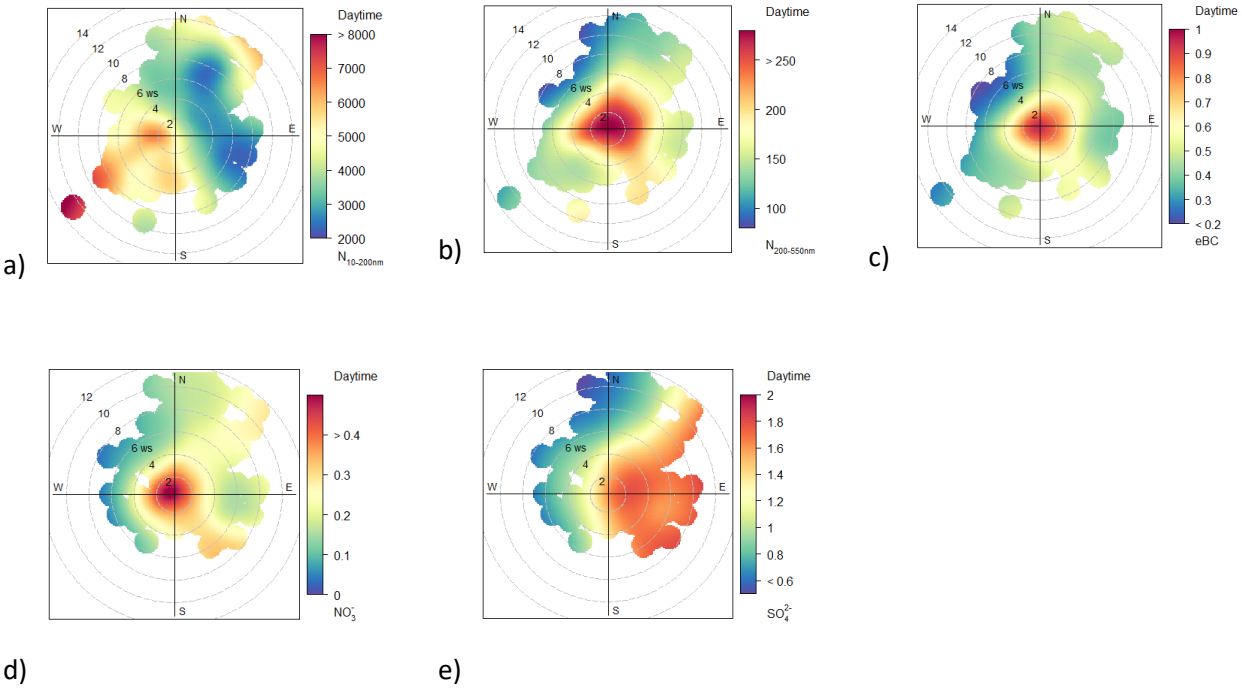

Figure 7.7. Wind polar plots of (a) $N_{10-200nm}$ [cm^{-3}], (b) $N_{200-550nm}$ [cm^{-3}], (c) eBC [$\mu g\ m^{-3}$], (d) NO_3^- [$\mu g\ m^{-3}$]and (e) SO_4^{2-} [$\mu g\ m^{-3}$] during the daytime, respectively. The radial distance from the middle of the plot corresponds to the wind speed, while the color-scale corresponds to the concentration of each pollutant.

In Figure 7.7a, a significant increase of concentrations in the $N_{10-200nm}$ mode particles is observed over the AMA with wind flows within the S – NW sectors, due to the locally formed sea breeze cell. This is because the S – NW sector refers to the city center, and as a result, the emitted aerosols are advected over the DEM site, causing recirculation of the pollutants along the NE–SW axis (Kallos et al., 1993; Kalabokas et al., 1999; Diapouli et al., 2017a). Another sea breeze cell is formed over the Mesogea plain at the eastern side of Hymettus and blows mainly from *NE* to *SE* (during daytime) and from W to NNW (during the nighttime) (Kallos et al., 1993). The Mesogea Plain is generally less populated, and with lower vehicular traffic, compared to the AMA. Therefore, when low winds occur, relative "clean" air masses are transported over the DEM site, characterized by low particle number concentrations in both size ranges (10-200 nm and 200-550 nm) (Kostenidou et al., 2015; Vratolis et al., 2019).

On the other hand, we used the SO_4^{2-} concentrations, as a tracer for regional anthropogenic aerosol and continental pollution, since there are no significant sources of SO_4^{2-} within AMA (Zografou et al., 2022). In Figure 7.7e we observe higher SO_4^{2-} concentrations when the wind flows within the NE-SE sector (Diapouli et al., 2014; Vratolis et al., 2019). This pattern remains the same during the nighttime conditions (*c.f.* Figure 7.7e).

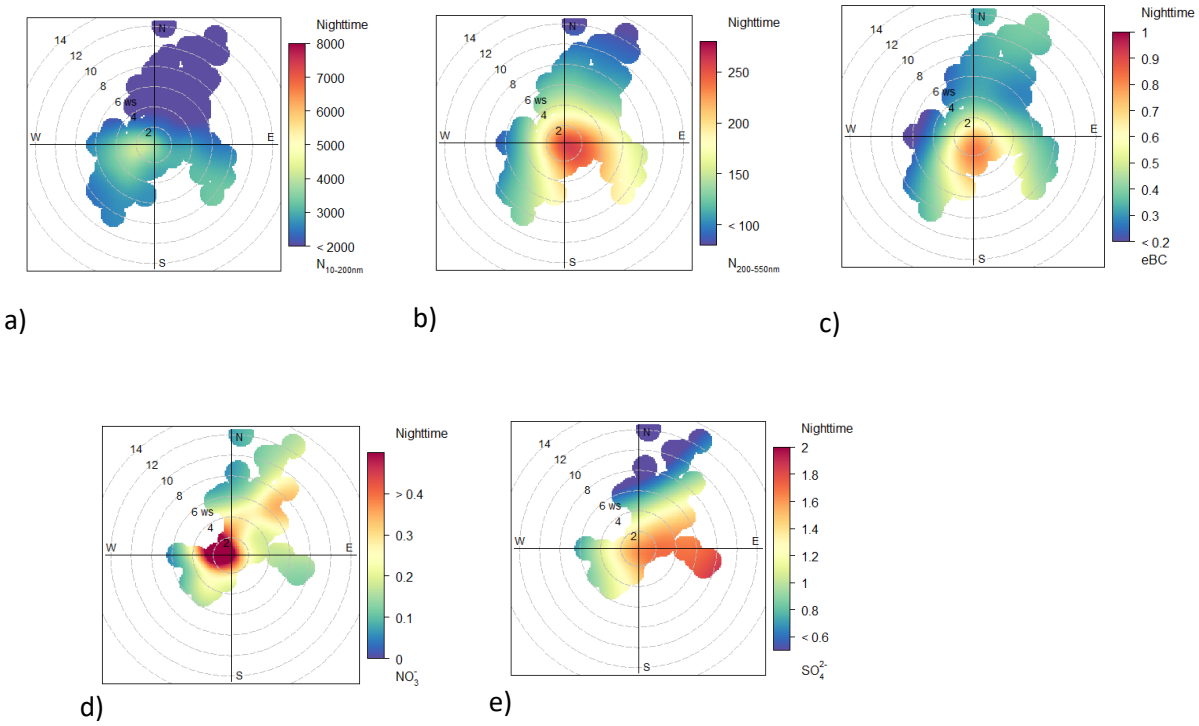

Figure 7.8. Wind polar plots of (a) $N_{10\text{-}200nm}$ [cm^{-3}], (b) $N_{200\text{-}550nm}$ [cm^{-3}], (c) eBC [$\mu g\ m^{-3}$], (d) NO_3^- [$\mu g\ m^{-3}$] and (e) SO_4^{2-} [$\mu g\ m^{-3}$] during the night-hours, respectively. The radial distance from the middle of the plot corresponds to the wind speed, while the color-scale corresponds to the concentration of each pollutant.

According to Amanatidis et al. (1992), the katabatic flows inside a basin like AMA surrounded by mountains are very important, since they enhance the air pollution episodes. When the katabatic flows occur, the pre-existed and emitted aerosols within the PBL, are trapped in poor pollutant dilution and dispersion along low winds and temperature inversion, and as a result, the pollution episodes become more intense. Additionally, Flocas et al. (1998) found the same direction for the katabatic winds, a finding indicating that the increase in the particle number concentration we observe, originates from particle layers aloft transported by the katabatic flow regime. This can be seen in Figure 7.8b, and c, in which an increment of the $N_{200\text{-}550nm}$ and the *eBC* concentrations is observed when the winds blow within the sectoral range 130˚- 190˚. As a result, the air masses from the mount Hymettus are brought over the station lowering the nocturnal PBLH, and occasionally increasing the particle number concentration (Flocas et al., 1998). When stagnant conditions occur during nighttime, then the observed $N_{200\text{-}550nm}$, *eBC*, and NO_3^- concentrations correspond to local emissions without a strong contribution to the aerosol load (*c.f.* Figure 7.8c, d, and e).

7.2.4.2 Clustering of local transport patterns

Moreover, for the day- and night- time data series of $N_{10\text{-}200nm}$, and $N_{200\text{-}550nm}$, we performed a cluster analysis to group the data with respect to the aerosol load, the wind direction and speed. During this process, we can identify an optimum number of clusters (sectors), so that the aerosol observations within each sector correspond to similar (wind speed and direction) conditions.

As mentioned before in this study we used the PAM clustering, while the number of the sectors was estimated by using the optimization technique of selection of the optimal number of clusters.

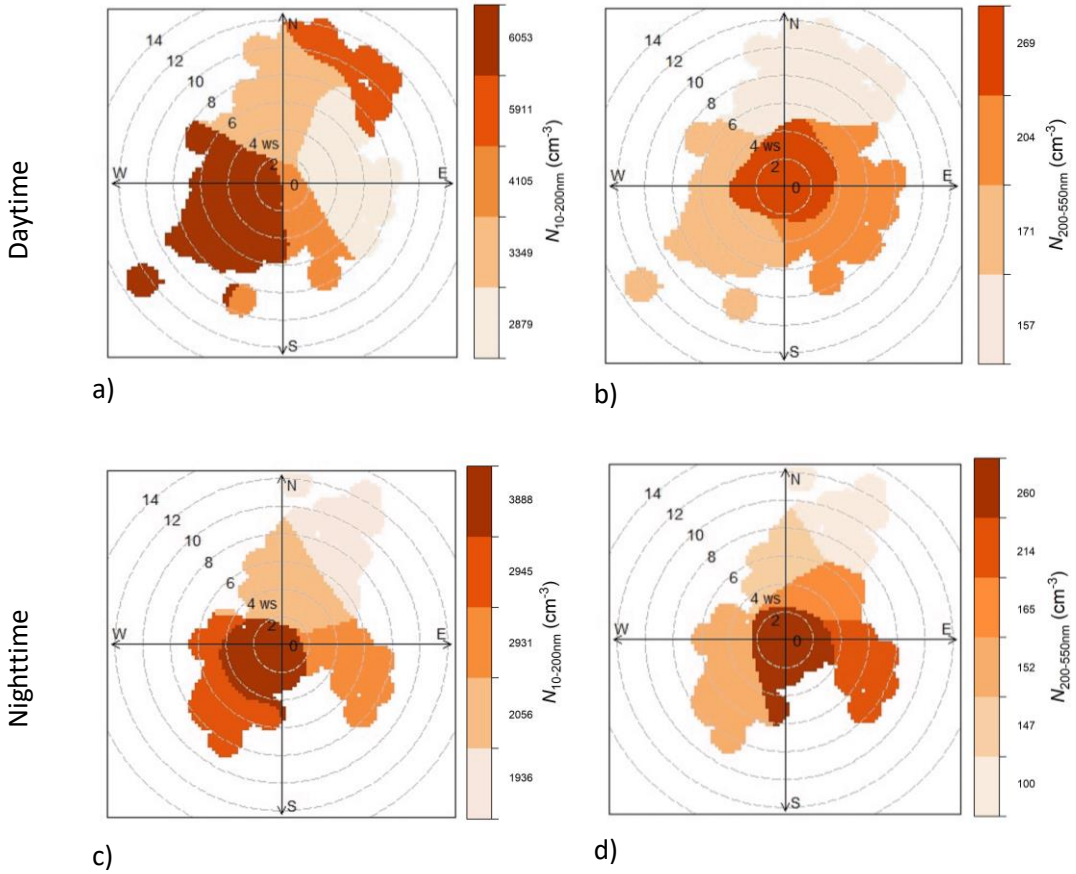

Figure 7.9. Clustering results of $N_{10\text{-}200nm}$ and $N_{200\text{-}550nm}$ based on aerosol load in respect to the prevailing meteorological conditions for the day- and night- hour samples, respectively. Here the color-tone of each cluster indicates higher mean concentrations when the color becomes darker.

Regarding the daytime periods, the $N_{10\text{-}200nm}$ and $N_{200\text{-}550nm}$ concentrations can be clustered into five and four sectors (*c.f.* Figure 7.9a, b); for ultrafine and accumulation mode particles, respectively (see Table 7.2-5).

Sectors	Averaged Concentration (cm^{-3})	Averaged horizontal velocity (V_h) ($m\ s^{-1}$)
NE-SE	2879 ± 1832	4.2 ± 1.3
NW-NE	3349 ± 2095	5.1 ± 1.6
SE-S	4105 ± 1705	2.4 ± 2.1
N-NE	5911 ± 3252	9.8 ± 2.3
S-NW	6053 ± 3784	3 ± 1.7

Table 7.2. Summary table of the averaged concentrations and the horizontal velocities that were measured at each cluster, regarding the daytime periods both for $N_{10-200nm}$.

Sectors	Averaged Concentration (cm^{-3})	Averaged horizontal velocity (V_h) ($m\ s^{-1}$)
NE-SE	1936 ± 1508	7.8 ± 2.2
N-NE	2056 ± 1041	3.9 ± 1.3
NW-NE	2931 ± 1770	4.1 ± 1.7
S-NW	2945 ± 1054	5.2 ± 0.9
local	3888 ± 1970	1.6 ± 1.2

Table 7.3. Summary table of the averaged concentrations and the horizontal velocities that measured at each cluster, regarding the nighttime periods both for $N_{10-200nm}$.

Thus, the main clusters were observed within the following sectors: the NE-SE sector, which corresponds to a residential or parkland area at the lee side of Hymettus with dense aerosol sources, except for the fast traffic Athens Ring-road (Figure 7.9a, b). More specifically Figure 7.9a presents the lowest aerosol concentration values in average (2879 ± 1832 cm^{-3} and 204 ± 127 cm^{-3} for ultrafine and accumulation mode particles, respectively); the NW-NE sector which is characterized by a densely populated urban/suburban area with typical local traffic emissions, has slightly high values on average (3349 ± 2095 cm^{-3} and 157 ± 78 cm^{-3} in ultrafine and accumulation mode particles, respectively); the S-NW sector in which, the freshly emitted aerosol particles from traffic are transported from the major AMA urban and city-center sectors towards our experimental site, driven by the synoptic S winds or the sea breeze from the Saronikos Gulf. In this case, we found the highest aerosol loads (6053 ± 3784 cm^{-3} and 171 ± 123 cm^{-3} in ultrafine and accumulation mode particles, respectively); Finally, a narrow sector starting from the lee side of Hymettus to the SE-S direction, displayed occasional events of a slightly high load of ultrafine mode particles, equal to 4105 ± 1705 cm^{-3}. Moreover, in the case of the ultrafine mode particles, we found even more increased values on average equal to 5911 ± 3252 cm^{-3} within the N-NE sector, where windy conditions frequently occur. Usually, this is a preferred pattern for long-range transported continental pollution intrusions along the Balkans-Aegean Sea axis (Diapouli et al., 2014; Vratolis et al., 2019). Finally, one extra sector has been found in the case of accumulation mode particles which corresponds to the local emissions during stagnant conditions (valid when the wind speed is below 4 $m\ s^{-1}$). In total, the local aerosol emissions were estimated to appear equal to 269 ± 153 cm^{-3}.

Sectors	Averaged Concentration (cm^{-3})	Averaged horizontal velocity (V_h) ($m\ s^{-1}$)
NW-NE	157 ± 78	6.6 ± 1.5
S-NW	171 ± 123	4.2 ± 2.2
NE-S	204 ± 127	3.8 ± 2.5
local	269 ± 153	1.1 ± 1.9

Table 7.4. Summary table of the averaged concentrations and the horizontal velocities that measured at each cluster, regarding the daytime periods both for $N_{200\text{-}550nm}$.

Sectors	Averaged Concentration (cm^{-3})	Averaged horizontal velocity (V_h) ($m\ s^{-1}$)
N-NE	100 ± 49	8.6 ± 1.7
NW-N	147 ± 92	5.9 ± 1.1
S-SW	152 ± 94	4.2 ± 1.4
N-NE	165 ± 99	4.1 ± 1.0
NE-SE	214 ± 152	5.6 ± 1.2
local	260 ± 160	0.4 ± 1.1

Table 7.5. Summary table of the averaged concentrations and the horizontal velocities that measured at each cluster, regarding the nighttime periods both for $N_{200\text{-}550nm}$.

Concerning the nighttime periods the $N_{10\text{-}200nm}$ and $N_{200\text{-}550nm}$ concentrations, they can be clustered into five and six sectors (*c.f.* Figure 7.9c, d); for ultrafine and accumulation mode particles, respectively (see Table 7.2-5), similarly to the daytime analysis the major aerosol concentrations were observed within the following sectors: the sector which is associated to local emissions during stagnant conditions (for wind speeds < 4 m s^{-1}) in for both ultrafine (3888 ± 1970 cm^{-3}) and accumulation (260 ± 160 cm^{-3}) mode particles; the S-NW sector, which is affected by aerosol emissions from the city-center (2945 ± 1054 cm^{-3} and 152 ± 94 cm^{-3}); the NE and SE sectors are now associated with the katabatic flows from Hymettus, where we found an increase in the average aerosol load (2931 ± 1770 cm^{-3} and 214 ± 152 cm^{-3} for wind speeds over 4 m s^{-1}) most probably originating from decoupled aerosol layers aloft (Papayannis and Balis, 1998); the NW, N and NE sectors (for the fine mode particles) are unified showing concentrations of 2056 ± 1041cm^{-3}, while in the case of accumulation mode particles this sector is divided into NW-N and N-NE sectors, respectively (147 ± 92 cm^{-3} and 165 ± 99 cm^{-3}); and finally, the N-NE sector when wind speeds > 6 m s^{-1} (1936 ± 1508 cm^{-3} and 100 ± 49 cm^{-3}).

The overall assessment of the 3D air flow around DEM station reveals a strong influence of mainly stagnant conditions being responsible for the high concentrations observed for aerosol metrics like particle number and *eBC*. This indicates that sources within the Athens valley are the main influence for the site. It is observed that metrics related to fresh emissions ($N_{10\text{-}200nm}$, *eBC*) display a tendency to arrive from the W/SW sector (city center and main urban area) at higher wind

speeds, while SO_4 which is characteristic of regional distant sources tend to arrive from the eastern sector outside the Athens valley rather than the west sector.

7.2.4.3 PBLH decoupling on aerosol monitoring - Case Study Analysis (9 May 2020)

In this section, we will analyze the diurnal evolution of the PBLH during the case study of 9 May 2020. At first, we present in Figure 7.10a, b, c, the spatio-temporal evolution of the RCS, *w* and σ_w, respectively, from the ground up to 3 km height, where the red dots denote the PBLH. As noted in Section 4.1.1.1, by applying the σ_w threshold technique, the PBLH can be estimated, where σ_w takes values > 0.2 m s^{-1}.

In Figure 5a we observe that the PBLH is increasing during daytime, reaching its maximum height of ~2000 m a.g.l. at 15:00 ~LTC. During its diurnal evolution (09:00-20:00 LTC) the PBL contains well-mixed aerosols, as a result of strong air mass updrafts (the positive part of the vertical velocities). More specifically, after 09:00 LTC the ground surface temperature starts increasing due to solar heating, producing a positive (upward) radiative flux. Thus, the air parcels located close to the ground absorb part of that energy and get warmer and, finally, a convective process starts following the buoyancy rules. Therefore, heat is transferred vertically, from lower to higher altitudes inside the PBL. This vertical motion forces the nearby air parcels to fill the gap near the ground, thus, increasing the turbulence. Following the daily cycle, the development of the PBLH continues as long as the net radiative flux is positive. When the sun is on zenith (~15:00 LTC), the solar net flux together with the PBLH reaches their maximum values, as the PBLH does. Later, during the afternoon and the sunset, the PBLH decreases gradually since the heat transfer from the ground reduces, and the turbulence becomes weaker.

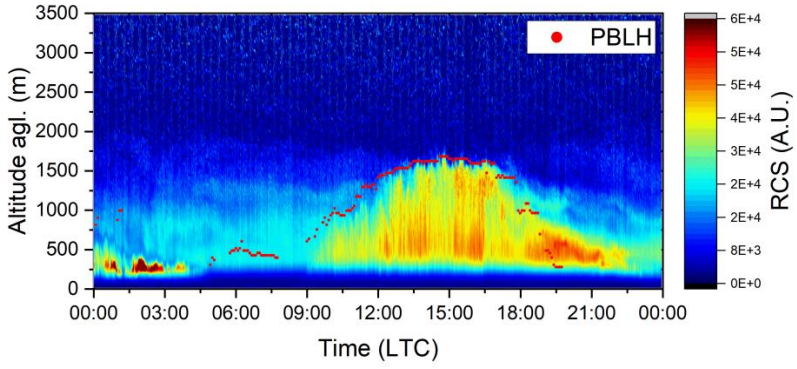

a)

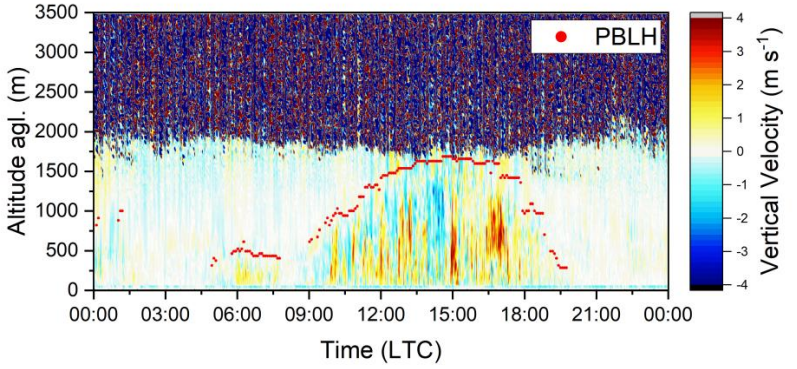

b)

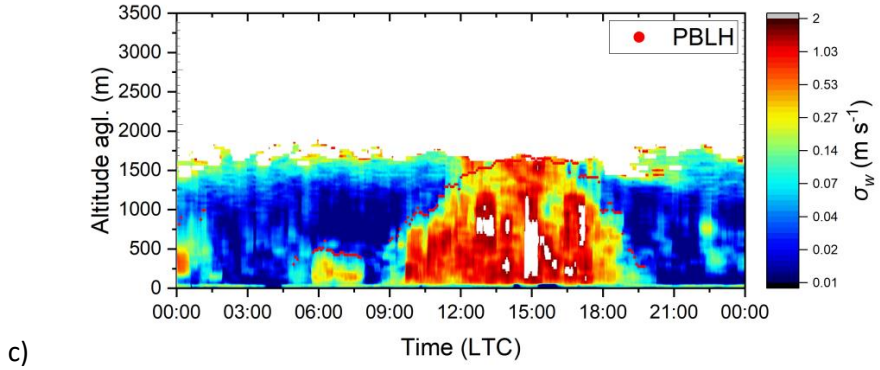

Figure 7.10. Spatio-temporal evolution of (a) RCS in arbitrary units, (b) vertical velocities in m s^{-1}, and (c) σ_w in m s^{-1} of 9-May 2020, respectively. The red dots indicate the temporal evolution of the PBLH (Foskinis et al., Under Review)

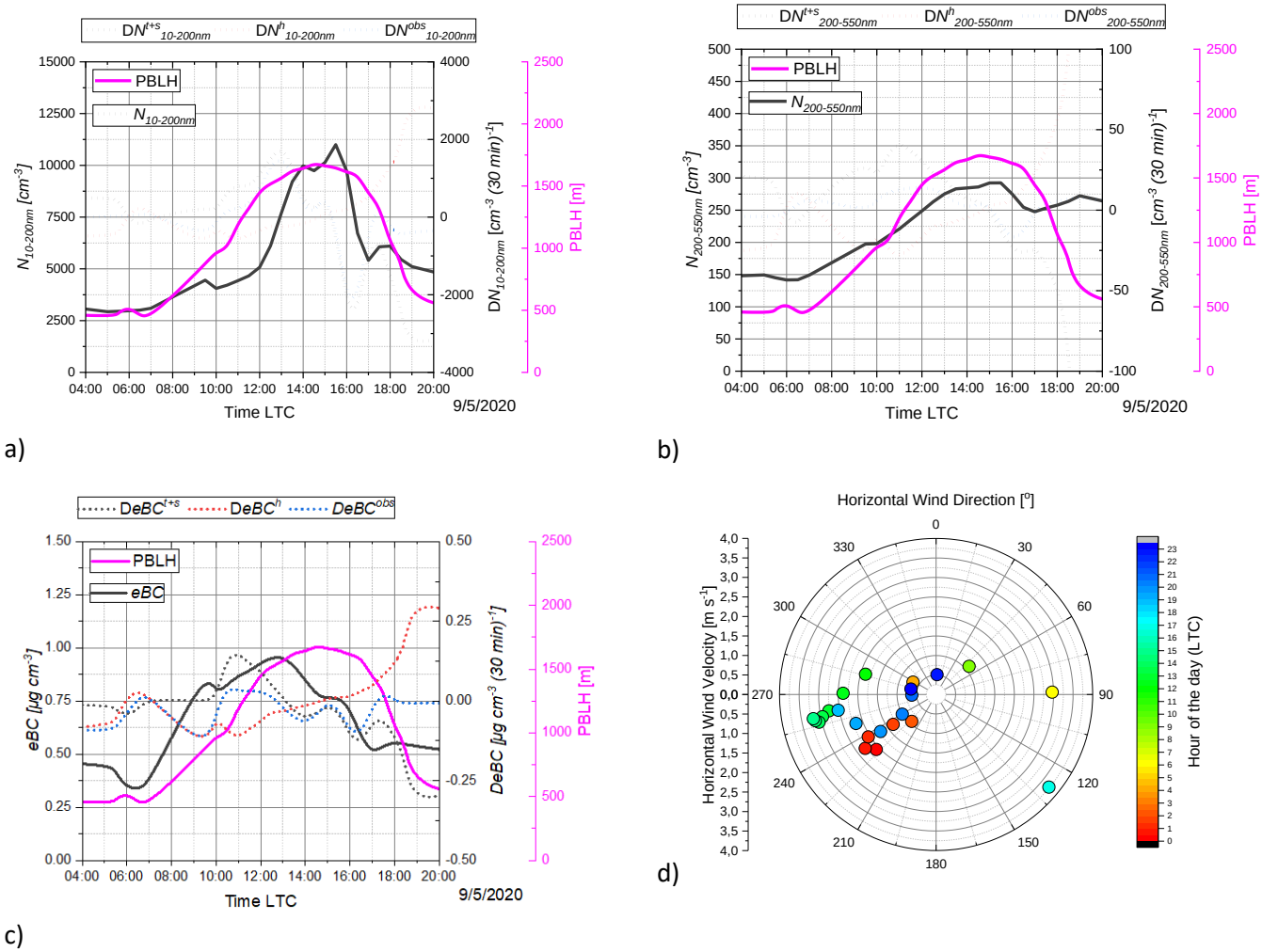

Figure 7.11. Diurnal evolution of a) $N_{10\text{-}200nm}$, b) $N_{200\text{-}500nm}$, and c) eBC concentrations (9 May 2020), along with the decoupled evolutions of horizontal transport or source/sinks fraction and the PBLH enhancement fraction. The black line corresponds to the concentration of the pollutant (left axis), the dot lines correspond on the right axis to the decoupled concentration rate of change of each pollutant, where the horizontal transport or source/sinks fraction is in black, the PBLH enhancement is in red, the measured change in blue. The magenta line corresponds to the second axis on the right and presents the PBLH. d) The temporal evolution of the wind velocity and direction with respect to local time, for the case of 9 May 2020.

Furthermore, by solving Eq. 6.2.2 for each aerosol cluster, we calculated the decoupled DC_i^{t+s} and DC_i^{h} values along the DC_i^{obs} for the $N_{10\text{-}200nm}$, $N_{200\text{-}500nm}$, and *eBC* values, respectively. The diurnal evolution of DC_i^{t+s}, DC_i^{h}, DC_i^{obs}, $N_{10\text{-}200nm}$, $N_{200\text{-}500nm}$, and *eBC* is presented in Figure 7.11a, b and c, respectively, along with the PBLH values. Finally, the wind rose plot presented in Figure 7.11d, shows which flow direction contributes more to the aerosol advection inside the PBL.

We note, here, that the positive fraction of DC_i^{t+s} indicates the advection of air masses (and pollutants), while the negative values indicate dilution and removal processes. The horizontal advection process is also related to the PBLH, since a deep PBL drives the advection, while a shallow PBL is characterized by weak horizontal wind velocities, along with frictional drag effects close to the surface. Indeed, this can be seen in Figure 7.11b and d, between 10:00-15:00 LTC, as the PBL is developing and horizontal wind velocities are increasing, advecting freshly emitted particles from the city's center towards our measurement site. As a result, the DC_i^{t+s} values become positive, for all particles (ultrafine, accumulation mode particles and *eBC)*. Meanwhile, the inflation of the PBL has a negative impact on the DC_i^{h} values, due to the increase in the total atmospheric volume below the PBL. However, despite this decrease, the DC_i^{t+s} dominates over the DC_i^{h} and results to an overall increase in concentrations, for both ultrafine, accumulation mode particles, as well as the *eBC*.

Once the PBL stops growing (15:00-17:00 LTC), the wind flow changes from W to SE direction, ventilating the site and transferring purer air masses toward our site. This causes a reduction in the aerosol load (both in ultrafine, accumulation mode particles and the *eBC* concentrations). Finally, from 17:00 to 20:00 LTC, the PBL rapidly shrinks down, leading to a positive DC_i^{h} enhancement. Overall, the observed aerosol concentrations increase and stabilize to a certain level, indicating an enhancement from the suppression of PBLH, without any significant transport from sources. The PBL diurnal variation appears to have a significant impact on aerosol concentrations observed at this background location and this can be quantitatively demonstrated by the present study. Although it does not alter the strong features of the diurnal variability of representative aerosol pollutant metrics, some characteristic behaviour of the rate of change in concentrations is observed. More specifically, the increase of PBLH in the morning hours advects fresh pollutants at a rate which would be higher if not diluted by the increased PBLH. This is more pronounced for fresh particle emissions and *eBC*. In the evening hours, concentration levels are retained to higher levels or display peaks, while they would otherwise decline sharply.

7.2.4.4 Diurnal variations of pollutants inside the PBL

In this section, we used the same methodology described for the case study above, to the entire period of measurements. In Figure 7.12a, b and c, we present the diurnal variations of the same parameters (as in Figure 7.11) along with their decoupled fractions, for the period 15 March to 2 July of 2020. Here the colored-shadows correspond to the standard deviation of each variable calculated for each hour, respectively.

Based on Figure 7.12a, we can observe the diurnal cycles of $N_{10\text{-}200nm}$ and PBL. The diurnal cycle of $N_{10\text{-}200nm}$ is shown to have a clear dependence on the anthropogenic emissions since the cycle matches to vehicular traffic pattern within the AMA. The average $N_{10\text{-}200nm}$ concentrations were found to be equal to 2500cm^{-3}, 8750cm^{-3}, and 3750cm^{-3} at 06:00, 13:00, and 19:00 LTC, respectively. In contrast, the $N_{200\text{-}500nm}$ concentrations did not show a strong diurnal cycle, ranging on average between 200 to 300cm^{-3}. Additionally, the *eBC* concentrations exhibited two peaks: the first peak (06:00-10:00 LTC) was related to vehicular traffic, while the second peak (18:00-23:00 LTC) was related to the residential heating emissions in agreement with a study conducted in the same period

(Eleftheriadis et al., 2021). Throughout the studied period, the PBLH revealed a clear diurnal cycle, fluctuating between 500 and 1200m agl. (06:00 to 21:00 LTC).

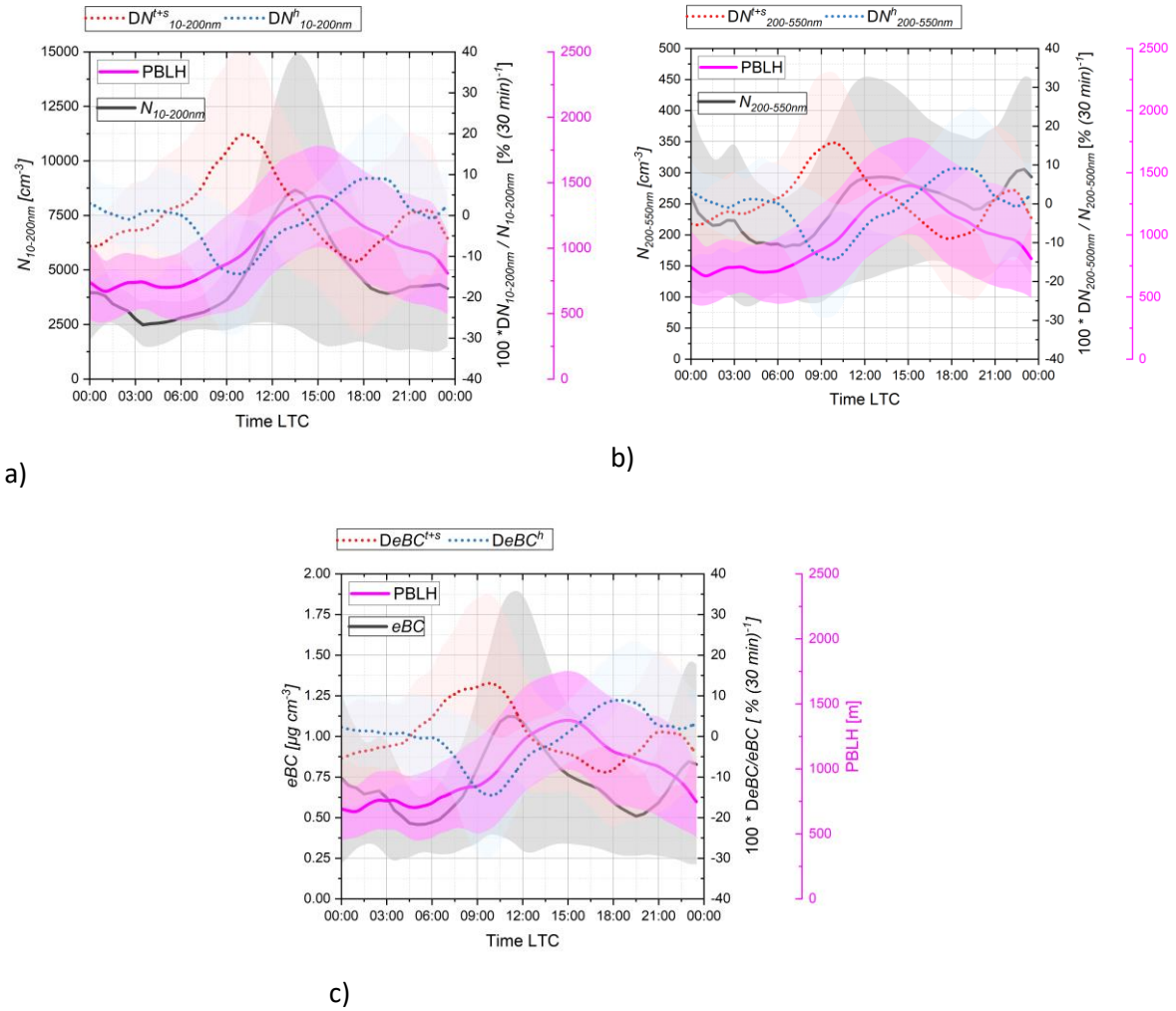

Figure 7.12. Diurnal evolution of a) $N_{10\text{-}200nm}$, b) $N_{200\text{-}500nm}$, and c) eBC concentrations, along with the decoupled evolutions of horizontal transport or source/sinks fraction and the PBLH enhancement fraction. The black line corresponds to the concentration of the pollutant (left axis), the dot lines correspond on the right axis to the decoupled concentration change of each pollutant, where the horizontal transport or source/sinks fraction is in black, the PBLH enhancement is in red, the measured change in blue. The magenta line corresponds to the second axis on the right and presents the PBLH.

In general, the decoupled DN_i^{t+s} and DN_i^{h} fractions were found to be anticorrelated to each other. This means that when the PBLH is growing, it promotes the air mass advection, leading to an increase in DN_i^{t+s} values. At the same time, the relevant aerosol concentrations are reduced, as the atmospheric volume in which they are embedded increases (*i.e.* vice versa decrease of the DN_i^{h} values compared to DN_i^{t+s} ones). Consequently, the observed rate of change (DN_i^{obs}) is fluctuating between the DN_i^{h} and DN_i^{t+s} values.

Throughout this study, it is demonstrated that during the transition periods of rising or contracting PBL a rate of change in the range of 10-20 % is dynamically induced and modulates the concentration levels of aerosol pollutants. In Figure 7.12 this corresponds to different levels based on the relative concentration of each species. However, if one looks at the change induced by the rate of change of PBL height alone all aerosol parameters are affected in the same way, behaving like passive tracers at the given time resolution. The effect is not pronounced to the point of altering the

diurnal pattern related to the urban emission sources but must be considered for interpreting the temporal evolution of observed concentration levels.

7.2.5 CONCLUSIONS

The local transport patterns of fresh and aged particles, as well as their diurnal variations and their relation to the boundary layer top height, are analyzed and discussed here. For the implementation of the study, we utilized measurements of horizontal wind speed, aerosol size distribution, and chemical composition, using both remote sensing and in situ techniques during the time period from March 15th to July 2nd 2020, over the Athens megacity, Greece. According to our findings, the combination of topography and atmospheric dynamics plays an important role in the local ventilation and air quality conditions. More precisely, in the Athens valley background conditions at DEM station, the aerosol particle concentration increases significantly in the S-NW sector due to traffic and vehicle emissions (6053 ± 3784 cm^{-3} and 171 ± 123 cm^{-3} in ultrafine and accumulation mode particles, respectively), as well as during windy conditions from the N-NE axis in case of ultrafine particles (5911 ± 3252 cm^{-3}). Moderate wind flows from NE-SE axis are mostly related to regional background air masses from the Mesogea plain (2879 ± 1832 cm^{-3} and 204 ± 127 cm^{-3} for ultrafine and accumulation mode particles).

Using the SO_4^{2-} as a tracer, we identified the long-range transport, as it is mostly derived from and continental pollution and shipping emissions. During nighttime, we found that the katabatic flows from Hymettus Mountain may either provide background clean air from higher altitudes, while occasionally transferring pollutants decoupled to higher layers, enhancing pollution episodes, while during stagnant conditions this effect becomes more intense (2931 ± 1770 cm^{-3} and 214 ± 152 cm^{-3} when wind speed > 4 m s^{-1}). Moreover, the role of PBLH variation on the measured aerosol load is also examined in this study. The estimation of PBLH was achieved using a threshold technique and then a dynamic box approach was used to decouple the effect of PBLH on the concentrations of pollutants (i.e., $N_{200\text{-}500nm}$, and *eBC*).

Our analysis reveals that the variation of PBL height has a quantitative effect on aerosol concentrations observed at the ground. This is because any change in the aerosol concentration is partially related to changes in sources or sink emissions, horizontal transport effects and the variance of the height of the PBL. Additionally, the height of PBL by itself, affects the ability of the aerosols to be transported horizontally since a deep PBL conducts the advection with no significant surface effects, in contrast within a shallow PBL the frictional drag effects close to the surface reducing the horizontal wind velocity by it, resulting in reduced the horizontal transport of aerosols. The significance of our results, demonstrate the importance of considering PBLH variations in understanding the impact of pollutants and their sources on air quality, especially in urban areas of complex topography. The methodology described in the study can be applied to other regions with similar conditions to estimate PBLH and its impact on air quality.

7.3 Paper III: The Influence of the Planetary Boundary Layer on the Atmospheric State at an Orographic Site at the Eastern Mediterranean

7.3.1 Summary

In this study, we presented the influence of the PBL on the air masses sampled by the $(HAC)^2$ and the corresponding cloud formation at Mount Helmos during the CALISTHO Campaign. The PBLH was determined from the σ_w measured by a wind Doppler lidar (over a 30-min time window with 30 m spatial resolution), using a characteristic threshold value of σ_w; when σ_w drops below 0.1 m s^{-1} the air masses are situated above the PBL, thus, the corresponding PBLH can be estimated. The air masses sampled at $(HAC)^2$ can be also characterized as coming from the PBL or from the free troposphere based on *in situ* aerosol measurements of the *eBC*, their fluorescent content, size distribution, and the air mass absolute humidity.

We found that the PBLH cycle concerning the location of $(HAC)^2$, regulates the temporal cycle of aerosol-related parameters measured at the $(HAC)^2$ with a distinct diurnal cycle being present when the station is inside the PBL and a complete lack thereof when the site is in the FTL. Additionally, we identified transition periods, where the $(HAC)^2$ site location alternates between the FTL (usually during the early morning hours) and the PBL (usually during the midday hours and sometimes during night hours, before the PBL shrinks due to radiation cooling), during which the concentration and characteristics of the aerosols vary the most. It is during these periods when orographic clouds are formed, forced by the largest aerosol diversity. Our analysis showed that the highest PBLH values occur in September [400m above $(HAC)^2$] followed by a transition period in November, while the lowest one occurs in January [200m below $(HAC)^2$]. We found also that the PBLH increases by 15 m per 1°C increase in surface temperature.

7.3.2 Objectives

In the case of the orographic environments, the PBLH estimation poses a particular challenge, given their topographic complexity and the large diurnal forcing. The wind Doppler lidar technique can constrain the PBLH like no other method, with high temporal and spatial resolution (Emeis, 2011). In this study, we deploy the HALO lidar system to establish a σ_w threshold value for the PBLH determination at the $(HAC)^2$ station at Mount Helmos (Greece), using *in situ* observations of the yearly variations of the PBL dynamics and ultimately determine when the $(HAC)^2$ station (and corresponding orographic clouds) is influenced exclusively by PBL or FTL air masses – or a combination of those.

The objective of this study is to to establish a σ_w threshold value for the PBLH determination at the $(HAC)^2$ station at Mount Helmos (Greece), using *in situ* observations of the yearly variations of the PBL dynamics and ultimately determine when the $(HAC)^2$ station (and corresponding orographic clouds) is influenced exclusively by PBL or FTL air masses – or a combination of those. Therefore, we adopted the usage of Doppler lidar technique, which enables detection of vertical profiles of aerosols as well as their velocity as "tracers" of the air mass movements. This technique, based on the

detection of the minimum of the gradient of the backscattered elastic lidar signal vertical profile or on the vertical wind velocity *w* profile, can provide the PBLH with very high spatial (a few meters) and temporal (a few seconds) resolution (Tsaknakis et al., 2011; Wang et al., 2021; Duc et al., 2022).

7.3.3 METHODOLOGY

The origin of the sampled air masses at $(HAC)^2$ is initially characterized through *in situ* measurements by a set of instruments consisting of an AE31 for measuring the *eBC*, a TSI 3563 to measure the light-scattering coefficient of aerosol particles at 550 nm(*sc550* and *bc500*), a WIBS-5/NEO to measure the presence of biological particles (pollen, bacteria and fungi), and a SMPS to determine the total concentration of particles (N_{Total}), as well as the concentration of particles between 90 and 800 μm ($N_{90\text{-}800nm}$). *In situ* meteorological data (ambient temperature and pressure, Relative Humidity (RH), and horizontal wind) are provided by a meteorological station which was located at $(HAC)^2$, while the absolute humidity (q) was calculated based on the ambient temperature and pressure (Wallace and Hobbs, 2006)

The strong contrast between the PBL and FTL air masses, using all these *in situ* parameters as proxy, is used to constrain when the PBLH crosses the $(HAC)^2$ altitude. A wind Doppler Lidar, placed at the VL location provided the vertical profiles of σ_w throughout the atmospheric column. Using this setup, we were able to follow the vertical movements of air masses between $(HAC)^2$ and VL and measure the σ_w at the level of $(HAC)^2$ thus, identifying when this site is above or inside the PBL. The latter is then used to determine the appropriate σ_w threshold for defining the PBLH.

Given that the black carbon mostly originates from anthropogenic fossil fuel emissions (the wildfire cases are not considered in our study) within the PBL, we can also use the *eBC* as an index to determine the regimes where $(HAC)^2$ is within the PBL or the FTL, when the *eBC* concentration obtains large or small values respectively (Lund et al., 2018; Motos et al., 2020). Additionally, given that increased aerosol concentrations are typically found within the PBL, the relevant total scattering coefficient tends to obtain large values (Farah et al., 2018) when $(HAC)^2$ is within the PBL, hence, the scattering intensity was used as a proxy to identify regimes where the $(HAC)^2$ is within the PBL or FTL, while, in this study, we used the aerosol total scattering and backscattering coefficients at 550nm (*sc550* and *bc500*, respectively).

7.3.3.1 Wind lidar system and PBLH retrieval

During CALISHTO, the wind lidar HALO was deployed at the VL site and was performing a 3-dimensional scan HALO can provide the vertical profile of the vertical wind velocity (updraft velocity) (w) with accuracy ±0.038 m s^{-1} for every 30 m with 2 s temporal resolution, while in a staring mode, the maximum distance range varies from 2 to 3 km depending on the atmospheric aerosol load.

Additionally, to minimize possible noise effects on the retrieved σ_w, we digitally filtered the backscattered lidar signal using the technique proposed by Barlow et al. (2011), Newsom and Krishnamurthy (2020). Thus, we excluded the data with a signal-to-noise ratio (SNR) lower than -20

dB from our dataset to obtain a noise-corrected dataset. The purpose of this methodology is to prevent the Doppler spectrum from systematic variations in the noise floor. Secondly, we created data segments containing sub-datasets using a 30-minute time-moving window (Schween et al., 2014) of the noise-corrected dataset for every 5 min (Lenschow et al., 2012), and finally, we calculated the standard deviation σ_w for each height level.

The average time window of 30 min describes the time needed by a convective air plume to travel up and down within a well-mixed PBL. Considering that a plume has on average, an ascent speed of 1 m s^{-1} and that a typical mixing layer at $(HAC)^2$ is of the order of 1 km, the average time interval is about twice the lifetime of the plume. This period is also typical for the derivation of turbulent fluxes from eddy covariance stations according to Schween et al. (2014). Finally, we calculated the σ_w at the $(HAC)^2$'s level height, and we combined the *in situ* measurements from the SMPS, ToF-ACSM, AE31, TSI 3563, WIBS, and meteorological parameters to derive a threshold of the value of σ_w to delineate whether $(HAC)^2$ is confined within the PBL or above (in the FTL), or in a transition zone between these two regions.

7.3.4 Results & Discussion

Figure 7.13 presents the RH, T, and horizontal wind velocity recorded at $(HAC)^2$. As previously mentioned, the aerosol scattering (*sc550*) and backscattering (*bc550*) coefficients were derived from the Nephelometer; the $N_{90\text{-}800nm}$ and the N_{Total} were derived from the SMPS data; the *eBC* concentrations were derived from the Aethalometer data; the AB and ABC signals were obtained from WIBS; while the σ_w was derived from HALO at the level of $(HAC)^2$.

Under cloud-free conditions at $(HAC)^2$, the sampled air masses contain low levels of moisture (q: 0-2.5 g kg^{-1}, RH: 0-40%) and σ_w usually varies between 0-0.25 m s^{-1}. In these cases, the fine particles (below 90 nm) dominate the aerosol number ($N_{90\text{-}800nm}/N_{Total} < 0.25$), and $N_{90\text{-}800nm}$ varies between 0 and 120 cm^{-3} and the aerosol scattering coefficients (*sc550* and *bc550*) and the *eBC* concentrations approach zero values. When the RH at $(HAC)^2$ ranges between 40 and 90%, the sampled air masses are more humid (q increases from 2.5 to 7 g kg^{-1}), σ_w exceeds 0.25 m s^{-1} and the number of accumulation-mode particles ($N_{90\text{-}800nm}$) increases substantially. This pattern, is indicative for the arrival of air masses originating from the PBL, with elevated $N_{90\text{-}800nm}$, σ_w and RH values.

Therefore, given that the PBL is a region of intense air mass mixing (especially in the studied orographic region), low σ_w values correspond to pure and dry free tropospheric air masses, while large σ_w values correspond to polluted and humid air masses originating from the PBL. When $(HAC)^2$ is close to PBLH, then the PBL transition zone (so-called “entrainment” or ”detrainment zone”) is influenced by both FTL and PBL air masses; in this case, strong temporal gradients are observed in all *in situ* measured properties and σ_w, which are characteristic of mixing between the FTL and PBL air masses (*c.f.* Figure 7.13).

In Figure 7.14a-e, we present the correlation of each above-cited variable (*eBC*; *sc550* and *bc550*; BC and ABC; $N_{90\text{-}800nm}$ and N_{Total}; and RH with q) with σ_w separately, to identify how each parameter changes with σ_w. These figures clearly show that the increase of the σ_w values leads to a relevant increase of RH, q, *sc550* and *bc550,* $N_{90\text{-}800nm}$, N_{Total}, *eBC*, BC and ABC. We observed that when σ_w exceeds 0.10 ± 0.01 m s^{-1}, the *eBC*, *sc550*, absolute (q > 2.5 g kg^{-1}) and relative humidity (RH > 40%) show increased values, confirming the arrival of PBL air masses at $(HAC)^2$. Additionally, the concentrations of the BC- and ABC-class particles from WIBS (*c.f.* Figure 7.14c) can be used to identify

the transition of the $(HAC)^2$ from being in the FTL to the PBL, since high values of these two parameters are related to the presence of bioaerosols emitted from the nearby forests, which are confined within the PBL. Moreover, we found that an increase of the BC values (*c.f.* Figure 7.14c) is observed when the σ_w values exceed 0.1 m s^{-1}, which corresponds to the 85% of the dataset.

Based on these findings we can, thus, conclude that when σ_w > 0.1 m s^{-1} and σ_w < 0.1 m s^{-1}, then $(HAC)^2$ is inside and outside the PBL, respectively, while, when σ_w = 0.1 m s^{-1}, the mountaintop site is within the PBL entrainment (transition) zone. Thus, the value of σ_w = 0.10 ± 0.01 m s^{-1} can be regarded as a threshold to conclude when $(HAC)^2$ resides within the PBL or the FTL, or within the PBL transition zone.

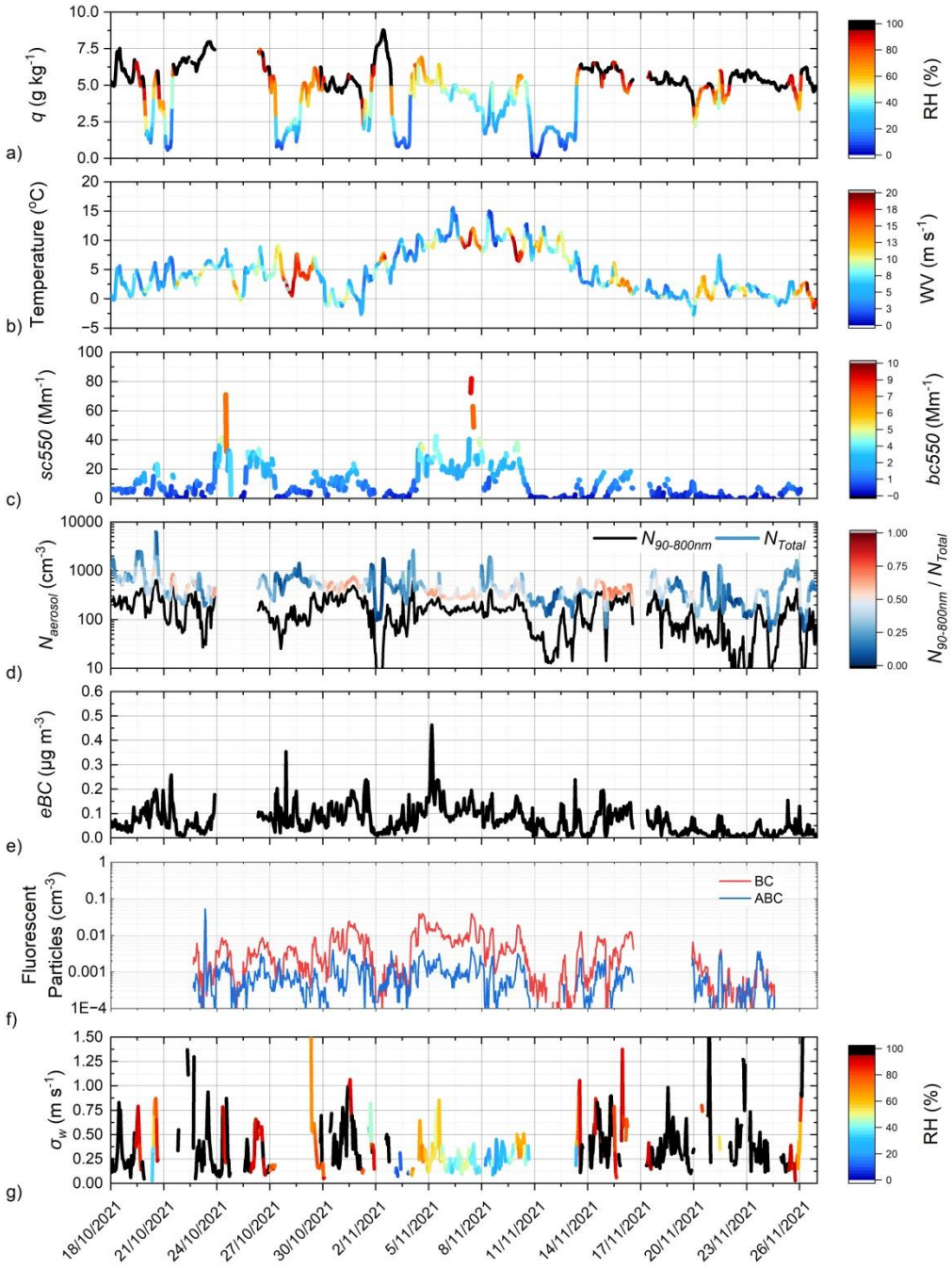

Figure 7.13. Timeseries of a) q (g kg^{-1}) and RH (%), b) ambient temperature (^{o}C) and horizontal wind velocity (m s^{-1}), c) scattering coefficients sc550 and bc550 (Mm^{-1}), d) $N_{90\text{-}800nm}$, N_{tot} (cm^{-3}) and $N_{90\text{-}800nm}/N_{tot}$, e) eBC (µg m^{-3}), f) fluorescent particles BC and ABC (cm^{-3}), and f) σ_w (m s^{-1}), as measured by the synergy of in situ and remote sensing techniques at the (HAC)^2 height level.

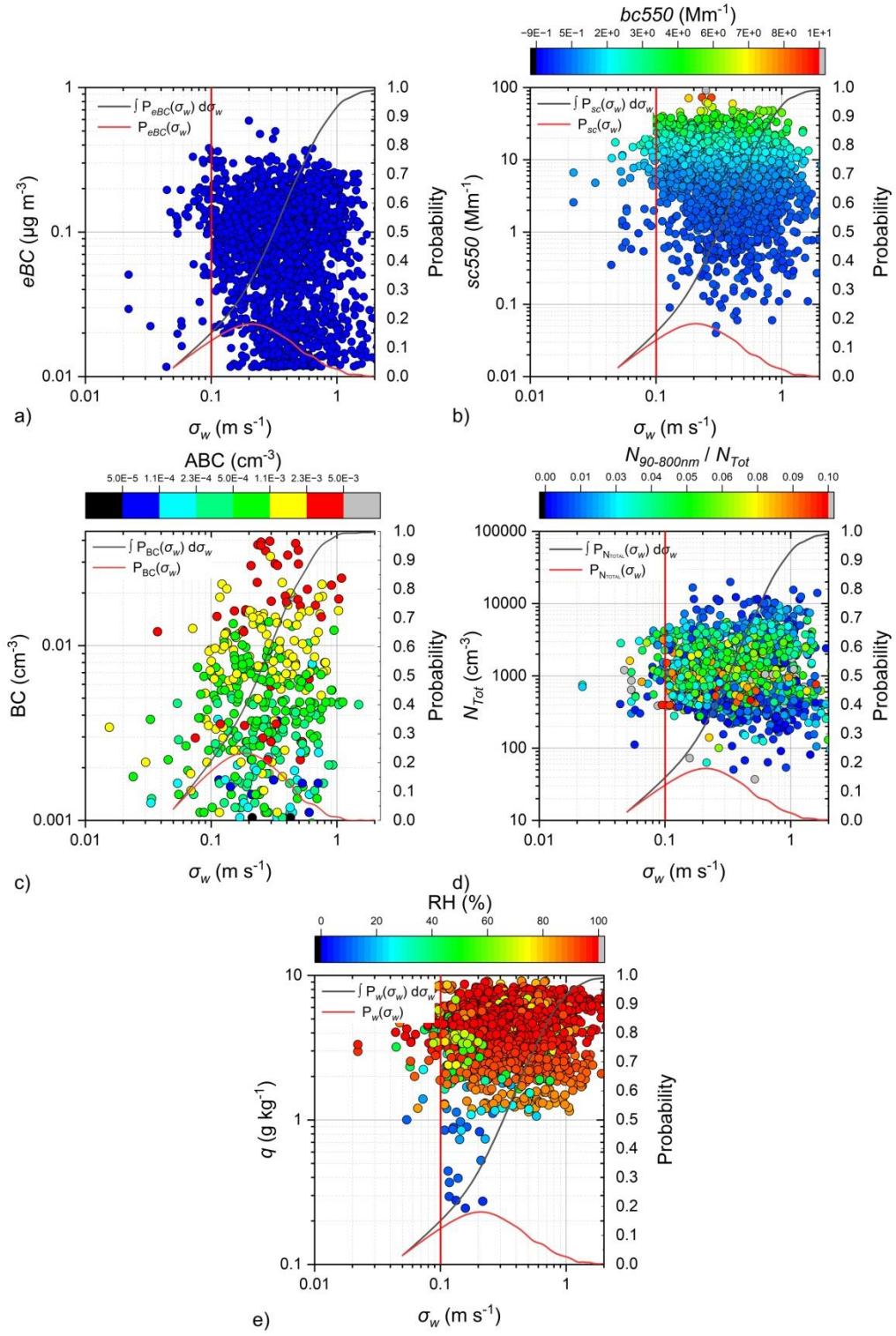

Figure 7.14. Scatter plots corresponding to a) eBC (µg m^{-3}), b) sc550 and bc550 (Mm^{-1}), c) BC and ABC (cm^{-3}), d) N_{tot} (cm^{-3}) and $N_{90\text{-}800nm}$ /N_{tot} and e) q (g kg^{-1}) and RH (%) in respect of σ_w (m s^{-1}) as measured by HALO at (HAC)^2. The red lines represent the normalized frequency of each measurement (called "Probability"), while the black lines are the integral of the normalized frequency of measurement (from the smallest σ_w value up to the given σ_w). The vertical red lines correspond to the threshold value of 0.1 m s^{-1} which indicates the transition between the PBL to the FTL regimes.

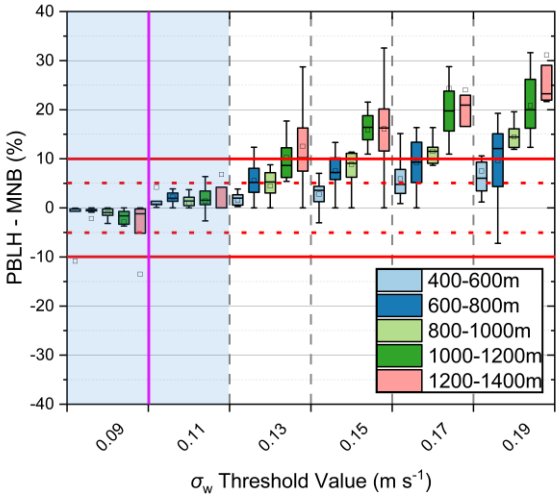

Figure 7.15. The PBLH-MNB (%) using σ_w threshold values 0.09 to 0.19 m s^{-1} compared to 0.1 m s^{-1} (magenta vertical line) at different PBLH ranges 400-600m up to 1200-1400m, respectively. The horizontal red solid and dashed lines correspond to a bias of ±5% and ±10%, while the shadow area depicts the σ_w threshold values where the MNB-PBLH (%) remains within ±15%.

We also calculated the Mean Normalized Bias (MNB) of the PBLH values against those retrieved using a σ_w threshold value of 0.1m s^{-1}. The PBLH values are aggregated into five different height ranges, from 400 to 1400m with a step of 200m (*c.f.* Figure 7.15). When the threshold σ_w values range within 0.09 - 0.11 m s^{-1}, the MNB-PBLH varies within ± 5%, which is roughly consistent with observations by Schween et al. (2014). However, we found that the bias of the estimated PBLH compared to the true one, increases in respect to the height. Thus, when using a σ_w threshold value equal to 0.13 m s^{-1}, in the case where the true PBLH is lower than 600m, the bias of the estimated PBLH is < ± 5%, while in the case where the true PBLH is higher than 1200m, results in > ± 10%. This bias is amplified significantly up to 30% when using even larger σ_w threshold values leading to a significant overestimation of the PBLH especially in the case of deep planetary boundary layers**.** In conclusion, the threshold values of σ_w ranging from 0.09 to 0.11 m s^{-1}, leading to a retrieval of the PBLH with a bias of ± 5%.

7.3.4.1 Diurnal Evolution of the PBLH, AE31, WIBS and SMPS data

In this section, we aim to examine the reliability of the threshold of σ_w of 0.1 m s^{-1} based on the diurnal evolution of the *in situ* measurements. The airmasses and their corresponding diurnal cycles are distinctly different in load inside and outside the PBL. Therefore, we split the whole dataset into three subsets (*c.f.* Figure 7.16) based on the position of the (HAC)^2 station compared to PBLH (retrieved using a σ_w = 0.1 m s^{-1}), being the days where the PBLH:

i. exceeds the (HAC)^2 altitude throughout the entire day, which occurs for 14 days (15-16, 18, 26, 30-31 October 2021; 5-7, 9 and 15-18 November 2021),
ii. fluctuates above and below the (HAC)^2 height during the day, which occurs for 24 days in the dataset (13-14, 17, 19, 20-23, and 27-29 October 2021; 1-4, 8, 10, 12-14, 19-21 and 23 November 2021),

iii. remains below the $(HAC)^2$ altitude throughout the entire day, which occurs for 3 days in the dataset (11, 22 and 24 November 2021).

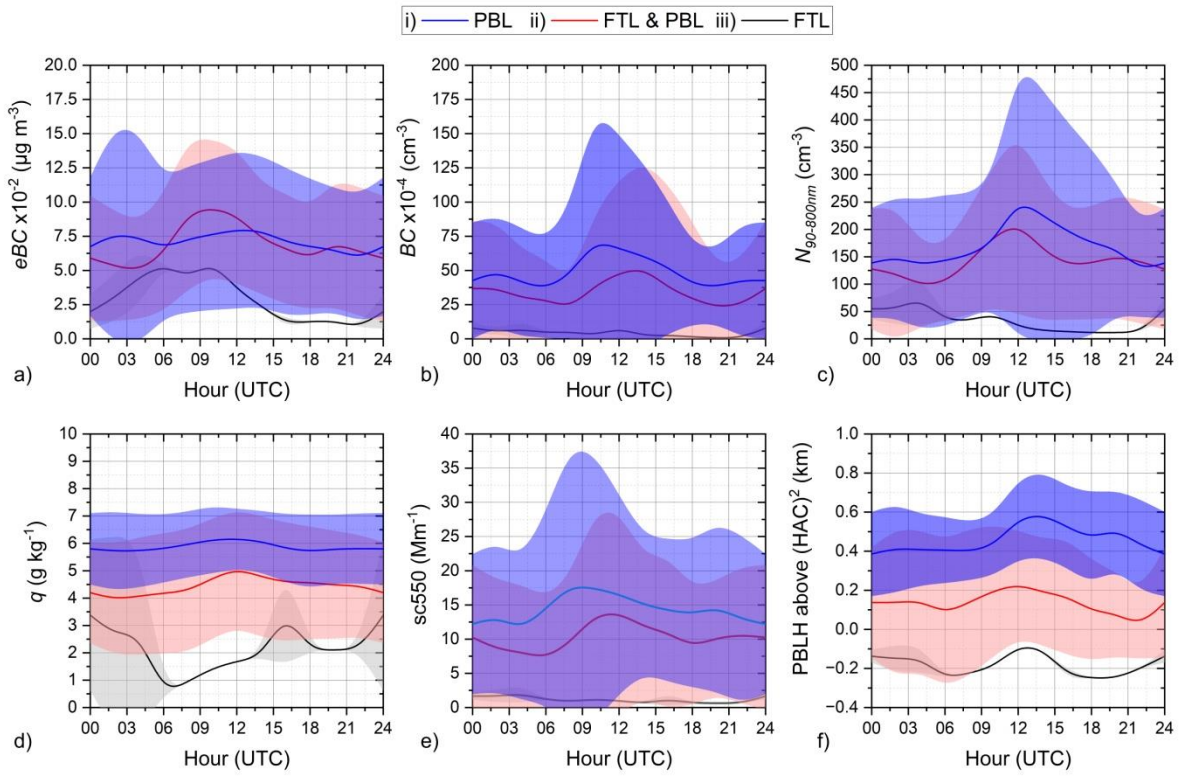

Figure 7.16. The diurnal cycle of a) eBC, b) BC, c) $N_{90\text{-}800nm}$, d) q, e) sc550 and f) PBLH for the three different subsets when $(HAC)^2$ is i) within the PBL throughout the day (blue), ii) switches between the FTL and the PBL during the day (red), and iii) when is within the FTL the entire day (black).

Thus, we found that when $(HAC)^2$ is within the FTL, the aerosol and bioaerosol concentrations do not show a distinct diurnal cycle and are related to dry air masses (*c.f.* Figure 7.16), as all the *in situ* measured parameters have significantly lower values compared to the other subsets. Furthermore, a distinct diurnal cycle of the of *eBC*, BC, $N_{90\text{-}800nm}$, *q, sc550* was also observed in subsets i) and ii), where $(HAC)^2$ is either within the PBL throughout or part of the day (*e.g.* usually between 06:00-18:00 UTC about 60% of the days as shown in Figure 7.17a and b). All the in *situ* measured parameters obtain large values, especially in subset i) which corresponds to the highest PBLH value.

Additionally, we calculated the mean diurnal variability of the PBLH for each month of the CALISHTO campaign, from September 2021 to March 2022 (*c.f.* Figure 7.17a), as well as the relative frequency of each subset (*c.f.* Figure 7.18a), and correspond them to three climatological regimes (Kallos et al.,1993): as follows: dry summer months (June-September), rainy winter months (November-February), and spring and autumn months (March-May and October), the latter are characterized by a transient season where the summer- and winter-type of weather patterns are interchanging.

In Figure 7.17 we can distinguish a seasonal cycle of the PBLH throughout the different seasons; thus, the maximum averaged PBLH is found during summer, while during November the PBLH values showed the largest variability compared to the other months. This is because November is characterized by frequent surface cyclonic systems over the greater Greek area, accompanied by a cold and a warm front moving westerly across Greece (Kouroutzoglou et al., 2011). As a result, $(HAC)^2$ alternates between a cold and a warm domain of the barometric system, with important impacts on

the PBLH: varying between 0 and 400m above $(HAC)^2$ for the first half of November and 200 to 400m below $(HAC)^2$ level for the second half of the month. During the subsequent months, the PBLH and its variability decrease gradually until January, while later it increases steadily up to March. The average maximum values of the PBLH with respect to the $(HAC)^2$ level per month were found equal to +400m, +200m, +50m, -10m, and -200m, for September up to January, respectively.

Moreover, we calculated the total hours where the $(HAC)^2$ is within the FTL or PBL per month, only during cloud-free conditions (*c.f.* Figure 7.18a). We found that in March and from September to November, the $(HAC)^2$ alternates most of the time between the FTL and PBL, residing about half of the time within each layer. In contrast, between December and February, the $(HAC)^2$ resides mostly within the FTL (around 85% of the time on average).

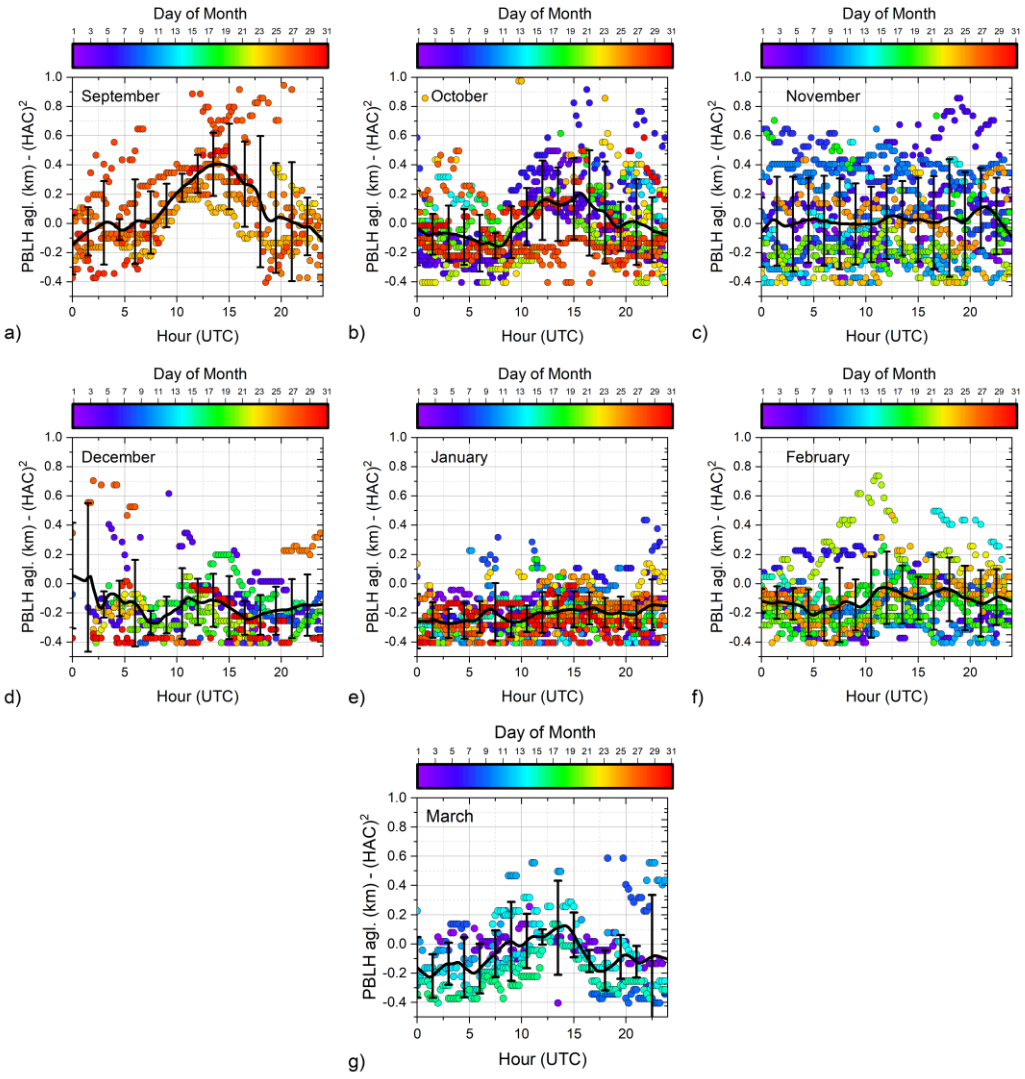

Figure 7.17. The monthly average diurnal cycle of PBLH for a) September 2021 up to g) March 2022. The PBLH values are colored by the day of the month. The solid black line corresponds to the hourly averaged values of the PBLH, while the error bars are the standard deviation of the PBLH values of each month, respectively.

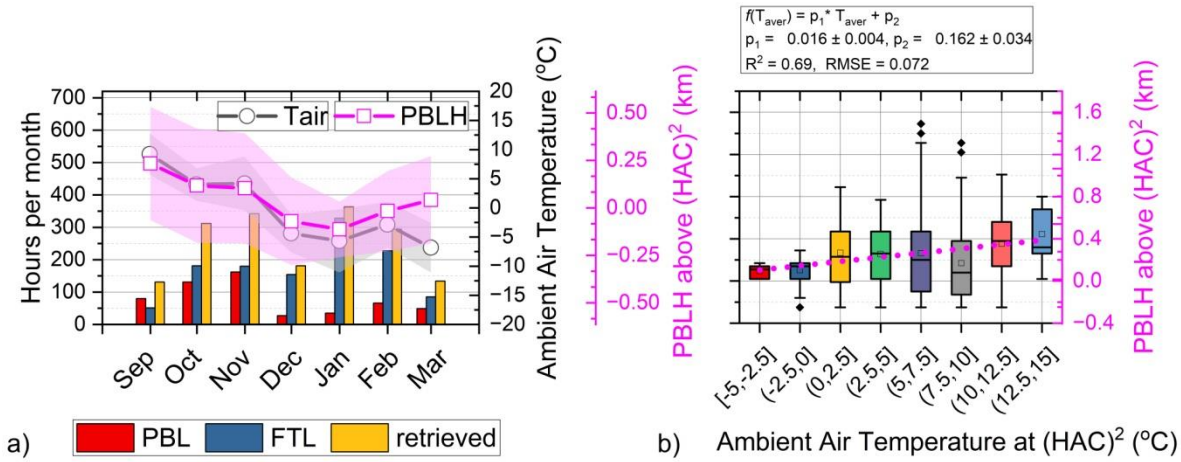

Figure 7.18. a) The histogram of the total hours where the $(HAC)^2$ was within the PBL or FTL, and the seasonal trend of PBLH and the ambient air temperature, respectively; b) Boxplots of the PBLH values under cloud-free conditions based on the ambient air temperature at $(HAC)^2$, grouped in bins from -5 up to 15°C with a step of 2.5°C, while the magenta dot line shows a linear relation between the ambient air temperature and the PBLH.

Finally, we grouped the dataset into nine groups (from -5° to 15°C with a step of 2.5 °C), and we examined how PBLH varies with respect to the averaged ambient temperature at $(HAC)^2$ level (c.f. Figure 7.18b). Thus, we calculated the averaged value of the PBLH for each temperature range separately and we interpolated a linear function between them. The interpolation (with R^2=0.69) showed that an increase of 1°C of the surface mean temperature causes an increase of 16 ± 4 m on the averaged PBLH. This result is very useful as it can provide valuable input data to climate models applied at high-altitude stations in the Mediterranean region, in connection to Global Warning scenarios.

7.3.5 CONCLUSIONS

We studied the variation of the PBL top height in the vicinity of the $(HAC)^2$ station at Mount Helmos, Greece. The identification of the PBLH was based on a synergy of data from a wind Doppler lidar and *in situ* instrumentation at the $(HAC)^2$ station. The lidar was used to measure the vertical velocity of air masses and calculate the standard deviation of the updraft currents as an indicator of the vertical mixing in the PBL and the corresponding PBLH. The *in situ* aerosol data obtained from a set of instruments (Aethalometer, Nephelometer, WIBS-5/NEO, SMPS), and data from a meteorological station, were used to determine the characteristics of the aerosols sampled, when $(HAC)^2$ was within the PBL or in the FTL, respectively. We found that during daytime when $(HAC)^2$ is within the PBL, the *in situ* sampled air masses are characterized by increased aerosol concentrations and increased humidity, while when $(HAC)^2$ is within the FTL, the sampled air masses are characterized by low aerosol/bioaerosol concentrations and relatively low humidity. Therefore, given that these air masses are distinctly different in terms of their aerosol load and humidity inside or outside the PBL, showing intense diurnal cycles, we concluded that a threshold value of σ_w = 0.10 ±

0.01 m s^{-1} can be used to identify the PBLH at the $(HAC)^2$ site and, thus, discriminate the transition zone between the PBL and the FTL.

We also examined the diurnal cycle of PBLH throughout the studied period and found that higher PBLH values are observed in September (400 m above $(HAC)^2$), followed by a transition period in November, while the lower ones (200 m below $(HAC)^2$) are observed during winter (December to February). The average maximum values of the PBLH with respect to the $(HAC)^2$ level per month, ranged from +400m down to -200m (in respect to $(HAC)^2$ level), from September to January, respectively. It is important to mention that in March and from September to November, the $(HAC)^2$ alternates most of the time between the FTL and PBL, residing about half of the time within each layer. In contrast, between December and February $(HAC)^2$ resides mostly within the FTL.

Moreover, a positive trend between the mean ambient air temperature at $(HAC)^2$ and mean PBLH was revealed, showing that an increase of 1°C of the surface temperature corresponds to an increase of 16 m in the relevant PBLH. This finding could be a valuable input in global warming models to better represent atmospheric processes and atmospheric boundary layer dynamics in elevated areas.

Finally, our methodology described here can be implemented to identify the origin of aerosols that feed orographic clouds and thus, potentially facilitate the retrieval of critically important parameters on the cloud formation, such as the cloud supersaturation, the cloud droplet number and the droplet sizes (**Paper IV**).

7.4 Paper IV: Drivers of Droplet Formation in East Mediterranean Orographic Clouds

7.4.1 Summary

In this study, we focused on the drivers of cloud droplet formation in orographic clouds. We used a combination of modeling, *in situ* and remote sensing measurements at the $(HAC)^2$ station during the CALISTHO campaign to examine the origins of the aerosols (i.e., local aerosol from the PBL, or long-range transported aerosol from the FTL) contributing to the CCN, their characteristics (hygroscopicity, size distribution and mixing state), as well as the vertical velocities distributions and resulting supersaturations.

We found that the characteristics of the PBL aerosol were considerably different from FTL aerosol and used the aerosol particle number (N_{10}, particles above 10 nm) and equivalent mass concentration of the *eBC* to determine when the $(HAC)^2$ was within the FTL or PBL based on timeseries of the height of the PBL. During the $(HAC)^2$ cloud events, we sample a mixture of interstitial aerosol and droplet residues, which we characterize using a new approach that utilizes the *in situ* droplet measurements to determine time periods where the aerosol sample is purely interstitial. From the dataset we determine the properties (size distribution and hygroscopicity) of the pre-cloud, activated and interstitial aerosol. The hygroscopicity of activated aerosol is found to be higher than that of the interstitial or pre-cloud aerosol. A series of closure studies with the droplet parameterization shows that N_d and supersaturation can be predicted to be within ± 25% of observations when the aerosol size distributions correspond to pre-cloud conditions. Analysis of the characteristic supersaturation of each aerosol population indicates that droplet formation in clouds

is aerosol-limited when formed in FTL airmasses – hence droplet formation is driven by aerosol variations, while clouds formed in the PBL tend to be velocity limited and droplet variations are driven by fluctuations in vertical velocity. Given that the cloud dynamics do not vary significantly between airmasses, the variation in aerosol concentration and type is mostly responsible for these shifts in cloud microphysical state and sensitivity to aerosol. With these insights, remote sensing of cloud droplets in such clouds can be used to infer either CCN spectra (when in the FTL) or vertical velocity (when in the PBL). In conclusion, we show that a coordinated measurement of aerosol and cloud properties, together with the novel analysis approaches presented here allow for the determination of the drivers of droplet formation in orographic clouds and their sensitivity to aerosol and vertical velocity variations.

7.4.2 OBJECTIVES

The objective of this study is to understand the aerosol involved in cloud droplet formation (CCN), and why the remaining particles, called "interstitial", do not activate. Hence, given that $(HAC)^2$ was equipped with a single-inlet which was able to collect ambient particulate matter with an aerodynamic diameter of 10μm or less, and given that during the cloudy moments, the droplet size changes continuously in time and varies in size within 5–20 μm (Rogers and Yau, 1996; Pierce et al., 2015), had as a result, a fraction of a droplet to penetrate into the inlet, get dried, and mixed again with the interstitial aerosol particles. Thus, there was a need to find a way to efficiently separate the interstitial aerosols from cloud droplets when sampling within clouds, to determine the properties of the interstitial aerosols. For this purpose, we developed a visual filtering technique where the *in situ* measurements of droplet size were used to guide the subsequent analysis, which in the end, was found able to separate interstitials from evaporated cloud droplets in single-inlet systems if there are *in situ* measurements of droplet size that allows applying a temporal filter (e.g., consider only parts of the timeseries for which droplet do not pass through the inlet) on the timeseries.

7.4.3 METHODOLOGY

In this study, we used one SMPS at $(HAC)^2$ to measure the in-cloud aerosol and one at VL as a pre-cloud proxy; a ToF-ACSM to measure the non-refractory submicron aerosol mass and chemical composition; an AE31 to determine the *eBC*; a PVM-100 to measure the N_d and further to determine the Cloudy and Cloud Free regimes; a CCN-100 to measure the CCN spectra, and thus to calculate the aerosol hygroscopicity, the critical size, and the cloud supersaturation; and last but not least, a wind doppler lidar that was deployed at VL, to measure the vertical wind velocity and so to estimate the standard deviation of updrafts - σ_w. Additionally, the aerosol measurements (derived either from the SMPS form $(HAC)^2$ or VL), the chemical composition, and the σ_w was used to initialize the aerosol activation parameterization, which was used to calculate the *in situ* derived N_d and the cloud maximum supersaturation.

7.4.3.1 Understanding the aerosol sampled at $(HAC)^2$

A major parameter controlling the aerosol sampled at any given time, since $(HAC)^2$ can be either within the FTL or within the PBL, is the PBLH (Foskinis et al., under review). Thus, when the PBLH exceeds that of $(HAC)^2$, the site resides within the PBL, which is rich in bioaerosol particles originating from the nearby forest, and anthropogenic emissions originating from the greater region. When the PBLH is below $(HAC)^2$, the site is in the FTL and receives airmasses and aerosol from long-range transport: continental when originating from Europe and the Balkans; marine from the Mediterranean, and dust from the Sahara (Papayannis et al., 2005, 2008; Kallos et al., 2007; Kaskaoutis et al., 2012; Soupiona et al., 2018). Thus, when a cloud forms at $(HAC)^2$, which is at a high frequency, especially during the wintertime (Foskinis et al., in review), the CCN can originate either from the PBL or the FTL. Hence, combined with the wide diversity of airmass origin at the site makes the site ideal for studying aerosols-clouds interactions for warm and slightly to moderately supercooled clouds.

7.4.3.2 Determining CCN Spectra and Hygroscopicity

The CCN concentrations as a function of supersaturation ("CCN spectra") were measured by the CCN-100. The hygroscopicity was also determined from a combination of the CCN and SMPS data, as follows. For each supersaturation, the corresponding SMPS distribution is integrated from the largest resolved size backwards until a characteristic size D_{cr} that gives an aerosol number equal to the observed CCN concentration. By doing this process for each supersaturation cycle, we calculated the characteristic critical supersaturation (s^*), where according to Cerully et al. (2011) the s^* is defined as the supersaturation value where half of the ambient of the CCN population is activated to droplets. A sigmoid function was fitted to each CCN spectrum measured using the following form of Cerully et al. (2011):

$$R_a(s) = \frac{E}{1 + (\frac{S}{S^*})^C},$$

where E is the maximum fraction of particles that activate at high supersaturations and it was considered equal to the total particle number derived from SMPS, C is the slope of $R_a(s)$. The characteristic hygroscopicity parameter (κ^*) of each CCN spectrum is then calculated from κ-Kölher theory (Petters and Kreidenweis, 2007), as $\kappa^* = \left(\frac{4\,A^3}{27\,{D_{cr}}^{*3}\,s^{*2}}\right)$, and ${D_{cr}}^*$ that gives an aerosol number equal to the $R_a(s^*)$, while for this purpose we used the hourly particle size distribution derived by the SMPS that was deployed at $(HAC)^2$. This κ^*, although strictly corresponding to the hourly averaged hygroscopicity for particles of size ${D_{cr}}^*$, is used to characterize the hygroscopicity of the resolved CCN spectrum and used for subsequent droplet formation calculations. The calculation also assumes that particles are primarily internally mixed, which for periods of sampling FTL is an excellent assumption while for PBL-dominated periods also is a good assumption owing to the remote location of the station. During periods where particles at the station will originate from both PBL and FTL, it is expected that there is a degree of mixing that will introduce some uncertainty in subsequent calculations.

7.4.3.3 Determining the *in situ* derived N_d and cloud supersaturation

Lastly, we used a physically based aerosol activation parameterization developed by Nenes and Seinfeld (2003) and further expanded by Fountoukis and Nenes (2005, 2007), Barahona et al., (2010) and Morales Betancourt and Nenes (2014) to calculate the droplet number of the formatted clouds using the wind vertical velocity and the aerosol characteristics. In principle, the droplet activation parameterization solves the equations of motion of an ascending air parcel which contains aerosols and water vapor and calculates the point where the supersaturation becomes maximum ($s_{max,}$) as well as the N_d. The inputs to this parameterization are the pressure, temperature, aerosol size distribution measured by SMPS, the bulk hygroscopicity parameter κ which was calculated using ISORROPIA II, and the updraft velocities obtained by HALO.

7.4.4 Results & Discussion

7.4.4.1 Dataset Overview

In this part of the study, we focused on the *in situ* and remote sensing measurements of the non-cloudy periods (*c.f.* Figure 7.19), as well as the possible regimes of $(HAC)^2$ based on the PBLH. Figure 7.19a shows the movements where $(HAC)^2$ is in the FTL and PBL based on the relative position of the PBLH (given by Foskinis et al. (2023b)) compared the $(HAC)^2$ altitude (shown in black horizontal line). When the station is in the FTL, the PBLH is below $(HAC)^2$ line and vice versa when it is in the PBL.

The airmass separation is in agreement with what is seen in terms of the moisture content, since under cloud-free conditions, the FTL airmasses are markedly dryer (RH=34 ± 26 %) than the PBL airmasses (RH = 65 ± 16 %) (Figure 7.19c). Also, when the $(HAC)^2$ is in the FTL, we observed two prevailing wind directions, one at 30° N and one at 80° N, where, in both the N_{Total} gets the lower values observed (~45 cm^{-3}), and *eBC* levels approach its detection limit (~0.01 μg m^{-3}). These wind directions are directly related to the long-range transported airmass; when arriving from the north, it usually originates from E. Europe and the Balkans and is rich in sulfur (Stavroulas et al., 2021). When the airmass arrives from the E or SE, it often carries dust aerosols. When the $(HAC)^2$ is within the PBL, we identified three prevailing wind directions, that correspond to the local transport patterns from 90°, 180° and 320° N, where the N_{Total} obtains its maximum values (~3300 cm^{-3}), and the *eBC* values increase up to ~0.4 μg m^{-3} when the wind speed exceeds 6 m s^{-1} and becomes maximum when the wind blows from 160 - 220°. Additionally, we found a dependence of the PBLH on the wind direction, since when the wind passes over mountain-tops before reaching the site, the PBLH tends to be higher and the σ_w tends to be lower. We observed that the increase of the aerosol content (from ~250 cm^{-3} to ~750 cm^{-3}) leads to an increase of N_d (from ~100 cm^{-3} to ~300 cm^{-3}), and decrease of the cloud droplet size (from ~17.5 μm to ~10 μm), consistent with the Twomey effect (Twomey, 1977) of aerosols on clouds and cloud albedo (IPCC, 2023).

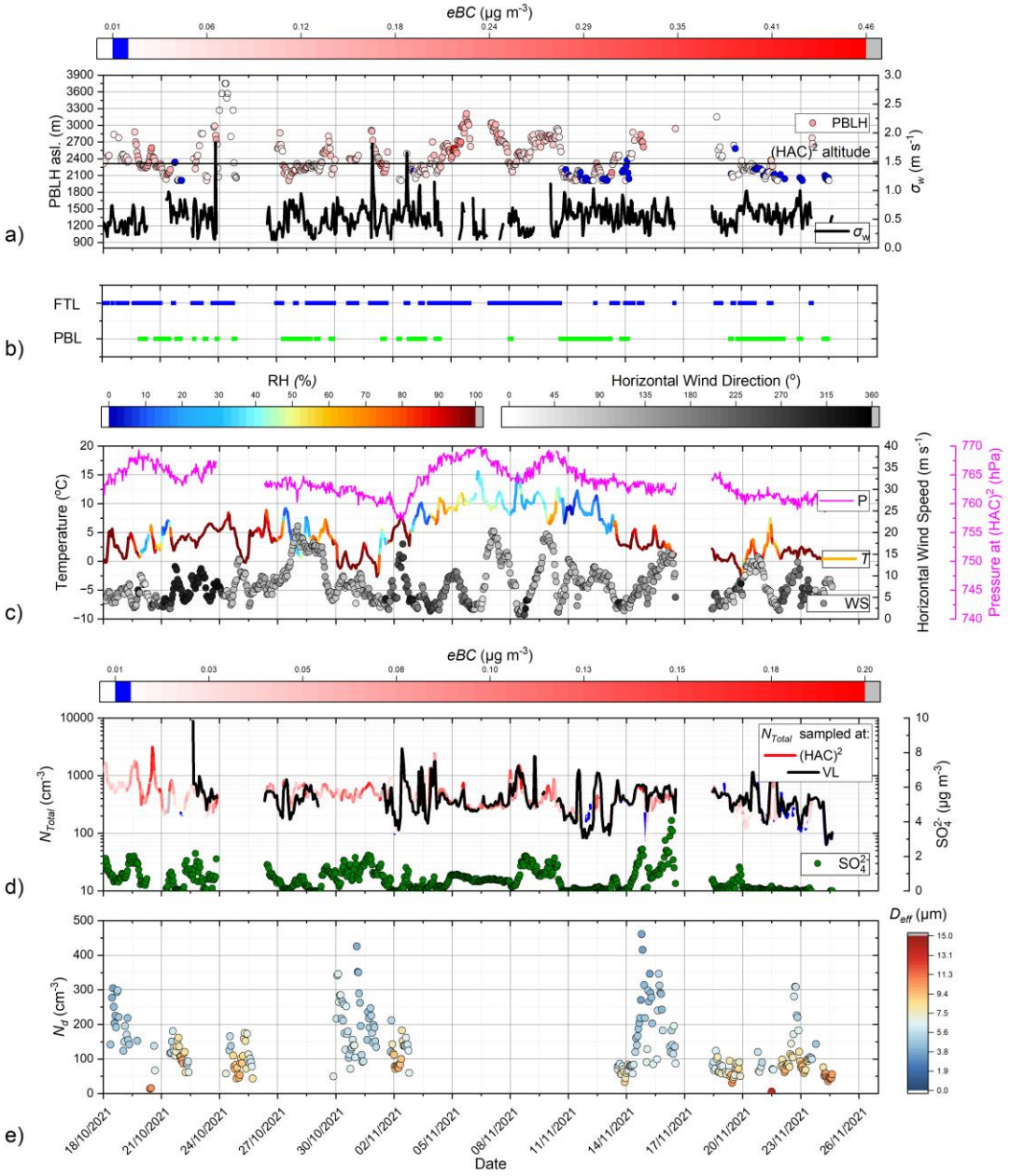

Figure 7.19. Summarized the level-1 measurements obtained by in situ or remote sensing instrumentation.

7.4.4.2 Separating Interstitial Aerosol from Cloud Droplet Residuals

Aerosol particles that act as CCN have dry diameters of the order of 100 nm and grow at least 10-fold when they activate into cloud droplets (Figure 7.20) (Rogers and Yau, 1996; Pierce et al., 2015). Indeed, when the $(HAC)^2$ station was fully covered by the clouds, the droplet effective

diameter, D_{eff}, varied between 2 and 15 μm (Figure 7.19). When the clouds formed with FTL aerosol, the D_{eff} was on average 17.0 ± 2.7 μm, and 10.3 ± 1.9 μm when formed with PBL aerosol. The average size differences between the two types of airmasses can be explained by the different CCN concentrations in them. The FTL has fewer CCN, hence droplets are generally larger than in PBL airmasses. In both cases, the aerosol inlet (which is a PM_{10} inlet - 10μm cut-off diameter) would sample inactivated (known as "interstitial") aerosol together with some of the droplets. These droplets subsequently evaporate in the heated inlet and contribute to the size distribution and other aerosol characteristics measured by the online *in situ* aerosol instrumentation. This means that when the station is in-cloud, the aerosol sampled from the PM_{10} inlet corresponds to a mixture of interstitial aerosol and evaporated cloud droplet residuals. However, D_{eff} varies considerable during a cloud event (Figure 7.19), and often exceeds 10 μm. This implies that considering subsets of the in-cloud timeseries when the D_{eff} is large enough can ensure that the aerosol sampled by the PM_{10} inlet is interstitial aerosol, as droplets would be too large to pass through the inlet.

We therefore consider the above concept and develop a "virtual filter" technique to define the D_{eff} threshold (measured *in situ* and continuously by the PVM-100) that ensures that the aerosol sampled by the PM_{10} inlet does not contain droplets that have penetrated the inlet, but only interstitial aerosols. In applying this filter, we ignore periods of the respective measurements during which the *in situ* D_{eff} of the droplets is less than the threshold. We selected the periods during which we were sampling at least 30 minutes continuously in cloud-free conditions followed by (or proceeded by) at least 30 minutes of cloudy conditions, to allow multiple size distribution measurements during the pre-/post- and the in-cloud phases. The distributions under cloud-free conditions are then averaged, to give the "total aerosol distribution". The in-cloud distributions are averaged for periods where the droplet D_{eff} exceeds a predefined threshold (starting from 10μm). The in-cloud distributions are averaged for different values of the D_{eff} threshold, until 16 μm.

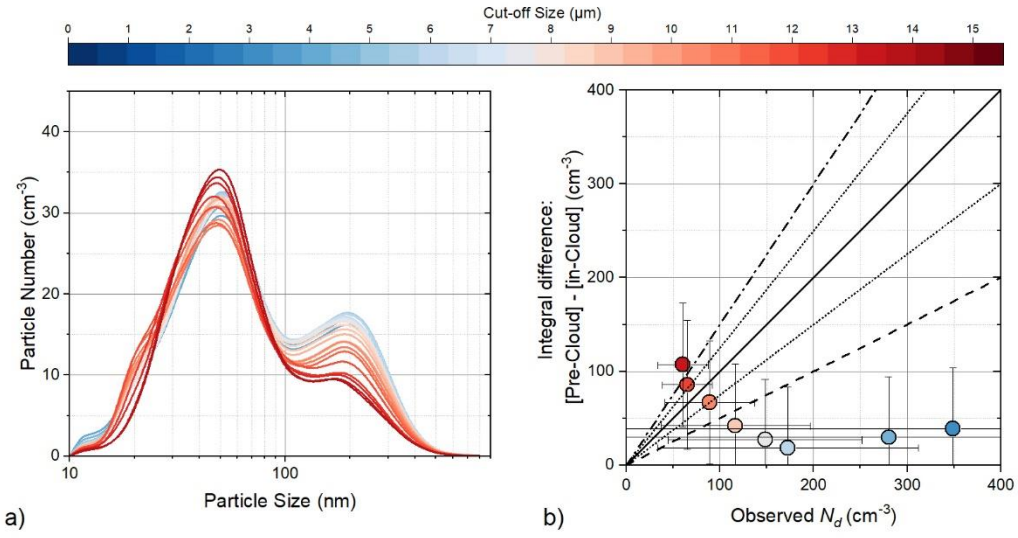

Figure 7.20. a) The results of the sensitivity analysis using differential cut-off size threshold and the droplet size threshold (D_{eff} as measured in situ with the PVM-100) applied are represented by the color-scale. b) The integrated difference between pre-cloud and in-cloud aerosol size distributions from ~70 nm to the largest sizes when compared to the droplet number measured in situ concurrently by the PVM-100. Each symbol corresponds to the application of a different D_{eff} threshold (as indicated by the symbol color, using the same scheme as in a), while the errorbars correspond to the standard deviation.

We select as the optimum D_{eff}, the minimum value above which the measured aerosol size distribution becomes insensitive to the chosen threshold value. Figure 7.20 displays an example of

this process applied to a segment of data from CALISHTO. We find in this case that a D_{eff} threshold of 13.5 μm is the minimum for which the observed size distribution stopped to be sensitive to the changes in the cut-off size (Figure 7.20a). Additionally, we compare the difference between the aerosol size distribution pre-cloud and the interstitial aerosol distribution (i.e., with the application of the 13.5 μm threshold) with the observed droplet number, and we found that indeed, the integrated difference between these distributions (from ~70 nm to the largest sizes measured by the SMPS) matches with the droplet number obtained *in situ* with the PVM-100 to within ±25% (Figure 7.20b). Thus, we confirm that this threshold is consistent with allowing only interstitial to pass through the inlet. Given that *in situ* closure studies often involve this degree of uncertainty (**Paper II** and relevant references cited therein), in addition to any other uncertainties that may exist at this particular site (e.g., variations of aerosol entering the cloud, sampling efficiency of the inlet and uncertainties in the droplet number determination with the PVM-100), we conclude that the latter distribution is indeed representative of the interstitial aerosol. Additional support for this conclusion is provided later by the ability to predict cloud droplet number as it requires the correct parameters of hygroscopicity, size distribution and vertical velocity.

7.4.4.3 Differences among the properties of total, activated, and interstitial aerosol

In this part of the study, we identified more than 20 periods of cloud-free/cloudy transitions during the CALISHTO campaign. We applied the methodology of Section 7.4.4.2 to estimate the corresponding cloud-free, interstitial-only, and mixed aerosol (cloud residues and interstitial combined) size distributions. We then determined *s** and *κ** of the cloud-free (κ_{cf}), interstitial (κ_i) and interstitial-droplet residues aerosol mixture (Figure 7.21a). Assuming that the pre-/post-cloud hygroscopicity is the volume average hygroscopicity of the interstitial and activated aerosol, we estimate the hygroscopicity of the activated aerosol, κ_a, using the mixing rules of Petters and Kreidenweis (2007) as $\kappa_a = \frac{\kappa_{cf} V_{cf} - \kappa_i V_i}{V_{cf} - V_i}$, where V_{cf} is the total volume of pre-/post-cloud aerosols and V_i is the total volume of interstitial aerosols, respectively. The estimation of κ_a assumes that all populations are internally mixed and the activated cloud aerosol plus the interstitial aerosol is equal to the pre-/post-cloud aerosol volume. This is a reasonable assumption given that Brownian losses affect the smallest particle sizes which have a minor contribution to the aerosol volume.

Figure 7.21 presents the results of our analysis. Figure 7.21a shows the characteristic supersaturation, s*, for each aerosol population. Typically, s* is higher for interstitial aerosol and lower for the mixed. This is consistent with the expectation that particles that activate to form droplets tend to be more hygroscopic than the interstitial aerosol (e.g., Cerully et al., 2011). Indeed, during periods where cloud formation is influenced by FTL airmasses, the average *κ** was 0.34 ± 0.09 % for pre-/post-cloud, 0.31 ± 0.15% for interstitial, and 0.45 ± 0.20% for activated aerosol. During periods that clouds were forming on PBL aerosol, the average *κ** was 0.43 ± 0.12% for pre-cloud, 0.29 ± 0.19% for interstitial and 0.44 ± 0.18% for activated aerosols (Figure 7.21b).

The average *s** (Figure 7.21c), during the periods where cloud formation is influenced by FTL airmasses, was found equal to 0.56 ± 0.21% and 0.59 ± 0.22%, while during PBL influenced periods, was found 0.27 ± 0.18% and 0.28 ± 0.16% for the pre-/post-cloud and interstitial aerosols,

respectively. These results showed little sensitivity to airmasses origins, i.e., FTL or PBL. Clearly, the interstitial aerosol is less hygroscopic on average, and the activated aerosol can be up to twice as hygroscopic. This is important for understanding the role of cloud processing on aging of particles and transferring hygroscopic material to evaporated cloud residuals.

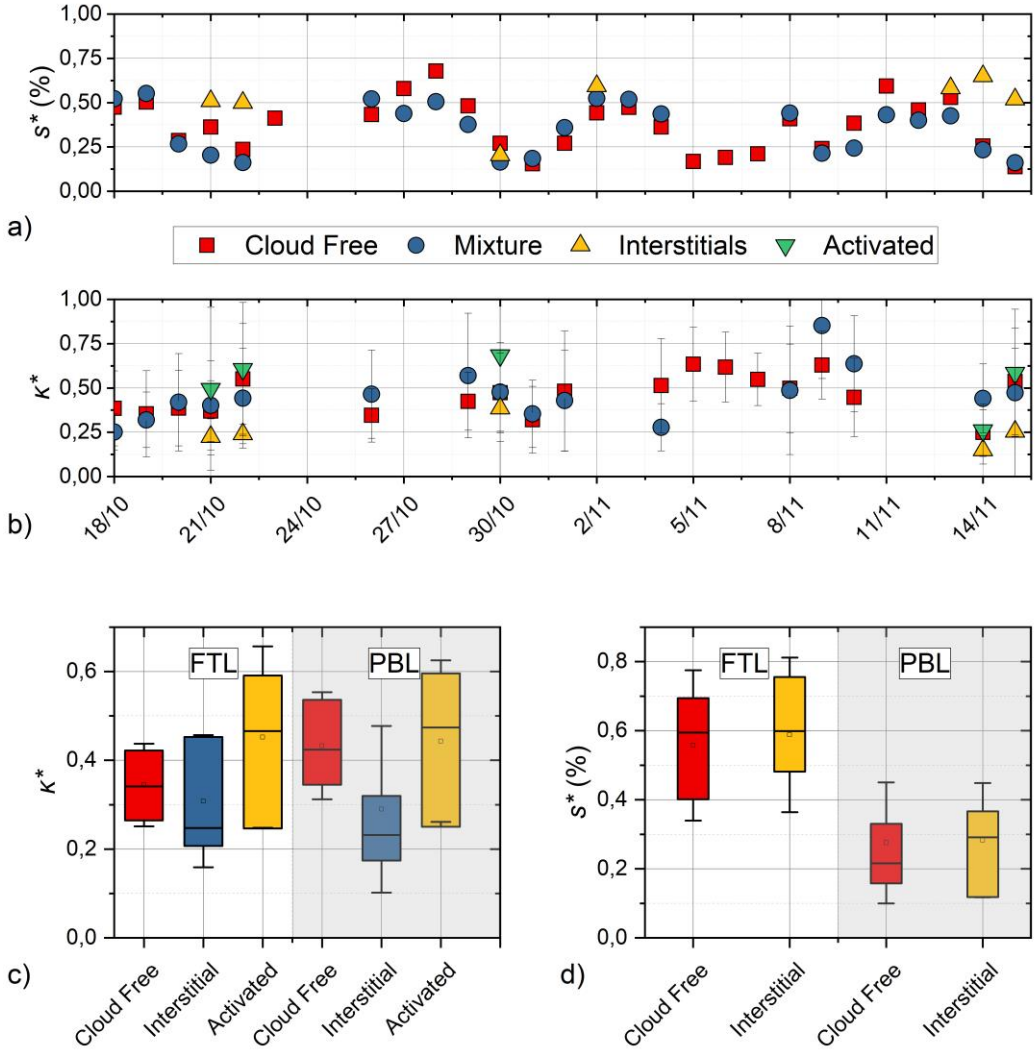

Figure 7.21. a) Daily averaged a) s and b) κ* of the aerosol in cloud free regimes, of the mixture of interstitial aerosols and some droplets residues, and of the activated aerosols; The c) and d) the distributions of κ* and s* when the airmass originating from the FTL or the PBL, respectively.*

Analysis of *s** of the activated aerosol can provide important insights about cloud formation when FTL or PBL airmasses are involved. The critical supersaturation of most of the activated cloud droplet residuals should be close to the maximum supersaturation in the cloud. Indeed, when cloud s_{max} is high, droplet formation is aerosol limited and vice versa when droplet formation is velocity limited. According to Georgakaki et al., (2021) and Motos et al., (2023), clouds are velocity-limited when the s_{max} is ~0.15% or lower, and aerosol-limited otherwise. Indeed, using *s** of the activated aerosol population as a proxy of s_{max} we see that clouds formed from FTL airmasses have *s** > 0.5%, hence the corresponding clouds are highly aerosol-sensitive. In contrast, clouds formed in PBL airmasses have a much lower *s**, reaching even 0.15% (Figure 7.21d) hence their formation tends to be velocity-sensitive. Given that the σ_w does not change significantly when clouds form upon FTL or

PBL airmasses (σ_w = 0.58 ± 0.25 m s^{-1}), and given that the N_{Total} in PBL airmasses was roughly three times higher than the N_{Total} in FTL airmasses (approximately 750cm^{-3} and 250cm^{-3}, respectively), much of this distinction between aerosol- and velocity-limited conditions is driven by variations in aerosol, rather than variations in cloud dynamics (i.e., σ_w).

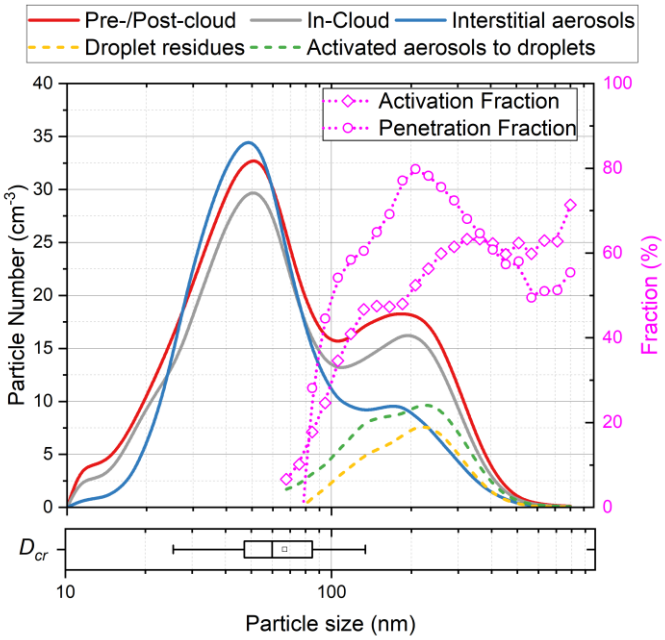

Figure 7.22. Averaged particle size distributions for pre-/post-cloud moments, in-cloud, and interstitial (using the D_{eff} threshold of 13.5 μm). Shown also are two estimations of the activated aerosol distribution, the droplet residues or "dried droplets" distribution (yellow dashed line), estimated from the difference between the measured in-cloud and the interstitial aerosols, and the "activated droplets" distribution (green line) estimated by the difference between the pre-cloud and the interstitial aerosol distribution, respectively. The latter gives an estimate of the aerosol that gives droplets that are too large to be sampled at any size threshold by the inlet, while the former provides the activated aerosol from droplets that are sampled by the inlet when in-cloud. The activation and the penetration fraction were estimated similarly by counting the ratio between the "activated droplets" and "pre-/post-cloud aerosols", and, "dried droplets" to "pre-/post-cloud aerosols", respectively.

Figure 7.22 shows that is measured on average during the cloud sampling through PM_{10} in respect of the aerosols and the droplet residues. The pre-/post-cloud and the in-cloud datasets here are the same that were used in Section 7.4.4.2 (the periods during were we sampled at least 30 minutes continuously in cloud-free conditions followed by (or proceeded by) at least 30 minutes of cloudy conditions) and the interstitial aerosols dataset derived after removing from the in-cloud dataset the data were the D_{eff} was exceeding the threshold of 13.5 μm. Thus, we calculated the average size distributions of the pre-/post- and the in-cloud phases as well as the interstitial aerosols. Then, the average size distribution of the activated droplets was derived by the difference between the cloud free and the interstitial size distribution, and the average size distribution of the droplet residuals by the difference between the in-cloud and the interstitial size distribution. At last, we calculated the size-resolved "activation fraction" as the ratio of the interstitial aerosols to the pre-/post cloud aerosols (from 70nm and above, given that smaller particles are not expected to activate), and the size-resolved "penetration fraction" as the ratio of droplet residues to the in-cloud aerosols. Hence, we found that when we are sampling within the clouds through a PM_{10} inlet, the penetration fraction on average can reach up to 80%. This means that comparison of pre-/post- and in-cloud aerosol distributions may provide qualitatively consistent microphysical insights that are however subject to an uncertainty of around 40%. In the end, we calculated the size distribution of the aerosols

that activated droplets by the difference between the in-cloud and the interstitial averaged size distributions, and the size-resolved activation fraction as the ratio of the activated aerosols to droplets against the pre-/post- aerosols. We found that the activation fraction is roughly 60% for most of the activated aerosol sizes (Figure 7.22), while about 50% of them constitute the droplet residues that penetrated the PM_{10} inlet.

7.4.4.4 Closure Study of N_d and s^*

In the last part of the study, we applied the droplet activation parameterization of Morales Betancourt and Nenes (2014), using the size distributions measured at the $(HAC)^2$ and the VL, and the σ_w and bulk hygroscopicity parameter κ measured at $(HAC)^2$, to predict the N_d and s^* of the clouds formed at $(HAC)^2$. It is important to mention here that the droplet activation parameterization of Morales Betancourt and Nenes (2014) is designed to calculate the s_{max} and the N_d when it is initialized by the ambient aerosols, and that's why we used the size distributions that was measured at VL. On the other hand, when the use of the in-cloud aerosol size distributions measured at $(HAC)^2$, given that this a combination both of interstitial aerosols and droplet residues, these distributions we have already shown in Section 7.4.4.3 that differ from each other, which result in underestimations on the N_d. Here we examine under which conditions the use of the in-cloud aerosol can give reliable results compared to the *in situ* observations of N_d and s^*, and to evaluate the internal consistency of the dataset and analysis carried out in the previous section, as well as to evaluate the ability of the parameterization to predict microphysical quantities for clouds influenced by the types of airmasses (FTL, PBL) considered.

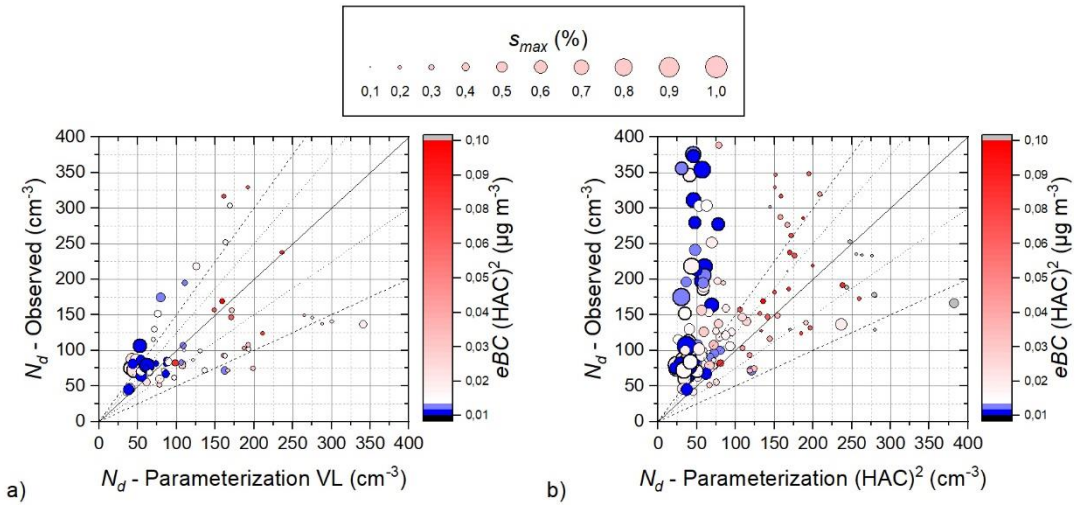

Figure 7.23. a-b) N_d from PVM-100 observations at the $(HAC)^2$ (vertical axis) against parameterization predictions (horizontal axis) using observed aerosol distributions from the VL and b) $(HAC)^2$, respectively. The symbol color corresponds to the eBC amount, and symbol size corresponds to the parameterization-predicted s_{max}. The dashed lines indicate regions of ±25 and ±50% deviation from the 1:1 line.

We found that we can obtain N_d closure to within ± 25%, when using the aerosol distributions from VL (Figure 7.23a) - even when the *eBC* levels are low. This may imply that VL may at times also reside in the FTL or at the catabatic region of the cloud during these specific periods, and hence its aerosol distributions may be representative of the total aerosol, including that which activated into cloud droplets. On the other hand, by using the aerosol from $(HAC)^2$ we obtained a reasonable closure only

where *eBC* is high and the s_{max} is low– in other words when $(HAC)^2$ cloud droplets were formed upon aerosol from the PBL. However, when aerosol at $(HAC)^2$ is influenced by the PBL (*eBC* is high, more than >0.01 μg m^{-3}), N_d is obtained within ± 25% (Figure 7.23b). That means that, when the in-cloud aerosol distributions from $(HAC)^2$ are used as input to the parameterization and clouds form in FTL airmasses (i.e., *eBC* is very low, less than <0.01 μg m^{-3}), the parameterization highly underestimates N_d (Figure 7.23b), because activated droplets were not sampled by the PM_{10} inlet. Concluding that the usage of the $(HAC)^2$ distributions lead to underprediction of droplet number (50% or more) especially when the measured *eBC* levels are low, consistent with the view that VL aerosol is less representative of FTL.

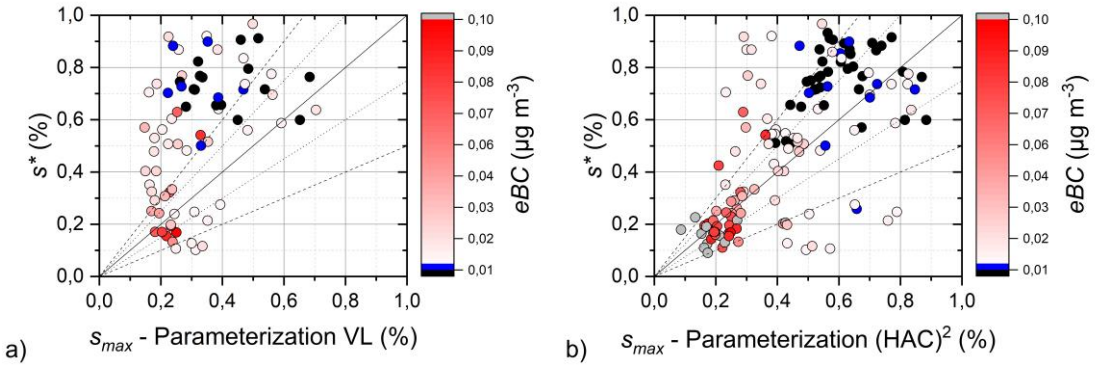

Figure 7.24. a) s of the total aerosol distribution (vertical axis) against parameterization predictions (horizontal axis) using observed aerosol distributions from the VL (a; left panel) and b) $(HAC)^2$, respectively. The symbol color corresponds to the eBC amount, while the dashed lines indicate regions of ±25 and ±50% deviation from the 1:1 line.*

Additionally, we found that when we used the aerosol from VL, *s** agree with s_{max} to within ±25% when *eBC* was high (~0.1 μg m^{-3}) (Figure 7.24a). When we used the aerosol from $(HAC)^2$ the *s** match with s_{max} to within ±25% most of the time (Figure 7.24b); this is because when in cloud, aerosol exposed at lower supersaturation values than the s_{max} have already been activated to droplets. Thus, the residuals give *s** values close to s_{max}.

When applying the parameterization to size distributions observed at VL, we expect that the predicted N_d (and s_{max}) will be close to observations when the cloud at $(HAC)^2$ is dominated by PBL aerosol and deviate largely when FTL airmasses are at the $(HAC)^2$. Similarly, $(HAC)^2$ pre-cloud aerosol distributions should provide good predictions of N_d when the airmass at the site is from the FTL. Use of in-cloud aerosol distributions is expected to result in deviations of the predicted from the observed N_d given that nucleation scavenging will lead to cloud droplets that are not sampled by the aerosol inlet, hence will not be measured. The magnitude of this deviation depends on the size of the droplets sampled, which in turn depends also on the amount of aerosol that is available for activation because cloud droplet sizes are expected to become progressively smaller as CCN concentrations increase.

7.4.5 Conclusions

We study the drivers of cloud droplet formation in orographic clouds using a combination of modeling, *in situ* and remote sensing measurements at the $(HAC)^2$ station during the CALISTHO. We study the origins of the aerosols, (e.g., local aerosol from the PBL, or long-range transport from the FTL) which can be used to understand their characteristics (hygroscopicity, size distribution and mixing state), contribution to CCN, N_d and resulting supersaturations.

We found that the N_{Total} and the *eBC* within the FTL get low values (~45 cm^{-3} and ~0.01 μg m^{-3}), while within the PBL they both get considerably larger values (~3300 cm^{-3} and ~0.4 μg m^{-3}). That means that the PBL has more CCN, which result to more (from ~100 cm^{-3} to ~300 cm^{-3}) and smaller droplets (from ~17.5 μm to ~10 μm).

We also study the aerosol characteristics of those that involved in cloud droplet formation, and those that do not activate (i.e., interstitial aerosols). To accomplish this, we develop a new algorithm applied to the aerosol timeseries measured with the PM_{10} single-inlet system, which can sample interstitial aerosol and droplets with sizes up to the inlet's cut-off size (thus the droplet residues get dried and mixed with the interstitial aerosols) when in cloud. This separation algorithm involves applying a "virtual filter" to the aerosol timeseries from the PM_{10} inlet based on a droplet size threshold (13.5 μm) derived from *in situ* observations (PVM-100) that determines when the aerosol sampled does not contain droplet residuals. Thus, when the in-situ average droplet size exceeds the threshold, droplets would be too large to pass through the inlet so that the aerosol sampled by the PM_{10} inlet is interstitial aerosol. Not considering this filter can considerably bias the results, as up to ~ 80% of aerosol can be dried droplet residuals.

By using this approach, we separated the dataset to pre-/post-cloud and interstitials regimes and we studied the characteristics of the pre-/post-cloud, interstitials as well as of the activated aerosols to droplets. Thus, we found that when the airmasses originated from the FTL, the κ^* was on average 0.34 ± 0.09 % for pre-/post-cloud, 0.31 ± 0.15% for interstitial, and 0.45 ± 0.20% for activated aerosol, while when the airmasses were originated from the PBL, the κ^* was on average 0.43 ± 0.12% for pre-cloud, 0.29 ± 0.19% for interstitial and 0.44 ± 0.18% for activated aerosols, respectively. That means that the interstitial aerosols are less hygroscopic on average, and the activated aerosols can be up to twice as hygroscopic. This is important for understanding the role of cloud processing on aging of particles and transferring hygroscopic material to evaporated cloud residuals.

Additionally, the average s^*, during the periods where cloud formation is influenced by FTL, was found equal to 0.56 ± 0.21% and 0.59 ± 0.22%, while during PBL influenced periods, was found 0.27 ± 0.18% and 0.28 ± 0.16% for the pre-/post-cloud and interstitial aerosols, respectively. These results showed little sensitivity to airmasses origins, i.e., FTL or PBL, but also that when a cloud is formed in FTL airmasses, the droplet formation in clouds is more sensitive to changes in the aerosol load, while when a cloud is formed in the PBL airmasses tends to be more sensitive in changes on the velocity. Given that the cloud dynamics do not vary significantly between airmasses, the variation in aerosol concentration is mostly responsible for these shifts in cloud microphysical state and sensitivity to aerosol.

Finally, a series of closure studies with the droplet parameterization is carried out to determine its ability to predict droplet number, supersaturation and constrain the cloud microphysical state (i.e., whether it is velocity- or aerosol-limited) and shows that the N_d can be predicted to be within 25% of observations when the aerosol size distributions best approximate the pre-cloud distributions. The high degree of droplet and supersaturation closure ensures that the model-data fusion and novel approaches for determining the aerosol populations (interstitial and activated cloud droplets) are consistent, provide a realistic assessment of cloud state and can be applied in future studies. In conclusion, we present a coordinated, innovative approach that allows the determination of the drivers of droplet formation in orographic clouds and their sensitivity to aerosol and vertical velocity variations.

8 THESIS CONCLUSIONS

This doctoral dissertation thesis aims to implement and further improve existing remote sensing approaches that are used for the retrieval of N_d in non-precipitating PBLC, as well as the Planetary Boundary Layer (PBL) dynamics, using a combination of *in situ* observations, ground-based remote sensing data and model data.

In **Paper I**, we expanded an established satellite droplet number retrieval algorithm (Grosvenor et al., 2018), by adding the explicit dependence on the spectral dispersion of droplets on the N_d. The revised algorithm illustrates the cloud microphysical variables derived by the METEOSAT (τ, r_{eff} and T_{ct}) and the assimilated ERA5 atmospheric pressure-temperature profiles (Hersbach et al., 2018) for a realistic approach to the total condensation rate (Zhu et al., 2018) concerning cloud top height. Then, we calculated the retrieved N_d^{sat} values by using the literature-based explicit relations of spectral dispersion of droplets to N_d^{sat}, and we evaluated them against the *in situ* N_d estimations obtained by a state-of-the-art droplet activation parameterization. We found that when using a constant value of β such as, Z06, GCMs, and F11, the droplet number is captured to on average ±16% and a bias of -34%. When using a linear relation between ε or β to N_d^{sat}, such as PL03, N_d^{sat} overestimates N_d by 13.2% ±34.8%. In the case of using more complex relation of β to N_d, such as of M94 or RL03, the bias of N_d^{sat} increases significantly. Additionally, we proposed a new β-N_d expression, based on the *in situ* N_d estimations, that minimize the bias of closure between N_d^{sat} and N_d (8.4% ±33.4%), which is comparable to the closure levels obtained from *in situ* observations. Although more work needs to be done to evaluate the extent to which our approach can be applied elsewhere in the globe, the results presented here are both encouraging and may suggest ways to develop high-value products for climate models that can take advantage of the rich ground-based aerosol datasets available to the community.

In **Paper II**, we investigated the local transport patterns at the DEM station of fresh and aged particles, as well as their diurnal variations and their relation to the boundary layer top height; using a wind Doppler lidar to measure the height of PBL (PBLH) and horizontal wind speed and direction, and *in situ* techniques to measure aerosol size distribution, and chemical composition during the period from March 15th to July 2nd, 2020, over the megacity Athens, Greece. We found that the aerosol particle concentration increases significantly in the *S-NW* sector due to traffic and vehicle emissions (6053 ± 3784 cm^{-3} and 171 ± 123 cm^{-3} in ultrafine and accumulation mode particles, respectively), as well as during windy conditions from the *N-NE* axis in case of ultrafine particles (5911 ± 3252 cm^{-3}); while when moderate wind flows from *NE-SE* axis are mostly related to regional background air masses from the Mesogea plain (2879 ± 1832 cm^{-3} and 204 ± 127 cm^{-3} for ultrafine and accumulation mode particles). Additionally, we captured katabatic flows, during nighttime, from Hymettus Mountain that occasionally transfer pollutants decoupled to higher layers, enhancing pollution episodes, or providing background clean air from higher altitudes, while during stagnant conditions this effect was found to be more intense (2931 ± 1770 cm^{-3} and 214 ± 152 cm^{-3} when wind speed > 4 m s^{-1}). Furthermore, we used a dynamic box approach to decouple the effect of PBLH on the concentrations of pollutants (i.e. $N_{10\text{-}200nm}$, $N_{200\text{-}500nm}$, and *eBC*), and our analysis reveals that the variation of PBL height has a quantitative effect on aerosol concentrations observed at the ground, and that's because any change in the aerosol concentration is partially related to changes in sources or sinks emissions, horizontal transport effects and the variance of the height of the PBL. However, the PBLH by itself, affects the ability of the aerosols to be transported horizontally since a deep PBL

conducts the advection with no significant surface effects, in contrast, the frictional drag effects close to the surface become important in a shallow PBL reducing the horizontal wind velocity and resulting in reduced the horizontal transport of aerosols.

In **Paper III**, we aimed to determine a reliable threshold which is used in a common-used method which uses wind Doppler lidars to obtain atmospheric turbulence profile and then to determine the PBLH at the height where the turbulence falls below this threshold value. To implement this study, we utilize *in situ* measurements provided by $(HAC)^2$ station, at Helmos Mountain, in Greece, and we obtain the atmospheric turbulence profile using a HALO lidar which was located at lower at the lee side of the mountain. Thus, we correlated the *in situ* observations of aerosol (e.g. *eBC*, bioaerosols, aerosol concentrations) and meteorological data (e.g. moisture) with the turbulence (σ_w) at the mountaintop and we identified three possible regimes of $(HAC)^2$ station: a) being within the PBL, characterized by increased aerosol concentrations and humid airmasses, b) being in the transition zone between PBL and FTL, and c) being within the FTL, characterized by low aerosol and bioaerosol concentrations and relatively dry airmasses. Concluding that a threshold value of σ_w = 0.1 m s^{-1} can be used to identify the PBLH at the $(HAC)^2$ site since this threshold shows good agreement with the covariances both of *in situ* measurements and the diurnal cycle of PBLH.

In **Paper IV**, we study the drivers of cloud droplet formation in orographic clouds using a combination of modeling, *in situ* and remote sensing measurements in respect to the origins of the aerosols, (e.g., local aerosol from the PBL, or from long-range transport from the FTL), to be used to understand their characteristics (hygroscopicity, size distribution and mixing state), contribution to CCN, N_d and resulting supersaturations.

We found that when the airmasses originated from the FTL, the κ^* was on average 0.34 ± 0.09 % for pre-/post-cloud, 0.31 ± 0.15% for interstitial, and 0.45 ± 0.20% for activated aerosol, while when the airmasses were originated from the PBL, the κ^* was on average 0.43 ± 0.12% for pre-cloud, 0.29 ± 0.19% for interstitial and 0.44 ± 0.18% for activated aerosols, respectively. That means that the interstitial aerosols are less hygroscopic on average, and the activated aerosols can be up to twice as hygroscopic. This is important for understanding the role of cloud processing on aging of particles and transferring hygroscopic material to evaporated cloud residuals.

Moreover, we found that the average s^*, during the periods where cloud formation is influenced by FTL, was found equal to 0.56 ± 0.21% and 0.59 ± 0.22%, while during PBL influenced periods, was found 0.27 ± 0.18% and 0.28 ± 0.16% for the pre-/post-cloud and interstitial aerosols, respectively. These results showed little sensitivity to airmasses origins, i.e., FTL or PBL, but also that when a cloud is formed in FTL airmasses, the droplet formation in clouds is more sensitive to changes in the aerosol load, while when a cloud is formed in the PBL airmasses tends to be more sensitive in changes on the velocity.

Given that the cloud dynamics do not vary significantly between airmasses, the variation in aerosol concentration are mostly responsible for these shifts in cloud microphysical state and sensitivity to aerosol.

Finally, we performed a series of closure studies with the droplet parameterization is carried out to determine its ability to predict droplet number, supersaturation and constrain the cloud microphysical state (i.e., whether it is velocity- or aerosol-limited) and shows that the N_d can be predicted to be within ± 25% of observations when the aerosol size distributions best approximate the pre-cloud distributions. The high degree of droplet and supersaturation closure ensures that the model-data fusion and novel approaches for determining the aerosol populations (interstitial and

activated cloud droplets) are consistent, provide a realistic assessment of cloud state and can be applied in future studies.

BIBLIOGRAPHY

Amanatidis, G.T., Papadopoulos, K.H., Bartzis, J.G., Helmis, C.G., 1992. EVIDENCE OF KATABATIC FLOWS DEDUCED FROM A 84 m METEOROLOGICAL TOWER IN ATHENS, GREECE.

Anderson, R.J., Miller, R.C., Kassner, J.L., Hagen, D.E., 1980. A Study of Homogeneous Condensation-Freezing Nucleation of Small Water Droplets in an Expansion Cloud Chamber. Journal of the Atmospheric Sciences 37, 2508–2520. https://doi.org/10.1175/1520-0469(1980)037<2508:ASOHCF>2.0.CO;2

Anderson, T. L., & Ogren, J. A., 1998. Deteriming aerosol radiative properties using the TSI 3563 Integrating Nephelometer. Aerosol Science and Technology, 29, 57–69.

Andrews, D.L., 2017. Rayleigh Scattering and Raman Effect, Theory, in: Encyclopedia of Spectroscopy and Spectrometry. Elsevier, pp. 924–930. https://doi.org/10.1016/B978-0-12-409547-2.11337-X

Ansmann, A., Tesche, M., Seifert, P., Althausen, D., Engelmann, R., Fruntke, J., Wandinger, U., Mattis, I., Müller, D., 2009. Evolution of the ice phase in tropical altocumulus: SAMUM lidar observations over Cape Verde. Journal of Geophysical Research: Atmospheres 114, 17208. https://doi.org/10.1029/2008JD011659

Atkinson, J.D., Murray, B.J., Woodhouse, M.T., Whale, T.F., Baustian, K.J., Carslaw, K.S., Dobbie, S., O'Sullivan, D., Malkin, T.L., 2013. The importance of feldspar for ice nucleation by mineral dust in mixed-phase clouds. Nature 2013 498:7454 498, 355–358. https://doi.org/10.1038/nature12278

Barahona, D., West, R.E.L., Stier, P., Romakkaniemi, S., Kokkola, H., Nenes, A., 2010. Comprehensively accounting for the effect of giant CCN in cloud activation parameterizations. Atmospheric Chemistry and Physics 10, 2467–2473. https://doi.org/10.5194/acp-10-2467-2010

Baray, J.-L., Deguillaume, L., Colomb, A., Sellegri, K., Freney, E., Rose, C., van Baelen, J., Pichon, J.-M., Picard, D., Fréville, P., Bouvier, L., Ribeiro, M., Amato, P., Banson, S., Bianco, A., Borbon, A., Bourcier, L., Bras, Y., Brigante, M., … Laj, P., 2020. Cézeaux-Aulnat-Opme-Puy De Dôme: a multi-site for the long-term survey of the tropospheric composition and climate change. Atmospheric Measurement Techniques, 13(6), 3413–3445. https://doi.org/10.5194/amt-13-3413-2020

Barlow, J.F., Dunbar, T.M., Nemitz, E.G., Wood, C.R., Gallagher, M.W., Davies, F., O'Connor, E., Harrison, R.M., 2011. Boundary layer dynamics over London, UK, as observed using Doppler lidar during REPARTEE-II. Atmospheric Chemistry and Physics 11, 2111–2125. https://doi.org/10.5194/acp-11-2111-2011

Beddows, D.C.S., Dall'Osto, M., Harrison, R.M., 2009. Cluster analysis of rural, urban, and curbside atmospheric particle size data. Environmental Science & Technology 43, 4694–4700. https://doi.org/10.1021/ES803121T/SUPPL_FILE/ES803121T_SI_001.PDF

Beddows, D.C.S., Donovan, R.J., Harrison, R.M., Heal, M.R., Kinnersley, R.P., King, M.D., Nicholson, D.H., Thompson, K.C., 2004. Correlations in the chemical composition of rural background atmospheric aerosol in the UK determined in real time using time-of-flight mass spectrometry. Journal of Environmental Monitoring 6, 124–133. https://doi.org/10.1039/B311209H

Bell, M.L., Ebisu, K., Peng, R.D., Samet, J.M., Dominici, F., 2009. Hospital admissions and chemical composition of fine particle air pollution. American Journal of Respiratory and Critical Care Medicine179, 1115–1120. https://doi.org/10.1164/RCCM.200808-1240OC

Benas, N., Meirink, J.F., Stengel, M., Stammes, P., 2019. Sensitivity of liquid cloud optical thickness and effective radius retrievals to cloud bow and glory conditions using two SEVIRI imagers. Atmospheric Measurement Techniques 12, 2863–2879. https://doi.org/10.5194/amt-12-2863-2019

Bennartz, R., 2007. Global assessment of marine boundary layer cloud droplet number concentration from satellite. Journal of Geophysical Research 112, D02201. https://doi.org/10.1029/2006JD007547

Bennartz, R., Rausch, J., 2017. Global and regional estimates of warm cloud droplet number concentration based on 13 years of AQUA-MODIS observations. Atmospheric Chemistry and Physics 17, 9815–9836. https://doi.org/10.5194/ACP-17-9815-2017

Biskos, G., Buseck, P.R., Martin, S.T., 2009. Hygroscopic growth of nucleation-mode acidic sulfate particles. Journal of Aerosol Science 40, 338–347. https://doi.org/10.1016/j.jaerosci.2008.12.003

Bond, T.C., Doherty, S.J., Fahey, D.W., Forster, P.M., Berntsen, T., DeAngelo, B.J., Flanner, M.G., Ghan, S., Kärcher, B., Koch, D., Kinne, S., Kondo, Y., Quinn, P.K., Sarofim, M.C., Schultz, M.G., Schulz, M., Venkataraman, C., Zhang, H., Zhang, S., Bellouin, N., Guttikunda, S.K., Hopke, P.K., Jacobson, M.Z., Kaiser, J.W., Klimont, Z., Lohmann, U., Schwarz, J.P., Shindell, D., Storelvmo, T., Warren, S.G., Zender, C.S., 2013. Bounding the role of black carbon in the climate system: A scientific assessment. Journal of Geophysical Research: Atmospheres 118, 5380–5552. https://doi.org/10.1002/jgrd.50171

Boucher, O., Randall, D., Artaxo, P., Bretherton, C., Feingold, G., Forster, P., Kerminen, V.-M., Kondo, Y., Liao, H., Lohmann, U., Rasch, P., Satheesh, S.K., Sherwood, S., Stevens, B., Zhang, X.Y., 2013. Clouds and Aerosols, in: Intergovernmental Panel on Climate Change (Ed.), Climate Change 2013 - The Physical Science Basis. Cambridge University Press, Cambridge, pp. 571–658. https://doi.org/10.1017/CBO9781107415324.016

Bougiatioti, A., Nenes, A., Lin, J.J., Brock, C.A., De Gouw, J.A., Liao, J., Middlebrook, A.M., Welti, A., 2020. Drivers of cloud droplet number variability in the summertime in the southeastern United States. Atmospheric Chemistry and Physics 20, 12163–12176. https://doi.org/10.5194/acp-20-12163-2020

Bougiatioti, A., Stavroulas, I., Kostenidou, E., Zarmpas, P., Theodosi, C., Kouvarakis, G., Canonaco, F., Prévôt, A.S.H., Nenes, A., Pandis, S.N., Mihalopoulos, N., 2014. Processing of biomass-burning aerosol in the eastern Mediterranean during summertime. Atmospheric Chemistry and Physics 14, 4793–4807. https://doi.org/10.5194/ACP-14-4793-2014

Bousiotis, D., Brean, J., Pope, F.D., Dall'Osto, M., Querol, X., Alastuey, A., Perez, N., Petäjä, T., Massling, A., Nøjgaard, J.K., Nordstrøm, C., Kouvarakis, G., Vratolis, S., Eleftheriadis, K., Niemi, J. V., Portin, H., Wiedensohler, A., Weinhold, K., Merkel, M., Tuch, T., Harrison, R.M., 2021. The effect of meteorological conditions and atmospheric composition in the occurrence and development of new particle formation (NPF) events in Europe. Atmospheric Chemistry and Physics 21, 3345–3370. https://doi.org/10.5194/acp-21-3345-2021

Brenguier, J.-L., Pawlowska, H., Schüller, L., Preusker, R., Fischer, J., Fouquart, Y., 2000. Radiative Properties of Boundary Layer Clouds: Droplet Effective Radius versus Number Concentration. Journal of the Atmospheric Sciences 57, 803–821. https://doi.org/10.1175/1520-0469(2000)057<0803:RPOBLC>2.0.CO;2

Brook, R.D., Rajagopalan, S., Pope, C.A., Brook, J.R., Bhatnagar, A., Diez-Roux, A. V., Holguin, F., Hong, Y., Luepker, R. V., Mittleman, M.A., Peters, A., Siscovick, D., Smith, S.C., Whitsel, L., Kaufman, J.D., 2010. Particulate matter air pollution and cardiovascular disease: An update to the scientific statement

from the american heart association. Circulation 121, 2331–2378. https://doi.org/10.1161/CIR.0B013E3181DBECE1

Browning, K.A., Wexler, R., 1968. The Determination of Kinematic Properties of a Wind Field Using Doppler Radar. Journal of Applied Meteorology 7, 105–113. https://doi.org/10.1175/1520-0450(1968)007<0105:TDOKPO>2.0.CO;2

Budisulistiorini, S.H., Canagaratna, M.R., Croteau, P.L., Baumann, K., Edgerton, E.S., Kollman, M.S., Ng, N.L., Verma, V., Shaw, S.L., Knipping, E.M., Worsnop, D.R., Jayne, J.T., Weber, R.J., Surratt, J.D., 2014. Intercomparison of an Aerosol Chemical Speciation Monitor (ACSM) with ambient fine aerosol measurements in downtown Atlanta, Georgia. Atmospheric Measurement Techniques 7, 1929–1941. https://doi.org/10.5194/amt-7-1929-2014

Cabada, J.C., Khlystov, A., Wittig, A.E., Pilinis, C., Pandis, S.N., 2004. Light scattering by fine particles during the Pittsburgh Air Quality Study: Measurements and modeling. Journal of Geophysical Research: Atmospheres 109, 16–19. https://doi.org/10.1029/2003JD004155

Calvin, K., Dasgupta, D., Krinner, G., Mukherji, A., Thorne, P.W., Trisos, C., Romero, J., Aldunce, P., Barrett, K., Blanco, G., Cheung, W.W.L., Connors, S., Denton, F., Diongue-Niang, A., Dodman, D., Garschagen, M., Geden, O., Hayward, B., Jones, C., Jotzo, F., Krug, T., Lasco, R., Lee, Y.-Y., Masson-Delmotte, V., Meinshausen, M., Mintenbeck, K., Mokssit, A., Otto, F.E.L., Pathak, M., Pirani, A., Poloczanska, E., Pörtner, H.-O., Revi, A., Roberts, D.C., Roy, J., Ruane, A.C., Skea, J., Shukla, P.R., Slade, R., Slangen, A., Sokona, Y., Sörensson, A.A., Tignor, M., van Vuuren, D., Wei, Y.-M., Winkler, H., Zhai, P., Zommers, Z., Hourcade, J.-C., Johnson, F.X., Pachauri, S., Simpson, N.P., Singh, C., Thomas, A., Totin, E., Alegría, A., Armour, K., Bednar-Friedl, B., Blok, K., Cissé, G., Dentener, F., Eriksen, S., Fischer, E., Garner, G., Guivarch, C., Haasnoot, M., Hansen, G., Hauser, M., Hawkins, E., Hermans, T., Kopp, R., Leprince-Ringuet, N., Lewis, J., Ley, D., Ludden, C., Niamir, L., Nicholls, Z., Some, S., Szopa, S., Trewin, B., van der Wijst, K.-I., Winter, G., Witting, M., Birt, A., Ha, M., 2023. IPCC, 2023: Climate Change 2023: Synthesis Report. Contribution of Working Groups I, II and III to the Sixth Assessment Report of the Intergovernmental Panel on Climate Change [Core Writing Team, H. Lee and J. Romero (eds.)]. IPCC, Geneva, Switzerland. https://doi.org/10.59327/IPCC/AR6-9789291691647

Carslaw, D.C., Beevers, S.D., 2013. Characterising and understanding emission sources using bivariate polar plots and k-means clustering. Environmental Modeling and Software 40, 325–329. https://doi.org/10.1016/J.ENVSOFT.2012.09.005

Carslaw, D.C., Beevers, S.D., Ropkins, K., Bell, M.C., 2006. Detecting and quantifying aircraft and other on-airport contributions to ambient nitrogen oxides in the vicinity of a large international airport. Atmospheric Environment 40, 5424–5434. https://doi.org/10.1016/J.ATMOSENV.2006.04.062

Caya, D., Zawadzki, I., 1992. VAD Analysis of Nonlinear Wind Fields. Journal of Atmospheric and Oceanic Technology 9, 575–587. https://doi.org/10.1175/1520-0426(1992)009<0575:VAONWF>2.0.CO;2

Chanin, M.-L., Hauchecorne, A., 1981. Lidar observation of gravity and tidal waves in the stratosphere and mesosphere. Journal of Geophysical Research Oceans 86, 9715–9721. https://doi.org/10.1029/JC086IC10P09715

Charlson, R.J., Langner, J., Rodhe, H., Leovy, C.B., Warren, S.G., 2016. Perturbation of the northern hemisphere radiative balance by backscattering from anthropogenic sulfate aerosols*. New pub: Stockholm uni Press 43, 152–163. https://doi.org/10.3402/TELLUSA.V43I4.11944

Chen, J., Liu, Y., Zhang, M., Peng, Y., 2018. Height Dependency of Aerosol-Cloud Interaction Regimes. Journal of Geophysical Research: Atmospheres 123, 491–506. https://doi.org/10.1002/2017JD027431

Chen, J., Liu, Y., Zhang, M., Peng, Y., 2016. New understanding and quantification of the regime dependence of aerosol-cloud interaction for studying aerosol indirect effects. Geophysical Research Letters 43, 1780–1787. https://doi.org/10.1002/2016GL067683

Collaud Coen, M., Andrews, E., Alastuey, A., Petkov Arsov, T., Backman, J., Brem, B.T., Bukowiecki, N., Couret, C., Eleftheriadis, K., Flentje, H., Fiebig, M., Gysel-Beer, M., Hand, J.L., Hoffer, A., Hooda, R., Hueglin, C., Joubert, W., Keywood, M., Eun Kim, J., Kim, S.-W., Labuschagne, C., Lin, N.-H., Lin, Y., Lund Myhre, C., Luoma, K., Lyamani, H., Marinoni, A., Mayol-Bracero, O.L., Mihalopoulos, N., Pandolfi, M., Prats, N., Prenni, A.J., Putaud, J.-P., Ries, L., Reisen, F., Sellegri, K., Sharma, S., Sheridan, P., Patrick Sherman, J., Sun, J., Titos, G., Torres, E., Tuch, T., Weller, R., Wiedensohler, A., Zieger, P., Laj, P., Piedras Campus, R., Juan, S., Rico, P., 2020. Multidecadal trend analysis of aerosol radiative properties at a global scale. https://doi.org/10.5194/acp-2019-1174

Collaud Coen, M., Andrews, E., Aliaga, D., Andrade, M., Angelov, H., Bukowiecki, N., Ealo, M., Fialho, P., Flentje, H., Hallar, A.G., Hooda, R., Kalapov, I., Krejci, R., Lin, N.-H., Marinoni, A., Ming, J., Nguyen, N.A., Pandolfi, M., Pont, V., Ries, L., Rodríguez, S., Schauer, G., Sellegri, K., Sharma, S., Sun, J., Tunved, P., Velasquez, P., Ruffieux, D., 2018. Identification of topographic features influencing aerosol observations at high altitude stations. Atmospheric Chemistry and Physics 18, 12289–12313. https://doi.org/10.5194/acp-18-12289-2018

Cuesta-Mosquera, A., Močnik, G., Drinovec, L., Müller, T., Pfeifer, S., Minguillón, M. C., Briel, B., Buckley, P., Dudoitis, V., Fernández-García, J., Fernández-Amado, M., Ferreira De Brito, J., Riffault, V., Flentje, H., Heffernan, E., Kalivitis, N., Kalogridis, A.-C., Keernik, H., Marmureanu, L., … Wiedensohler, A., 2021. Intercomparison and characterization of 23 Aethalometers under laboratory and ambient air conditions: procedures and unit-to-unit variabilities. Atmospheric Measurement Techniques, 14(4), 3195–3216. https://doi.org/10.5194/amt-14-3195-2021

Cronin, T.W., Tziperman, E., 2015. Low clouds suppress Arctic air formation and amplify high-latitude continental winter warming. Proceedings of the National Academy of Sciences USA 112, 11490–11495. https://doi.org/10.1073/PNAS.1510937112/SUPPL_FILE/PNAS.201510937SI.PDF

Demott, P.J., Sassen, Kenneth, Poellot, Michael R, Baumgardner, Darrel, Rogers, David C, Brooks, Sarah D, Prenni, Anthony J, Kreidenweis, Sonia M, Sassen, K, Poellot, M R, Baumgardner, D, Rogers, D C, Brooks, S D, Prenni, A J, Kreidenweis, S M, 2003. African dust aerosols as atmospheric ice nuclei. Geophysical Research Letters 30, 1732. https://doi.org/10.1029/2003GL017410

Diapouli, E., Kalogridis, A.C., Markantonaki, C., Vratolis, S., Fetfatzis, P., Colombi, C., Eleftheriadis, K., 2017a. Annual Variability of Black Carbon Concentrations Originating from Biomass and Fossil Fuel Combustion for the Suburban Aerosol in Athens, Greece. Atmosphere 2017, Vol. 8, Page 234 8, 234. https://doi.org/10.3390/ATMOS8120234

Diapouli, E., Manousakas, M.I., Vratolis, S., Vasilatou, V., Pateraki, S., Bairachtari, K.A., Querol, X., Amato, F., Alastuey, A., Karanasiou, A.A., Lucarelli, F., Nava, S., Calzolai, G., Gianelle, V.L., Colombi, C., Alves, C., Custódio, D., Pio, C., Spyrou, C., Kallos, G.B., Eleftheriadis, K., 2017b. AIRUSE-LIFE +: Estimation of natural source contributions to urban ambient air PM10 and PM2.5 concentrations in southern

Europe - Implications to compliance with limit values. Atmospheric Chemistry and Physics 17, 3673–3685. https://doi.org/10.5194/acp-17-3673-2017

Diapouli, E., Popovicheva, O., Kistler, M., Vratolis, S., Persiantseva, N., Timofeev, M., Kasper-Giebl, A., Eleftheriadis, K., 2014. Physicochemical characterization of aged biomass burning aerosol after long-range transport to Greece from large scale wildfires in Russia and surrounding regions, Summer 2010. Atmospheric Environment 96, 393–404. https://doi.org/10.1016/j.atmosenv.2014.07.055

Dockery, D.W., Pope, C.A., 1994. Acute respiratory effects of particulate air pollution. Annual Review of Public Health 15, 107–132. https://doi.org/10.1146/ANNUREV.PU.15.050194.000543

Drinovec, L., Močnik, G., Zotter, P., Prévôt, A. S. H., Ruckstuhl, C., Coz, E., Rupakheti, M., Sciare, J., Müller, T., Wiedensohler, A., & Hansen, A. D. A., 2015. The "dual-spot" Aethalometer: an improved measurement of aerosol black carbon with real-time loading compensation. Atmospheric Measurement Techniques, 8(5), 1965–1979. https://doi.org/10.5194/amt-8-1965-2015

Dubovik, O., King, M.D., 2000. A flexible inversion algorithm for retrieval of aerosol optical properties from Sun and sky radiance measurements. Journal of Geophysical Research: Atmospheres 105, 20673–20696. https://doi.org/10.1029/2000JD900282

Duc, H.N., Rahman, M.M., Trieu, T., Azzi, M., Riley, M., Koh, T., Liu, S., Bandara, K., Krishnan, V., Yang, Y., Silver, J., Kirley, M., White, S., Capnerhurst, J., Kirkwood, J., 2022. Study of Planetary Boundary Layer, Air Pollution, Air Quality Models and Aerosol Transport Using Ceilometers in New South Wales (NSW), Australia. Atmosphere (Basel) 13, 176. https://doi.org/10.3390/atmos13020176

Duplissy, J., DeCarlo, P.F., Dommen, J., Alfarra, M.R., Metzger, A., Barmpadimos, I., Prevot, A.S.H., Weingartner, E., Tritscher, T., Gysel, M., Aiken, A.C., Jimenez, J.L., Canagaratna, M.R., Worsnop, D.R., Collins, D.R., Tomlinson, J., Baltensperger, U., 2011. Relating hygroscopicity and composition of organic aerosol particulate matter. Atmospheric Chemistry and Physics 11, 1155–1165. https://doi.org/10.5194/acp-11-1155-2011

Eleftheriadis, K., Colbeck, I., Housiadas, C., Lazaridis, M., Mihalopoulos, N., Mitsakou, C., Smolík, J., Ždímal, V., 2006. Size distribution, composition and origin of the submicron aerosol in the marine boundary layer during the eastern Mediterranean "SUB-AERO" experiment. Atmospheric Environment 40, 6245–6260. https://doi.org/10.1016/J.ATMOSENV.2006.03.059

Eleftheriadis, K., Gini, M.I., Diapouli, E., Vratolis, S., Vasilatou, V., Fetfatzis, P., Manousakas, M.I., 2021. Aerosol microphysics and chemistry reveal the COVID19 lockdown impact on urban air quality. Scientific Reports 2021 11:1 11, 1–11. https://doi.org/10.1038/s41598-021-93650-6

Eleftheriadis, K., Ochsenkuhn, K.M., Lymperopoulou, T., Karanasiou, A., Razos, P., Ochsenkuhn-Petropoulou, M., 2014. Influence of local and regional sources on the observed spatial and temporal variability of size resolved atmospheric aerosol mass concentrations and water-soluble species in the Athens metropolitan area. Atmospheric Environment 97, 252–261. https://doi.org/10.1016/J.ATMOSENV.2014.08.013

EUMETSAT, 2015. Optimal Cloud Analysis Product Guide [WWW Document]. URL www.eumetsat.int

Farah, A., Freney, E., Chauvigné, A., Baray, J.L., Rose, C., Picard, D., Colomb, A., Hadad, D., Abboud, M., Farah, W., Sellegri, K., 2018. Seasonal Variation of Aerosol Size Distribution Data at the Puy de Dôme Station with Emphasis on the Boundary Layer/Free Troposphere Segregation. Atmosphere 2018, Vol. 9, Page 244 9, 244. https://doi.org/10.3390/ATMOS9070244

Feingold, G., Remer, L.A., Ramaprasad, J., Kaufman, Y.J., 2001. Analysis of smoke impact on clouds in Brazilian biomass burning regions: An extension of Twomey's approach. Journal of Geophysical Research: Atmospheres 106, 22907–22922. https://doi.org/10.1029/2001JD000732

Flocas, H.A., Helmis, C.G., Blikas, S.N., Asimakopoulos, D.N., Bartzis, J.G., Deligiorgi, D.G., 1998. Mean Characteristics of the Katabatic Flow of a 1024 m High Knife Edge Mountain. Theoretical and Applied Climatology 1998 59:3 59, 237–249. https://doi.org/10.1007/S007040050027

Foskinis, R., Nenes, A., Papayannis, A., Georgakaki, P., Eleftheriadis, K., Vratolis, S., Gini, M.I., Komppula, M., Vakkari, V., Kokkalis, P., 2022. Towards reliable retrievals of cloud droplet number for non-precipitating planetary boundary layer clouds and their susceptibility to aerosol. Frontiers in Remote Sensing 3. https://doi.org/10.3389/frsen.2022.958207

Foskinis, R., Gini, M., Kokkalis, P., Diapouli, E., Vratolis, S., Granakis, K., Zografou, O., Komppula, M., Vakkari, V., Nenes, A., Papayannis, A., Eleftheriadis, K., 2023. On the Relation between the Planetary Boundary Layer Height and in Situ Surface Observations of Atmospheric Aerosol Pollutants in Athens, Greece (Under Review). Under Review. https://doi.org/10.2139/SSRN.4536471

Fouladinejad, F., Matkan, A., Hajeb, M., and Brakhasi, F. 2019: HISTORY AND APPLICATIONS OF SPACE-BORNE LIDARS, Int. Arch. Photogramm. Remote Sens. Spatial Inf. Sci., XLII-4/W18, 407–414, https://doi.org/10.5194/isprs-archives-XLII-4-W18-407-2019.

Fountoukis, C., Nenes, A., 2007. ISORROPIA II: a computationally efficient thermodynamic equilibrium model for K+–Ca2+–Mg2+–NH4+–Na+–SO42−–NO3−–Cl−–H2O aerosols. Atmospheric Chemistry and Physics 7, 4639–4659. https://doi.org/10.5194/acp-7-4639-2007

Fountoukis, C., Nenes, A., 2005. Continued development of a cloud droplet formation parameterization for global climate models. Journal of Geophysical Research: Atmospheres 110. https://doi.org/https://doi.org/10.1029/2004JD005591

Fraczek, M., Behrendt, A., Schmitt, N., 2012. Laser-based air data system for aircraft control using Raman and elastic backscatter for the measurement of temperature, density, pressure, moisture, and particle backscatter coefficient. Appl Opt 51, 148. https://doi.org/10.1364/AO.51.000148

Freud, E., Rosenfeld, D., 2012. Linear relation between convective cloud droplet number concentration and depth for rain initiation. Journal of Geophysical Research: Atmospheres 117. https://doi.org/10.1029/2011JD016457

Fröhlich, R., Cubison, M.J., Slowik, J.G., Bukowiecki, N., Prévôt, A.S.H., Baltensperger, U., Schneider, J., Kimmel, J.R., Gonin, M., Rohner, U., Worsnop, D.R., Jayne, J.T., 2013. The ToF-ACSM: a portable aerosol chemical speciation monitor with TOFMS detection. Atmospheric Measurement Techniques 6, 3225–3241. https://doi.org/10.5194/amt-6-3225-2013

Fu, W.Q., 2006. Radiative Transfer, in: Atmospheric Science. Elsevier, pp. 113–152. https://doi.org/10.1016/B978-0-12-732951-2.50009-0

Georgakaki, P., Bougiatioti, A., Wieder, J., Mignani, C., Ramelli, F., Kanji, Z.A., Henneberger, J., Hervo, M., Berne, A., Lohmann, U., Nenes, A., 2021. On the drivers of droplet variability in alpine mixed-phase clouds. Atmospheric Chemistry and Physics 21, 10993–11012. https://doi.org/10.5194/acp-21-10993-2021

Ghan, S.J., Guzman, G., Abdul-Razzak, H., 1998. Competition between Sea Salt and Sulfate Particles as Cloud Condensation Nuclei. Journal of the Atmospheric Sciences 55, 3340–3347. https://doi.org/10.1175/1520-0469(1998)055<3340:CBSSAS>2.0.CO;2

Gini, M., Manousakas, M., Karydas, A.G., Eleftheriadis, K., 2022. Mass size distributions, composition and dose estimates of particulate matter in Saharan dust outbreaks. Environmental Pollution 298. https://doi.org/10.1016/J.ENVPOL.2021.118768

Grosvenor, D. P., Sourdeval, O., Zuidema, P., Ackerman, A., Alexandrov, M. D., Bennartz, R., Boers, R., Cairns, B., Chiu, J. C., Christensen, M., Deneke, H., Diamond, M., Feingold, G., Fridlind, A., Hünerbein, A., Knist, C., Kollias, P., Marshak, A., McCoy, D., … Quaas, J., 2018. Remote Sensing of Droplet Number Concentration in Warm Clouds: A Review of the Current State of Knowledge and Perspectives. Reviews of Geophysics, 56(2), 409–453. https://doi.org/10.1029/2017RG000593

Gysel, M., Crosier, J., Topping, D. O., Whitehead, J. D., Bower, K. N., Cubison, M. J., Williams, P. I., Flynn, M. J., McFiggans, G. B., & Coe, H., 2007. Closure study between chemical composition and hygroscopic growth of aerosol particles during TORCH2. Atmospheric Chemistry and Physics, *7*(24), 6131–6144. https://doi.org/10.5194/acp-7-6131-2007

Hamill, P., Giordano, M., Ward, C., Giles, D., Holben, B., 2016. An AERONET-based aerosol classification using the Mahalanobis distance. Atmospheric Environment 140, 213–233. https://doi.org/10.1016/j.atmosenv.2016.06.002

Hanna, S.R., Briggs, G.A., Hosker, R.P.Jr., 1982. Handbook on atmospheric diffusion. https://doi.org/10.2172/5591108

Hansen, A.D.A., Rosen, H., Novakov, T., 1982. Real-time measurement of the absorption coefficient of aerosol particles. Applied Optics, Vol. 21, Issue 17, pp. 3060-3062 21, 3060–3062. https://doi.org/10.1364/AO.21.003060

Hansen, J., Nazarenko, L., Ruedy, R., Sato, M., Willis, J., Del Genio, A., Koch, D., Lacis, A., Lo, K., Menon, S., Novakov, T., Perlwitz, J., Russell, G., Schmidt, G.A., Tausnev, N., 2005. Climate Change: Earth's energy imbalance: Confirmation and implications. Science (1979) 308, 1431–1435. https://doi.org/10.1126/SCIENCE.1110252/SUPPL_FILE/PAPV2.PDF

Hansen, J.E., 1971. Multiple Scattering of Polarized Light in Planetary Atmospheres Part II. Sunlight Reflected by Terrestrial Water Clouds. Journal of the Atmospheric Sciences 28, 1400–1426. https://doi.org/10.1175/1520-0469(1971)028<1400:MSOPLI>2.0.CO;2

Hartmann, D.L., Ockert-Bell, M.E., Michelsen, M.L., 1992. The Effect of Cloud Type on Earth's Energy Balance: Global Analysis. Journal of Climate 5, 1281–1304. https://doi.org/10.1175/1520-0442(1992)005<1281:TEOCTO>2.0.CO;2

Haywood, J., 2021. Atmospheric aerosols and their role in climate change. Climate Change: Observed Impacts on Planet Earth, Third Edition 645–659. https://doi.org/10.1016/B978-0-12-821575-3.00030-X

Henderson, S.W., Gatt, P., Rees, D., Huffaker, R.M., 2005. Wind Lidar, in Laser Remote Sensing, Eds. Fujii and Fukuchi, CRC Press, Taylor and Francis Group, Boca Raton, FL 469–722.

Hersbach, H., Bell, B., Berrisford, P., Biavati, G., Horányi, A., Sabater Muñoz, J., Nicolas, J., Peubey, C., Radu, R., Rozum, I., Schepers, D., Simmons, A., Soci, C., Dee, D., Thépaut, J.-N., 2018. ERA5 hourly data on

pressure levels from 1979 to present. Copernicus Climate Change Service (C3S) Climate Data Store (CDS). (Accessed on 01-Jan-2021). https://doi.org/10.24381/cds.bd0915c6

Hinds, W.C., 1999. Aerosol Technology Properties, Behavior, and Measurement of Airborne Particles Second Edition.

Hulst, H.C. van de, 1958. Light scattering by small particles. By H. C. van de Hulst. New York (John Wiley and Sons), London (Chapman and Hall), 1957. Pp. xiii, 470; 103 Figs.; 46 Tables. 96s. Quarterly Journal of the Royal Meteorological Society 84, 198–199. https://doi.org/10.1002/qj.49708436025

Illingworth, A.J., Cimini, D., Haefele, A., Haeffelin, M., Hervo, M., Kotthaus, S., Löhnert, U., Martinet, P., Mattis, I., O'Connor, E.J., Potthast, R., 2019. How Can Existing Ground-Based Profiling Instruments Improve European Weather Forecasts? Bulletin of the American Meteorological Society 100, 605–619. https://doi.org/10.1175/BAMS-D-17-0231.1

Intrieri, J.M., Fairall, C.W., Shupe, M.D., Persson, P.O.G., Andreas, E.L., Guest, P.S., Moritz, R.E., 2002. An annual cycle of Arctic surface cloud forcing at SHEBA. Journal of Geophysical Research Oceans 107. https://doi.org/10.1029/2000JC000439

IPCC, 2007a. Summary for Policymakers. In: Climate Change 2007: The Physical Science Basis. Contribution of Working Group I to the Fourth Assessment Report of the Intergovernmental Panel on Climate Change [Solomon, S., D. Qin, M. Manning, Z. Chen, M. Marquis, K.B. Averyt, M.Tignor and H.L. Miller (eds.)]. Cambridge University Press, Cambridge, United Kingdom and New York, NY, USA.

IPCC, 2007b. AR4 Climate Change 2007: Synthesis Report — IPCC.

IPCC, 2013. IPCC, 2013. Summary for policymakers. In: Stocker, T.F., Qin, D., Plattner, G.-K., Tignor,M., Allen, S.K., Boschung, J., Nauels, A., Xia, Y., Bex, V., Midgley, P.M. (Eds.), Climate Change 2013: The Physical Science Basis. Contribution of Working Group I t.

IPCC, I.P. on C.C., 2014. Clouds and Aerosols. Climate Change 2013 the Physical Science Basis: Working Group I Contribution to the Fifth Assessment Report of the Intergovernmental Panel on Climate Change 9781107057999, 571–658. https://doi.org/10.1017/CBO9781107415324.016

IPCC, 2021. on C.C. 2021: the Physical Science Basis, the Working Group I contribution to the Sixth Assessment Report | UNEP - UN Environment Programme [WWW Document]. URL https://www.unep.org/resources/report/climate-change-2021-physical-science-basis-working-group-i-contribution-sixth (accessed 1.10.22).

IPCC, I. P. on C. C. 2023: The Earth's Energy Budget, Climate Feedbacks and Climate Sensitivity, in: Climate Change 2021 – The Physical Science Basis, Cambridge University Press, 923–1054, https://doi.org/10.1017/9781009157896.009.

Jiang, Y., Xin, J., Wang, Z., Tian, Y., Tang, G., Ren, Y., Wu, L., Pan, X., Wang, Y., Jia, D., Ma, Y., Wang, L., 2022. The dynamic multi-box algorithm of atmospheric environmental capacity. Science of The Total Environment 806, 150951. https://doi.org/10.1016/J.SCITOTENV.2021.150951

Kacarab, M., Thornhill, K.L., Dobracki, A., Howell, S.G., O'Brien, J.R., Freitag, S., Poellot, M.R., Wood, R., Zuidema, P., Redemann, J., Nenes, A., 2020. Biomass burning aerosol as a modulator of the droplet number in the southeast Atlantic region. Atmospheric Chemistry and Physics 20, 3029–3040. https://doi.org/10.5194/acp-20-3029-2020

Kaimal, J.C., Wyngaard, J.C., Haugen, D.A., Coté, O.R., Izumi, Y., Caughey, S.J., Readings, C.J., 1976. Turbulence Structure in the Convective Boundary Layer. Journal of Atmospheric Sciences 33, 2152–2169. https://doi.org/10.1175/1520-0469(1976)033<2152:TSITCB>2.0.CO;2

Kalabokas, P., Viras, L., Repapis, C., 1999. Analysis of the 11-year Record (1987-1997) of Air Pollution measurements in Athens, Greece. Part I: Primary air pollutants. Global NEST Journal 1, 157–167. https://doi.org/10.30955/GNJ.000135

Kallos, George, Kassomenos, P., Pielke, R.A., 1993. Synoptic and mesoscale weather conditions during air pollution episodes in Athens, Greece. Boundary Layer Meteorology 62, 163–184. https://doi.org/10.1007/BF00705553/METRICS

Kalogridis, A.-C., Vratolis, S., Liakakou, E., Gerasopoulos, E., Mihalopoulos, N., Eleftheriadis, K., 2018. Assessment of wood burning versus fossil fuel contribution to wintertime black carbon and carbon monoxide concentrations in Athens, Greece. Atmospheric Chemistry and Physics 18, 10219–10236. https://doi.org/10.5194/acp-18-10219-2018

Kanji, Z.A., Ladino, L.A., Wex, H., Boose, Y., Burkert-Kohn, M., Cziczo, D.J., Krämer, M., 2017. Overview of Ice Nucleating Particles. Meteorological Monographs 58, 1.1-1.33. https://doi.org/10.1175/AMSMONOGRAPHS-D-16-0006.1

Katsoulis, B.D., 1996. The relationship between synoptic, mesoscale and microscale meteorological parameters during poor air quality events in Athens, Greece. Science of The Total Environment 181, 13–24. https://doi.org/10.1016/0048-9697(95)04953-3

Koenig, M., 2020. Description of the parallax correction functionality [WWW Document]. URL https://cwg.eumetsat.int/parallax-corrections/ (accessed 1.1.22).

Köhler, H., 1936. The nucleus in and the growth of hygroscopic droplets. Transactions of the Faraday Society 32, 1152–1161. https://doi.org/10.1039/TF9363201152

Kokkalis, P., Alexiou, D., Papayannis, A., Rocadenbosch, F., Soupiona, O., Raptis, P.-I., Mylonaki, M., Tzanis, C.G., Christodoulakis, J., 2020. Application and Testing of the Extended-Kalman-Filtering Technique for Determining the Planetary Boundary-Layer Height over Athens, Greece. Boundary Layer Meteorology 176, 125–147. https://doi.org/10.1007/s10546-020-00514-z

Kostenidou, E., Florou, K., Kaltsonoudis, C., Tsiflikiotou, M., Vratolis, S., Eleftheriadis, K., Pandis, S.N., 2015. Sources and chemical characterization of organic aerosol during the summer in the eastern Mediterranean. Atmospheric Chemistry and Physics 15, 11355–11371. https://doi.org/10.5194/acp-15-11355-2015

Kotthaus, S., Bravo-Aranda, J.A., Collaud Coen, M., Guerrero-Rascado, J.L., Costa, M.J., Cimini, D., O'Connor, E.J., Hervo, M., Alados-Arboledas, L., Jiménez-Portaz, M., Mona, L., Ruffieux, D., Illingworth, A., Haeffelin, M., 2023. Atmospheric boundary layer height from ground-based remote sensing: a review of capabilities and limitations. Atmospheric Measurement Techniques 16, 433–479. https://doi.org/10.5194/amt-16-433-2023

Laden, F, Schwartz, J., … F.S.-A. journal of, 2006, undefined, 2006. Reduction in fine particulate air pollution and mortality: extended follow-up of the Harvard Six Cities study. atsjournals.org 173, 667–672. https://doi.org/10.1164/rccm.200503-443OC

Laden, Francine, Schwartz, J., Speizer, F.E., Dockery, D.W., 2006. Reduction in fine particulate air pollution and mortality: Extended follow-up of the Harvard Six Cities study. American Journal of Respiratory and Critical Care Medicine173, 667–672. https://doi.org/10.1164/RCCM.200503-443OC

Lead, C.-O., Penner Lead, J.E., Andreae, M., Annegarn, H., Barrie, L., Feichter, J., Hegg, D., Jayaraman, A., Leaitch, R., Murphy, D., Nganga, J., Pitari, G., Ackerman, A., Adams, P., Austin, P., Boers, R., Boucher, O., Chin, M., Chuang, C., Collins, B., Cooke, W., Demott, P., Feng, Y., Fischer, H., Fung, I., Ghan, S., Ginoux, P., Gong, S.-L., Guenther, A., Herzog, M., Higurashi, A., Kaufman, Y., Kettle, A., Kiehl, J., Koch, D., Lammel, G., Land, C., Lohmann, U., Madronich, S., Mancini, E., Mishchenko, M., Nakajima, T., Quinn, P., Rasch, P., Roberts, D.L., Savoie, D., Schwartz, S., Seinfeld, J., Soden, B., Tanré, D., Taylor, K., Tegen, I., Tie, X., Vali, G., Van Dingenen, R., Van Weele, M., Zhang, Y., 2001. Aerosols, their Direct and Indirect Effects 5 Contents.

Lelieveld, J., Pozzer, A., Pöschl, U., Fnais, M., Haines, A., Münzel, T., 2020. Loss of life expectancy from air pollution compared to other risk factors: a worldwide perspective. Cardiovascular Research 116, 1910–1917. https://doi.org/10.1093/CVR/CVAA025

Lenschow, D.H., Lothon, M., Mayor, S.D., Sullivan, P.P., Canut, G., 2012. A Comparison of Higher-Order Vertical Velocity Moments in the Convective Boundary Layer from Lidar with In Situ Measurements and Large-Eddy Simulation. Boundary Layer Meteorology 143, 107–123. https://doi.org/10.1007/S10546-011-9615-3

Li, J., Lv, Q., Zhang, M., Wang, T., Kawamoto, K., Chen, S., Zhang, B., 2017. Effects of atmospheric dynamics and aerosols on the fraction of supercooled water clouds. Atmospheric Chemistry and Physics 17, 1847–1863. https://doi.org/10.5194/acp-17-1847-2017

Li, N., Sioutas, C., Cho, A., Schmitz, D., Misra, C., Sempf, J., Wang, M., Oberley, T., Froines, J., Nel, A., 2003. Ultrafine particulate pollutants induce oxidative stress and mitochondrial damage. Environmental Health Perspect 111, 455–460. https://doi.org/10.1289/ehp.6000

Li, X., Huang, S., & Sun, Z., 2019. Technology and equipment development in laser-induced fluorescence-based remote and field detection of biological aerosols. Journal of Biosafety and Biosecurity, 1(2), 113–122. https://doi.org/10.1016/j.jobb.2019.08.005

Liu, C., Chen, R., Sera, F., Vicedo-Cabrera, A.M., Guo, Y., Tong, S., Coelho, M.S.Z.S., Saldiva, P.H.N., Lavigne, E., Matus, P., Valdes Ortega, N., Osorio Garcia, S., Pascal, M., Stafoggia, M., Scortichini, M., Hashizume, M., Honda, Y., Hurtado-Díaz, M., Cruz, J., Nunes, B., Teixeira, J.P., Kim, H., Tobias, A., Íñiguez, C., Forsberg, B., Åström, C., Ragettli, M.S., Guo, Y.-L., Chen, B.-Y., Bell, M.L., Wright, C.Y., Scovronick, N., Garland, R.M., Milojevic, A., Kyselý, J., Urban, A., Orru, H., Indermitte, E., Jaakkola, J.J.K., Ryti, N.R.I., Katsouyanni, K., Analitis, A., Zanobetti, A., Schwartz, J., Chen, J., Wu, T., Cohen, A., Gasparrini, A., Kan, H., 2019. Ambient Particulate Air Pollution and Daily Mortality in 652 Cities. New England Journal of Medicine 381, 705–715. https://doi.org/10.1056/nejmoa1817364

Liu, Y., Daum, P.H., 2002. Indirect warming effect from dispersion forcing. Nature 2002 419:6907 419, 580–581. https://doi.org/10.1038/419580a

Liu, Y., Daum, P.H., Lu, C., 2014. Comment on “Cloud droplet spectral width relationship to CCN spectra and vertical velocity” by Hudson et al. Journal of Geophysical Research: Atmospheres 119, 1874–1877. https://doi.org/10.1002/2012JD019207

Lohmann, U., 2017. Anthropogenic Aerosol Influences on Mixed-Phase Clouds. Current Climate Change Reports 3, 32–44. https://doi.org/10.1007/s40641-017-0059-9

Lohmann, U., Feichter, J., 2005. Global indirect aerosol effects: A review. Atmospheric Chemistry and Physics 5, 715–737. https://doi.org/10.5194/ACP-5-715-2005

Lund, M.T., Samset, B.H., Skeie, R.B., Watson-Parris, D., Katich, J.M., Schwarz, J.P., Weinzierl, B., 2018. Short Black Carbon lifetime inferred from a global set of aircraft observations. Journal of Climate and Atmospheric Science 2018 1:1 1, 1–8. https://doi.org/10.1038/s41612-018-0040-x

Lynch, D.K., 1996. Cirrus clouds: Their role in climate and global change. Acta Astronautica 38, 859–863. https://doi.org/10.1016/S0094-5765(96)00098-7

Maiman, T.H., 1960. Stimulated Optical Radiation in Ruby. Nature 187, 493–494. https://doi.org/10.1038/187493a0

Martin, G.M., Johnson, D.W., Spice, A., 1994. The Measurement and Parameterization of Effective Radius of Droplets in Warm Stratocumulus Clouds. Journal of the Atmospheric Sciences 51, 1823–1842. https://doi.org/10.1175/1520-0469(1994)051<1823:TMAPOE>2.0.CO;2

McClung, F.J., Hellwarth, R.W., 1962. Giant Optical Pulsations from Ruby. Journal of Applied Physics 33, 828–829. https://doi.org/10.1063/1.1777174

McCormick, R.A., Ludwig, J.H., 1967. Climate Modification by Atmospheric Aerosols. Science (1979) 156, 1358–1359. https://doi.org/10.1126/SCIENCE.156.3780.1358

Meirink, J.F., Karlsson, K.-G., Solodovnik, I., Hüser, I., Benas, N., Johansson, E., Håkansson, N., Stengel, M., Selbach, N., Marc, S., Hollmann, R., 2022. CLAAS-3: CM SAF CLoud property dAtAset using SEVIRI - Edition 3. https://doi.org/10.5676/EUM_SAF_CM/CLAAS/V003

Meirink, J.F., Roebeling, R.A., Stammes, P., 2013. Inter-calibration of polar imager solar channels using SEVIRI. Atmospheric Measurement Techniques 6, 2495–2508. https://doi.org/10.5194/AMT-6-2495-2013

Meskhidze, N., 2005. Dust and pollution: A recipe for enhanced ocean fertilization? Journal of Geophysical Research 110, D03301. https://doi.org/10.1029/2004JD005082

Middleton, W.E.K., Spilhaus, A.F., 1954. Meteorological Instruments. Quarterly Journal of the Royal Meteorological Society, 80(345), 484–484. Quarterly Journal of the Royal Meteorological Society 80, 484. https://doi.org/https://doi.org/10.1002/qj.49708034532

Mie, G., 1908. Beiträge zur Optik trüber Medien, speziell kolloidaler Metallösungen. Annals of Physics 330, 377–445. https://doi.org/10.1002/ANDP.19083300302

Milne, W.P., Taylor, D.G., 1922. Relation Between Apolarity and the Pippian-Quippian Syzygetic Pencil. Proceedings of the London Mathematical Society s2-20, 101–106. https://doi.org/10.1112/PLMS/S2-20.1.101

Moosmüller, H., Chakrabarty, R.K., Arnott, W.P., 2009. Aerosol light absorption and its measurement: A review. Journal of Quantitative Spectroscopy and Radiative Transfer 110, 844–878. https://doi.org/10.1016/J.JQSRT.2009.02.035

Morales Betancourt, R., Nenes, A., 2014. Droplet activation parameterization: the population splitting concept revisited. Geoscientific Model Development Discussions 7, 2903–2932. https://doi.org/10.5194/gmd-7-2345-2014

Morales, R., Nenes, A., Jonsson, H., Flagan, R.C., Seinfeld, J.H., 2011. Evaluation of an entraining droplet activation parameterization using in situ cloud data. Journal of Geophysical Research 116, D15205. https://doi.org/10.1029/2010JD015324

Morales, R., & Nenes, A. 2010. Characteristic updrafts for computing distribution-averaged cloud droplet number and stratocumulus cloud properties. Journal of Geophysical Research, *115*(D18), D18220. https://doi.org/10.1029/2009JD013233

Mosca, S., Conti, C., Stone, N., & Matousek, P., 2021. Spatially offset Raman spectroscopy. Nature Reviews *Methods Primers*, *1*(1), 21. https://doi.org/10.1038/s43586-021-00019-0

Motos, G., Corbin, J.C., Schmale, J., Modini, R.L., Bertò, M., Kupiszewski, P., Baltensperger, U., Gysel-Beer, M., 2020. Black Carbon Aerosols in the Lower Free Troposphere are Heavily Coated in Summer but Largely Uncoated in Winter at Jungfraujoch in the Swiss Alps. Geophysical Research Letters 47, e2020GL088011. https://doi.org/10.1029/2020GL088011

Nabat, P., Somot, S., Cassou, C., Mallet, M., Michou, M., Bouniol, D., Decharme, B., Drugé, T., Roehrig, R., Saint-Martin, D., 2020. Modulation of radiative aerosols effects by atmospheric circulation over the Euro-Mediterranean region. https://doi.org/10.5194/acp-2019-1183

Nakajima, T., King, M.D., 1990. Determination of the Optical Thickness and Effective Particle Radius of Clouds from Reflected Solar Radiation Measurements. Part I: Theory. Journal of the Atmospheric Sciences 47, 1878–1893. https://doi.org/10.1175/1520-0469(1990)047<1878:DOTOTA>2.0.CO;2

Nakayama, T., Zhao, W., Zhang, W., 2021. Measurements of aerosol optical properties using spectroscopic techniques, in: Advances in Spectroscopic Monitoring of the Atmosphere. Elsevier, pp. 345–412. https://doi.org/10.1016/B978-0-12-815014-6.00003-8

Nenes, A., Ghan, S., Abdul-Razzak, H., Chuang, P.Y., Seinfeld, J.H., 2001. Kinetic limitations on cloud droplet formation and impact on cloud albedo. Tellus B: Chemical and Physical Meteorology 53, 133–149. https://doi.org/10.3402/tellusb.v53i2.16569

Nenes, A., Seinfeld, J.H., 2003. Parameterization of cloud droplet formation in global climate models. Journal of Geophysical Research: Atmospheres 108, 4415. https://doi.org/https://doi.org/10.1029/2002JD002911

Newsom, R., Krishnamurthy, R., 2020. Doppler lidar (DL) instrument handbook. U.S. Department of Energy, Office of Science, DOE/SC-ARM-TR-101. Available at: https://www.arm.gov/publications/tech_reports/handbooks/dl_handbook.pdf.

Ng, N.L., Herndon, S.C., Trimborn, A., Canagaratna, M.R., Croteau, P.L., Onasch, T.B., Sueper, D., Worsnop, D.R., Zhang, Q., Sun, Y.L., Jayne, J.T., 2011. An Aerosol Chemical Speciation Monitor (ACSM) for Routine Monitoring of the Composition and Mass Concentrations of Ambient Aerosol. Aerosol Science and Technology 45, 780–794. https://doi.org/10.1080/02786826.2011.560211

Olstrup, H., Johansson, C., Forsberg, B., Åström, C., 2019. Association between Mortality and Short-Term Exposure to Particles, Ozone and Nitrogen Dioxide in Stockholm, Sweden. International Journal of

Environmental Research and Public Health 2019, Vol. 16, Page 1028 16, 1028. https://doi.org/10.3390/IJERPH16061028

Ostro, B., Broadwin, R., Green, S., Feng, W.Y., Lipsett, M., 2006. Fine Particulate Air Pollution and Mortality in Nine California Counties: Results from CALFINE. Environmental Health Perspectives 114, 29–33. https://doi.org/10.1289/EHP.8335

Papanikolaou, C.-A., Papayannis, A., Mylonaki, M., Foskinis, R., Kokkalis, P., Liakakou, E., Stavroulas, I., Soupiona, O., Hatzianastassiou, N., Gavrouzou, M., Kralli, E., Anagnou, D., 2022. Vertical Profiling of Fresh Biomass Burning Aerosol Optical Properties over the Greek Urban City of Ioannina, during the PANACEA Winter Campaign. Atmosphere (Basel) 13, 94. https://doi.org/10.3390/atmos13010094

Pearson, G., Davies, F., Collier, C., 2010. Remote sensing of the tropical rain forest boundary layer using pulsed Doppler lidar. Atmos. Chem. Phys 10, 5891–5901. https://doi.org/10.5194/acp-10-5891-2010

Peng, Y., Lohmann, U., 2003. Sensitivity study of the spectral dispersion of the cloud droplet size distribution on the indirect aerosol effect. Geophysical Research Letters 30, n/a-n/a. https://doi.org/10.1029/2003GL017192

Perring, A. E., Schwarz, J. P., Baumgardner, D., Hernandez, M. T., Spracklen, D. v., Heald, C. L., Gao, R. S., Kok, G., McMeeking, G. R., McQuaid, J. B., Fahey, D. W., 2015. Airborne observations of regional variation in fluorescent aerosol across the United States. Journal of Geophysical Research: Atmospheres, 120(3), 1153–1170. https://doi.org/10.1002/2014JD022495

Petters, M.D., Kreidenweis, S.M., 2007. A single parameter representation of hygroscopic growth and cloud condensation nucleus activity. Atmospheric Chemistry and Physics 7, 1961–1971. https://doi.org/10.5194/acp-7-1961-2007

Petty, G.W., Huang, W., 2011. The Modified Gamma Size Distribution Applied to Inhomogeneous and Nonspherical Particles: Key Relationships and Conversions. Journal of the Atmospheric Sciences 68, 1460–1473. https://doi.org/10.1175/2011JAS3645.1

Petzold, A., Ogren, J.A., Fiebig, M., Laj, P., Li, S.M., Baltensperger, U., Holzer-Popp, T., Kinne, S., Pappalardo, G., Sugimoto, N., Wehrli, C., Wiedensohler, A., Zhang, X.Y., 2013. Recommendations for reporting black carbon measurements. Atmospheric Chemistry and Physics 13, 8365–8379. https://doi.org/10.5194/ACP-13-8365-2013

Platnick, S., Meyer, K.G., King, M.D., Wind, G., Amarasinghe, N., Marchant, B., Arnold, G.T., Zhang, Z., Hubanks, P.A., Holz, R.E., Yang, P., Ridgway, W.L., Riedi, J., 2017. The MODIS Cloud Optical and Microphysical Products: Collection 6 Updates and Examples From Terra and Aqua. IEEE Transactions on Geoscience and Remote Sensing 55, 502–525. https://doi.org/10.1109/TGRS.2016.2610522

Platnick, S., Twomey, S., 1994. Determining the Susceptibility of Cloud Albedo to Changes in Droplet Concentration with the Advanced Very High Resolution Radiometer. Journal of Applied Meteorology 33, 334–347. https://doi.org/10.1175/1520-0450(1994)033<0334:DTSOCA>2.0.CO;2

Quaas, J., Arola, A., Cairns, B., Christensen, M., Deneke, H., Ekman, A.M.L., Feingold, G., Fridlind, A., Gryspeerdt, E., Hasekamp, O., Li, Z., Lipponen, A., Mülmenstädt, J., Nenes, A., Penner, J.E., Rosenfeld, D., Schrödner, R., Sinclair, K., Sourdeval, O., Stier, P., Tesche, M., Van Diedenhoven, B., Wendisch, M., 2020. Constraining the Twomey effect from satellite observations: Issues and perspectives. Atmospheric Chemistry and Physics 20, 15079–15099. https://doi.org/10.5194/acp-20-15079-2020

Quaas, J., Jia, H., Smith, C., Albright, A. L., Aas, W., Bellouin, N., Boucher, O., Doutriaux-Boucher, M., Forster, P. M., Grosvenor, D., Jenkins, S., Klimont, Z., Loeb, N. G., Ma, X., Naik, V., Paulot, F., Stier, P., Wild, M., Myhre, G., & Schulz, M., 2022. Robust evidence for reversal of the trend in aerosol effective climate forcing. Atmospheric Chemistry and Physics, 22(18), 12221–12239. https://doi.org/10.5194/acp-22-12221-2022

Ramachandran, S., Rupakheti, M., 2020. Inter-annual and seasonal variations in columnar aerosol characteristics and radiative effects over the Pokhara Valley in the Himalayan foothills – Composition, radiative forcing, and atmospheric heating. Environmental Pollution 264, 114799. https://doi.org/10.1016/J.ENVPOL.2020.114799

Raman, C. V., Krishnan, K.S., 1928. A New Type of Secondary Radiation. Nature 1928 121:3048 121, 501–502. https://doi.org/10.1038/121501c0

Ramanathan, V., Cess, R.D., Harrison, E.F., Minnis, P., Barkstrom, B.R., Ahmad, E., Hartmann, D., 1989. Cloud-Radiative Forcing and Climate: Results from the Earth Radiation Budget Experiment. Science (1979) 243, 57–63. https://doi.org/10.1126/SCIENCE.243.4887.57

Reutter, P., Su, H., Trentmann, J., Simmel, M., Rose, D., Gunthe, S.S., Wernli, H., Andreae, M.O., Pöschl, U., 2009. Aerosol- and updraft-limited regimes of cloud droplet formation: influence of particle number, size and hygroscopicity on the activation of cloud condensation nuclei (CCN). Atmospheric Chemistry and Physics 9, 7067–7080. https://doi.org/10.5194/acp-9-7067-2009

Roberts, G.C., Nenes, A., 2005. A Continuous-Flow Streamwise Thermal-Gradient CCN Chamber for Atmospheric Measurements. Aerosol Science and Technology 39, 206–221. https://doi.org/10.1080/027868290913988

Roebeling, R.A., Feijt, A.J., Stammes, P., 2006. Cloud property retrievals for climate monitoring: Implications of differences between Spinning Enhanced Visible and Infrared Imager (SEVIRI) on METEOSAT-8 and Advanced Very High Resolution Radiometer (AVHRR) on NOAA-17. Journal of Geophysical Research: Atmospheres 111, 20210. https://doi.org/10.1029/2005JD006990

Rosenfeld, D., Zheng, Y., Hashimshoni, E., Pöhlker, M.L., Jefferson, A., Pöhlker, C., Yu, X., Zhu, Y., Liu, G., Yue, Z., Fischman, B., Li, Z., Giguzin, D., Goren, T., Artaxo, P., Barbosa, H.M.J., Pöschl, U., Andreae, M.O., 2016. Satellite retrieval of cloud condensation nuclei concentrations by using clouds as CCN chambers. Proceedings of the National Academy of Sciences 113, 5828–5834. https://doi.org/10.1073/pnas.1514044113

Rotstayn, L.D., Liu, Y., 2009. Cloud droplet spectral dispersion and the indirect aerosol effect: Comparison of two treatments in a GCM. Geophysical Research Letters 36, L10801. https://doi.org/10.1029/2009GL038216

Rotstayn, L.D., Liu, Y., 2003. Sensitivity of the First Indirect Aerosol Effect to an Increase of Cloud Droplet Spectral Dispersion with Droplet Number Concentration. Journal of Climate 16, 3476–3481. https://doi.org/10.1175/1520-0442(2003)016<3476:SOTFIA>2.0.CO;2

Rousseeuw, P.J., 1987. Silhouettes: A graphical aid to the interpretation and validation of cluster analysis. Journal of Computational and Applied Mathematics 20, 53–65. https://doi.org/10.1016/0377-0427(87)90125-7

Salma, I., Balásházy, I., Winkler-Heil, R., Hofmann, W., Záray, G., 2002. Effect of particle mass size distribution on the deposition of aerosols in the human respiratory system. Journal of Aerosol Science 33, 119–132. https://doi.org/10.1016/S0021-8502(01)00154-9

Schawlow, A.L., Townes, C.H., 1958. Infrared and Optical Masers. Physical Review 112, 1940–1949. https://doi.org/10.1103/PhysRev.112.1940

Schmetz, J., Pili, P., Tjemkes, S., Just, D., Kerkmann, J., Rota, S., Ratier, A., 2002. Supplement to An Introduction to Meteosat Second Generation (MSG). Bulletin of the American Meteorological Society 83, 992–992. https://doi.org/10.1175/BAMS-83-7-Schmetz-2

Schween, J. H., Hirsikko, A., Löhnert, U., Crewell, S., 2014. Mixing-layer height retrieval with ceilometer and Doppler lidar: from case studies to long-term assessment. Atmospheric Measurement Techniques 7, 3685–3704. https://doi.org/10.5194/amt-7-3685-2014

Seinfeld J. H., Pandis S. N., 2016. Atmospheric Chemistry and Physics: From Air Pollution to Climate Change., 3rd ed. John Wiley & Sons, Hoboken New Jersey.

Seinfeld, J.H., 2003. TROPOSPHERIC CHEMISTRY AND COMPOSITION | Aerosols/Particles. Encyclopedia of Atmospheric Sciences 2349–2354. https://doi.org/10.1016/B0-12-227090-8/00438-3

Seinfeld, J.H., Bretherton, C., Carslaw, K.S., Coe, H., DeMott, P.J., Dunlea, E.J., Feingold, G., Ghan, S., Guenther, A.B., Kahn, R., Kraucunas, I., Kreidenweis, S.M., Molina, M.J., Nenes, A., Penner, J.E., Prather, K.A., Ramanathan, V., Ramaswamy, V., Rasch, P.J., Ravishankara, A.R., Rosenfeld, D., Stephens, G., Wood, R., 2016. Improving our fundamental understanding of the role of aerosol-cloud interactions in the climate system. Proceedings of the National Academy of Sciences U S A 113, 5781–5790. https://doi.org/10.1073/PNAS.1514043113/-/DCSUPPLEMENTAL

Singh, A.B., Kumar, P., 2022. Climate change and allergic diseases: An overview. Frontiers in Allergy 3, 964987. https://doi.org/10.3389/FALGY.2022.964987

Sinyuk, A., Dubovik, O., Holben, B., Eck, T.F., Breon, F.-M., Martonchik, J., Kahn, R., Diner, D.J., Vermote, E.F., Roger, J.-C., Lapyonok, T., Slutsker, I., 2007. Simultaneous retrieval of aerosol and surface properties from a combination of AERONET and satellite data. Remote Sens Environmental 107, 90–108. https://doi.org/10.1016/j.rse.2006.07.022

Smullin, L., Fiocco, G. Optical Echoes from the Moon. Nature 194, 1267 (1962). https://doi.org/10.1038/1941267a0

Soupiona, O., Samaras, S., Ortiz-Amezcua, P., Böckmann, C., Papayannis, A., Moreira, G.A., Benavent-Oltra, J.A., Guerrero-Rascado, J.L., Bedoya-Velásquez, A.E., Olmo, F.J., Román, R., Kokkalis, P., Mylonaki, M., Alados-Arboledas, L., Papanikolaou, C.A., Foskinis, R., 2019. Retrieval of optical and microphysical properties of transported Saharan dust over Athens and Granada based on multi-wavelength Raman lidar measurements: Study of the mixing processes. Atmospheric Environment 214, 116824. https://doi.org/10.1016/J.ATMOSENV.2019.116824

Srivastava, P., Dey, S., Srivastava, A.K., Singh, S., Tiwari, S., 2019. Suppression of aerosol-induced atmospheric warming by clouds in the Indo-Gangetic Basin, northern India. Theoretical and Applied Climatology 2019 137:3 137, 2731–2741. https://doi.org/10.1007/S00704-019-02768-1

Stafoggia, M., Bellander, T., 2020. Short-term effects of air pollutants on daily mortality in the Stockholm county – A spatiotemporal analysis. Environmental Research 188, 109854. https://doi.org/10.1016/J.ENVRES.2020.109854

Stafoggia, M., Schneider, A., Cyrys, J., Samoli, E., Andersen, Z.J., Bedada, G.B., Bellander, T., Cattani, G., Eleftheriadis, K., Faustini, A., Hoffmann, B., Jacquemin, B., Katsouyanni, K., Massling, A., Pekkanen, J., Perez, N., Peters, A., Quass, U., Yli-Tuomi, T., Forastiere, F., 2017. Association between Short-term Exposure to Ultrafine Particles and Mortality in Eight European Urban Areas. Epidemiology 28, 172–180. https://doi.org/10.1097/EDE.0000000000000599

Stephens, G.L., 1978. Radiation Profiles in Extended Water Clouds. II: Parameterization Schemes. Journal of the Atmospheric Sciences 35, 2123–2132. https://doi.org/10.1175/1520-0469(1978)035<2123:RPIEWC>2.0.CO;2

Stephens, G.L., Christensen, M., Andrews, T., Haywood, J., Malavelle, F.F., Suzuki, K., Jing, X., Lebsock, M., Li, J.F., Takahashi, H., Sy, O., 2019. Cloud physics from space. Quarterly Journal of the Royal Meteorological Society 145, 2854–2875. https://doi.org/10.1002/qj.3589

Stevens, B., Feingold, G., 2009. Untangling aerosol effects on clouds and precipitation in a buffered system, Nature. Nature Publishing Group.

Stull, R.B., 1988. An introduction to boundary layer meteorology. An introduction to boundary layer meteorology. https://doi.org/10.1007/978-94-009-3027-8

Su, T., Li, Z., Kahn, R., 2018. Relationships between the planetary boundary layer height and surface pollutants derived from lidar observations over China: regional pattern and influencing factors. Atmospheric Chemistry and Physics 18, 15921–15935. https://doi.org/10.5194/acp-18-15921-2018

Sullivan, S.C., Lee, D., Oreopoulos, L., Nenes, A., 2016. Role of updraft velocity in temporal variability of global cloud hydrometeor number. Proceedings of the National Academy of Sciences U S A 113, 5791–6. https://doi.org/10.1073/pnas.1514039113

Synge, E.H., 1930. XCI. A method of investigating the higher atmosphere. The London, Edinburgh, and Dublin Philosophical Magazine and Journal of Science 9, 1014–1020. https://doi.org/10.1080/14786443008565070

Taylor, G.I., 1935. Statistical theory of turbulenc. Proceedings of the Royal Society of London 151, 421–444. https://doi.org/10.1098/RSPA.1935.0158

Titos, G., Cazorla, A., Zieger, P., Andrews, E., Lyamani, H., Granados-Muñoz, M.J., Olmo, F.J., Alados-Arboledas, L., 2016. Effect of hygroscopic growth on the aerosol light-scattering coefficient: A review of measurements, techniques and error sources. Atmospheric Environment 141, 494–507. https://doi.org/10.1016/J.ATMOSENV.2016.07.021

Tomasi, C., Lupi, A., 2016. Primary and Secondary Sources of Atmospheric Aerosol. Atmospheric Aerosols 1–86. https://doi.org/10.1002/9783527336449.CH1

Träumner, K., Kottmeier, C., Corsmeier, U., Wieser, A., 2011. Convective Boundary-Layer Entrainment: Short Review and Progress using Doppler Lidar. Boundary-Layer Meteorology 2011 141:3 141, 369–391. https://doi.org/10.1007/S10546-011-9657-6

Tsaknakis, G., Papayannis, A., Kokkalis, P., Amiridis, V., Kambezidis, H.D., Mamouri, R.E., Georgoussis, G., Avdikos, G., 2011. Inter-comparison of lidar and ceilometer retrievals for aerosol and Planetary

Boundary Layer profiling over Athens, Greece. Atmospheric Measurement Techniques 4, 1261–1273. https://doi.org/10.5194/AMT-4-1261-2011

TSI 3563 Nephelometer description by NOAA Earth System Research Laboratory Global Monitoring Division. 2015. http://www.esrl.noaa.gov/gmd/aero/instrumentation/neph_desc.html, accessed on November 30, 2023.

Tucker, S.C., Senff, C.J., Weickmann, A.M., Brewer, W.A., Banta, R.M., Sandberg, S.P., Law, D.C., Hardesty, R.M., 2009b. Doppler Lidar Estimation of Mixing Height Using Turbulence, Shear, and Aerosol Profiles. Journal of Atmospheric and Oceanic Technology 26, 673–688. https://doi.org/10.1175/2008JTECHA1157.1

Twersky, V., 1964. Rayleigh Scattering. *Applied Optics*, *3*(10), 1150. https://doi.org/10.1364/AO.3.001150

Twomey, S., 1991. Aerosols, clouds and radiation. Atmospheric Environment. Part A. General Topics 25, 2435–2442. https://doi.org/10.1016/0960-1686(91)90159-5

Twomey, S., 1974. Pollution and the planetary albedo. Atmospheric Environment (1967) 8, 1251–1256. https://doi.org/10.1016/0004-6981(74)90004-3

Twomey, S., Warner, J., 1967. Comparison of Measurements of Cloud Droplets and Cloud Nuclei. Journal of the Atmospheric Sciences 24, 702–703. https://doi.org/10.1175/1520-0469(1967)024<0702:COMOCD>2.0.CO;2

Vasilatou, V., Diapouli, E., Abatzoglou, D., Bakeas, E.B., Scoullos, M., Eleftheriadis, K., 2017. Characterization of PM2.5 chemical composition at the Demokritos suburban station, in Athens Greece. The influence of Saharan dust. Environmental Science and Pollution Research 24, 11836–11846. https://doi.org/10.1007/s11356-017-8684-3

Vratolis, S., Fetfatzis, P., Argyrouli, A., Soupiona, O., Mylonaki, M., Maroufidis, J., Kalogridis, A.-C., Manousakas, M., Bezantakos, S., Binietoglou, I., Labzovskiı, L., Solomos, S., Papayannis, A., Mocnik, G., O'Connor, E.J., Muller, D., Tzanis, C.G.G., Eleftheriadis, K., Kalogridis, A.-C., Manousakas, M., Bezantakos, S., Binietoglou, I., Labzovskii, L.D., Solomos, S., Papayannis, A., Močnik, G., O' Connor, E., Müller, D., Tzanis, C.G.G., Eleftheriadis, K., 2020. Comparison and complementary use of in situ and remote sensing aerosol measurements in the Athens Metropolitan Area. Atmospheric Environment 228, 117439. https://doi.org/10.1016/j.atmosenv.2020.117439

Vratolis, S., Gini, M.I., Bezantakos, S., Stavroulas, I., Kalivitis, N., Kostenidou, E., Louvaris, E., Siakavaras, D., Biskos, G., Mihalopoulos, N., Pandis, S.N., Pilinis, C., Papayannis, A., Eleftheriadis, K., 2019. Particle number size distribution statistics at City-Centre Urban Background, urban background, and remote stations in Greece during summer. Atmospheric Environment 213, 711–726. https://doi.org/10.1016/j.atmosenv.2019.05.064

Wallace, J.M., Hobbs, P. V., 2006. Atmospheric Science, An Introductory Survey. Elsevier https://doi.org/10.1016/C2009-0-00034-8

Wandinger, U., 2005. Introduction to Lidar, in: Weitkamp, C. (Ed.), Lidar: Range-Resolved Optical Remote Sensing of the Atmosphere. Springer New York, New York, NY, pp. 1–18. https://doi.org/10.1007/0-387-25101-4_1

Wang, F., Yang, T., Wang, Z., Chen, X., Wang, H., Guo, J., 2021. A comprehensive evaluation of planetary boundary layer height retrieval techniques using lidar data under different pollution scenarios. Atmos Res 253, 105483. https://doi.org/10.1016/J.ATMOSRES.2021.105483

Wang, M., Peng, Y., Liu, Yangang, Liu, Yu, Xie, X., Guo, Z., 2020. Understanding Cloud Droplet Spectral Dispersion Effect Using Empirical and Semi-Analytical Parameterizations in NCAR CAM5.3. Earth and Space Science 7, e2020EA001276. https://doi.org/10.1029/2020EA001276

Weitkamp, C., 2005. Lidar. Springer-Verlag, New York. https://doi.org/10.1007/b106786

Werner, C., 2005. Doppler Wind Lidar, in: Weitkamp, C. (Ed.), Lidar: Range-Resolved Optical Remote Sensing of the Atmosphere. Springer New York, New York, NY, pp. 325–354. https://doi.org/10.1007/0-387-25101-4_12

Wiedensohler, A., Birmili, W., Nowak, A., Sonntag, A., Weinhold, K., Merkel, M., Wehner, B., Tuch, T., Pfeifer, S., Fiebig, M., Fjäraa, A.M., Asmi, E., Sellegri, K., Depuy, R., Venzac, H., Villani, P., Laj, P., Aalto, P., Ogren, J.A., Swietlicki, E., Williams, P., Roldin, P., Quincey, P., Hüglin, C., Fierz-Schmidhauser, R., Gysel, M., Weingartner, E., Riccobono, F., Santos, S., Grüning, C., Faloon, K., Beddows, D., Harrison, R., Monahan, C., Jennings, S.G., O'Dowd, C.D., Marinoni, A., Horn, H.-G., Keck, L., Jiang, J., Scheckman, J., McMurry, P.H., Deng, Z., Zhao, C.S., Moerman, M., Henzing, B., de Leeuw, G., Löschau, G., Bastian, S., 2012. Mobility particle size spectrometers: harmonization of technical standards and data structure to facilitate high quality long-term observations of atmospheric particle number size distributions. Atmospheric Measurement Techniques 5, 657–685. https://doi.org/10.5194/amt-5-657-2012

WMO, 2022. WMO Greenhouse Gas Bulletin. No. 2, September 2022. World Meteorological Organization (WMO).

WMO, 2007. Health relevance of particulate matter from various sources Report on a WHO Workshop. Report on a WHO Workshop Bonn.

Zamora, L.M., Kahn, R.A., Huebert, K.B., Stohl, A., Eckhardt, S., 2018. A satellite-based estimate of combustion aerosol cloud microphysical effects over the Arctic Ocean. Atmospheric Chemistry and Physics 18, 14949–14964. https://doi.org/10.5194/acp-18-14949-2018

Zhang, D., Liu, D., Luo, T., Wang, Z., Yin, Y., 2015. Aerosol impacts on cloud thermodynamic phase change over East Asia observed with CALIPSO and CloudSat measurements. Journal of Geophysical Research: Atmospheres 120, 1490–1501. https://doi.org/10.1002/2014JD022630

Zhao, C., Tie, X., Brasseur, G., Noone, K.J., Nakajima, T., Zhang, Q., Zhang, R., Huang, M., Duan, Y., Li, G., Ishizaka, Y., 2006. Aircraft measurements of cloud droplet spectral dispersion and implications for indirect aerosol radiative forcing. Geophysical Research Letters 33, L16809. https://doi.org/10.1029/2006GL026653

Zhu, Y., Rosenfeld, D., Li, Z., 2018. Under What Conditions Can We Trust Retrieved Cloud Drop Concentrations in Broken Marine Stratocumulus? Journal of Geophysical Research: Atmospheres 123, 8754–8767. https://doi.org/10.1029/2017JD028083

Zografou, O., Gini, M., Manousakas, M.I., Chen, G., Kalogridis, A.C., Diapouli, E., Pappa, A., Eleftheriadis, K., 2022. Combined organic and inorganic source apportionment on yearlong ToF-ACSM dataset at a suburban station in Athens. Atmospheric Measurement Techniques 15, 4675–4692. https://doi.org/10.5194/AMT-15-4675-2022

LIST OF ACRONYMS

$(HAC)^2$	Hellenic Atmospheric Aerosol and Climate Change Station
A.U.	Arbitrary Units
ABC	Fluorescent particles detected in channels FL1-(excitation at 280 nm, emission 310-400nm), FL2-(excitation at 280nm, emission 420-650nm) and FL3-(excitation at 370nm, emission 420-650nm)
ACI	Aerosol-cloud interactions
ACTRIS	Aerosol, Clouds and Trace Gases Research Infrastructure
AE31	Aethalometer
AMA	Athens Metropolitan Area
APDs	Avalanche Photodiodes
BC	Fluorescent particles detected in channels FL2-(excitation at 280nm, emission 420-650nm) and FL3-(excitation at 370nm, emission 420-650nm) only
*bc*500	Backscattering at 550nm
C·STACC	Center of Studies on Air quality and Climate Change
CALIOP	Cloud-Aerosol Lidar with Orthogonal Polarization
CALISTHO	International Cloud-AerosoL InteractionS in the Helmos background TropOsphere Campaign
CCN	Cloud Condensation Nuclei
CE	Collection Efficiency Factor
CLAAS	CLoud property dAtAset using SEVIRI
CM SAF	Satellite Application Facility on Climate Monitoring
D_{cr}	Critical Dry Diameter
DEM	Demokritos
e	Water vapor pressure
e_s	Saturated water vapor pressure
eBC	Equivalent Black Carbon
eV	Electonvolt
ECMWF	European Center for Medium-range Weather Forecasts
EPFL	Swiss Federal Institute of Technology in Lausanne
ERA5	Fifth-generation European Center for Medium-range Weather Forecasts reanalysis model data
ERF	Effective Radiative Forcing
EUMETSAT	European Organization for the Exploitation of Meteorological Satellites
FMI	Finnish Meteorological Institute
FORTH	Foundation for Research and Technology Hellas
FTL	Free Troposphere Layer
GAW	Global Atmospheric Watch network
GCM	Global Climate Models
HALO	Wind Doppler Lidar
H_{ct}	Cloud Top Height
ICE-HT	Institute of Chemical Engineering
IN	Ice Nuclei
INRASTES	Institute of Nuclear & Radiological Sciences & Technology, Energy & Safety
IPCC	Intergovernmental Panel on Climate Change
LiDAR	LIght Detection And Ranging

LRSU	Laboratory of Optoelectronics and Lasers both at the Physics Department of the School of Applied Mathematics and Physical Sciences of the National Technical University of Athens
LTC	Longitudinal time code - Athens
LWC	Liquid Water Content
METEOSAT	Geostationary Meteorological Satellites
MNB	Mean Normalized Bias
MODIS	Moderate Resolution Imaging Spectroradiometer
MSG	METEOSAT Second Generation
M_w	Molar Mass of Water
m	Meter
Mm	Megameter
μm	Micrometer
nm	Nanometer
$N_{10\text{-}200nm}$	Aerosol Number concentrations between 10-200nm
$N_{200\text{-}550nm}$	Aerosol Number concentrations between 200-500nm
$N_{90\text{-}800nm}$	Aerosol Number concentrations between 90-800nm
NADH	Tryptophan and Nicotinamide Adenine Dinucleotide
NCSRD	National Center for Scientific Research-Demokritos
N_d	Cloud droplet number concentration
Nd:YAG	Neodymium-doped Yttrium Aluminum garnet; Nd:$Y_3Al_5O_{12}$
N_d^{lim}	Limiting droplet number
N_d^{sat}	Satellite retrieved cloud droplet number concentration
N_{Total}	Aerosol number concentrations between 10-800nm
NTUA	National Technical University of Athens
NWP	Numerical Weather Prediction
OCA	Optimal Cloud Analysis
OPC	Optical Particle Counter
PAM	Partition Around Medoids
PANACEA	PANhellenic infrastructure for Atmospheric Composition and climatE chAnge
PBL	Planetary Boundary Layer
PBLC	Planetary Boundary Layer Clouds
P_{ct}	Cloud Top Pressure
PDF	Probability Density Function
PM_1	Fine inhalable particles, with diameters that are generally 1 micrometer and smaller.
PM_{10}	Fine inhalable particles, with diameters that are generally 10 micrometers and smaller.
$PM_{2.5}$	Fine inhalable particles, with diameters that are generally 2.5 micrometers and smaller.
PMTs	PhotoMultiplier Tubes
R	Universal gas constant
RCS	Range Corrected Signal
RH	Relative Humidity
sc550	Total scattering at 550nm
SEVIRI	Spinning Enhanced Visible and Infrared Imager
s	Supersaturation
s_{max}	Maximum supersaturation
s^*	Characteristic supersaturation
SMPS	Scanning Mobility Particle Sizer
SNR	Signal-to-Noise-Ratio

T	Ambient temperature
T_{ct}	Cloud top temperature
TOA	Top Of the Atmosphere
ToF-ACSM	Time-of-Flight Aerosol Chemical Speciation Monitor
UTC	Coordinated Universal Time
UV	UltraViolet radiation
VAD	Vertical Azimuth Display mode
V_{dir}	Direction of horizontal wind
V_h	Horizontal wind speed
VIIRS	Visible Infrared Imaging Radiometer Suite
VL	Vathia Lakka
V_r	Radial velocity
V_ϑ	Azimuthal wind direction
w	Vertical velocity
q	Absolute humidity
w^*	Characteristic vertical velocity
WCCAP	World Calibration Centre for Aerosol Physics
WIBS	Wideband Integrated Bioaerosol Sensor
WMO	World Meteorological Organization
β	Effective radius factor
ε	Relative dispersion of the droplet spectrum
$\tilde{\varepsilon}$	The entrainment parameter
ENRACT	Environmental Radioactivity & Aerosol technology for atmospheric and Climate impacT Laboratory
κ	Particle hygroscopicity parameter
λ	characteristic nondimensional velocity
ρ_w	Density of liquid water
σ	Surface tension of the solution droplet
σ_w	Standard deviation of the updrafts
τ	Cloud optical thickness
r_{eff}	Effective radius of the cloud droplets
D_{eff}	Effective diameter of the cloud droplets
Q_{ext}	Mie extinction efficiency factor

LIST OF FIGURES

LIST OF TABLES

CURICULUM VITAE

Romanos Foskinis

Personal information:

June 28, 1993, Athens, Greece

Citizenship: Greek

Contact:

Work address:

- National Technical University of Athens, Department of Physics, 9 Iroon Polytechniou, GR-15780 Zografou, Athens, Greece.
- Center of Studies on Air quality and Climate Change (C-STACC), Foundation for Research and Technology HELLAS Institute of Chemical Engineering Sciences (FORTH/ICE-HT), Stadiou St., Platani Patras GR-26504, Greece.
- Laboratory of Atmospheric Processes and their Impacts (LAPI), Swiss Federal Institute of Technology in Lausanne (EPFL)

Home address: Neofytou 14, Nea Politia Oropou, 19015, Greece.

Tel: + 30-6980-099580 *(mobile)*

E-mail: r.foskinis@gmail.com

EDUCATION:

National Technical University of Athens (NTUA) 2019-today

PhD., *Physical and Technological Applications*, Department of Physics, National Technical University of Athens – Title: Aerosol-Cloud Interaction Study by using Remote Sensing Techniques. Three-member Committee: Supervisors: Alexandros Papayannis (NTUA Professor), Members: Athanasios Nenes (EPFL Professor), Konstantinos Eleftheriadis (Research Director, NCSRD).

National Kapodistrian University of Athens (NKUA) 2017-2019

M.Sc. in Applied Physics with a specialization in "Environmental Physics", Department of Physics, Department of Meteorology and Environmental Physics - Thesis Title: Estimation of Rainfall Intensity in Medium Scale Thunderstorm Systems using Satellite Data and Neural Networks. Three-member Committee: Supervisors: Konstantinos Kartalis (Professor, NKUA), Members: Efthymios Lekkas (Professor, NKUA), Konstantinos Lagouvardos (NOA Research Director).

University of Crete (UoC) 2011-2017

B.Sc. in Physics, Department of Physics - Thesis Title: Study of macromolecular architecture on the self-assembly behavior of copolymers in a selective polymer host. Three-member Committee: Supervisors: Evangelos Harmandaris (Professor), Anastasia Risanou (Associate Professor), Members: Glynos Emmanouil (Associate Professor), Kominis Ioannis (Professor), 2017. Degree: 6.79

FELLOWSHIPS

Basic Research Program, NTUA (PEVE) under contract PEVE0011/2021 - Aerosol clOud Interaction sTudy (AphrOdITe).

PARTICIPATION IN RESEARCH PROGRAMS

1. Researcher in the Research Program of the European Union (Horizon 2020: INFRASTRUCTURE) in the Laboratory of Optoelectronics, Lasers & Applications, of the Physics Department of the Technical University of Athens. Project title: "ACTRIS II: Aerosols, Clouds, and Trace gases Research InfraStructure Network" in the framework of the Horizon 2020 Program (2015-2021).

2. Researcher in the Laboratory of Optoelectronics, Lasers & Applications, of the Physics Department of the National Technical University of Athens. Project title: "Detection of suspended bio-aerosols by LIDAR-LIF techniques" (2019-2020).

3. Researcher in the National Infrastructure Research Program - OP "Competitiveness, Entrepreneurship and Innovation 2014-2020", in the Laboratory of Optoelectronics, Lasers & Applications, of the Physics Department of the National Technical University. Project title: "Nationwide Infrastructure for Atmospheric Composition and Climate Change: PANACEA" and MIS 5021516 (2018-2022).

4. Researcher in the Research Program Science at the service of the State and Society for tackling Climate Change" — CLIMPACT — "Horizon 2020", at the Laboratory of Radioactivity and Environment of NCSR Demokritos.

5. Researcher in the Research Program "Pyrogenic Transformations Affecting Climate and Health", Grant Agreement number: 726165 — PyroTRACH — ERC-2016-COG, which is implemented under the H2020-EU.1.1. - EXCELLENT SCIENCE - European Research Council (ERC), at the Laboratory of Center of Studies on Air quality and Climate Change (C·STACC)

PARTICIPATION IN RESEARCH CAMPAIGNS

1. 1st PANACEA CAMPAIGN - 12-30/7/2019. Field measurements with the mobile Lidar system AIAS, Volos, Greece.

2. Pre - Campaign Helmos - 15-17/11/2019. Field measurements with the mobile Lidar system AIAS, Helmos, Greece.

3. 2nd PANACEA CAMPAIGN - 10/1 -7/2/2020. Field measurements with the mobile Lidar system AIAS, Ioannina, Greece.

4. Pre - Campaign DEMOKRITOS - 18/3-2/7/2020. Field measurements with the mobile Lidar system AIAS, and the mobile Wind Doppler Lidar (HALO) at NCSR "Demokritos" facilities, Athens, Greece.

5. CALISTHO Campaign - 1/10-30/11/2021. Field measurements with the mobile Lidar system AIAS, and the mobile Wind Doppler Lidar (HALO), Cloud Radar (WProf), and Micro Rain Radar (MRR), Helmos, Greece.

6. PERICLES Campaign - 12/5-12/6/2023. Field measurements with a Fluorescence Lidar, Payerne, Switzerland.

INFRASTRUCTURE PROJECTS

1. Development of a Meteorological and Solar Radiation Network at NTUA, in the framework of the project, ELKE, NTUA (Contract No 652267) (2020-2022).

RELATED ACADEMIC RESEARCH WORKS

Elaboration of a Research Paper on the topic: "Spectral unmixing analysis for the city of Athens, using high spatial resolution of satellite recordings" using the multispectral sensors of the MODIS satellite. Supervisors: Dr. N. Chrysoulakis, Dr. Z. Mitraka.

PUBLICATIONS IN INTERNATIONAL JOURNALS WITH REVIEWS

1. **Foskinis R.**, Gao K., Violaki K., Motos G., Gini, M. I., Zografou O., Diapouli E., Vratolis S., Granakis K., Kommpula M., Vakkari V., Aktypis A., Kaltsonoudis, C., Pandis S., Eleftheriadis K., Papayannis A., and Nenes A. (2024). Drivers of droplet formation and cloud supersaturation during the CALISTHO Campaign (Under Submission – *Atmospheric Chemistry and Physics*).

2. **Foskinis R.**, Gao K., Gini, M. I., Diapouli E., Vratolis S., Granakis K., Zografou O., Kokkalis P., Kommpula M., Vakkari V., Eleftheriadis K., Nenes A., and Papayannis A. (2024). On the determination of the Planetary Boundary Layer top-height using a wind Doppler lidar and *in situ* measurements at an Eastern Mediterranean orographic site (Under Submission – *Atmospheric Research*).

3. **Foskinis, R.**, Gini, M., Kokkalis, P., Diapouli, E., Vratolis, S., Granakis, K., Zografou, O., Komppula, M., Vakkari, V., Nenes, A., Papayannis, A., and Eleftheriadis, K. (2024). On the Relation between the Planetary Boundary Layer Height and in situ surface observations of atmospheric aerosol pollutants in Athens, Greece. *Atmospheric Environment*. https://doi.org/10.2139/SSRN.4536471 (Under Submission – *Atmospheric Research*).

4. **Foskinis, R.**, Nenes, A., Papayannis, A., Georgakaki, P., Eleftheriadis, K., Vratolis, S., Gini, M. I., Komppula, M., Vakkari, V., & Kokkalis, P. (2022). Towards reliable retrievals of cloud droplet number for non-precipitating planetary boundary layer clouds and their susceptibility to aerosol. *Frontiers in Remote Sensing*, **3**. https://doi.org/10.3389/frsen.2022.958207

5. Papanikolaou, C. A., Kokkalis, P., Soupiona, O., Solomos, S., Papayannis, A., Mylonaki, M., Anagnou, D., Foskinis, R., & Gidarakou, M. (2022). Australian Bushfires (2019–2020): Aerosol Optical Properties and Radiative Forcing. *Atmosphere*, *13*(6). https://doi.org/10.3390/ATMOS13060867

6. Papanikolaou, C. A., Papayannis, A., Mylonaki, M., **Foskinis, R.**, Kokkalis, P., Liakakou, E., Stavroulas, I., Soupiona, O., Hatzianastassiou, N., Gavrouzou, M., Kralli, E., & Anagnou, D. (2022). Vertical Profiling of Fresh Biomass Burning Aerosol Optical

Properties over the Greek Urban City of Ioannina, during the PANACEA Winter Campaign. *Atmosphere*, *13*(1). https://doi.org/10.3390/ATMOS13010094

7. Mylonaki, M., Papayannis, A., Papanikolaou, C.-A., **Foskinis, R.**, Soupiona, O., Maroufidis, G., Anagnou, D., & Kralli, E. (2021). Tropospheric vertical profiling of the aerosol backscatter coefficient and the particle linear depolarization ratio for different aerosol mixtures during the PANACEA campaign in July 2019 at Volos, Greece. *Atmospheric Environment*, *247*, 118184. https://doi.org/10.1016/j.atmosenv.2021.118184

8. Mylonaki, M., Papayannis, A., Anagnou, D., Veselovskii, I., Papanikolaou, C. A., Kokkalis, P., Soupiona, O., **Foskinis, R.**, Gidarakou, M., & Kralli, E. (2021). Optical and microphysical properties of aged biomass burning aerosols and mixtures, based on 9-year multiwavelength raman lidar observations in athens, greece. *Remote Sensing*, *13*(19). https://doi.org/10.3390/RS13193877

9. Kokkalis, P., Soupiona, O., Papanikolaou, C. A., **Foskinis, R.**, Mylonaki, M., Solomos, S., Vratolis, S., Vasilatou, V., Kralli, E., Anagnou, D., & Papayannis, A. (2021). Radiative effect and mixing processes of a long-lasting dust event over athens, greece, during the COVID-19 period. Atmosphere, 12(3). https://doi.org/10.3390/ATMOS12030318

10. Soupiona, O., Papayannis, A., Kokkalis, P., **Foskinis, R.**, Sánchez Hernández, G., Ortiz-Amezcua, P., Mylonaki, M., Papanikolaou, C. A., Papagiannopoulos, N., Samaras, S., Groß, S., Mamouri, R. E., Alados-Arboledas, L., Amodeo, A., & Psiloglou, B. (2020). EARLINET observations of Saharan dust intrusions over the northern Mediterranean region (2014-2017): Properties and impact on radiative forcing. Atmospheric Chemistry and Physics, 20(23), 15147–15166. https://doi.org/10.5194/acp-20-15147-2020

11. Soupiona, O., Papayannis, A., Kokkalis, P., **Foskinis, R.**, Sánchez Hernández, G., Ortiz-Amezcua, P., Mylonaki, M., Papanikolaou, C.-A., Papagiannopoulos, N., Samaras, S., Groß, S., Mamouri, R.-E., Alados-Arboledas, L., Amodeo, A., & Psiloglou, B. (2020). Saharan dust intrusions over the northern Mediterranean region in the frame of EARLINET (2014–2017): Properties and impact in radiative forcing. Atmospheric Chemistry and Physics, 1–22. https://doi.org/10.5194/acp-2020-611

12. Soupiona, O., Samaras, S., Ortiz-Amezcua, P., Böckmann, C., Papayannis, A., Moreira, G. A., Benavent-Oltra, J. A., Guerrero-Rascado, J. L., Bedoya-Velásquez, A. E., Olmo, F. J., Román, R., Kokkalis, P., Mylonaki, M., Alados-Arboledas, L., Papanikolaou, C. A., & **Foskinis, R.** (2019). Retrieval of optical and microphysical properties of transported Saharan dust over Athens and Granada based on multi-wavelength Raman lidar

measurements: Study of the mixing processes. *Atmospheric Environment*, *214*, 116824. https://doi.org/10.1016/j.atmosenv.2019.116824

13. Richardson, S. C., Mytilinaios, M., **Foskinis, R.**, Kyrou, C., Papayannis, A., Pyrri, I., Giannoutsou, E., & Adamakis, I. D. S. (2019). Bioaerosol detection over Athens, Greece using the laser induced fluorescence technique. *Science of The Total Environment*, *696*, 133906. https://doi.org/10.1016/j.scitotenv.2019.133906

14. Bačová, P., **Foskinis, R.**, Glynos, E., Rissanou, A. N., Anastasiadis, S. H., & Harmandaris, V. (2018). Effect of macromolecular architecture on the self-assembly behavior of copolymers in a selective polymer host. *Soft Matter*, *14*(47), 9562–9570. https://doi.org/10.1039/c8sm01421c

POSTER PRESENTATIONS AT INTERNATIONAL CONFERENCES

1. **Foskinis, R.**, Papayannis, A., Nenes, A., Eleftheriadis, K., Vratolis, S., Fetfatzis, P., Gini, M., Diapouli, E., Zografou, O., Granakis, K., Berne, A., Billault-Roux, A.-C. M., Komppula, M., & Vakkari, V. (2023). Evaluating and improving the retrieval of cloud droplet number: case studies in an urban region and orographic environments in the E. Mediterranean. *EGU23*. https://doi.org/10.5194/EGUSPHERE-EGU23-16043

2. Georgakaki, P., Billault-Roux, A.-C., Perrin, E., **Foskinis, R.**, Sotiropoulou, G., Vogel, F., Gini, M., Eleftheriadis, K., Moehler, O., Takahama, S., Berne, A., & Nenes, A. (2023). Unraveling secondary ice production in winter orographic clouds through a synergy of in-situ observations, remote sensing and modeling. *EGU23*. https://doi.org/10.5194/EGUSPHERE-EGU23-14023

3. **Foskinis R.**, Papayannis A., Nenes A., Eleftheriadis K., Vratolis S., Fetfatzis P., Gini M., Spitieri C., Diapouli E., Zografou O., Granakis K., Motos G., Berne A., Billault-Roux A.-C., Komppula M., Vakkari V., Papanikolaou C.-A., Anagnou D., Soupiona O., Kokkalis P. , Mylonaki M., Gidarakou M.-E., Kaltsonoudis C., Moutafidou A., Aktypis A., Vogel F., Möhler O., and S. N. Pandis. Aerosol-Cloud Interaction studies during the CALISHTO-HELMOS Campaign using a synergy of remote sensing and in situ techniques. The 11th International Aerosol Conference (IAC 2022), 4-9 September 2022, Athens, Greece.

4. Möhler O., Vogel F., Fetfatzis P., Gini M., Zografou O., **Foskinis R.**, Höhler K., Lacher L., Nenes A., Eleftheriadis K. Ice-nucleating particle measurements during CALISHTO campaign at Mt. Helmos. The 11th International Aerosol Conference (IAC 2022), 4-9 September 2022, Athens, Greece.

5. Gini M., Fetfatzis P., Zografou O., Granakis K., Spitieri C., Vasilatou V., Diapouli E., **Foskinis R.**, Motos G., Berne A., Billault-Roux A.-C., Kaltsonoudis C., Moutafidou A., Aktypis A., Pandis S. N., Komppula M., Vakkari V., Papanikolaou C.-A., Anagnou D., Soupiona O., Kokkalis P., Mylonaki M., Gidarakou M.-E., Vogel F., Möhler O., Papayannis A., Nenes A., Eleftheriadis K. The CALISHTO-HELMOS Campaign on Aerosol-Cloud Interactions. An overview on aerosol microphysics, composition and origin by means of remote sensing and in situ observations. The 11th International Aerosol Conference (IAC 2022), 4-9 September 2022, Athens, Greece.

6. Papanikolaou C.-A., Papayannis A., Anagnou D., Soupiona O., Kokkalis P., Mylonaki M., Gidarakou M.-E., **Foskinis R**. Extreme Saharan dust event over Athens, Greece (March 2022): aerosol optical properties and radiative impact. The 11th International Aerosol Conference (IAC 2022), 4-9 September 2022, Athens, Greece.

7. Papayannis A., C.- A. Papanikolaou, D. Anagnou, **Foskinis R.**, Moutafidou A., Aktypis A., Eleftheriadis K., Nenes A., Gini M., Motos G., Fetfatzis P., Gidarakou M.-E., Granakis K., Zografou O., Spitieri C., Diapouli E., Komppula M., Vakkari V., Berne A., Vogel F., Möhler O., Kokkalis P., Mylonaki M., Soupiona O., Solomos S., Podvin T., Goloub P., Kaltsonoudis C., Pandis S., Highlights of tropospheric aerosol transport from a coastal to a high-altitude station based on in situ and remote sensing measurements during the CALISHTO-HELMOS Campaign. The 11th International Aerosol Conference (IAC 2022), 4-9 September 2022, Athens, Greece.

8. Papayannis A., Papanikolaou C.-A., Anagnou D., **Foskinis R.**, Soupiona O., Mylonaki M., Gidarakou M.-E. Optical properties and radiative forcing estimations of high-altitude aerosol transport based on laser remote sensing techniques: Highlights from the CLIMPACT Campaign at the Helmos mountain (September 2021). The 11th International Aerosol Conference (IAC 2022), 4-9 September 2022, Athens, Greece.

9. **Foskinis R.**, Papayannis A., Komppula M., Bossioli E., Tombrou M.-T., Soupiona O., Kralli E., Papanikolaou C.-A. & Mylonaki M. Aerosol effects on Low Cloud formation over the Attica region, Greece. The 2nd European Lidar Web Conference, Poster Presentation 18-20 November 2020, Granada, Spain.

10. Richardson S.-C., M. Mytilinaios, **Foskinis R.**, C. Kyrou, A. Papayannis, Pyrri I., Giannoutsou E. & Adamakis IDS. Bioaerosol Detection Over Athens, Greece Using the Laser Induced Fluorescence Technique. The 2nd European Lidar Conference, 18-20 November 2020, Granada, Spain.

11. Mylonaki M., Papayannis A., Papanikolaou C.-A., **Foskinis R.**, Soupiona O. & Maroufidis I., Aerosol Typing from AIAS Depolarization Lidar Data, Observed over Volos City, during PANACEA Campaign, July 2019. The 2nd European Lidar Web Conference, Poster Presentation 18-20 November 2020, Granada, Spain.

12. Soupiona O., **Foskinis R.**, Papayannis A., Sánchez-Hernández G., Ortiz-Amezcua P., Mylonaki M., Papanikolaou C.-A., Alados-Arboledas L. & Psiloglou B., Radiative effects of Saharan dust spheroidal aerosols over the Northern Mediterranean using didin retrieved signals as inputs in LibRadtran model. The 2nd European Lidar Web Conference, Poster Presentation18-20 November 2020, Granada, Spain.

13. Papanikolaou C.-A., Papayannis A., Mylonaki M., Soupiona O., E. Giannakaki & **Foskinis R.**, Australian bushfires during January 2020: biomass burning aerosol properties retrieved from satellite observations. The 2nd European Lidar Web Conference, Poster Presentation 18-20 November 2020, Granada, Spain.

14. Kralli E., Papayannis A., **Foskinis R.**, Soupiona O., Lastic H.-X., Mylonaki M. & Papanikolaou C.-A., Systematic water vapor Raman Lidar Measurements over the free troposphere of Athens, Greece using the EOLE Raman lidar system: Implication for Stratospheric-Tropospheric Exchanges. The 2nd European Lidar Web Conference, Poster Presentation 18-20 November 2020, Granada, Spain.

15. Papayannis A., Papanikolaou C.-A., **Foskinis R.**, Mylonaki M., Soupiona O., Kralli E., Tombrou M.-T., Bossioli E.& Maroufidis I., Saharan Dust Particles Observed by Elastic-Raman Depolarization Lidars over Three Greek Urban Sites (Volos, Ioannina and Athens) During the Panacea Campaigns 2019-2020. The 2nd European Lidar Web Conference, Poster Presentation 18-20 November 2020, Granada, Spain.

16. **Foskinis R.**, Papayannis A., Kokkalis P., Soupiona O., Bossioli E., Tombrou M.-T., Komppula M., Mylonaki M., Papanikolaou C.-A., Anagnou D. & Kralli E. (2020). Study of the Planetary Boundary Layer Height over selected sites in Greece during Panacea Campaigns (2019-2020) using multi-wavelength aerosol systems. The 2nd Scientific Conference PANACEA, Web Conferencing, Poster Presentation, 29 September - 1 October, 2020.

17. Vratolis S., **Foskinis R.**, Fetfatzis P., Gini M., Papayannis A. & Eleftheriadis K. (2020). Comparison of in situ and remote sensing instruments at the Helmos free troposphere background station. The 2nd Scientific Conference PANACEA, Web Conferencing, Poster Presentation, 29 September - 1 October, 2020.

18. Papanikolaou C.-A., M. Mylonaki, Papayannis A., **Foskinis R.**, Soupiona O., Kokkalis P., Kralli. E. & Anagnou D. The impact of biomass burning for heating on Ioannina city air quality during winter time. The 2nd Scientific Conference PANACEA, Web Conferencing, Oral Presentation, 29 September - 1 October, 2020.

19. Soupiona O., Papayannis A., Bossioli E., Methymaki G., Tombrou M., **Foskinis R.**, Mylonaki M., Papanikolaou C.-A., Anagnou D. & Kralli E. (2020). Aerosol optical, chemical and radiative properties of a 3-day dust event observed over Athens, Greece using laser remote sensing and modeling. The 2nd Scientific Conference PANACEA, Web Conferencing, Poster Presentation, 29 September - 1 October, 2020.

20. Papayannis A., Mylonaki M., Papanikolaou C.-A., Kokkalis P., Soupiona O., **Foskinis R.**, Kralli E. & Anagnou D. (2020). Intercomparison of three collocated multi-wavelength aerosol laden systems at the National Technical University of Athens' Campus during 2020 (May, July and September 2020). The 2nd Scientific Conference PANACEA, Web Conferencing, Poster Presentation, 29 September - 1 October, 2020.

21. Stathopoulos VK., Soupiona O., Korras-Carraca M.-B., Samaras S., Papayannis, A., Mylonaki M., Papanikolaou C.-A., **Foskinis R.**, Hatzianastassiou N., Vardavas I. & Matsoukas C ., Case study analysis of aerosol shortwave radiative forcing over Athens, using the FORTH radiative transfer model, multi-wavelength Raman-lidar measurements and satellite observations. The 2nd Scientific Conference PANACEA, Web Conferencing, Oral Presentation, 29 September - 1 October, 2020.

22. **Foskinis R.**, Papayannis A., Mylonaki M, Papanikolaou C.-A., Soupiona O., Kralli E. & Solomos S. (2019). Lee-Wave Cloud observed by simultaneous Lidar profiling and satellite observations during the 1st PANACEA Greek Campaign, The 1st Scientific Conference PANACEA, University of Crete, Heraklion, Oral Presentation, Heraklion, 23-24 September, 2019.
23. Georgakaki P., Bossioli E., **Foskinis R.**, Sotiropoulou G., Papayannis A., Savre J., Ekman A., Nenes A. & Tombrou M.-T., Cloud formation in a marine environment. A simulation approach. The 1st Scientific Conference PANACEA, University of Crete, Heraklion, Oral Presentation, Heraklion, 23-24 September, 2019.

24. Mylonaki M., Papayannis A., Papanikolaou C.-A., Soupiona O., **Foskinis R.**, P. Kokkalis, Kralli E., Karagiozidis D. & Bais A., Highlights of the vertical distribution of the Aerosol Optical and Geometrical properties retrieved over the city of Volos, Greece, during the 1st PANACEA campaign (July 2019). The 1st Scientific Conference PANACEA, University of Crete, Heraklion, Oral Presentation, Heraklion, 23-24 September, 2019.

25. Papanikolaou C.-A., Mylonaki M., Soupiona O., Alexandros Papayannis, **Foskinis R.** & Kralli E., Aerosol Detection in the Free Troposphere over the city of Volos, Greece, during the 1st PANACEA campaign (July 2019). The 1st Scientific Conference PANACEA, University of Crete, Heraklion, Poster Presentation, Heraklion, 23-24 September, 2019.

26. Papayannis A., Vassilatou V., Mylonaki M., Papanikolaou C.-A., Vratolis S., Eleftheriadis K., **Foskinis R.**, Soupiona O., Kralli E. & Saharidis G. Vertical Profiling and characterization of Aerosols in the planetary boundary layer retrieved over the city of Volos, Greece, during the 1st PANACEA campaign (July 2019). The 1st Scientific Conference PANACEA, University of Crete, Heraklion, Poster Presentation, Heraklion, 23-24 September, 2019.

27. **Foskinis R.**, Papayannis A., Soupiona O., Kokkalis P., Mylonaki M., Papanikolaou C.-A., Argyrouli A., Komppula M., Vratolis S., Eleftheriadis K., A Case Study of Interaction Between Aerosols and Clouds based on HYGRA Campaign Measurements. Proc, The 29th International Laser Radar Conference, Poster Presentation, 24-28 June 2019, Hefei China.

28. Richardson S.-C., Mytilinaios M., **Foskinis R.**, Kyrou C., Papayannis A., Pyrri I., Giannoutsou E., Adamakis IDS,Pollen Detection over Athens, Greece, using the Laser Induced Fluorescence Multi-Spectral LiDAR Technique. Proc, The 29th International Laser Radar Conference, Poster Presentation, 24-28 June 2019, Hefei China.

29. Papayannis, Kokkalis P., Mylonaki M., R. Soupiona, Papanikolaou C.-A., **Foskinis R.**, and Giakoumaki A., Recent Upgrades of the EOLE and AIAS LiDAR Systems of National Technical University of Athens Operating since 2000 in Athens, Greece. Proc, The 29th International Laser Radar Conference, Poster Presentation, 24-28 June 2019, Hefei China.

30. Soupiona O., Böckmann C., Papayannis A., Mylonaki M., Kokkalis P., Papanikolaou C.-A. & **Foskinis R.**, Lidar-based inversions of aerosol microphysical parameters from long-range transported events over Athens. Proc. 1st European Lidar Conference, Poster Presentation, 3-5 July 2018, Thessaloniki, Greece.

31. Papayannis A., Mylonaki M., Soupiona O., Kokkalis P., G. Tsaknakis, Papanikolaou C.-A. & **Foskinis R.**, Highlights of biomass burning events from 10-year profiling over

Athens, Greece in the framework of EARLINET (2007-2017), Proc. 1st European Lidar Conference, Poster Presentation, 3-5 July 2018, Thessaloniki

32. Gavriil P., Georgakaki P., Granakis K., Lalos K., Lamprinidou S., Mylonaki M., Papanikolaou C.-A., Tsikoudi I., **Foskinis R**. and Giannakaki E. Study of the air quality levels for a 10-year period in the greater Athens, COMECAP 2018 14th International Conference on Meteorology, Climatology and Atmospheric Physics, October 15-17, 2018, Alexandroupolis, Greece.

PARTICIPATION IN CONFERENCES AND TRAININGS

1. The 1st European Lidar Conference, 3-5 July 2018, Thessaloniki, Greece.
2. The 14th International Conference on Meteorology Climatology and Atmospheric Physics (COMECAP 2018), October 15-17, 2018, Alexandroupolis, Greece.
3. The 2nd ACRIS-Cloudnet Training, 11-15 March 2019, LMU Munich, Germany.
4. The 29th International Laser Radar Conference, 24-28 June 2019, Hefei China.
5. The 1st Scientific Conference PANACEA, 23 - 24 September 2019, Heraklion, Crete, Greece.
6. The 2nd Scientific Conference PANACEA, 18-20 September 2020, Web-Conference, Greece.
7. EUMETSAT 2021 - Meteorological Satellite Conference, 20-24 September 2021, Virtual.
8. 11th International Aerosol Conference (IAC 2022), 4-9 September 2022, Athens, Greece.
9. European Geosciences Union EGU23 General Assembly, 23–28 April 2023, Vienna, Austria.